THREE-DIMENSIONAL NON-LINEAR FINITE ELEMENT ANALYSIS OF REINFORCED CONCRETE BEAMS IN TORSION

Reinforced concrete members under torsion and bending are analysed up to failure. A non-linear concrete model for general states of stress including compressive strength degradation due to cracking is described.

Ihsan Ali Saib AL-SHAARBAF

Bsc., Msc.

Submitted for the degree of
Doctor of Philosophy

Department of Civil Engineering

University of Bradford

1990

ABSTRACT

Three-dimensional non-linear finite element analysis of reinforced concrete beams in torsion.

I.A.S. Al-Shaarbaf, Bsc., Msc.

Keywords: Torsion, Non-linear, Finite element, Three-dimensional, Reinforced concrete, Beams, Cracking, Plasticity, Shear, Bending.

This thesis describes a non-linear finite element model suitable for the analysis of reinforced concrete, or steel, structures under general three-dimensional states of loading. The 20 noded isoparametric brick element has been used to model the concrete and reinforcing bars are idealised as axial members embedded within the concrete elements. The compressive behaviour of concrete is simulated by an elasto-plastic work hardening model followed by a perfectly plastic plateau which is terminated at the onset the crushing. In tension, a smeared crack model with fixed orthogonal cracks has been used with the inclusion of models for the retained post-cracking stress and the reduced shear modulus.

The non-linear equations of equilibrium have been solved using an incremental-iterative technique operating under load control. The solution algorithms used are the standard and the modified Newton-Raphson methods. Line searches have been implemented to accelerate convergence. The numerical integration has been generally carried out using 15 point Gaussian type rules. Results of a study to investigate the performance of these rules show that the 15 point rules are accurate and computationally efficient compared with the 27(3X3X3) point Gaussian rule.

The three- dimensional finite element model has been used to investigate the problem of elasto-plastic torsion of homogeneous members. The accuracy of the finite element solutions obtained for beams of different cross-sections subjected to pure and warping torsion have been assessed by comparing them with the available exact or approximate analytical solutions.

Because the present work is devoted towards the analysis of reinforced concrete members which fail in shear or torsional modes, the computer program incorporates three models to account for the degradation in the compressive strength of concrete due to presence of tensile straining of transverse reinforcement. The numerical solutions obtained for reinforced concrete panels under pure shear and beams in torsion and combined torsion and bending reveal that the inclusion of a model for reducing the compressive strength of cracked concrete can significantly improve the correlation of the predicted post-cracking stiffness and the computed ultimate loads with the experimental results.

Parametric studies to investigate the effects of some important material and solution parameters have been carried out. It is concluded that in the presence of a compression strength reduction model, the tension-stiffening parameters required for reinforced concrete members under torsion should be similar to those used for members in which bending dominates.

CONTENTS

To my parents

ACKNOWLEDGEMENTS

The Author would like to express his gratitude to Dr. I.M May for his supervision, valuable advice and encouragement throughout the course of this work.

A special word of thank goes to my colleagues, Dr. J. Naji, N. Al-Ramadhani, and W. Tizani for many useful discussions.

My thanks are due to the staff of the Computer Centre of the University of Bradford in particular Miss. S. Erye for her help and cooperation.

The scholarship of the Ministry of Higher Education of the Republic of Iraq to this research is gratefully acknowledged.

Finally, I would like to express my gratitude to my wife for her patience and constant encouragement throughout the research period.

NOTATIONS

The major symbols used in the text are listed below, others are defined as they first appear. When duplication occurs, the notation used is clearly defined within the text.

General Symbols

A, a	scalars
$\underset{\sim}{A}$, $\underset{\sim}{a}$	matrix $\underset{\sim}{A}$, and vector $\underset{\sim}{a}$
$\underset{\sim}{A}^T$, $\underset{\sim}{a}^T$	transpose of matrix $\underset{\sim}{A}$ and vector $\underset{\sim}{a}$
$\underset{\sim}{A}^{-1}$	inverse of matrix $\underset{\sim}{A}$
d, ∂	differentiation symbols
Δ	denotes incremental quantity
δ	denotes iterative quantity
| |	determinant of a matrix, or absolute value
|| ||	norm symbol

Scalars

A_0	cross-sectional area bounded by centroidal line of equivalent compression stress block
A_1	cross-sectional area bounded by centre line of a closed stirrup
A_2	cross-sectional area bounded by the lines connecting the centres of the corner longitudinal bars
A_c	cross-sectional area within the outer perimeter of concrete
A_l	cross-sectional area of the total longitudinal bars
A_s	cross-sectional area of a reinforcing bar

A_t cross-sectional area of one stirrup leg

b width of a rectangular cross-section, or width of a flange in a flanged section

b_w thickness of the web of a flanged section

c material constant

c_p pasticity coefficient

$d\lambda$ plastic multiplier

E modulus of elasticity

E_s modulus of elasticity of reinforcing bars

f function

f'_c uniaxial compressive strength of concrete

f_l allowable stress of longitudinal bars

f_{ly} yield strength of longitudinal bars

f_r modulus of rupture of concrete

f_s allowable stress of stirrups

f_{sy} yield strength of stirrups

f_t uniaxial tensile strength of concrete

G shear modulus

G_f fracture energy

h height of a cross-section

h_f thickness of the flange

H' hardening parameter

I_1 first stress invariant

I'_1 first strain invariant

I_2 second stress invariant

I_3 third stress invariant

J Jacobian

J_2 second deviatoric stress invariant

J'_2 second deviatoric strain invariant

J_3 third deviatoric stress invariant

k ratio of the average concrete compression stress to the peak stress

k_1 concrete compressive strength reduction parameter

l length of a cantilever

l_c crack characteristic length

m ratio of volumes of longitudinal bars to stirrups

p_1 perimeter of the centre line of a stirrup

p_c outer perimeter of concrete cross-section

r radius of a circular cross-section

S surface area

s spacing between stirrups

T applied torque

T_c torsional moment contributed by concrete

T_e elastic torque

T_{ep} elasto-plastic torque

T_n nominal torsional strength of a cross-section

T_p plastic torque

T_0 fully plastic torque in presence of warping restraint

t_d depth of the equivalent compression stress block

u perimeter of the area A_1

V volume

W work, or weight of a sampling point

W_c unit weight of concrete

w crack width

x shorter side of a cross-section

x_1 smaller centre to centre dimension of a stirrup

y longer side of a cross-section

y_1 larger centre to centre dimension of a stirrup

C,S	direction cosines of in-plane principal stresses
l,m,n	direction cosines of principal stresses
u,v,w	displacement components
x,y,z	cartesian coordinates
α	angle of inclination of concrete struts, or material constant
α_1,α_2	tension-stiffening parameters
α_e	elastic torsion coefficient
α_p	plastic torsion coefficient
β	shear retention factor, or material constant
γ	shear strain
$\gamma_1,\gamma_2,\gamma_3$	shear retention parameters
ϵ	strain
ϵ_{cu}	ultimate strain
ϵ_p	effective plastic strain
ϵ_0	strain corresponding to peak uniaxial compressive stress
ϵ_0'	total strain corresponding to the parabolic part of uniaxial compressive stress-strain curve
λ	compressive strength reduction factor of concrete
η	step length factor
θ	angle of twist per unit length
λ_s	efficiency coefficient of reinforcement
ν	Poisson's ratio
σ	stress
σ_0	effective stress at onset of plastic deformation
$\bar{\sigma}$	effective stress
τ	shear stress
τ_n	torsional stress
Φ	total potential energy
ψ	convergence tolerance for line search, or warping function

ξ, η, ζ natural coordinates

Matrices

$\underset{\sim}{A}$ displacement gradient matrix

$\underset{\sim}{B}$ strain displacement matrix

$\underset{\sim}{D}$ constitutive matrix

$\underset{\sim}{J}$ Jacobian matrix

$\underset{\sim}{K}$ stiffness matrix

$\underset{\sim}{N}$ shape functions

$\underset{\sim}{T}$ transformation matrix

$\underset{\sim}{T}_p$ in-plane transformation matrix

$\underset{\sim}{\alpha}$ diagonal acceleration matrix

Vectors

$\underset{\sim}{a}$ nodal displacement, or flow vector

$\underset{\sim}{b}$ body forces

$\underset{\sim}{f}$ external load vector

$\underset{\sim}{p}$ internal load vector

$\underset{\sim}{r}$ residual load vector

$\underset{\sim}{t}$ surface tractions

$\underset{\sim}{u}$ displacement vector

$\underset{\sim}{\varepsilon}$ strain vector

$\underset{\sim}{\sigma}$ srtess vector

Subscripts and Superscripts

c concrete

cr	cracking
e	elastic component, or element quantity
ep	elasto-plastic
n	normal
p	plastic component
s	steel
T	tangential
t	tension
y	yielding
x,y,z	denotes cartesian coordinates
1,2,3	denotes principal directions
'	prime denotes local quantity

CHAPTER ONE

INTRODUCTION AND REVIEW OF PREVIOUS WORK

1.1 Introduction

Many reinforced concrete structures and parts of structures are subjected to large torsional moments in addition to bending and shear. Typical cases are space frames, spandrel beams, beams supporting balconies or cantilever slabs, spiral staircases, horizontally curved beams, skew bridges, ... etc. However, despite the fact that torsional stresses can frequently occur, torsion was generally ignored in design of reinforced concrete members before the 1960s. The large safety factors incorporated in flexural design were assumed to be sufficient to accomodate the effects of torsion. This assumption has been responsible for many cases of torsional distress and failure [1].

Torsion has been assigned an increasingly greater importance by engineers since the 1960s when the new ultimate strength design methods were introduced. In these methods, flexural analysis of reinforced concrete members was refined and safety factors were more accurately defined so that torsion must be accounted for explicitly. Moreover, the rapid advances in the applications of computers to structural analysis allowed designers to consider torsion with a minimum of effort.

Although reinforced concrete members are rarely designed to resist torsion alone, most of the experimental ivestigations to understand the basic torsional behaviour have been carried out under this condition. Some experimental tests have also been conducted to investigate the interaction between torsion, shear and bending. As a result of this work design recommendations have been included in various national Codes of practice. In 1969, the first ACI torsion design criteria were formulated based on extensive experimental research during 1960s promoted by ACI Committee 438. The criteria were incorporated in the design provisions of the 1971 ACI Building Code [2]. The British Code [3], on the other hand, included recommendations for torsion design for the first time in 1972.

Current design methods utilise the various versions of the space truss analogy and the skew-bending theory developed to predict the torsional strength of reinforced concrete members. Unfortunately, the first space truss theory developed by Rausch [4] in 1929 overestimates the actual torsional strength. Since then extensive experimental and theoretical studies have been carried out to investigate the behaviour of reinforced concrete members under torsion and to modify Rausch's theory. However, in spite of the extensive work, there are still aspects of torsional behaviour which are not well understood. In fact, the skew-bending theory and most of the modified space truss analogies are actually based on arbitrary assumptions to bring design formulae in line with test results and no fully rational method for torsion design has been yet evolved.

At present, the finite element method offers a powerful and general analytical and research tool to investigate the behaviour of

reinforced concrete structures. In this method, the different aspects of behaviour previously ignored or treated in a very approximate way can be modelled rationally. These aspects include cracking, tension-stiffening, non-linear multiaxial material properties, complex steel-concrete interface behaviour and so on. For members in which torsion or shear dominates, an important aspect which affects both the structural response and the ultimate strength is the degradation of concrete compressive strength in the presence of transverse tensile straining. This aspect of behaviour can be accurately simulated within the material model used in the finite element analysis

Applications of the finite element method to reinforced concrete non-linear behaviour are mainly devoted to study flexure and shear. This is because most of the available models utilise the two-dimensional finite element idealisation. Such an idealisation is not suitable for investigating torsion once cracking of concrete occurs because the behaviour becomes three-dimensional. Therefore, a full three-dimensional non-linear finite element model is required to study the behaviour of reinforced concrete members under torsion.

The three-dimensional finite element idealisation can also be successfully used to investigate elasto-plastic torsion of homogeneous solid members. For this problem, the exact expressions are only available for circular shafts and prismatic beams with long narrow rectangular cross-sections [5]. Furthermore, approximate analytical solutions have only been obtained for prismatic members with relatively simple cross-sections. In this field of application, the finite element method can offer solutions for non-prismatic

members of irregular as well as regular cross-sections under general loading.

1.2 Review of Previous Work

In this section a review of the research into the elasto-plastic torsion of homogeneous members under torsion is given. The theories developed to predict the torsional strength of plain and reinforced concrete members are also described. A comprehensive discussion of these theories and their applications is given by Hsu [1].

1.2.1 Torsion of Homogeneous Elastic and Plastic Members

Attempts to analyse problems involving torsion go back a long way. In 1784, Coulomb [6] found that the torsional moment of an elastic circular shaft was proportional to the twisting angle. A theoretical equation for torsion of an elastic circular member was derived by Navier [7] in 1826. Three decades later and after the development of the necessary mathematical tools, Fourier series and theory of elasticity, Saint-Venant [8] used the semi-inverse method to solve the problem of pure torsion of elastic non-circular members and predicted a precise expression for the warping of cross-sections.

In 1903, Prandtl [9] showed the similarity between the stress function in the torsion problem and the deflection of a uniformly tensioned thin elastic membrane loaded by a uniform pressure. Prandtl's membrane analogy was extended to the case of plastic

material when Nadai [10] applied the sand heap analogy to calculate the fully plastic torque of solid sections. Sadowsky [11] extended Nadai's sand heap analogy to apply to plastic sections with holes.

Although the analytical solutions for elastic or perfectly plastic sections are available, solutions for cross-sections which are partly elastic and partly plastic are extremely complex because of the difficulty of locating the elasto-plastic boundaries. The boundaries between the elastic and the plastic regions move with changes of the applied torque. Therefore, numerical methods such as the finite differences method and the finite element method have to be used to achieve solutions for this type of problem. The available analytical and numerical investigations for elasto-plastic members under torsion are summarised in the following section.

1.2.1.1 Torsion of elasto-plastic members

For non-circular members which have elasto-plastic material properties subjected to pure torsion, analytical solutions have been only obtained for prismatic bars of simple cross-sections. Sokolovsky [12] obtained an analytical elasto-plastic solution for an oval section and Christopherson [13] used relaxation methods to find the elasto-plastic solution for an I-section. Nadai [14] obtained an approximate solution for various elasto-plastic cross-sections by combining the membrane and the sand heap analogies. Smith and Sidebottom [5] developed an analytical solution for prismatic bars of rectangular cross sections which have elasto-plastic material properties. The analysis is based on the Rayleigh-Ritz expansion and

the principle of stationary complementary energy.

In members with warping restraint, Augusti [15], Boulton [16] and Dinno and Merchant [17] have proposed approximate methods to calculate the fully plastic torque for an I-section cantilever beam. No analytical solutions for elasto-plastic warping torsion have been reported. However, an experimental study of the elasto-plastic behaviour of I-section cantilever beams with warping restraint has been carried out by Dinno and Gill [18].

Numerical solutions for elasto-plastic pure torsion of uniform square solid members using the finite differences method have been given by Greenberg et al [19]. Itani [20] and Yamada et al [21] developed solutions for solid bars under torsion using stress based finite elements. Johnson [22] has analysed torsion in members which have anisotropic material properties using stress functions. Zhen-Sheng [23] used the boundary element method to solve the problem of elasto-plastic torsion of solids of revolution.

Baba and Kajita [24] have developed a special formulation for pure and warping torsion using the finite element displacement method. The formulation is based on a combination of a two noded, 4 degrees of freedom, beam element for torsion analysis and a four noded, 12 degrees of freedom, rectangular 'section-element' for warping analysis of the section. Their non-linear solution strategy is based on the determination of the warping function according to the state of stress distribution, and the stress distribution is again determined according to the newly obtained warping function. Bathe and Chaudhary [25] proposed warping displacement functions for

beams of rectangular cross-sections, these functions were employed in the formulation of a 2 noded Hermitian based beam element and the formulation of a variable number of nodes isoparametric beam element so as to make these elements applicable to linear and non-linear analysis of torsion. Rajasekaran [26] described a general formulation for the elasto-plastic warping torsion of a thin-walled beam using a one-dimensional beam element. Bathe and Wiener [27] used the Hermitian beam element and the 9 noded shell element to solve the elasto-plastic problem for I-beams with warping restraint.

1.2.2 Torsion of Plain Concrete Members

The torsional behaviour of plain concrete rectangular members can be demonstrated by the series of experimental torque-twist curves shown in Fig. 1.1. The behaviour is essentially linear at low torques becoming slightly non-linear at higher torques. Failure is brittle and the members fail by a bending mechanism about an axis parallel to the wider face at an angle of 45 degrees to the longitudinal axis of the member [1,28]. Three approaches have been developed to predict the torsional strength of plain concrete members. These are based on elastic theory, plastic theory and skew-bending theory. Each of the approaches are discussed briefly in the following sections.

1.2.2.1 Elastic theory

The elastic approach assumes that the concrete is a homogeneous material and the stresses are distributed according to Saint-Venant's

theory. Torsional failure of a plain concrete member occurs when the maximum principal tensile stress equals the concrete tensile strength, f_t. For a rectangular member, the elastic failure torque, T_e, can be expressed as:

$$T_e = \alpha_e x^2 y f_t \qquad (1.1)$$

Where x and y are the shorter and the longer sides of the cross-section respectively and α_e is Saint Venant's coefficient which is a function of the ratio y/x. α_e varies from 0.208 for y/x = 1.0 to 0.333 for y/x = ∞. Experimental tests have shown that the actual ultimate strength is about 50% greater than that predicted by equation (1.1) [28].

1.2.2.2 Plastic theory

To account for the excessive observed strength, Nylander [29] proposed to replace Saint Venant's elastic coefficient α_e by a plastic coefficient α_p. This approach assumes a plastic distribution for the torsional shear stresses throughout the section. Failure is assumed to occur when the concrete tensile strength is exceeded. By applying the sand heap analogy, the plastic failure torque, T_p, of a rectangular member can be expressed as:

$$T_p = (0.5 - x/6y) x^2 y f_t = \alpha_p x^2 y f_t \qquad (1.2)$$

The plastic coefficient varies from 0.333 for y/x = 1.0 to 0.5 for y/x = ∞.

Although the plastic theory is able to account approximately for the observed extra strength, the approach is theoretically unsound because no significant plastic rotation has been observed and the failure is quite brittle, Fig. 1.1. In addition, the theory can not account for size effects observed in the tests. Experimental tests indicate that as the size of the member becomes smaller the calculated plastic torques are usually smaller than test values [28].

1.2.2.3 Skew-bending theory

Because of the difficulties involved in applying the classical elastic and plastic theories to plain concrete members, Hsu [28] investigated the torsional failure mechanism of rectangular beams using a high speed movie camera. The movie showed that the first crack appeared at the front face of the beam at an angle of 45 degrees to the longitudinal axis of the beam. The crack gradually widened and spread across the top of the beam. Finally, the concrete crushed on the back face. Failure was similar to that of a plain concrete flexural member. These characteristics were noted earlier by Marshal and Tembe [30].

Based on the use of a bending mechanism for torsional failure, Hsu [28] derived, for the ultimate torsional strength of a plain concrete member, the expression

$$T_n = \frac{1}{3} x^2 y \, (0.85 f_r) \qquad (1.3)$$

where f_r is the modulus of rupture of concrete. The reduction

factor, 0.85, appears in the equation to account for the effect of the orthogonal principal compressive stress on the tensile strength of the concrete. It may be noted that for an element on the surface of a member loaded in pure torsion, the resulting state of pure shear is equivalent to equal tension and compression principal stresses. Tests by McHenry and Karni [31] have shown that the presence of compressive stress perpendicular to the applied tension stress will reduce the tensile strength by about 15%. Consequently, the modulus of rupture should be also reduced by a factor of 0.85.

Comparing the elastic, plastic and skew-bending theories, it can be seen that they all include the same geometric parameter x^2y. They only differ in the values of the non-dimensional coefficient and the material strength properties.

For the flanged sections commonly used in practice such as T, L and I sections, the torsional strength can be calculated approximately using equations (1.1-1.3). For these sections, the total torsional strength is taken as the sum of the torsional strengths of each of the component rectangles [1].

1.2.3 Torsion of Reinforced Concrete Members

Concrete members subjected to torsion can be reinforced either with longitudinal bars only or with longitudinal bars and stirrups. The former type was found ineffective in resisting torsional moments after cracking. In the case of heavy reinforcement, the ultimate torque may at most exceed the cracking torque by about 15% [1].

Therefore, members reinforced with longitudinal steel alone do not have significant practical importance and can be treated as plain concrete members for calculating the torsional strength.

To resist torsion, reinforcement must consist of longitudinal bars and closed stirrups. Fig. 1.2 shows the torque-twist curves of a series of rectangular beams having the same cross-sections and reinforced with different percentages of longitudinal and transverse reinforcement. Each curve can be divided into two distinct stages of behaviour: these are before and after cracking. Before cracking, the behaviour is essentially similar to that of a plain concrete member. The amount of reinforcement has a negligible effect on the torsional stiffness of the member and therefore Saint Venant's elastic theory can be used to predict the behaviour at this stage.

Immediately after cracking, the angle of twist increases under a constant torque, Fig. 1.2. The stresses in the reinforcement increased suddenly and a new equilibrium configuration is established by transferring the load to the reinforcement.

The cracks were inclined at 45 degrees with the longitudinal axis. They occurred simultaneously on the wider and shorter faces of the member [32]. An interesting phenomenon occurs after cracking in which the length of member increases as the applied torque increases. The lengthening of the member causes the longitudinal bars to stretch. This stretching is necessary to develop tensile forces in the longitudinal bars which are required to maintain post-cracking equilibrium. If a member is restrained longitudinally, which is the case for most edge beams in reinforced concrete buildings, a

compression force will be induced in the member. As a result of this self-generated compression a concentrically prestress force will be induced and therefore the torsional strength will increase [1].

Referring to Fig. 1.2, it can be seen that following to the increase of twist under constant torque the torque–twist curve rises again with a torsional stiffness of only a fraction of that before cracking. The post–cracking torsional stiffness and the ultimate torsional strength are strongly dependent on the percentage of reinforcement provided. At the ultimate stage, the longitudinal bars and the stirrups can both reach yield when small percentages of steel were used, for example beam B2 [32].

The theories developed to calculate the ultimate strength of members reinforced with longitudinal bars and stirrups can be divided into two categories. These are the space truss analogy and the skew–bending theory. In the following sections, these approaches and the improvements they have undergone in recent years are described.

1.2.3.1 Space truss analogy

The first theory to predict the torsional strength of reinforced concrete members was proposed by Rausch [4] in 1929. The theory postulates that a member with an arbitrary solid cross–section is assumed to act like a tube so that the external torsional moment is resisted by the circulatory shear flow in the wall of the tube. Each wall segment of the tube is assumed to act like a plane truss where the longitudinal bars serve as the cord members while the stirrups

and the concrete within the segment serve as the web members. After cracking, the concrete is separated by the diagonal helical cracks into a series of inclined struts. The cracks are assumed to be inclined at 45 degrees to the longitudinal axis of the member. To resist the shear flow caused by the external torque the concrete struts should be in compression, while both the stirrups and the longitudinal bars are in tension.

The theory assumes that the space truss is made up of 45 degree diagonal concrete struts, longitudinal bars and stirrups. The diagonal concrete members carry only axial compression and the reinforcement carries only axial tension, i.e the shear resistance of concrete and the dowel action of reinforcement are neglected. In addition, the concrete core does not contribute to the ultimate torsional resistance. Experimental tests by Hsu [32] revealed that the behaviour close to failure and the ultimate capacity of a solid rectangular member are identical to those of a member of hollow section with the same overall dimensions, material properties and steel arrangement. These results confirmed Rausch's assumption that the torsional moment is carried mainly by the outer shell.

The space truss model considered is shown in Fig. 1.3 for a rectangular hollow member reinforced with four longitudinal corner bars and close stirrups with spacing s. By considering equilibrium conditions for this model, Rausch derived the following expression:

$$T = \frac{2 A_1 A_t f_s}{s} = \frac{2 A_1 A_l f_l}{u} \qquad (1.4)$$

where T is the torsional strength of the member, A_1 is the area bounded by the centre line of a closed stirrup, A_t is the cross-sectional area of the stirrup leg, A_l is the cross-sectional area of the total longitudinal bars, f_s and f_l are the allowable stresses of the stirrups and longitudinal bars respectively and u is the perimeter of the area A_1.

The above expression, which was based on the working stress design method, was adopted by several codes in the 1950s. Using the ultimate strength concept and assuming that both the longitudinal and transverse reinforcement reach yielding, the nominal torsional strength, T_n, can be expressed as:

$$T_n = \frac{2 A_1 A_t f_{sy}}{s} = \frac{2 A_1 A_l f_{ly}}{u} \qquad (1.5)$$

where f_{sy} and f_{ly} are the yield strengths of the stirrups and the longitudinal bars respectively.

Assuming that the stirrups and the longitudinal steel have the same yield stress, the total area of the longitudinal bars can be obtained from (1.5) as

$$A_l = A_t \frac{u}{s} = A_t \frac{2 (x_1 + y_1)}{s} \qquad (1.6)$$

Where x_1 and y_1 are the smaller and the larger centre to centre dimensions of the stirrup. Equation (1.6), which is the so-called equal volume principle, states that the volume of all longitudinal

bars within the spacing s should equal to the volume of one closed stirrup.

Although the space truss concept gives a clear understanding of the main function of concrete and reinforcement in resisting torsion, Rausch's equation significantly overestimates the actual strength of reinforced concrete members [1,32]. For this reason, several approaches have been developed over the past half-century to modify equation (1.5).

The first approach assumes that the reinforcement is only partially efficient. An efficiency factor, which is less than unity, to modify (1.5) was suggested by Andersen [33] in 1934. This is because Rausch's truss analogy assumes uniform stress along all the reinforcement which contradicts Saint Venant's stress distribution. For a rectangular member, the distribution of stresses according to Saint Venant's theory requires that maximum stress occurs at the middle of the wider face of the cross-section and zero stress occurs at the corners. In addition, Andersen suggested that the concrete also contributes to the torsional strength. Hence, in terms of ultimate strength, Andersen's equation can be expressed as:

$$T_n = T_e + \lambda_s \frac{2 A_1 A_t f_{sy}}{s} \qquad (1.7)$$

where T_e is the torsional resistance of the concrete predicted by Saint Venant's theory, equation (1.1), and λ_s is the efficiency coefficient of reinforcement which varies from about 0.667 to 1.0 depending on the shape of the cross-section and the number of

reinforcing bars [1].

Andersen's coefficient has not been widely accepted because it lacks rigour in derivation and is tedious to calculate [1]. In 1950, Cowan [34] obtained a simple and logical efficiency coefficient using the strain energy method and Saint Venant's strain and stress distribution for rectangular cross-sections. It was shown that the coefficient λ_s varies from 0.7898 to 0.844 for y_1/x_1 from 1.0 to 3.0. Taking λ_s as a constant value of 0.8, equation (1.7) can be modified to give

$$T_n = T_e + 1.6 \frac{A_1 A_t f_{sy}}{s} \qquad (1.8)$$

It should be noted that the Saint Venant's stress and strain distribution is only correct before cracking. Tests have shown that the stresses along the longitudinal steel and stirrups are essentially uniform in the post-cracking range and do not vary according Saint Venant's distribution [32].

The second modification to Rausch's equation was to reduce the area A_1 by making an arbitrary definition for the centre line of the shear flow. In 1969, Lampert and Thürlimann [35] assumed that the perimeter connecting the centroids of the corner longitudinal bars represented the centre line of the shear flow. In this approach, the 45 degree truss model is generalised in order for it to apply also for members under combined torsion and bending. It was assumed that the angle of inclination of the concrete struts could deviate from 45 degrees and was taken as a variable. The approach which is known as

the variable-angle truss model was adopted by the CEB-FIP Model Code [36]. According to this model, the torsional strength of a reinforced concrete member is given by

$$T_n = T_{cv} + 2 \frac{A_2 A_t f_{sy}}{s} \cot\alpha \qquad (1.9)$$

where A_2 is the area bounded by the lines connecting the centres of the corner longitudinal bars, α is the angle of inclination of the concrete struts, $3/5 \leq \tan\alpha \leq 5/3$, and T_{cv} is the torsional resistance contributed by concrete given by

$$T_{cv} = T_c \quad \text{for } T_n \leq T_c \qquad (1.10)$$

$$T_{cv} = 0.0 \quad \text{for } T_n \geq 3\ T_c \qquad (1.11)$$

Intermediate values for T_{cv} can be determined by linear interpolation. In the above expressions T_c can be found from

$$T_c = 2.5\ \tau_r\ t_d\ (2\ A_2) \qquad (1.12)$$

where t_d is the effective wall thickness taken as one-sixth of the diameter of the largest circle which can be contained within the area A_2 and

$$\tau_r = \frac{f_t}{4} = \frac{(0.124\ f'_c)^{2/3}}{4} \qquad (1.13)$$

In the above expression the concrete compressive strength f'_c and the tensile strength f_t are in MPa.

Because the longitudinal bars are always placed within the stirrups, the area A_2 will be less than A_1 and therefore the torsional strength obtained by (1.9) will be less than that of (1.5) even with the inclusion of T_{cv} and $\cot\alpha$ [37].

The third approach which was suggested by Collins and Mitchell [38] in 1980 assumes that the centre line of the shear flow coincides with the centroidal line of the equivalent compression stress block. In this approach, the concrete cover outside the centre line of the stirrups is assumed to be ineffective. Hence, the following expression was proposed

$$T_n = 2 \frac{A_0 A_t f_{sy}}{s} \cot\alpha \qquad (1.14)$$

where A_0 is the area bounded by the centroidal line of the equivalent compression stress block. An approximate value of A_0 is given by

$$A_0 = A_1 - p_1 t_d/2 \qquad (1.15)$$

where p_1 is the perimeter of the centre line of a stirrup and t_d is the depth of the equivalent compression stress block given by

$$t_d = \frac{A_1}{p_1} \left\{ 1 - \left[1 - \frac{T_n p_1}{0.85 f'_c A_1^2} \left[\tan\alpha + \frac{1}{\tan\alpha} \right] \right]^{\frac{1}{2}} \right\} \qquad (1.16)$$

Although the expression for the equivalent rectangular compression stress block has been found using both equilibrium and compatibility conditions, Collins and Mitchell's theory invokes the

crude assumption of neglecting the concrete cover. Hsu and Mo [37] have pointed out that the depth t_d calulated from (1.16) is too small because the standard cylinder compressive strength has been assumed for the strength of the concrete struts. In fact, the concrete compressive strength can be substantially degraded by the presence of diagonal cracking. Tests by Robinson and Demoriux [39] and by Vecchio and Collins [40] revealed that the tensile straining of transverse reinforcement can cause a significant reduction in the concrete compressive strength.

In 1985, Hsu and Mo [37] proposed a new variable-angle truss model using a reduced compressive strength for the concrete struts. Based on both equilibrium and compatibility, a set of eight equations were derived to predict the torsional strength, and to determine the angles of twist and the strains in the steel and concrete at any stage of loading. These equations are not suitable for design purposes because they need to be solved by a trial and error procedure. In a second paper, Hsu and Mo [41] proposed several simplifications for design including a simple formula to obtain the depth of the compression stress block and limits on the maximum and minimum reinforcement and concrete cover.

For the truss model proposed by Hsu and Mo, the torsional strength can be calculated using (1.14). In this case, an approximate value of the area bounded by the centroidal line of the equivalent stress block, A_0, is given by

$$A_0 = A_c - p_c\, t_d/2 \qquad (1.17)$$

where A_c is the cross-sectional area within the outer perimeter of concrete and p_c is the outer perimeter of the concrete cross-section. The depth of the equivalent compression stress block is given by

$$t_d = \frac{A_c}{p_c}\left\{1 - \left[1 - \frac{\tau_n}{k\,\lambda\,f'_c}\,\frac{2}{\sin 2\alpha}\right]^{\frac{1}{2}}\right\} \qquad (1.18)$$

where λ is the compression strength reduction factor of concrete, k is the ratio of the average concrete compression stress to the peak stress and τ_n is the torsional stress given by

$$\tau_n = \frac{T_n\,p_c}{A_c^2} \qquad (1.19)$$

Hsu and Mo [41] proposed a simplified form of (1.18) in which $k\lambda$ is taken as 0.4

$$t_d = \frac{A_c}{p_c}\left\{1 - \left[1 - \frac{\tau_n}{0.2\,f'_c}\,\frac{1}{\sin 2\alpha}\right]^{\frac{1}{2}}\right\} \qquad (1.20)$$

This assumption was found to be unsatisfactory because the depth t_d is quite sensitive to the coefficient $k\lambda$. A more logical expression has been obtained using a complex trial and error method for 61 selected specimens from tests reported in the literature. For specimens with equal volume of longitudinal and transverse steel and for which α = 45 degrees, a linear regression gave the following simplified expression

$$\frac{t_d\,p_c}{A_c} = 0.082 + 3.405\,\frac{\tau_n}{f'_c} \qquad (1.21)$$

The effect of α can be incorporated by dividing the right hand side of (1.21) by $\sin 2\alpha$, thus

$$\frac{t_d\, p_c}{A_c} = \left[0.082 + 3.405 \frac{\tau_n}{f_c'} \right] \frac{1}{\sin 2\alpha} \qquad (1.22)$$

1.2.3.2 Skew-bending theory

The second group of theories to determine the ultimate strength of reinforced concrete members under pure torsion and torsion plus bending use the skew-bending approach. The basic characteristic of this approach is the formation of a skew failure surface. The failure surface is initiated by a helical crack along three faces of the member. The ends of the helical crack are connected by a compression zone near the fourth face. The surface intersects both the closed stirrups and the longitudinal steel which are often assumed to reach yield at collapse. Based on this assumption, the torsional strength can be determined by considering the equilibrium of the internal forces which are transmitted across the failure surface.

The first skew-bending theory was proposed by Lessig [42] in 1958 for members subjected to torsion in combination with bending and shear. Two possible modes of failure for a rectangular reinforced concrete beam were suggested. Mode 1 failure, in which the flexure dominates, has the compression zone near the top face of the beam. In mode 2 failure, in which the torsional moment and shear force dominate, the compression zone is along a side face. For each mode of failure, two equilibrium conditions can be established by taking

moments about the neutral axis and resolving forces along the normal to the compression zone. A third equation was obtained by minimising the torsional strength of the member to determine the angle of inclination of the helical crack that initiates the failure surface. The set of the equations produced by Lessig can be solved by a trial and error procedure.

Lessig's theory was simplified and incorporated in the Russain Code of 1962 [43]. An empirical equation to avoid failure by shear was proposed and empirical limits were given in order to prevent the concrete crushing prior to yielding and to ensure yielding of both longitudinal and transverse reinforcement.

In 1968, Hsu [32] conducted a series of tests on solid and hollow rectangular reinforced concrete beams under pure torsion. The skew-bending mechanism of the torsional failure was investigated. It was suggested that to simplify the analysis the failure surface could be taken as a plane inclined at a 45 degrees to the longitudinal axis of the beam, Fig 1.4. By assuming that both the longitudinal bars and the stirrups yield at failure, Hsu derived an expression for the torsional strength of an underreinforced rectangular beam. The derivation is based on the equilibrium of internal forces transmitted across the failure plane. The equation proposed by Hsu is given by

$$T_n = T_c + \alpha_t \frac{x_1\, y_1\, A_t\, f_{sy}}{s} \qquad (1.23)$$

where T_c is the torsional resistance contributed by the concrete and is given by

$$T_c = \frac{x^2 y}{3} \left[2.4 f_c'^{\frac{1}{2}} \right] \qquad (1.24)$$

and α_t is a coefficient given by

$$\alpha_t = 0.66 m \frac{f_{ly}}{f_{sy}} + 0.33 \frac{y_1}{x_1} \leq 1.5 \qquad (1.25)$$

where m is the ratio of the volume of the longitudinal bars to stirrups.

It can be seen that the equation proposed by Hsu which was adopted by the ACI Building Codes since 1971 [2] takes the same form as equations (1.7-1.9) derived using the space truss analogy. The term T_c in (1.23) was originally assumed to be the contribution of the concrete core within the reinforcing cage. However, experimental tests by Hsu [32] revealed that, for the same overall dimensions and reinforcement, the failure torques of solid and hollow rectangular beams are equal. Therefore the term T_c can only be attributed to the contribution of shear resistance of the diagonal concrete struts [1].

The coefficient α_t used in Hsu's equation is considerably less than either Rausch's 2.0 or Cowan's 1.6. Tests by Hsu [32] showed that both Rausch's and Cowan's equations are unconservative. Based on additional experimental investigations carried out since 1968, Hsu [44] has updated the expression for the coefficient α_t to be given by

$$\alpha_t = m^{\frac{1}{2}} \frac{f_{ly}}{f_{sy}} \left[1 + 0.2 \frac{y_1}{x_1} \right] \leq 1.6 \qquad (1.26)$$

1.2.3.3 Finite element models

In the previous sections, the various versions of the space truss analogy and the skew-bending theory have been discussed. These approaches have been used for the design of reinforced concrete members and to predict their ultimate strength. It was found that the first space truss model proposed by Rausch overestimated the actual strength of the members. The various theories suggested to modify Rausch's equation were actually based on arbitrary assumptions such as applying an efficiency factor for reinforcement, assuming an arbitrary definition for the centre line of the shear flow or deleting the concrete cover.

Although these approaches are used for design purposes, they are, apart from the truss model proposed by Hsu and Mo, theoretically unsatisfactory because of the arbitrary assumptions used to bring Rausch's equation in line with test results. The unconservative nature of Rausch's equation is caused by the deterioration of the compressive strength of concrete due to presence of the tensile straining of the transverse reinforcement. This deterioration causes the centre line of the shear flow to shift towards the interior regions of the cross-section. Hence, the lever arms of the internal couples will decrease and finally the torsional resistance will reduce.

From the above it can been seen that the behaviour of reinforced concrete members loaded in torsion has received considerable attention. However, despite the numerous tests carried out on reinforced concrete beams and the significant developments in the

analysis of such members, there are still aspects of the torsional behaviour which are not well understood. The rapid increase in the power of digital computers in terms of both storage capacity and computational cost make it possible to investigate the response of reinforced concrete torsional members using the finite element analysis.

Most finite element models utilise two-dimensional idealisations for the analysis of reinforced concrete members. Very little work has been done to model reinforced concrete members as three-dimensional solids. However, such an idealisation may be necessary even for prismatic members under the relatively common states of loading, for example pure torsion, torsion in combination with bending and biaxial bending.

Mehlhorn and Gönner [45] developed a three-dimensional non-linear elasticity based finite element model. In this model, the 8 noded linear brick element was used to represent concrete. The reinforcement was idealised as discrete bar elements with a linear displacement function. The model was tested using the experimental results for a single reinforced concrete segment loaded in torsion. The finite element solution overestimated the experimental collapse torque. No further details were given in the study.

To predict the torsional strength of reinforced concrete members and in order to understand better their behaviour throughout the entire loading history, Mohamed [46] used a three-dimensional non-linear finite element analysis. In this study, the 20 noded isoparametric brick element and the embedded representation of

reinforcement were used. A non-linear elasticity based material model was adopted for concrete with the inclusion of crushing and cracking cirteria. No attempt was made to model the degradation in the concrete compressive strength due orthogonal cracking. The results of analysis of rectangular beams under pure torsion showed that the best fit to the experimental torque-twist curves was obtained by neglecting the tension-stiffening effects.

1.3 Objectives and Layout of the Thesis

The development of a general three-dimensional finite element model capable of simulating the behaviour of a variety of reinforced concrete structures subjected to general loading states would provided a valuable analytical and research tool. For such a model to succeed, the important material parameters governing the behaviour of reinforced concrete structures must be accounted for. For structures which fail in shear or torsional modes, special emphasis needs to be given to the modelling of the reduction in the concrete compressive strength produced by orthogonal cracking.

The main object of this research was therefore to develop a finite element computer program for the non-linear analysis of three-dimensional reinforced concrete or steel structures under monotonically increasing loads. Analysis of reinforced concrete panels in pure shear, beams in torsion and combined torsion plus bending and voided slab strips in pure bending have been carried out. The computer program has also been used to study the effects of some material and numerical parameters used in the finite element model.

The inclusion of models for both steel and concrete allowed the program to be used also to analyse homogeneous beams which have elasto-plastic material properties and subjected to torsion.

The basic concepts of the finite element method and the derivation of the governing equilibrium equations using the principle of virtual displacements are presented in Chapter 2. The 20 noded isoparametric brick element which has been used to model concrete and the embedded representation of reinforcement are described. The numerical integration rules used to determine the element stiffness matrices are also given.

In Chapter 3, the plasticity model used for concrete in compression and the smeared crack model used for concrete in tension are described together with the elastic linear work-hardening model used for the reinforcement.

Chapter 4 deals with the non-linear solution techniques used to solve the non-linear equations. The incremental-iterative Newton-Raphson methods and the line search technique used in this work are described.

In Chapter 5, analyses of elasto-plastic homogeneous beams loaded in torsion are described. The finite element solutions are compared with exact or approximate analytical solutions. Parametric studies to investigate the effects of mesh refinement, different types of element and integration rule are also described.

Chapter 6 deals with the analyses of reinforced concrete panels

loaded in pure shear and voided slab strips under pure bending. A study of the effect of reducing the concrete compressive strength in presence of orthogonal cracking is given.

In Chapter 7, The results of analysing a series of reinforced concrete rectangular beams under pure torsion and torsion plus bending are presented. The numerical tests carried out are compared with experimental results. A parametric study to investigate the effects of some of the material and numerical parameters is also presented.

Finally, Chapter 8 summarises the conclusions drawn from this research. Recommendations and suggestions for future work are given.

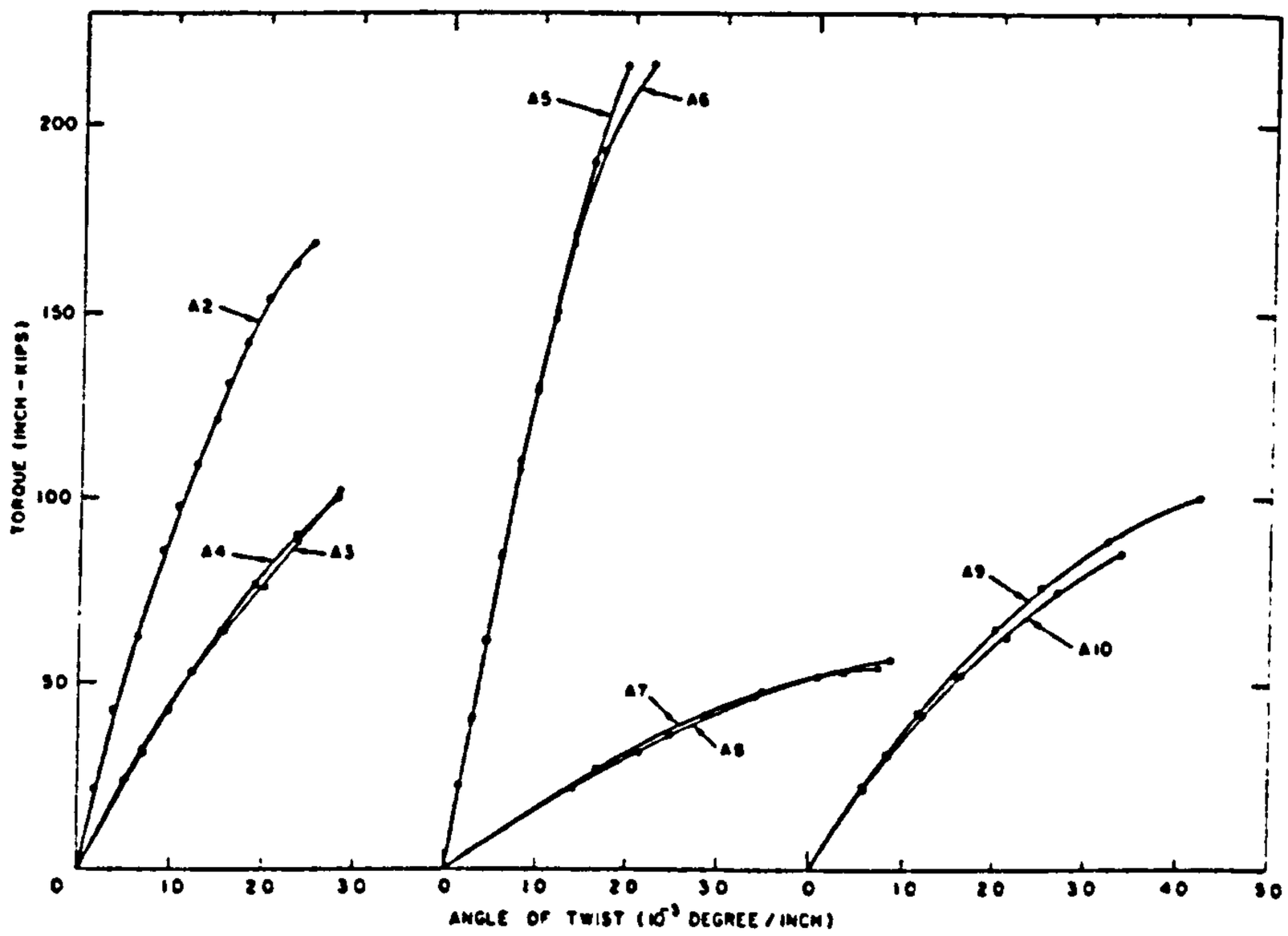

Fig. 1.1 Torque-twist curves of plain concrete beams (series A in Ref. 28).

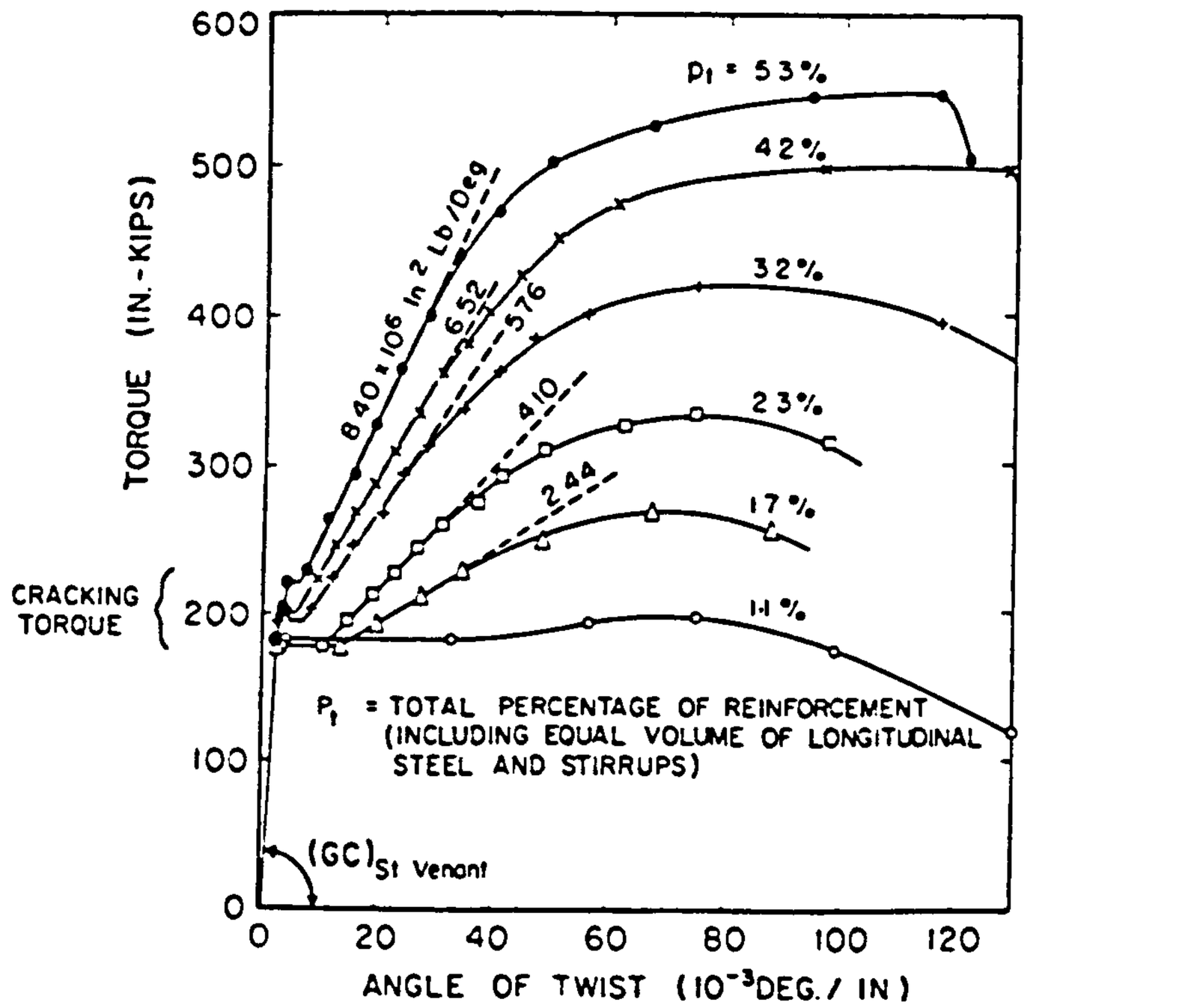

Fig. 1.2 Torque-twist curves of beams with various percentages of reinforcement (series B in Ref. 32).

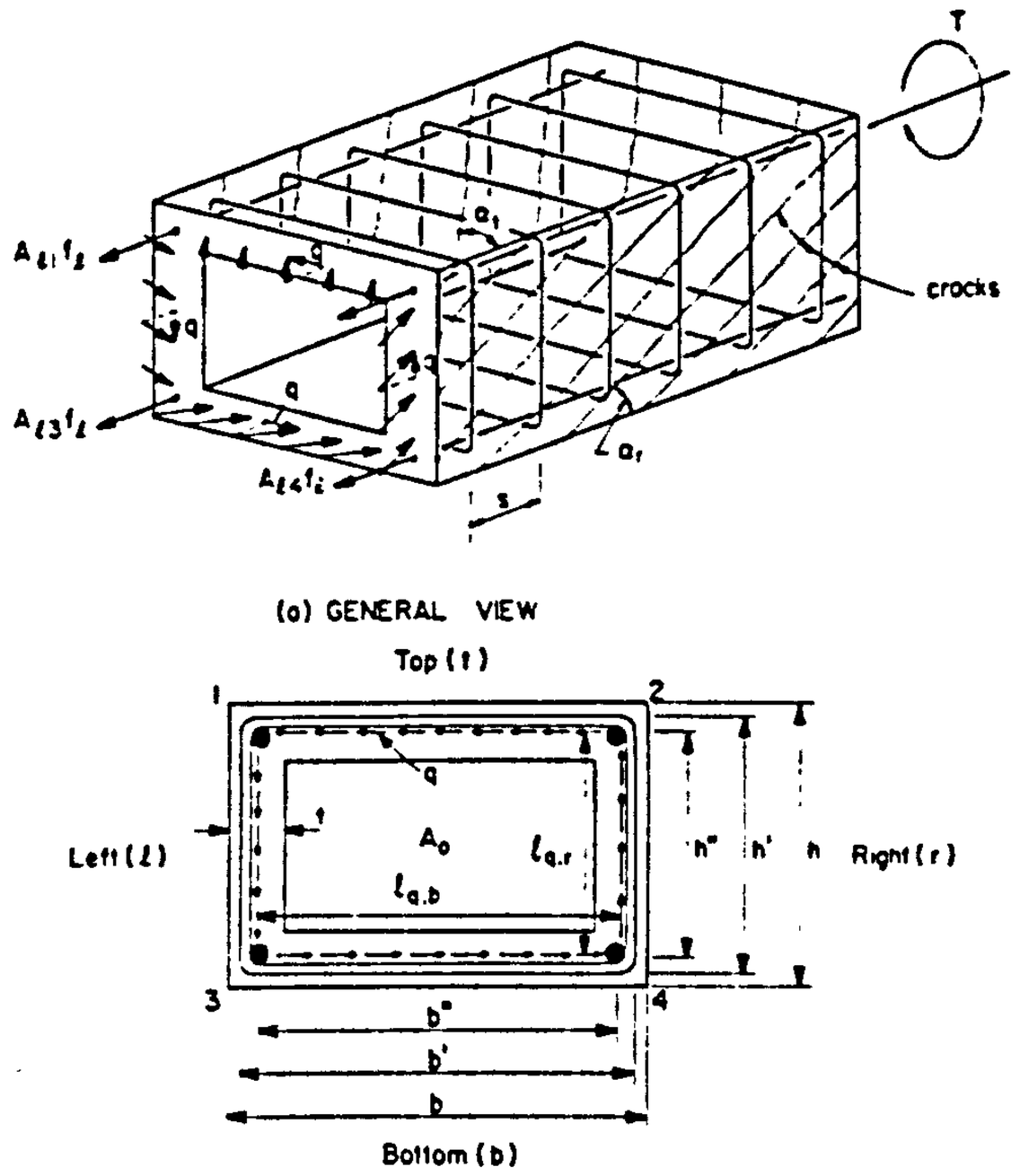

(a) GENERAL VIEW

Top (t)

(b) CROSS SECTION AND NOTATIONS

Fig. 1.3 Space truss model for a hollow rectangular reinforced concrete beam (Ref. 1).

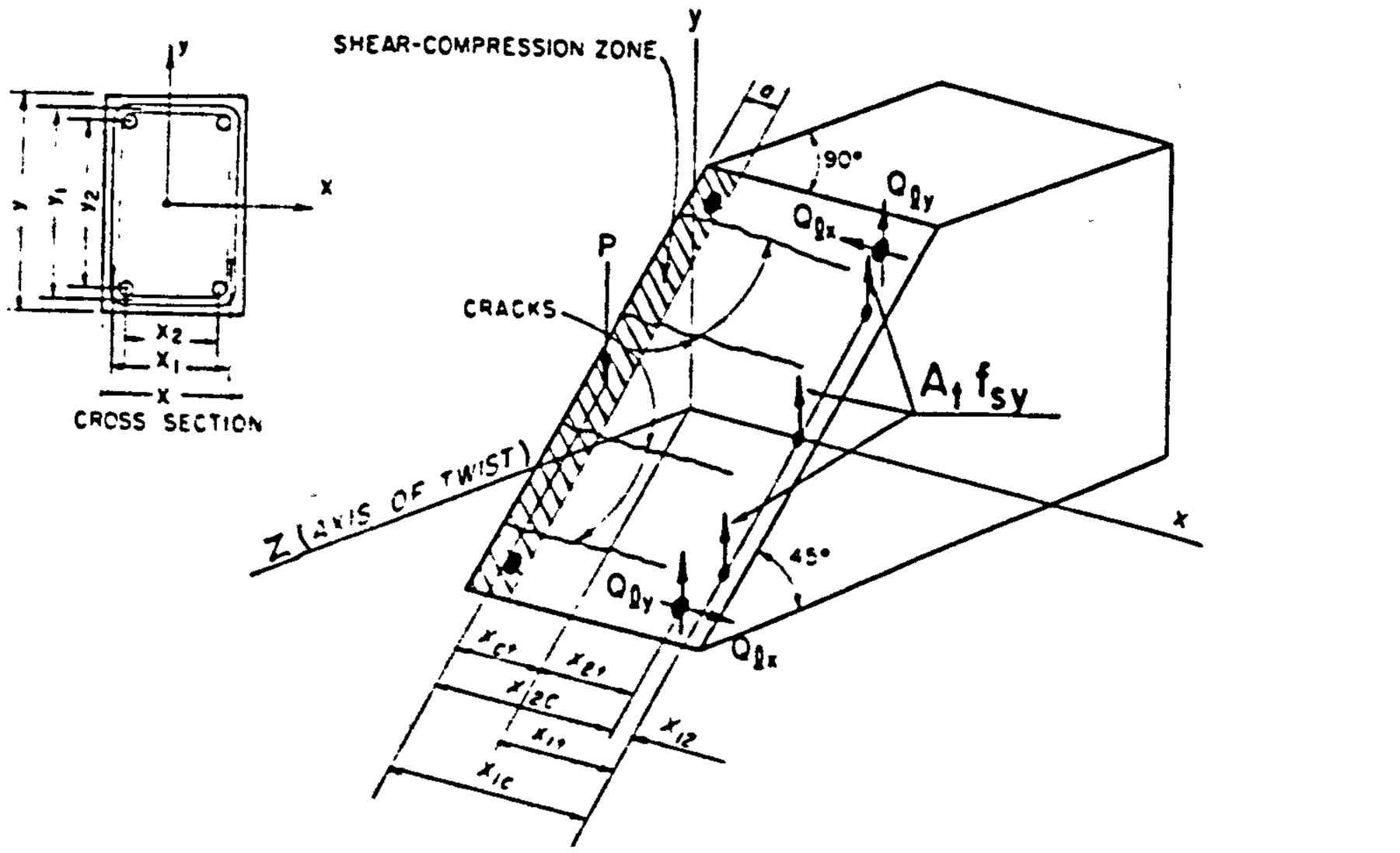

Fig. 1.4 Skew failure plane for a rectangular reinforced concrete beam (Ref. 1).

REFERENCES

1. Hsu, T.T.C., "Torsion of Reinforced Concrete", Van Nostrand Reinhold Company, New York, 1984.

2. (ACI 318-71), "Building Code Requirements for Reinforced Concrete", ACI Committee 318, Amer. Conc. Inst., Detroit, 1971.

3. CP110-1972, "Code of Practice for the Structural Use of Concrete", Part 1, Design, Material and Workmanship, British Standard Inst., London, 1972.

4. Rausch, E., "Design of Reinforced Concrete in Torsion" (Berechnung des Eisenbetons gegen Vendrehung), Ph.D. Thesis, Technische Hochsechule, Berlin, 1929 (in German).

5. Smith, J.O. and Sidebottom, O.M., "Inelastic Behaviour of Load Carrying Members", John Wiley and Sons, New York, 1965.

6. Coulomb, C.A., "Recherches théoriques et experimentales sur la force de torsion et sur l'élasticité des fils métal", Histoire de l'Academic Royale des Sciences, Paris, 1784; L'Imprimerie Royale, Paris, 1787, pp. 229-269.

7. Navier, C.L., Résumé des leçons données à l'école des ponts et chaussées sur l'application de la mécanique à l'établissement des constructions et des machines. Première partie, "continant les lecons sur la résistance des matériaux et sur l'établissement des consructions en terre, en maçonnerie et en charpente", Firmin Didet, Paris, 1826, (Article V, "de la résistance d'un corps prismatique à la torsion", pp. 71-76. Article VI, "de la resistance d'un corps prismatique à la rupture causée par la torsion", pp. 76-80).

8. Saint-Venant, B. de, Mémoire sur la torsion des prismes (lu à l'Académie le 13 juin 1853). Mémoires des savants étrangers, Mémoires présentés par divers savants à l'Académie des sciences, de l'Institut Imperial de France et imprimé par son ordre, V. 14, Imprimerie Impériale, Paris, 1856, pp. 233-256.

9. Prandtl, L., "Zur Torsion von prismatischen Staben", Physik Zeitschrift 4, 1903, p. 758.

10. Nadai, A., "Plasticity", McGraw-Hill, New York, 1931.

11. Sadowsky, M.A., "An Extension to the Sand Heap Analogy in Plastic Torsion Applicable to Cross-Sections Having One or More Holes", J. Appl. Mech., Vol. 62, 1944, pp. 166-168.

12. Sokolovsky, W.W, "Theory of Plasticity (in Russian)", Moscow, 1946.

13. Chrisopherson, D.G., "Theoretical Investigation of Plastic Torsion in an I-Beam", J. Appl. Mech., Vol. 62, 1940, pp. 1-4.

14. Nadai, A., "Theory of Flow and Fracture of Solids", New York, McGraw-Hill, 1950.

15. Augusti, G., "Full Plastic Torque of I-Beams", Int. J. Mech. Sci. Vol. 8, 1966, pp. 641-649.

16. Boulton, N.S., "Plastic Twisting and Bending of an I-Beam in Which the Warping is Restricted", Int. J. Mech. Sci., Vol. 4, 1962, pp. 491-502.

17. Dinno, K.S. and Merchant, W., "A Procedure for Calculating the Plastic Collapse of I-Sections under Bending and Torsion", Struct. Engr. Vol. 43, 1965, pp. 219-221.

18. Dinno, K.S. and Gill, S.S, "The Plastic Torsion of I-Sections with Warping Restraint", Int. J. Mech. Sci., Vol. 6, 1964, pp. 27-43.

19. Greenberg, H.O., Dorn, W.S. and Wetherell, E.H., "A Comparison of Flow and Deformation Theories in Plastic Torsion of a Square Cylinder", In Plasticity Proc. 2nd Symp. on Naval Structural Mechanics, Eds Lee, H.E and Symonds, P.S., Pergamon Press, New york, 1960.

20. Itani, R.Y., "Elasto-Plastic Torsion of Axisymmetric Bars", J. of the Eng. Mech. Div., ASCE, EMI 105, 1979, pp. 1-12.

21. Yamada, Y., Katagiri, S. and Taktsuka, K., "Elastic-Plastic Analysis of Saint-Venant Torsion Problem by a Hybrid Stress Model", Int. J. for Num. Meth. in Eng., Vol. 5, 1972, pp. 193-207.

22. Johnson, A.F., "Bending and Torsion of Anisotropic Beams", Int. J. Solids Struct., Vol. 9, 1973, pp. 527-551.

23. Zhen-Sheng, C., "A Boundary Element Solution to Elasto-Plastic Torsion of Solids of Revolution", Int. J. for Num. Meth. in Eng., Vol. 19, 1983, pp. 1193-1207.

24. Baba, S. and Kajita, T., "Plastic Analysis of Torsion of a Prismatic Beam", Int. J. for Num. Meth. in Eng., Vol. 18, 1982, pp. 927-944.

25. Bathe, K.J. and Chaudhary, A., "The Displacement Formulation of Torsion of Shafts with Rectangular Corss-Sections", Int. J. for Num. Meth. in Eng., Vol. 18, 1982, pp. 1565 - 1580.

26. Rajasekaran, S., "Finite Element Method for Plastic Beam-Columns", Chap. 12 in Theory of Beam-Columns, by W.F. Chen and T. Atsuta, McGraw-Hill, 1977, pp. 539 - 608.

27. Bathe, K.J. and Wiener, P.M., "On the Elastic-Plastic Analysis of I-Beams in Bending and Torsion", Comput. Struct., Vol. 17, 1983, pp. 711 - 718.

28. Hsu, T.T.C, "Torsion of Structural Concrete–Plain Concrete Rectangular Sections", Torsion of Structural Concrete, SP-18, Amer. Conc. Inst., Detroit, 1968, pp. 203–238.

29. Nylander, H., "Vridning och Vridningsinspanning vid Betong Knostruktiener (Torsion and Torsional Restraint By Concrete Structures), Statens Kommittee för Byggnadsforkning, Stockholm, Bull. No. 3, 1945.

30. Marshall, W.T. and Tembe, N.R., "Experiments on Plain and Reinforced Concrete in Torsion", Struct. Engr., Vol. 19, No. 11, November 1941, pp. 177-191.

31. McHenry, D. and Karni, J., "Strength of Concrete under Combined Tensile and Compressive Stresses", J. of the Amer. Conc. Inst., Vol. 54, April 1958, pp. 829-839.

32. Hsu, T.T.C, "Torsion of Structural Concrete-Behaviour of Reinforced Concrete Rectangular Members", Torsion of Structural Concrete, SP-18, Amer. Conc. Inst., Detroit, 1968, pp. 261-306.

33. Andersen, P., "Experiments with Concrete in Torsion", Proc., ASCE, Vol. 60, May 1934, pp. 641-652.

34. Cowan, H.J., "Elastic Theory for Torsional Strength of Rectangular Reinforced Concrete beams", Magazine of Concrete Research, Vol. 2, No. 4, July 1950, pp. 3-8.

35. Lampert, P. and Thürlimann, B., "Torsion Tests of Reinforced Concrete Beams (Torsionsversuche an Stahlbetonbalken)", Report No. 6506-2, June 1968; and "Torsion-Bending Tests on Reinforced Concrete Beams (Torsions-Biege-Versuch an Stahlbetonbalken)", Report No. 6506-3, January 1969, Institut für Baustatik, ETH, Zurich.

36. CEB-FIP Model Code for Concrete Structures, 3rd Edition, Comité Euro-International du Béton/Fédération Internationale de la Précontrainte, Paris, 1978.

37. Hsu, T.T.C. and Mo, Y.L., "Softening of Concrete in Torsional Members-Theory and Tests", J. of the Amer. Conc. Inst., May-June 1985, pp. 290-303.

38. Collins, M.P. and Mitchell, D., "Shear and Torsion Design of Prestressed and Non-Prestressed Concrete Beams", J. Prestressed Concrete Institute, Vol. 25, No. 5, September-October 1980, pp. 32-100.

39. Robinson, J.R. and Demorieux, J.M., "Essias de Traction-Compression sur Models d'ame de Poutre en Béton Armé", Institut de Recherches Applliquées du Béton Armé (IRABA), Part 1, June 1968 and Part 2, May 1972.

40. Vecchio, F. and Collins, M.P., "The Response of Reinforced Concrete to In-Plane Shear and Normal Stresses", Publication No. 82-03, University of Toronto, Canada, 1982.

41. Hsu, T.T.C. and Mo, Y.L., "Softening of Concrete in Torsional Members-Design and Recommendations ", J. of the Amer. Conc. Inst., July-August 1985, pp. 443-452.

42. Lessig, N.N., "Determination of the Load-Carrying Capacity of Rectangular Concrete Elements Subjected to Flexure and Torsion", Turdy No. 5, Institut Betona i Zhelezobetona (Concrete and Reinforced Concrete Institute), Moscow, 1959, pp. 5-28 (in Russian). Translated by Portland Cement Association, Foreign Literature Study No. 371.

43. State Committee on Construction of the USSR Council of Ministers, "Structural Standards and Regulations", SNIP II-B, 1-62, State Publishing Offices for Literature on Structural Engineering, Architecture and Structural Materials, Moscow, 1962 (in Russian).

44. Hsu, T.T.C., Discussion of "Pure Torsion in Rectangular Sections - A Re-examination", J. of the Amer. conc. Inst., Vol. 76, No. 6, June 1979, pp. 741-746.

45. Mehlhorn, G. and Gönner, G.S., "A Calculation of Reinforced Concrete Beams under Bending and Torsion Using Three Dimensional Finite Elements", IABSE Colloiquium on Advanced Mechanics of Reinforced Concrete, Delft, 1981, pp. 591-601.

46. Mohamed, M.S., "A Finite Element and Experimental Study of Reinforced Concrete Beams in Torsion", Ph.D. Thesis, University of Glasgow, 1986

CHAPTER TWO

BASIC CONCEPTS AND FINITE ELEMENT FORMULATION

2.1 Introduction

In the last two decades the finite element method has emerged as one of the most powerful techniques for the numerical solution of a variety of problems in engineering. The origins of the method go back to the lattice analogy concept of McHenry [1] and the early attempts of Hrenikof [2] who introduced the framework method to represent a plane elastic solid as a collection of discrete elements. In 1943, Courant [3] used an assemblage of triangular elements and the principle of minimum potential energy to find an approximate solution to the Saint Venant torsion problem. In the mid 50-s, Argyris and Kelsey [4] developed efficient solution techniques for analysing complicated structural configurations. These techniques were used in the aircraft industry. In the same period, Turner et al [5] gave the actual solution to plane stress problems using triangular elements. Clough [6] appears to be the first to use the term finite element in a paper on plane elasticity problems in 1960. Since then the method has received widespread use in the fields of engineering and mathematics.

The finite element method gained a foundation when it was recognised by many researchers [7-10] that it is a form of the Ritz method. It is applicable to many different variational problems in areas outside the field of solid mechanics such as fluid mechanics,

heat transfer, magnetic fields, etc.

The finite element method has been described extensively in the literature. A comprehensive discussion of the method and its applications is given in several texts [11-18] amongst which may be mentioned particularly that of Zienkiewicz [11]. Therefore, only a brief description of the finite element concept is given in section 2.2. The formulation of the equilibrium equations governing the behaviour of a continuum using the principle of virtual displacements is presented in section 2.3 and the discretisation process of the equilibrium equations is given in section 2.4. Section 2.5 deals with the convergence requirements for a discrete model. The finite element representation of concrete and reinforcement bars and the elements used in the present study are described in section 2.6. In section 2.7, the numerical calculation of stiffness matrices and the integration rules implemented in this work are presented.

2.2 The Finite Element Concept

In the context of structural mechanics, the classical analysis of continuous systems depends basically on consideration of the properties of small differential elements of the system. Equilibrium, compatibility and the constitutive relations associated with the infinitesimal element are established. Partial differential equations or integral equations governing the behaviour of the entire domain are obtained by allowing the dimensions of the element considered to approach zero as the number of the elements becomes infinitely large.

In practice, most of the problems are too complicated and exact mathematical solutions for the governing differential equations are only obtained for a limited class of structures of simple geometry and load carrying characteristics. Consequently, numerical methods such as the finite element method and the finite differences method have been used to achieve approximate solutions for realistic types of problem.

In the finite element displacement method, the continuum with an infinite number of degrees of freedom is represented by a discrete model which has a finite number of degrees of freedom. The discrete model is composed of subregions, or elements, of finite size which have a simpler geometry than that of the continuum. A finite number of points, or nodes, are identified on the element, where the finite elements are to be joined and conditions of equilibrium and compatibility are to be enforced. Displacement functions within each element are assumed so that the displacements at each point within the element are dependent upon nodal values. An important aspect of the finite element concept is that an individual element may be considered in isolation from the assemblage of finite elements. Therefore the displacement functions over the element in terms of the nodal values can be approximated independently of the ultimate location of the element within the discrete model. Thus, it is possible to develop an assemblage of various finite elements in which the nodal values of the assumed local displacement functions are left arbitrary [12,19].

2.3 Equations of Equilibrium

This section deals with the derivation of the equilibrium equations governing the behaviour of a continuum. Vectors and matrices will be distinguished from scalar quantities by underlying wavey lines. Small letters will be used for vectors and capital letters will be used for matrices.

Consider a general three-dimensional body, or continuum, acted upon by a system of external forces, let the cartesian coordinate system (x,y,z) be used to describe its spatial position. The external forces may comprise surface tractions, acting over part or whole of the external surface of the body,

$$\underset{\sim}{t} = [\ t_x \quad t_y \quad t_z\ ] \tag{2.1}$$

and body forces, acting through the volume of the body,

$$\underset{\sim}{b} = [\ b_x \quad b_y \quad b_z\ ] \tag{2.2}$$

Due to these forces a particle of the body located initially at a point p(x,y,z) undergoes a displacement having components u, v and w in the x, y and z directions respectively. Components of the displacement at point p are given by the vector:

$$\underset{\sim}{u} = [\ u \quad v \quad w\ ]^T \tag{2.3}$$

Since geometrical non-linearities are not considered in the present work, displacement gradients remain small throughout the loading

process and hence engineering components of strain can be expressed in terms of the first partial derivatives of the displacement components. Therefore, the linearised strain–displacement relationships may be written as:

$$\underset{\sim}{\varepsilon} = \begin{bmatrix} \epsilon_x \\ \epsilon_y \\ \epsilon_z \\ \gamma_{xy} \\ \gamma_{yz} \\ \gamma_{zx} \end{bmatrix} = \begin{bmatrix} \frac{\partial u}{\partial x} \\ \frac{\partial v}{\partial y} \\ \frac{\partial w}{\partial z} \\ \frac{\partial u}{\partial y} + \frac{\partial v}{\partial x} \\ \frac{\partial v}{\partial z} + \frac{\partial w}{\partial y} \\ \frac{\partial w}{\partial x} + \frac{\partial u}{\partial z} \end{bmatrix} \tag{2.4}$$

The corresponding vector of stresses is given by:

$$\underset{\sim}{\sigma} = [\ \sigma_x \quad \sigma_y \quad \sigma_z \quad \tau_{xy} \quad \tau_{yz} \quad \tau_{zx}\ ]^T \tag{2.5}$$

The vectors of stresses and strains are related through the constitutive matrix, $\underset{\sim}{D}$, as:

$$\underset{\sim}{\sigma} = \underset{\sim}{D}\ \underset{\sim}{\varepsilon} \tag{2.6}$$

The principle of virtual displacements of a deformable body is used to establish the governing equations of static equilibrium. It states that a deformable body is in equilibrium if the total work done by all the external forces plus the total work done by all the internal forces during any kinematically admissible virtual displacement is zero [20]. Symbolically the principle is expressed

as:

$$\delta W_{int} - \delta W_{ext} = 0 \tag{2.7}$$

The external work can be expressed as the work done in moving the body forces $\underset{\sim}{b}$ and the surface tractions $\underset{\sim}{t}$ through the virtual displacement, $\partial\underset{\sim}{u}$, as:

$$\delta W_{ext} = \int_V \partial\underset{\sim}{u}^T \underset{\sim}{b}\, dV + \int_S \partial\underset{\sim}{u}^T \underset{\sim}{t}\, dS \tag{2.8}$$

where V is the volume of the body and S is that part of the surface of the body where the external tractions are prescribed. The change in the strain energy, internal work, due to a set of virtual strains, $\partial\underset{\sim}{\varepsilon}$, corresponding to the virtual displacements is:

$$\delta Wint = \int_V \partial\underset{\sim}{\varepsilon}^T \underset{\sim}{\sigma}\, dV \tag{2.9}$$

Substitution of equation (2.6) into (2.9) yields:

$$\delta Wint = \int_V \partial\underset{\sim}{\varepsilon}^T \underline{D}\, \underset{\sim}{\varepsilon}\, dV \tag{2.10}$$

By making use of (2.8) and (2.10), equation (2.7) may be expressed as:

$$\int_V \partial\underset{\sim}{\varepsilon}^T \underset{\sim}{D}\ \underset{\sim}{\varepsilon}\ dV - \int_V \partial\underset{\sim}{u}^T \underset{\sim}{b}\ dV - \int_S \partial\underset{\sim}{u}^T \underset{\sim}{t}\ dS = \underset{\sim}{0} \qquad (2.11)$$

The above expression represents the equations of static equilibrium for a general body.

2.4 Discretisation of the Equilibrium Equations

In finite element analysis, the general three-dimensional body is approximated as an assemblage of an arbitrary number of finite elements, n, with the elements being interconnected at nodal points on the element boundaries.

Consider a finite element, e, of the discrete model and let the displacement vector at any point within the element, $\underset{\sim}{u}^e$, be interpolated as:

$$\underset{\sim}{u}^e = \underset{\sim}{N}\ \underset{\sim}{a}^e \qquad (2.12)$$

where $\underset{\sim}{N}$ is a matrix containing the interpolation functions which relates the displacements, $\underset{\sim}{u}^e$, to the nodal displacements, $\underset{\sim}{a}^e$. The corresponding strains, $\underset{\sim}{\varepsilon}^e$, are obtained by the differentiation of the displacements such that:

$$\underset{\sim}{\varepsilon}^e = \underset{\sim}{A}\ \underset{\sim}{u}^e \qquad (2.13)$$

where $\underset{\sim}{A}$ is a matrix which contains the differential operators. Substitution of equation (2.12) into (2.13) yields:

$$\underset{\sim}{\varepsilon}^e = \underset{\sim}{B}\ \underset{\sim}{a}^e \tag{2.14}$$

where $\underset{\sim}{B}$ is the strain-displacement matrix given by:

$$\underset{\sim}{B} = \underset{\sim}{A}\ \underset{\sim}{N} \tag{2.15}$$

The strain-displacement matrix gives values of strain, at any point within the element, due to unit values of nodal displacements. In the discrete model, the equations of equilibrium of the continuum may be written as the sum of the integrations over the volume and surface area for all the finite elements. Therefore, by making use of (2.12) and (2.14), equation (2.11) becomes:

$$\partial \underset{\sim}{a}^T \left\{ \sum_n \int_{V^e} \underset{\sim}{B}^T\ \underset{\sim}{D}\ \underset{\sim}{B}\ dV^e\ \underset{\sim}{a}^e - \sum_n \int_{V^e} N^T\ \underset{\sim}{b}^e\ dV^e - \sum_n \int_{S^e} \underset{\sim}{N}^T\ \underset{\sim}{t}^e\ dS^e \right\} = \underset{\sim}{0} \tag{2.16}$$

Since the vector of the virtual nodal displacements, $\partial \underset{\sim}{a}$, is arbitrary, the following set of algebraic equations may be obtained:

$$\underset{\sim}{K}\ \underset{\sim}{a} = \underset{\sim}{f} \tag{2.17}$$

where $\underset{\sim}{K}$ is the stiffness matrix of the element assemblage and is given by:

$$\underset{\sim}{K} = \sum_n \int_{V^e} \underset{\sim}{B}^T\ \underset{\sim}{D}\ \underset{\sim}{B}\ dV^e, \tag{2.18}$$

$\underset{\sim}{a}$ is the corresponding element assemblage nodal displacement vector and $\underset{\sim}{f}$ is the element assemblage external nodal force vector given by:

$$\underset{\sim}{f} = \sum_{n} \int_{V^e} \underset{\sim}{N}^T \underset{\sim}{b}^e \, dV^e + \sum_{n} \int_{S^e} \underset{\sim}{N}^T \underset{\sim}{t}^e \, dS^e \qquad (2.19)$$

The summation of the element volume integrals in (2.18) implies the direct addition of the element stiffness matrices to obtain the stiffness matrix of the total element assemblage. In the same way, the body force vector and the surface traction vector of equation (2.19) are calculated by direct addition of the element body force vectors and the element surface traction vectors. This process is referred to as the direct stiffness method [5].

2.5 Convergence Requirements of the Discrete Model

The analysis of an elastic continuum by the method of finite elements must converge to the results implied by the 'exact' theory as the network of elements is refined. To guarantee monotonic convergence, the interpolation functions of (2.12) have to be chosen so that completeness and compatibility requirements are satisfied [21,22].

The completeness requirement ensures that the displacement field representation allows for the possibility of rigid body displacement and constant strain states within the element. Because the infinitesimal elements of the original continuum represent a state of constant strain, the finite sized elements of the discrete model must

therefore be able to produce this state as they get smaller [23,11].

The compatibility requirement ensures that the displacement functions within the element and across its boundaries are continuous, i.e no interlement gaps or overlaps between adjacent elements are allowed to occur. Thus, the strains at the interface between elements must be finite [11]. In the case of three-dimensional elasticity, strains are defined by first derivatives, equation (2.4), and hence the displacements only have to be continuous, C^0 continuity [24,11].

Elements whose interpolation functions violate compatibility requirement are called incompatible or non-conforming. These elements may be valid and good results using such elements can still be obtained provided that the incompatibilities disappear with increasing mesh refinement. This condition is always achieved, if the completeness requirement is satisfied and the constant strain condition automatically ensures displacement continuity [11,13].

To investigate whether a group of non-conforming elements is complete, the patch test has been introduced by Irons [25,23]. It is a numerical test which extends the philosophy of the constant strain requirement from an individual element to an assemblage of elements. In this test an arbitrary group of elements is subjected to a set of nodal displacements corresponding to a constant state of strain throughout the patch. If the element strains then represent the constant strain state, the patch test is passed and the completeness requirement is satisfied by the element group.

2.6 Finite Element Idealisation

Because of the large amount of computational effort involved, very little work has been done in modelling reinforced concrete members as general three-dimensional solids. However, such representation is necessary for the finite element application to reinforced concrete beams in torsion. In the present study, concrete is simulated by hexahedral brick elements and reinforcement bars are modelled as one-dimensional embedded elements built into the three-dimensional concrete elements.

2.6.1 Concrete Idealisation

Two-dimensional finite element idealisation has been widely used in extensive investigations carried out over the last two decades to model the behaviour of reinforced concrete members. This type of idealisation is adequate to represent the state of stress in most cases and it is computationally cheaper than the full three-dimensional idealisation. Constant strain triangular elements were used in the early two-dimensional finite element applications because of their simplicity and their ability to model structures with irregular boundaries [26,27]. Linear isoparametric quadrilateral elements have also been implemented to represent concrete. The use of these elements allows increased element size within the mesh and reduces the total number of degrees of freedom compared with triangular elements [28]. Higher order isoparametric elements have also been used because of their ability to be distorted into more arbitrary shapes [29,11]. In particular, isoparametric

elements with quadratic or cubic shape functions become highly competitive because of their overall performance and versatility over simpler types of element. In spite of a high order element requiring more time to formulate, a considerable saving in computing effort is obtained due to the smaller number of elements required to conduct the analysis [11].

Although two-dimensional finite element modelling is adequate for many cases, full three-dimensional idealisation may be necessary even for prismatic reinforced concrete beams subjected to a relatively simple state of loading such as pure torsion, torsion plus bending and biaxial bending. In three dimensions, the elements equivalent to the triangle and rectangle are the tetraherdron and the hexahedron respectively . Simple tetrahedral elements appear to have been introduced in the literature by Gallagher et al [30], Melosh [31] and Argyris [32]. A major disdvantage of this type of element is the difficulty of subdividing a volume space into tetrahedral shapes as compared to the convenient subdivision into hexahedral bricks. A comparison of the numerical performance of a simple and a high order tetrahedra and a simple and a high order hexahedra has been made by Fjeld [33] using relatively simple elastic problems involving bending and torsion of stocky cantilever beams. It was concluded that for the same total number of degrees of freedom high order elements are superior to simple elements and hexahedral elements are superior to tetrahedral elements. Clough [34] has also considered some beam type problems using both tetrahedral and hexahedral elements. It was also concluded that hexahedral elements perform better than tetrahedral elements do. The hexahedral elements considered in the study were the linear eight noded element and the

quadratic 20 noded element. The later gave superior performance over the former on a solution–time basis.

In application to torsion, a major advantage of the 20 noded quadratic element over the 8 noded linear element is that the warping displacement of beam cross section, which is a quite complex function, can be adequately approximated with fewer elements within the cross section. Therefore, the 20 noded quadratic element has been adopted in this study in order to minimise the number of elements required to conduct the computationally expensive three–dimensional finite element analysis. This element has been successfully used in many three-dimensional non–linear reinforced concrete studies [35-37].

2.6.1.1 The 20 noded isoparametric element

The 20 noded isoparametric quadratic brick element shown in Fig. 2.1a is used throughout the present study to represent the concrete. The element employs serendipity shape functions to define the displacement field within its boundary in terms of displacement values at the nodes. Each nodal point has three translational degrees of freedom u, v and w along the cartesian coordinates x, y and z respectively. A total of sixty degrees of freedom are therefore specified for each element.

a) Shape functions

For an element, the natural local coordinate system (ξ,η,ζ) is usually used to express the displacement components. The origin of the local coordinate system is the centre of the element and each of the local coordinate lines ranges from -1 to +1, Fig. 2.1b. Displacement components at a particular point $p(\xi,\eta,\zeta)$ are defined using the nodal values at each of the twenty nodes and the quadratic shape functions such that:

$$u(\xi,\eta,\zeta) = \sum_{i=1}^{20} N_i(\xi,\eta,\zeta).u_i$$

$$v(\xi,\eta,\zeta) = \sum_{i=1}^{20} N_i(\xi,\eta,\zeta).v_i \qquad (2.20)$$

$$w(\xi,\eta,\zeta) = \sum_{i=1}^{20} N_i(\xi,\eta,\zeta).w_i$$

where $N_i(\xi,\eta,\zeta)$ is the shape function at the ith node at which the nodal displacements are u_i,v_i and w_i. The serendipity shape functions of the 20 noded brick element are given by:

For corner nodes $\quad \xi_i=\pm1 \quad \eta_i=\pm1 \quad \zeta_i=\pm1$

$$N_i(\xi,\eta,\zeta)= \frac{1}{8}(1+\xi\xi_i)(1+\eta\eta_i)(1+\zeta\zeta_i)(\xi\xi_i+\eta\eta_i+\zeta\zeta_i-2) \qquad (2.21)$$

For mid-side nodes $\quad \xi_i=0 \quad \eta_i=\pm1 \quad \zeta_i=\pm1$

$$N_i(\xi,\eta,\zeta) = \frac{1}{4}(1-\xi^2)(1+\eta\eta_i)(1+\zeta\zeta_i) \qquad (2.22)$$

For mid-side nodes $\xi_i = \pm 1$ $\eta_i = 0$ $\zeta_i = \pm 1$

$$N_i(\xi,\eta,\zeta) = \frac{1}{4}(1+\xi\xi_i)(1-\eta^2)(1+\zeta\zeta_i) \qquad (2.23)$$

For mid-side nodes $\xi_i = \pm 1$ $\eta_i = \pm 1$ $\zeta_i = 0$

$$N_i(\xi,\eta,\zeta) = \frac{1}{4}(1+\xi\xi_i)(1+\eta\eta_i)(1-\zeta^2) \qquad (2.24)$$

In order to satisfy a rigid body displacement of the element, each of the twenty shape functions has a value of unity at its specified node and the summation of all shape functions at any point within the element is also equal to unity.

In the isoparametric group of elements, the interpolation shape functions are also used to define the geometry of the element. Therefore, the cartesian coordinate values of any point $p(\xi,\eta,\zeta)$ within the element may be defined as:

$$x(\xi,\eta,\zeta) = \sum_{i=1}^{20} N_i(\xi,\eta,\zeta).x_i$$

$$y(\xi,\eta,\zeta) = \sum_{i=1}^{20} N_i(\xi,\eta,\zeta).y_i \qquad (2.25)$$

$$z(\xi,\eta,\zeta) = \sum_{i=1}^{20} N_i(\xi,\eta,\zeta).z_i$$

where x_i, y_i and z_i are the cartesian coordinates of node i.

b) Strain–displacement representation

For a three-dimensional finite element, cartesian component of strains are related to nodal displacements by equation (2.14) which may be written in the expanded form as:

$$\begin{bmatrix} \epsilon_x \\ \epsilon_y \\ \epsilon_z \\ \gamma_{xy} \\ \gamma_{yz} \\ \gamma_{zx} \end{bmatrix} = -\sum_{i=1}^{20} \begin{bmatrix} \frac{\partial N_i}{\partial x} & 0 & 0 \\ 0 & \frac{\partial N_i}{\partial y} & 0 \\ 0 & 0 & \frac{\partial N_i}{\partial z} \\ \frac{\partial N_i}{\partial y} & \frac{\partial N_i}{\partial x} & 0 \\ 0 & \frac{\partial N_i}{\partial z} & \frac{\partial N_i}{\partial y} \\ \frac{\partial N_i}{\partial x} & 0 & \frac{\partial N_i}{\partial z} \end{bmatrix} \begin{bmatrix} u_i \\ v_i \\ w_i \end{bmatrix} \qquad (2.26)$$

Since the shape functions N_i, given in (2.21–2.24), are functions of the local coordinates rather than the cartesian coordinates, a relationship needs to be established between the derivatives in the two coordinates systems. By using the chain rule for partial differentiation the relation can be expressed in matrix form as:

$$\begin{bmatrix} \frac{\partial N_i}{\partial \xi} \\ \frac{\partial N_i}{\partial \eta} \\ \frac{\partial N_i}{\partial \zeta} \end{bmatrix} = \begin{bmatrix} \frac{\partial x}{\partial \xi} & \frac{\partial y}{\partial \xi} & \frac{\partial z}{\partial \xi} \\ \frac{\partial x}{\partial \eta} & \frac{\partial y}{\partial \eta} & \frac{\partial z}{\partial \eta} \\ \frac{\partial x}{\partial \zeta} & \frac{\partial y}{\partial \zeta} & \frac{\partial z}{\partial \zeta} \end{bmatrix} \begin{bmatrix} \frac{\partial N_i}{\partial x} \\ \frac{\partial N_i}{\partial y} \\ \frac{\partial N_i}{\partial z} \end{bmatrix} = \underset{\sim}{J} \begin{bmatrix} \frac{\partial N_i}{\partial x} \\ \frac{\partial N_i}{\partial y} \\ \frac{\partial N_i}{\partial z} \end{bmatrix} \qquad (2.27)$$

The terms such as $\partial x/\partial \xi$ occurring in the Jacobian matrix $\underset{\sim}{J}$ can be obtained by differentiation of (2.25). The Jacobian matrix may be expressed as:

$$\underset{\sim}{J} = \begin{bmatrix} \sum \frac{\partial N_i}{\partial \xi} x_i & \sum \frac{\partial N_i}{\partial \xi} y_i & \sum \frac{\partial N_i}{\partial \xi} z_i \\ \sum \frac{\partial N_i}{\partial \eta} x_i & \sum \frac{\partial N_i}{\partial \eta} y_i & \sum \frac{\partial N_i}{\partial \eta} z_i \\ \sum \frac{\partial N_i}{\partial \zeta} x_i & \sum \frac{\partial N_i}{\partial \zeta} y_i & \sum \frac{\partial N_i}{\partial \zeta} z_i \end{bmatrix} \qquad (2.28)$$

In order to complete the definition of the strain displacement matrix, derivatives with respect to cartesian coordinates appearing in (2.26) are obtained by the inverse relationship of (2.27) as:

$$\begin{bmatrix} \frac{\partial N_i}{\partial x} \\ \frac{\partial N_i}{\partial y} \\ \frac{\partial N_i}{\partial z} \end{bmatrix} = \underset{\sim}{J}^{-1} \begin{bmatrix} \frac{\partial N_i}{\partial \xi} \\ \frac{\partial N_i}{\partial \eta} \\ \frac{\partial N_i}{\partial \zeta} \end{bmatrix} \qquad (2.29)$$

where $\underset{\sim}{J}^{-1}$ is the inverse of Jacobian matrix given by:

$$\underset{\sim}{J}^{-1} = \begin{bmatrix} \frac{\partial \xi}{\partial x} & \frac{\partial \eta}{\partial x} & \frac{\partial \zeta}{\partial x} \\ \frac{\partial \xi}{\partial y} & \frac{\partial \eta}{\partial y} & \frac{\partial \zeta}{\partial y} \\ \frac{\partial \xi}{\partial z} & \frac{\partial \eta}{\partial z} & \frac{\partial \zeta}{\partial z} \end{bmatrix} \tag{2.30}$$

c) Stiffness matrix calculation

For an element of volume V, the stiffness matrix presented in equation (2.18) may be expressed as:

$$\underset{\sim}{K}^e = \int_{V^e} \underset{\sim}{B}^T \underset{\sim}{D} \underset{\sim}{B} \, dV^e \tag{2.31}$$

For three-dimensional elements, the differential volume, dV^e, may be written as:

$$dV^e = dx \, dy \, dz \tag{2.32}$$

Equation (2.32) can be transformed into the natural coordinates as:

$$dV^e = |J| \, d\xi \, d\eta \, d\zeta \tag{2.33}$$

where $|J|$ is the determinant of the Jacobian matrix. The limits of integration in the natural coordinates become -1 and +1 and the element stiffness matrix can therefore be written as:

$$\underset{\sim}{K}^e = \int_{-1}^{+1}\int_{-1}^{+1}\int_{-1}^{+1} \underset{\sim}{B}^T \underset{\sim}{D} \underset{\sim}{B} |J| \, d\xi \, d\eta \, d\zeta \qquad (2.34)$$

In general it is not possible to evaluate the element stiffness matrix explicitly. Thus, numerical integration techniques have been usually used.

2.6.2 Reinforcement idealisation

In reinforced concrete members, three alternative representations have been usually used to simulate the reinforcement in the finite element method [27,38,39]:

a) discrete representation

b) distributed representation

c) embedded representation

A discrete representation by using one-dimensional elements to idealise the reinforcement has been widely used. Axial force members, or bar links, may be implemented and assumed to be pin connected with two degrees of freedom at each nodal point. Beam elements may also be used and assumed to resist axial force, shear and bending; three degrees of freedom are assumed at each end. In either case, the one-dimensional elements are easily superimposed on the multi-dimensional finite elements representing the concrete. The major advantages of the discrete representation are its simplicity and its capability to adequately account for bond-slip and dowel action phenomena [40,41]. In three-dimensional finite element

analyses of reinforced concrete beams, the locations of longitudinal bars and stirrups dictate mesh choice and size of the brick elements. Since the longitudinal bars are close to each other and concrete protection cover is relatively small compared with the dimensions of the member, a large number of brick elements would be required to model the member. Hence the cost of such analyses in terms of the computation time would be extremely expensive. Another serious disadvantage is that in order to keep the number of elements small the elements would become slender and hence the need to keep the aspect ratio as close to unity as possible would be violated. For these reasons, this approach is not used in the present study.

For a distributed representation, reinforcement bars are assumed to be distributed over the concrete element in any specified direction. A composite concrete–reinforcement constitutive relation is used in this case [27]. To derive such relation, perfect bond between the concrete and the steel bars must be assumed.

The embedded representation is often used with higher order isoparametric concrete elements [27,38]. The reinforcing bar is considered to be an axial member built into the isoparametric concrete element such that its displacements are consistent with those of the element, Fig. 2.2. Perfect bond between the steel and the concrete has been assumed in this case [42,43]. A major advantage of this approach is that the steel bars can be placed in their correct positions without imposing any restrictions on mesh choice and hence the finite element analysis can be carried out with a smaller number of brick elements compared to the discrete representation of reinforcement. Therefore, the embedded

representation is adopted in the present work.

2.6.2.1 Embedded representation for reinforcing bars

The concept of simulating the steel bars as line elements lie inside the boundary of the basic isoparametric element was first suggested for plane stress, plane strain and axisymmetric analyses [42,43] and extended to the three-dimensional case by Mohamed [37]. In the present study, reinforcement bars are embedded in the 20 noded quadratic brick element used to simulate the concrete and they are assumed to be capable of transmitting axial force only. It is further assumed that such bars are restricted to be parallel to the local coordinate lines ξ , η and ζ of the brick element.

The derivation given in references [37,43] is presented in this section for a bar parallel to the local coordinate axis ξ. A similar derivation can be used for bars parallel to η and ζ axes.

a) Displacement representations

Consider a bar lying parallel to the local coordinate axis ξ, with $\eta=\eta_c$ and $\zeta=\zeta_c$, Fig. 2.2. The coordinates of the bar are defined by using the same shape functions as the main element. Hence, the cartesian coordinates of any point p along this bar are obtained by substituting the constant values η_c and ζ_c into (2.25) such that:

$$x = \sum_{i=1}^{20} N_i(\xi).x_i$$

$$y = \sum_{i=1}^{20} N_i(\xi).y_i \qquad (2.35)$$

$$z = \sum_{i=1}^{20} N_i(\xi).z_i$$

Because full compatibility between the bar and the basic brick element is assured, displacements of the bar are obtained from basic element displacement field. Thus,

$$u = \sum_{i=1}^{20} N_i(\xi).u_i$$

$$v = \sum_{i=1}^{20} N_i(\xi).v_i \qquad (2.36)$$

$$w = \sum_{i=1}^{20} N_i(\xi).w_i$$

b) Strain–displacement representation

Since the bar is capable of transmitting axial force only, one component of strain contributes to the strain energy which is defined locally as:

$$\epsilon' = \frac{\partial u'}{\partial x'} \tag{2.37}$$

where x', y' and z' are defined as a local coordinate system at point p with y' and z' being normal to the line of the bar, and u', v' and w' are the corresponding displacements.

Let a distortion matrix $\underset{\sim}{S}$ at any point p be defined as:

$$\underset{\sim}{S} = \begin{bmatrix} \frac{\partial u}{\partial x} & \frac{\partial v}{\partial x} & \frac{\partial w}{\partial x} \\ \frac{\partial u}{\partial y} & \frac{\partial v}{\partial y} & \frac{\partial w}{\partial y} \\ \frac{\partial u}{\partial x} & \frac{\partial v}{\partial x} & \frac{\partial w}{\partial x} \end{bmatrix} - \sum_{i=1}^{20} \begin{bmatrix} \frac{\partial N_i}{\partial x} \\ \frac{\partial N_i}{\partial y} \\ \frac{\partial N_i}{\partial z} \end{bmatrix} \begin{bmatrix} u_i & v_i & w_i \end{bmatrix} \tag{2.38}$$

Substitution of equation (2.29) into (2.38) yields:

$$\underset{\sim}{S} = \sum_{i=1}^{20} \underset{\sim}{J}^{-1} \begin{bmatrix} \frac{\partial N_i}{\partial \xi} \\ \frac{\partial N_i}{\partial \eta} \\ \frac{\partial N_i}{\partial \zeta} \end{bmatrix} \begin{bmatrix} u_i & v_i & w_i \end{bmatrix} \tag{2.39}$$

As $\underset{\sim}{S}$ is a second order tensor, it transforms on coordinate rotation from x, y, z to x', y', z' according to:

$$\underset{\sim}{S}' = \begin{bmatrix} \frac{\partial u'}{\partial x'} & \frac{\partial v'}{\partial x'} & \frac{\partial w'}{\partial x'} \\ \frac{\partial u'}{\partial y'} & \frac{\partial v'}{\partial y'} & \frac{\partial w'}{\partial y'} \\ \frac{\partial u'}{\partial z'} & \frac{\partial v'}{\partial z'} & \frac{\partial w'}{\partial z'} \end{bmatrix} = \underset{\sim}{R}\ \underset{\sim}{S}\ \underset{\sim}{R}^T \tag{2.40}$$

where $\underset{\sim}{R}$ is the rotation matrix of direction cosines at point p defined as:

$$\underset{\sim}{R} = \begin{bmatrix} \frac{\partial x}{\partial x'} & \frac{\partial y}{\partial x'} & \frac{\partial z}{\partial x'} \\ \frac{\partial x}{\partial y'} & \frac{\partial y}{\partial y'} & \frac{\partial z}{\partial y'} \\ \frac{\partial x}{\partial z'} & \frac{\partial y}{\partial z'} & \frac{\partial z}{\partial z'} \end{bmatrix} \tag{2.41}$$

As x' and ξ coincide and differ only in magnitude,

$$\underset{\sim}{R} = \frac{1}{\left[\left(\frac{\partial x}{\partial \xi}\right)^2+\left(\frac{\partial y}{\partial \xi}\right)^2+\left(\frac{\partial z}{\partial \xi}\right)^2\right]^{\frac{1}{2}}} \begin{bmatrix} \frac{\partial x}{\partial \xi} & \frac{\partial y}{\partial \xi} & \frac{\partial z}{\partial \xi} \\ \frac{\partial y}{\partial \xi} & \frac{\partial x}{\partial \xi} & \frac{\partial y}{\partial \xi} \\ \frac{\partial x}{\partial \xi} & \frac{\partial z}{\partial \xi} & \frac{\partial z}{\partial \xi} \end{bmatrix} \tag{2.42}$$

From equations (2.37), (2.40) and (2.42), it follows that:

$$\epsilon' = \sum_{i=1}^{20} \frac{1}{h^2} \left[\left[c_1 \frac{\partial N_i}{\partial x} + c_2 \frac{\partial N_i}{\partial y} + c_3 \frac{\partial N_i}{\partial z} \right] . \left[c_2 \frac{\partial N_i}{\partial x} + c_4 \frac{\partial N_i}{\partial y} + c_5 \frac{\partial N_i}{\partial z} \right] . \left[c_3 \frac{\partial N_i}{\partial x} + c_5 \frac{\partial N_i}{\partial y} + c_6 \frac{\partial N_i}{\partial z} \right] \right] \begin{bmatrix} u_i \\ v_i \\ w_i \end{bmatrix} \tag{2.43}$$

where

$$h = \left[\left(\frac{\partial x}{\partial \xi} \right)^2 + \left(\frac{\partial y}{\partial \xi} \right)^2 + \left(\frac{\partial z}{\partial \xi} \right)^2 \right]^{\frac{1}{2}} \tag{2.44}$$

and

$$c_1 = \left[\frac{\partial x}{\partial \xi} \right]^2$$

$$c_2 = \frac{\partial x}{\partial \xi} \cdot \frac{\partial y}{\partial \xi}$$

$$c_3 = \frac{\partial x}{\partial \xi} \cdot \frac{\partial z}{\partial \xi}$$

$$c_4 = \left[\frac{\partial y}{\partial \xi} \right]^2 \qquad (2.45)$$

$$c_5 = \frac{\partial y}{\partial \xi} \cdot \frac{\partial z}{\partial \xi}$$

$$c_6 = \left[\frac{\partial z}{\partial \xi} \right]^2$$

Finally, equation (2.43) may be rewritten in the form:

$$\epsilon' = \underset{\sim}{B}' \, \underset{\sim}{a}^e \qquad (2.46)$$

where $\underset{\sim}{B}'$ is the strain–displacement matrix of the bar element.

c) Stiffness matrix calculation

The stiffness matrix of an axially loaded bar element given in (2.18) may be expressed as:

$$\underset{\sim}{K}'^{e} = \int_{V^e} \underset{\sim}{B}'^{T}\, \underset{\sim}{D}'\, \underset{\sim}{B}'\, dV^e \qquad (2.47)$$

The constitutive matrix $\underset{\sim}{D}'$ represents the modulus of elasticity of steel bars in this case. For a one dimensional bar element lying in direction parallel to the natural coordinate line ξ, the volume differential dV^e can be written as:

$$dV^e = A_s\, dx' = A_s\, h\, d\xi \qquad (2.48)$$

where A_s is the cross-sectional area of the bar. By substitution of equation (2.48) into (2.47), the stiffness matrix of the embedded bar can be expressed as:

$$\underset{\sim}{K}'^{e} = A_s \int_{-1}^{+1} \underset{\sim}{B}'^{T}\, \underset{\sim}{D}'\, \underset{\sim}{B}'\, h\, d\xi \qquad (2.49)$$

In this case, the numerical integration required to calculate the stiffness matrix is carried out in one direction only.

2.7 Numerical Integration

In general it is not possible to perform analytically the integration required to set up the stiffness matrices and the equivalent nodal loads for the elements used. Therefore, resort has to be made to some suitable scheme of numerical integration. In finite element work the Gaussian-Legendre quadrature scheme has been

found to be both very accurate and convenient. The scheme is presented in this section by considering the element stiffness matrix of the reinforcing bar given by equation (2.49) which is may be written in the form:

$$I = \int_{-1}^{+1} F(\xi)\, d\xi \qquad (2.50)$$

In the Gauss quadrature scheme, the integration is evaluated as a summation of m products of values of the function $F(\xi)$ at particular sampling points and appropriate weighting factors, W_i. Therefore, equation (2.50) can be calculated numerically as:

$$I = \sum_{i=1}^{m} W_i\, F(\xi_i) \qquad (2.51)$$

By using m sampling points, equation (2.51) integrates exactly a polynomial of order (2m-1).

For a hexahedral element, the required integral of (2.34) can be expressed formally as:

$$I = \int_{-1}^{+1}\int_{-1}^{+1}\int_{-1}^{+1} F(\xi,\eta,\zeta)\, d\xi\, d\eta\, d\zeta \qquad (2.52)$$

which may be calculated numerically as:

$$I = \sum_{i=1}^{m} \sum_{j=1}^{m} \sum_{k=1}^{m} W_i W_j W_k F(\xi_i, \eta_j, \zeta_k) \qquad (2.53)$$

In this case the scheme performs exactly the integration of a polynomial of order (2m-1) in each of the local directions by using (m x m x m) sampling points.

2.7.1 Integration Rules Implemented in the study

Three-dimensional finite element problems require a large amount of computation time when compared with two-dimensional problems. A considerable proportion of the total computations is used in the numerical integration. Therefore it is very important to choose a suitable integration scheme that is both accurate and computationally efficient. A comparison of the accuracy and the efficiency of the different rules considered in the present study is given in sections 5.5.1.2 and 7.2.4.2.3. The integration rules which have been used in this work are,

a) The 27 (3x3x3) and the reduced 8 (2x2x2) Gauss-quadrature integration rules.

b) Three Gauss-type integration rules, first presented by Irons [44], with 15 sampling points.

The later rules are designed to integrate complete polynomials [45,46]. They integrate correctly $\Sigma W_{ijk} x^i y^j z^k$, i+j+k=m and have been proved to be accurate and efficient [44,47]. Each of the three 15 sampling points rules can be expressed in the form:

$$I = -W_1\, f(0,0,0) + \qquad \text{(one term)}$$

$$W_2\{f(-b,0,0)+f(b,0,0)+f(0,-b,0)+\cdots\cdots\} + \quad \text{(6 terms)} \qquad (2.54)$$

$$W_3\{f(-c,-c,-c)+f(-c,-c,c)+f(-c,c,c)+\cdots\} \quad \text{(8 terms)}$$

The relative positions of the sampling points, for the 15 points rules, over the volume of the element are shown in Fig. 2.3, and the corresponding weights and abscissae are listed in Table 2.1. Details for Gauss–quadrature rules can be found in most finite element texts [11,20].

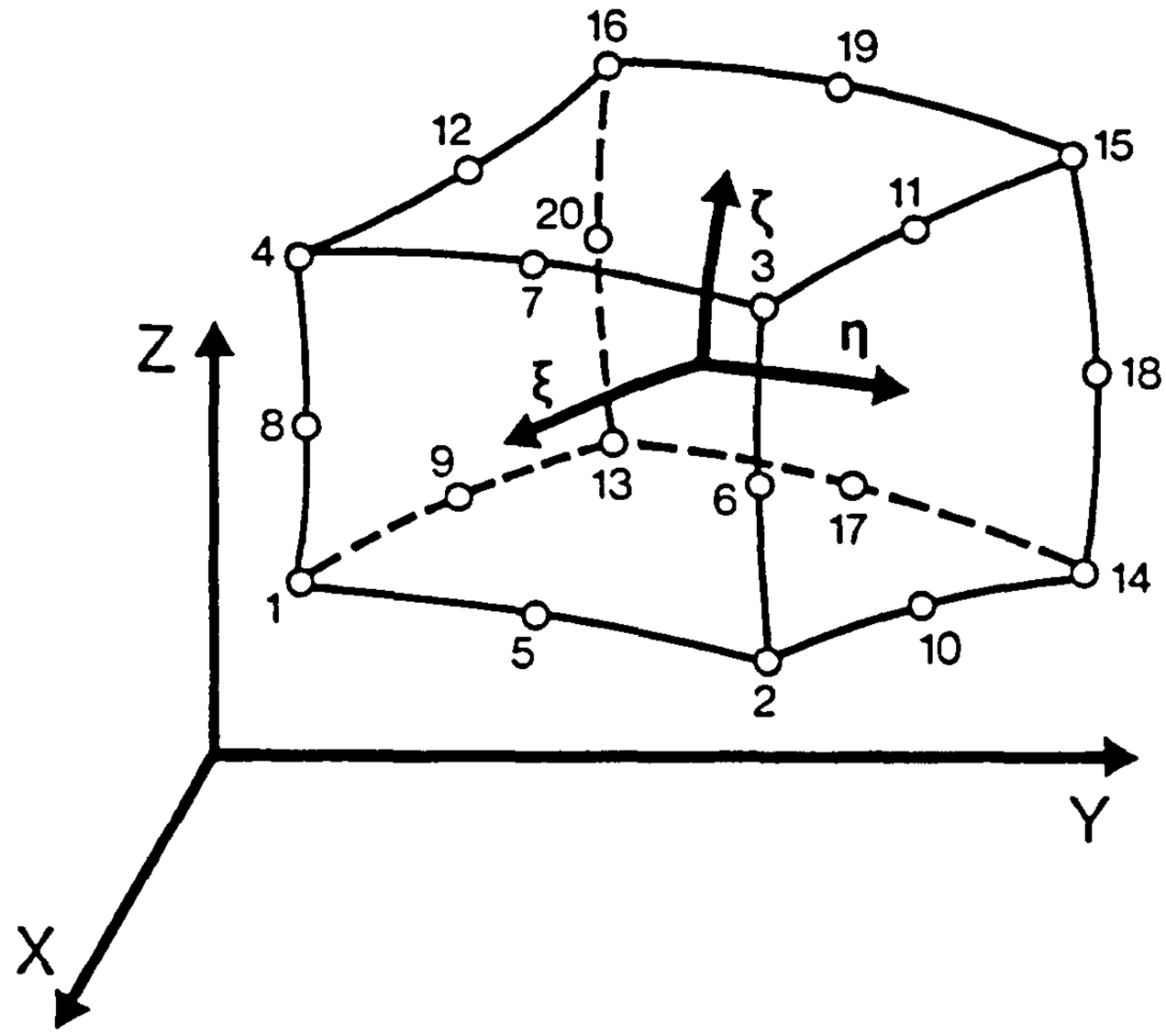

a) Cartesian coordinates

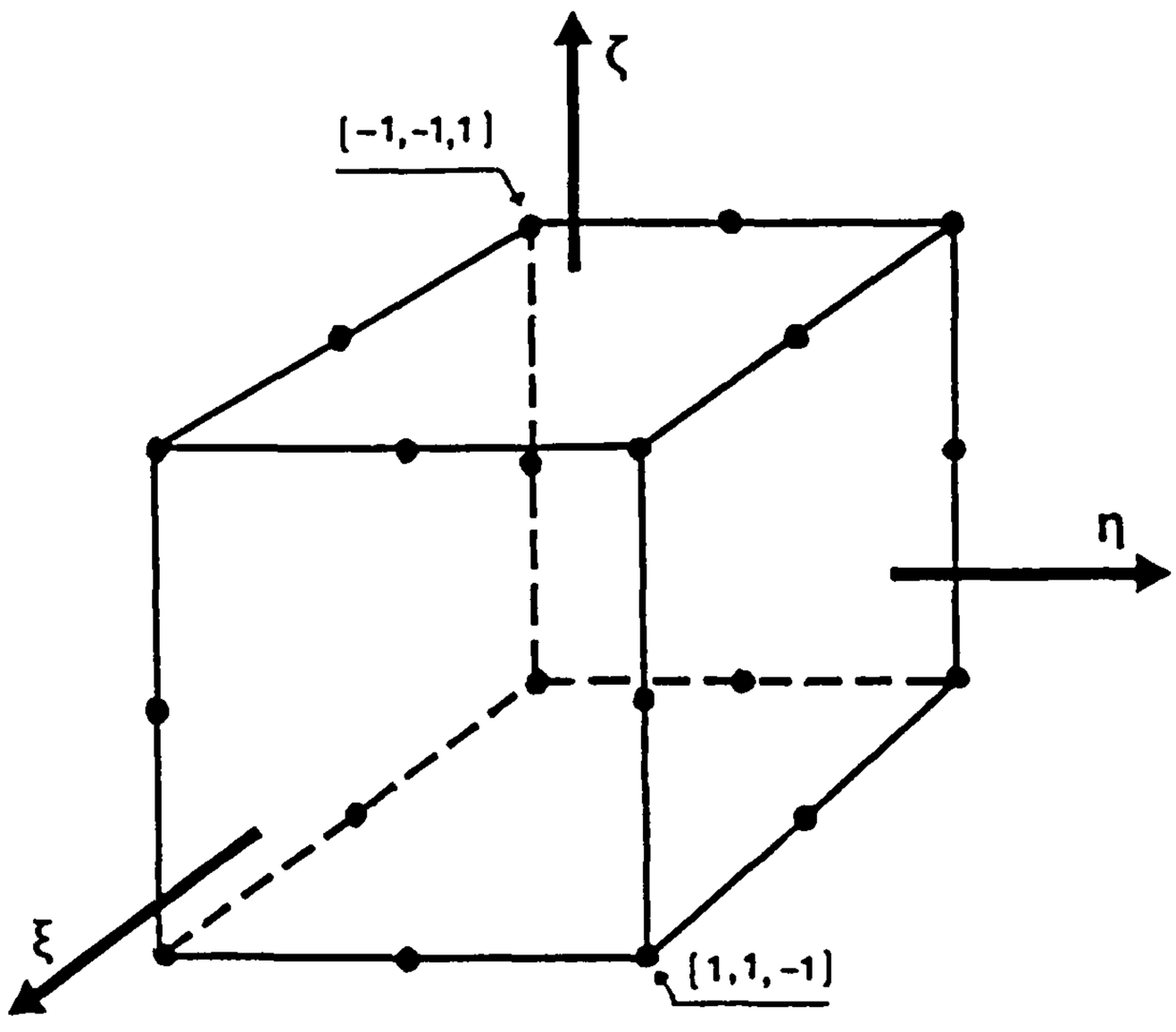

b) Local coordinates

Fig. 2.1 Twenty noded isoparametric brick element.

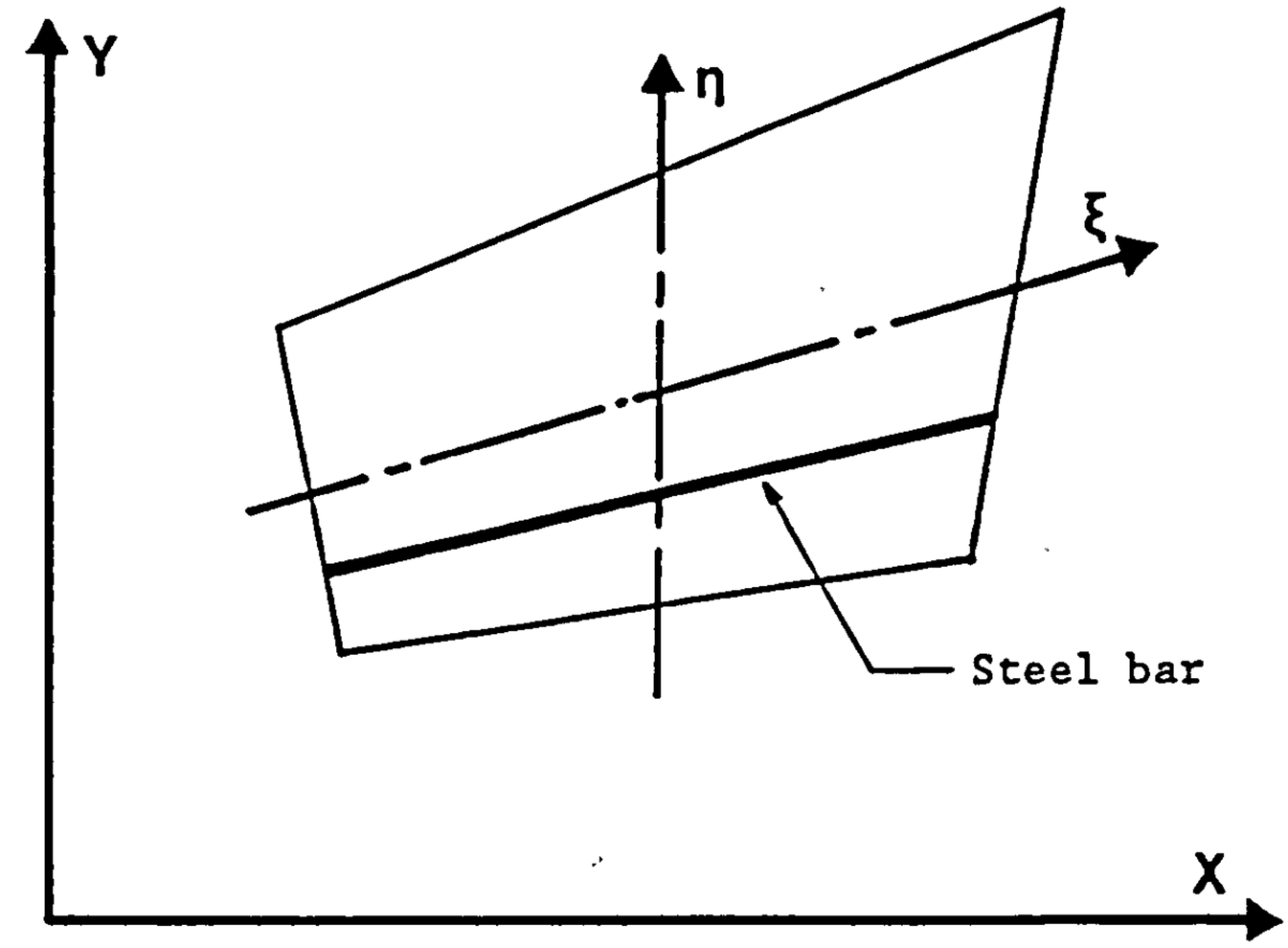

a) Two-dimensional representation.

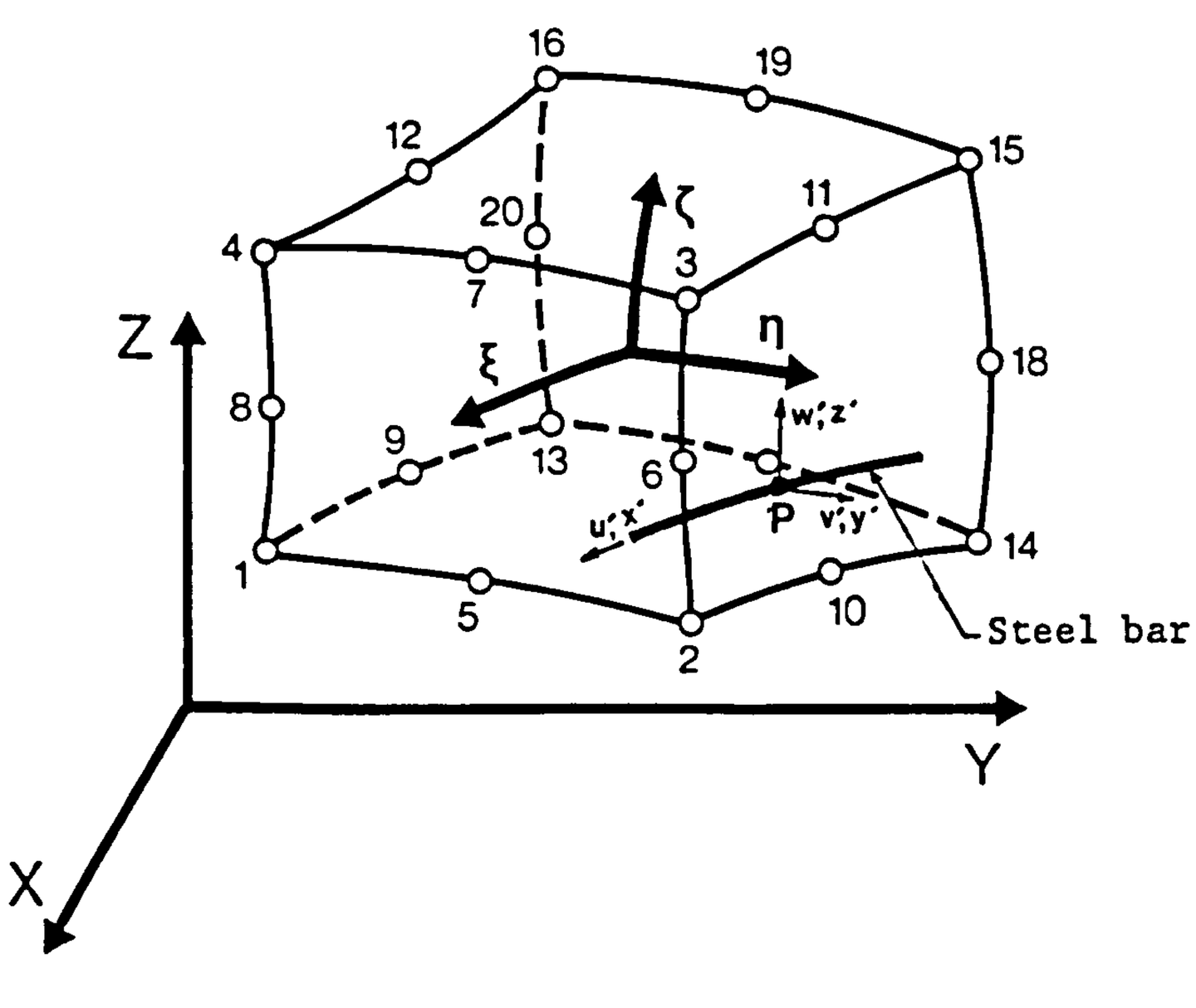

b) Three-dimensional representation.

Fig. 2.2 Embedded representation of reinforcement.

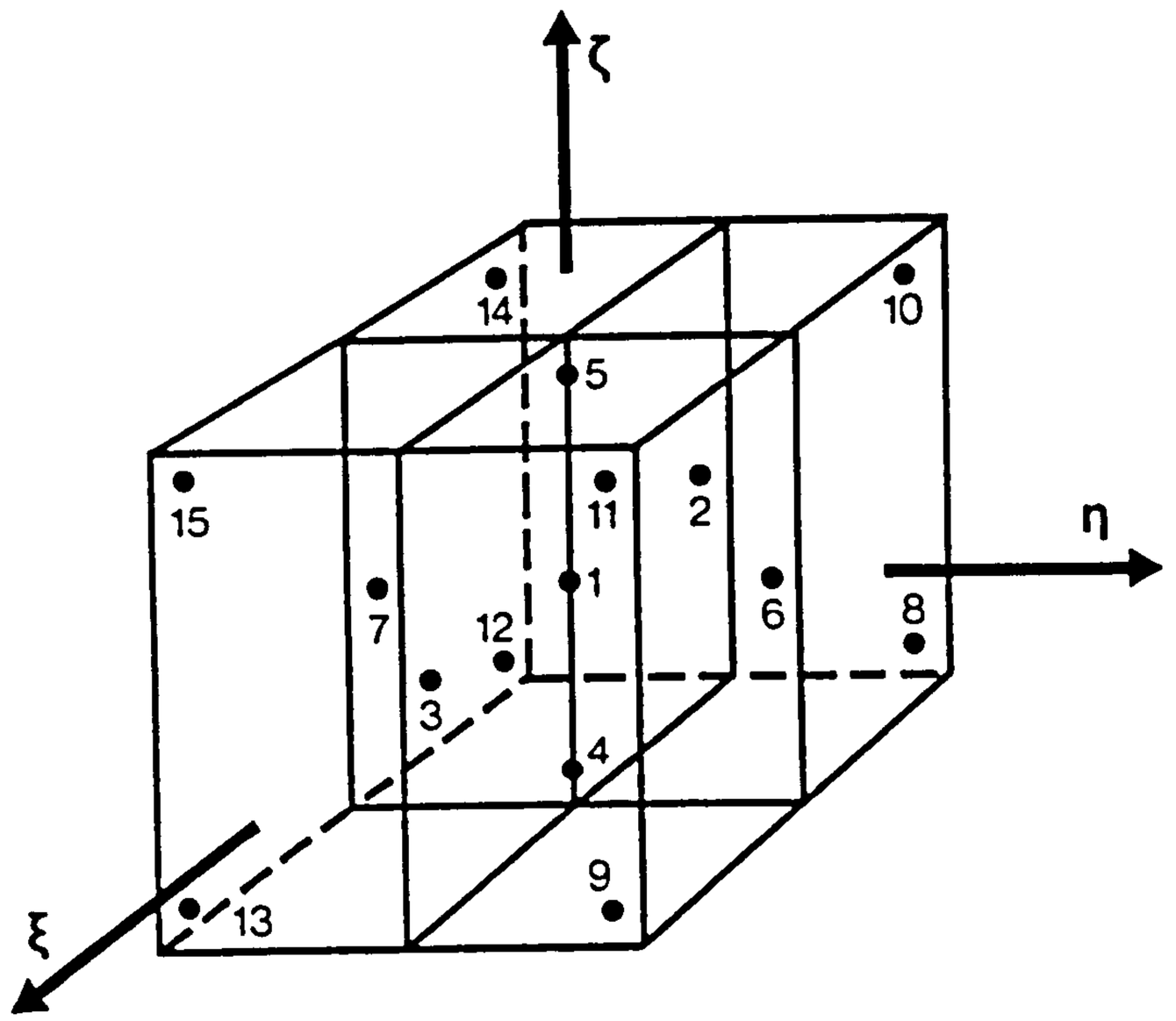

Fig. 2.3 Distribution of sampling points in 15 point rules.

Table 2.1 Weights and abscissae of sampling points in 15-point rules

Integration rule		Sampling point no.				
		1	2,3	4,5	6,7	8–15
Rule 14	ξ	0.0	±0.795822	0.0	0.0	±0.758787
	η	0.0	0.0	0.0	±0.795822	±0.758787
	ζ	0.0	0.0	±0.795822	0.0	±0.758787
	Weight	0.0	0.886427	0.886427	0.886427	0.335180
Rule 15a	ξ	0.0	±1.0	0.0	0.0	±0.67140
	η	0.0	0.0	0.0	±1.0	±0.67140
	ζ	0.0	0.0	±1.0	0.0	±0.67140
	Weight	1.564444	0.355556	0.355556	0.355556	0.537778
Rule 15b	ξ	0.0	±0.848418	0.0	0.0	±0.727662
	η	0.0	0.0	0.0	±0.848418	±0.727662
	ζ	0.0	0.0	±0.848418	0.0	±0.727662
	Weight	0.712137	0.686227	0.686227	0.686227	0.396312

REFERENCES

1. McHenry, D., "A Lattic Analogy for the Solution of Plane Stress Problems", J. Inst. Civ. Engrs., Vol. 21, 1943, pp. 59–82.

2. Hrenikoff, A., "Solution of Problems in Elasticity by the Framework Method", J. Appl. mech., Vol. 8, 1941, pp. 169–175.

3. Courant, R., "Variational Methods for the Solutions of Problems of Equilibrium and Vaibrations", Bull. Amer. Math. Soc., Vol. 49, 1943, pp. 1–23.

4. Argyris, J.H. and Kelsey, S., "Structural Analysis by the Matrix Force Method with Applications to Aircraft Wings", Wiss. Ges. Luftfahrt Jahrb., 1956, pp. 78–98.

5. Turner, M.J , Clough, R.W., Martin, H.C. and Topp, L.J., "Stiffness and Deflection Analysis of Complex Structures", J. Aeronautcal Soc., Vol. 23, No. 9, 1956, pp. 805–823.

6. Clough, R.W., "The Finite Element Method in Plane Stress Analysis", J. of the Struct. Div. , ASCE Proc. 2nd Conf. on Electronic Computation, New York, 1960, pp. 345–378.

7. Besseling, J.F., "The Complete Analogy Between the Matrix Equations and the Continuous Field Equations of Structural Analysis", Int. Symp. on Analogue and Digital Techniques Applied to Aeronautics, Belgium, 1963.

8. Melosh, R.J., "Basis for the Derivation of Matrices for the Direct Stiffness Method", AIAA J., Vol. 1, 1963, pp. 1631-1637.

9. Jones, R.E., "A Generalizationof the Direct Stiffness Method of Structural Analysis", AIAA J., Vol. 2, 1964.

10. Zienkiewicz, O.C. and Cheung, Y.K., "Finite Elements in the Solution of Field Problems", Engineer, Vol. 220, 1965.

11. Zienkiewicz, O.C., "The Finite Element Method", 3rd Ed., McGraw–Hill Book Company, New York, 1977.

12. Oden, J.T., "Finite Elements of Non-Linear Continua", McGraw-Hill Company, New York, 1972.

13. Cook, R.D., "Concepts and Applications of Finite Element Analysis", 2nd. Ed., John Wiely and Sons, New York, 1981.

14. Bathe, K.J. and Wilson, E.L., "Numerical Methods in Finite Element Analysis", Prentice–Hall, New Jersey, 1976.

15. Hinton, E., and Owen D.R.J., "Finite Element Programing", Academic Press, New York, 1977.

16. Owen, D.R.J. and Hinton E., "Finite Elements in Plasticity–Theory and Practice", Pineridge Press, Swansea, 1980.

17. Huebner, K.H. and Thornton, E.A. ,"The Finite Element for Engineers", John Wiley and Sons, New York, 1982.

18. Crisfield, M.A., "Finite Elements and Solution Procedures for Structural Analysis", Pineridge Press, Swansea, 1986.

19. Weaver, W.J. and Johanston, P.R., "Finite Elements for Structural Analysis", Prentice-Hall, New Jersey, 1984.

20. Dawe, D.J., "Matrix and Finite Element Displacement Analysis of Structures", Clarendon Press, Oxford, 1984.

21. Felippa, C.A. and Clough, R.W., "The Finite Element Method in Solid Mechanics," In SIAM-AMS Proc., Vol. 2, Amer. Math. Soc., 1970, pp. 210-252.

22. Olivera, E.R.A., "Theoretical Foundations of Finite Element Method", Int. J. Solids Struct., Vol. 4, 1968, pp. 929-952.

23. Bazeley, G.P., Cheung, Y.K., Irons, B.M. and Zienkiewicz, O.C., " Triangular Elements in Bending- Conforming and Non-Conforming Solutions", Proc. Conf. Matrix Methods in Struct. Mech., Air Force Inst. Tech., Wright-Patterson A.F. Base, Ohio, 1965.

24. Clough, R.W., "The Finite Element Method in Structural Mechanics," Chapter 7 of Stress Analysis, Eds. Zienkiewicz, O.C. and Holistor, G.S., John Wiley and Sons, 1965.

25. Irons, B.M., "Numerical Integration Applied to Finite Element Methods", Conf. on Use of Digital Computers in Struct. Eng., University of New-Castle, 1966.

26. Ngo, D. and Scordelis, A.C., "Finite Element Analysis of Concrete Beams", J. of the Struct. Div. , ASCE, Vol. 100, No. ST12, 1974.

27. ASCE Committee on Concrete and Masonry Structures, " A State of the Art Report on the Finite Element Analysis of Reinforced Concrete", Task Committee on Finite Element Analysis of Reinforced Concrete Structures, ASCE Spec. Publ., 1981.

28. Nayak, G.C., "Plasticity and Large Deformation Problems by the Finite Element Method", Ph.D. Thesis, University of Wales, Swansea, 1971.

29. Irons B.M., "Engineering Application in Stiffness Methods", AIAA J., Vol. 4, No. 11, 1966, pp. 2035-2037.

30. Gallagher, J., Padlog, P. and Bijlaard, P.P., "Stress Analysis of Heated Complex Shapes", J. Aerosp. Science, Vol. 32, 1962.

31. Melosh, R.J., "Structural Analysis of Solids", Proc. Amer. Soc. Civ. Eng., ST4, 205-23, 1963.

32. Argyris J.H., " Matrix Analysis of Three-Dimensional Elastic Media-Small and Large Displacement", AIAA , Vol.3, 1965, pp. 45-51.

33. Fjeld, S.A., "Three Dimensional Theory of Elasticity", In Finite Element Methods in Stress Analysis", Eds. Holand, I. and Bell, K., Tapir, Trondheim, 1969.

34. Clough, R.W., "Comparison of Three-Dimensional Finite Elements", Proc. Symp. on Appl. of Finite Element Methods in Civ. Eng., University of Vandebilt, ASCE ,Nashville, 1969.

35. Suidan, M.T. and Schnobrich, W.C., "Finite Element Analysis of Reinforced Concrete", J. of the Struct. Div., ASCE, Vol. 99, No. ST10, 1973

36. Cervera, M., "Non-Linear Analysis of Reinforced Concrete Structure Using Three Dimensional and Shell Finite Element Models", Ph.D. Thesis, University of Wales, Swansea, 1986.

37. Mohamed, M.S., "A Finite Element and Experimental Study of Reinforced Concrete in Torsion", Ph.D. Thesis, University of Glasgow, 1986.

38. Al-Mahaidi, R.S.H., "Non-Linear Finite Element Analysis of Reinforced Concrete Deep Members", Report No 79, Dept. of Struct. Eng., Cornell University, 1979.

39. Scordelis, A.C., "Finite Element Analysis of Reinforced Concrete Slabs", Struct. Eng. Research report No. 38, Dept of Civil Eng., University of Alberta, Edmonton, Canada, 1971.

40. Khouzan M., "A Finite Element Investigation of Reinforced Concrete Beams," Mech. Eng. Thesis, McGill University, Montreal, Canada, 1977.

41. Imbabi, M.S., "Non-Linear Analysis of Reinforced Concrete Planer Structures", Ph.D. Thesis, University of Liverpool, 1984.

42. Zienkiewicz, O.C., Owen, D.R.J., Phillips, D.V., and Nayak, G.C., "Finite Element Methods in the Analysis of Reactor Vessels", Nuclear Eng. and Design, Vol. 20, No. 2, 1972, pp. 507-541.

43. Phillips, D.V., and Zienkiewicz, O.C., "Finite Element Non-Linear Analysis of Concrete Structures", Proc. Inst. of Civ. Engrs., Vol. 61, Part 2, 1976, pp. 59-88.

44. Irons, B.M., "Quadrature Rules for Brick Based Finite Elements", Int. J. for Num. Meth. in Eng., Vol. 3, pp. 293-294, 1971.

45. Stroud A.H. and Don Secrest, "Gaussian Quadrature Formulas", Prentice-Hall, P. 40, 1966.

46. Miller, J.C.P., "Numerical Quadrature Over a Rectangular Domain in Two or More Dimensions", Maths. Comput., Vol. 14, 1960, pp. 130-138.

47. Cervera, M. and Hinton, E., " Non-Linear Analysis of Reinforced Concrete Plates and Shells Using a Three-Dimensional Model", Research Report, Dept. of Civ. Eng., University of Wales, Sawnsea, 1985.

CHAPTER THREE

MODELLING OF MATERIAL PROPERTIES

3.1 Introduction

One of the pieces of basic information required in any three-dimensional non-linear finite element analysis of reinforced concrete structures is the material constitutive model which describes the current multi-dimensional stress-strain relations governing the behaviour of the structure. Since the concrete and the reinforcing steel have very different material properties, the behaviour of the composite, reinforced concrete, is usually simulated by considering the constitutive relations of the constituents independently. Full interaction between the two materials has been assumed to exist throughout the present work. This Chapter outlines the constitutive models for the concrete and the steel used in the present study.

Due to its complex behaviour, the concrete constitutive model is given special emphasis. The observed behaviour of concrete under different loading conditions is outlined in section 3.2. Section 3.3 describes the different components required to model the concrete. A plasticity model for concrete in compression and a smeared crack model for concrete in tension have been adopted in the current study. These models are illustrated in section 3.4. The model used for the reinforcing steel is presented in section 3.5.

3.2 The Observed Behaviour of Concrete

Concrete is a material with a grossly heterogeneous internal structure. It consists of inert aggregate particles embedded within a binding paste made from portland cement and water. Fresh concrete hardens as a result of chemical reactions between the cement and water to form a solid and durable structural material. Due to incomplete hydration, hardening concrete usually contains capillary pores filled with air or water. The presence of capillary pores, internal flaws in the aggregate and bond micro-cracks at interfaces between the cement paste and the aggregate prior to any load application can be viewed as a source of weakness in the structure of concrete [1]. Many of these micro-cracks are caused by segregation, shrinkage and thermal movements in the mortar. Some micro-cracks may develop during loading because of the difference in stiffness between the aggregate and mortar [2]. The gradual growth of these micro-cracks with further loading contributes to the non-linear behaviour of concrete.

Concrete can behave as either a linear or a non-linear material depending on the nature and the level of the applied stresses. Stiffness and strength properties of concrete subjected to multiaxial loading conditions differ from those displayed under uniaxial compression. Under a low level of stresses, linear elastic behaviour is observed, while concrete exhibits a highly non-linear response at higher stress levels [3]. Many experimental studies of the behaviour of concrete under uniaxial and multiaxial loading conditions have been performed, for example see refs. [4-14]. The aims of such investigations have been to understand the complex response of

concrete for various imposed stress conditions and to provide the necessary data required to develop accurate numerical models for use in non-linear finite element analysis of concrete structures.

In the following sections, the response of concrete under uniaxial and multiaxial loading states are briefly described.

3.2.1 Uniaxial Behaviour of Concrete

A typical uniaxial compression stress-strain curve is shown in Fig. 3.1. Up to a stress level of about 30 percent of its uniaxial compressive strength, f'_c, concrete behaves as a linear elastic material. This stress level is termed the point of "onset of the localised cracking" and has been proposed as a limit of elasticity [15]. At stresses between 0.3 f'_c - 0.5 f'_c, the bond cracks start to extend due to stress concentrations at the crack tips and the stress-strain curve starts to show a slight non-linearity in this range of loading. When the stress exceeds 0.5 f'_c some cracks at nearby aggregate surfaces start to bridge in the form of mortar cracks with other cracks continuing to grow slowly. A gradual increase in the curvature of the stress-strain curve occurs up to about 0.75 f'_c. For compression stresses above this value, the rate of crack propagation increases rapidly and the stress-strain curve bends sharply until the peak stress level is reached [2,15]. Beyond the peak stress, concrete exhibits a strain-softening response characterised by the descending portion of the curve. This falling part of the stress-strain curve is mainly dependent on testing machine properties [1,16].

The initial modulus of elasticity of concrete is highly dependent on the compressive strength. In lieu of actual test data, the initial modulus of elasticity, E, can be calculated approximately from the empirical formula (ACI Code 318–77) [17]:

$$E = 33\, W_c^{1.5}\, f_c'^{0.5} \qquad (3.1)$$

where W_c is the concrete unit weight in pounds per cubic foot and E and f_c' are expressed in pounds per square inch.

The Poisson's ratio, ν, of concrete has been observed to remain approximately constant and ranges from about 0.15 to 0.22 up to a stress level of 80 percent of f_c' [1,3]. Beyond this level, Poisson's ratio increases rapidly and values in excess of 1.0 have been measured by Darwin and Pecknold [18] and Maekawa and Okamura [12].

Under tensile stress, the strength of concrete, f_t, is approximately a tenth of the compressive strength [19]. A typical tensile stress–strain curve is shown in Fig. 3.2. Up to a stress level of 60 percent of f_t the curve is linearly elastic [2]. beyond this level, the bond micro–cracks starts to grow and the non–linearity of the curve starts to increase as the stress level increases until the peak stress is reached. Following this level, a post softening regime is observed [19,20]. The elastic modulus in uniaxial tension is slightly greater than that in uniaxial compression, while the Poisson's ratio in tension is somewhat smaller than that in compression [10].

3.2.2 Multiaxial Behaviour of Concrete

Under multiaxial states of stress, concrete exhibits strength, stiffness and stress–strain behaviour somewhat different from that of the uniaxial state. Extensive experimental tests on concrete under biaxial stress states have been performed by many workers, amongst them Kupfer et al. [6], Liu et al. [7], Nelissen [8], Tasuji et al. [10] and Maekawa and Okamura [12]. A typical biaxial strength envelope is shown in Fig. 3.3. When subjected to biaxial compression, concrete has an increased compressive strength up to about 1.25 f'_c for a principal stress ratio of 0.5 and up to about 1.16 f'_c for a principal stress ratio of 1.0 [6-8,10]. Under biaxial tension–compression, the tensile strength decreases almost linearly as the applied compression increases. For biaxial tension states, concrete exhibits nearly constant tensile strength [6]. However, some investigators have reported a slight increase [10], and others have reported a slight decrease [21] in tensile strength.

When subjected to triaxial compression stress, concrete exhibits strength which increases with the increasing confining pressures. Under very high confining stresses, extremely high strengths have been recorded [22]. Experimental studies indicate that the three–dimensional failure envelope is a function of the three principal stresses [23]. Fig. 3.4 shows a schematic failure surface of concrete in three–dimensional stress space. The failure envelope is smooth, convex and its deviatoric sections (planes perpendicular to the hydrostatic axis σ_1=σ_2=σ_3) become more circular in shape for increasing hydrostatic pressures, along the σ_1=σ_2=σ_3 axis. For smaller hydrostatic pressures, these cross–sections are convex and

non-circular [2,3]. Experimental studies have indicated that the general formulation of the three-dimensional failure surface can be expressed in terms of the combination of three stress invariants, I_1, J_2 and J_3, where I_1 is the first invariant of the stress tensor and J_2 and J_3 are the second and the third invariants of the deviatoric stress tensor [2,24-27]. However, some analyses indicate that the failure envelope may be represented by two stress invariants only [3].

3.3 Numerical Modelling of Concrete

Numerical representation of concrete properties in connection with the non-linear finite element modelling of reinforced concrete members is one of the most important aspects of any realistic analysis. Because concrete has a very complex behaviour, involving phenomena such as cracking and inelastic response in compression, the modelling of all the aspects of its behaviour is extremely difficult and a unified numerical model has not yet been achieved. Linear representation of concrete was utilised in the earliest finite element reinforced concrete models [28]. Very rapidly non-linear behaviour in the form of cracking and compression softening were used to improve the realism of the solution. At present, many typical aspects of the experimental behaviour of concrete can be adequately simulated. The numerical modelling of concrete for use in a non-linear finite element program should include the following constituents:

1. A stress–strain model to represent the behaviour of concrete prior to failure.
2. Failure criteria to simulate cracking and crushing types of fracture.
3. A method of crack representation.
4. A post cracking stress–strain relationship.
5. Modelling the reduction in compressive strength due to orthogonal cracking.

These constituents are discussed in the following sections.

3.3.1 Stress–Strain Models

In general, there are several approaches for defining the complicated stress–strain behaviour of concrete under various stress states. They can be classified into:

1. Elasticity based models,
2. Plasticity based models,
3. Endochronic theory models.

Detailed discussions of these approaches are given in [2,25] and a comprehensive review of various models used in the finite element analysis of reinforced concrete structures are given in [3,29]. In the following sections, the basic concepts and the limitations of these approaches will briefly discussed.

3.3.1.1 Elasticity based models

Two different approches have been employed in the formulation of the non-linear elasticity based constitutive relations. These are the total and the incremental stress-strain formulations. In the total, secant, stress-strain models, the current state of stress is assumed to be uniquely expressed as a function of the current state of strain. This type of formulation is reversible and path-independent which is not true for concrete in general [3]. Therefore, such models are only suitable for monotonic or proportional loading regimes. However, when concrete experiences unloading these models fail to predict inelastic deformations. In spite of these shortcomings, the total stress-strain models have been used mainly because of their simplicity to predict the non-linear behaviour of concrete under biaxial and triaxial compressive stresses. Some of these models assume an isotropic stress-strain relation for concrete, e.g the models of Kupfer and Gerstle [9] for the biaxial states of stress and the model of Cedolin et al. [24] for the triaxial states. Other models are based on an orthotropic form of the stress-strain relation with the principal stress directions coinciding with the direction of orthotropy, e.g the models of Liu et al. [7], Tasuji et al. [10] and Cope and Rao [30].

The incremental, hypoelastic, stress-strain models are used to describe the behaviour of materials in which the state of stress depends on the current state of strain and the stress path followed to reach that state. In a hypoelastic material model, the stress and strain increment vector are linearly related through the tangential material stiffness matrix $\underline{D}_T$ as:

$$\underset{\sim}{d\sigma} = \underset{\sim}{D}_T \, \underset{\sim}{d\epsilon} \qquad (3.2)$$

where $\underset{\sim}{d\sigma}$ and $\underset{\sim}{d\epsilon}$ are the stress and the strain increment vectors respectively. This type of formulation is incrementally reversible and path dependent and therefore it provides a good representation of concrete behaviour under non-monotonic and non-proportional loading regimes as compared with the total stress formulation [2,3]. A number of useful isotropic and orthotropic incremental models have been developed and utilised in the finite element analysis of concrete structures. An example of an incrementally isotropic stress-strain relation is the biaxial model of Gerstle [31]. A model using the incrementally opthotropic relations is that of Darwin and Pecknold [32,33] for the biaxial states of stress and for triaxial states the models of Elwi and Murray [34] and Bathe et al. [35].

3.3.1.2 Plasticity based models

For concrete under compression, non-linear deformations occur when it is stressed beyond the limit of elasticity. These deformations are basically inelastic since upon unloading only a portion of the total strain can be recovered. Therefore, the total strain may be separated into recoverable and irrecoverable components. The recoverable part is treated within the framework of elasticity, while the treatement of the irrecoverable part is based on the theory of plasticity.

In the incremental theory of plasticity, the total strain increment vector $d\underset{\sim}{\epsilon}$ is assumed to be the sum of the elastic, $d\underset{\sim}{\epsilon}^e$, and

the plastic, $d\underline{\varepsilon}^P$, components, such that

$$d\underline{\varepsilon} = d\underline{\varepsilon}^e + d\underline{\varepsilon}^P \tag{3.3}$$

In addition to the strain decomposition, three other fundamental assumptions are required to formulate the constitutive relations for a work-hardening plastic material. They are:

1. The shape of an initial yield surface and subsequent loading surfaces.
2. The formulation of a suitable hardening rule that describes the evolution of subsequent loading surfaces.
3. The formulation of an appropriate flow rule that specifies the stress-strain relation in the plastic range.

The initial yield surface is required to mark the stress level at the onset of plastic deformations. It can be expressed as:

$$f(\underline{\sigma}) = k \tag{3.4}$$

where f is some function of stress and k is a material parameter to be determined experimentaly. When a work-hardening material is stressed beyond its limit of elasticity, the initial yield surface, a new yield surface, called the loading surface, is developed. This loading surface will change its configuration at any stage of plastic deformation and it may be expressed in terms of the plastic strain, $\underline{\varepsilon}^P$ and a hardening parameter, h, as:

$$f = f(\underline{\sigma}, \underline{\varepsilon}^P, h) \tag{3.5}$$

States for which $f = 0$ represent yield states, while elastic behaviour occurs when $f < 0$.

The evolution of subsequent loading surfaces during plastic deformation is described by specifying an appropriate hardening rule. Three types of hardening rule are frequently used in connection with the strain-hardening plasticity models. These are; isotropic, kinematic and mixed hardening rules. In an isotropic hardening model, the subsequent loading surfaces are a uniform expansion of the original yield surface. The kinematic hardening rule assumes that the subsequent loading surfaces preserve the shape and orientation of the initial yield surface during plastic flow but they translate in the stress space as rigid bodies. In the mixed hardening rule, the loading surface experiences a translation and a uniform expansion in all directions [2,36].

In order to establish the stress-strain relation in the plastic range, the concept of a plastic-potential function $g(\underline{\sigma})$ is introduced [2]. The plastic strain increment vector is assumed to be proportional to the stress gradients of the plastic potential function, so that

$$d\underline{\varepsilon}^P = d\lambda \frac{\partial g(\underline{\sigma})}{\partial \underline{\sigma}} \tag{3.6}$$

where $d\lambda$ is a positive scalar factor of proportionality. Equation (3.6) is termed the flow rule since it governs the plastic flow after yielding. The gradient of the potential surface $(\partial g(\underline{\sigma})/\partial \underline{\sigma})$ defines the direction of the plastic strain increment vector and the length

is determined by the factor $d\lambda$. When the current loading surface and the plastic potential function coincide, $f(\underline{\sigma}) \equiv g(\underline{\sigma})$, equation (3.6) becomes:

$$d\underline{\varepsilon}^P = d\lambda \frac{\partial f(\underline{\sigma})}{\partial \underline{\sigma}} \tag{3.7}$$

This relationship is known as the associated flow rule, because it is connected with the loading surface. And it is also called the normality condition since $(\partial f(\underline{\sigma})/\partial \underline{\sigma})$ represents a vector directed normal to the current loading surface at the stress point under consideration.

Plasticity based models have been extensively used to describe the behaviour of concrete, e.g the models of Buyukozturk [37], Chen [2], Chen and Chen [38], Owen and Figueiras [39], Imbabi and Cope [40] and Cervera and Hinton [41] amongst others. In general, models based on the theory of plasticity assume an elastic plastic hardening behaviour of concrete up to the ultimate strength followed by a rigid plastic response until the crushing surface is reached. After crushing, the concrete is assumed to lose completely its resistance against further deformation. Since decreasing of all stress components is impossible for strictly plastic behaviour satsisfying Drucker's stability postualte [42], such models are not capable of representing the degradation of stiffness and softening due to unstable fracturing of the material.

Recently a more refined approach based on plastic-fracturing theory has been developed and used in modelling the post failure,

softening, response of concrete [43-45]. The fracturing phenomea are better described in terms of loading surfaces that depend on strains rather than stresses since micro-fracturing can lead to a decrease in stress at constant strain. Therefore, two loading surfaces are required in the plastic-fracturing theory to account for the strain hardening and strain softening behaviour. In addition to strain decomposition of (3.3), the stress increment is also decomposed into an elastic stress increment and a fracture stress decrement [43].

3.3.1.3 Endochronic theory models

The endochronic theory of viscoplasticity was originally proposed by Valanis [46] and has been applied to predict the mechanical response of metals under complex strain histories. The first application to geo-materials and concrete as well as the first comprehensive endochronic constitutive equation was developed by Bazant and Bhat [47]. Unlike the elasticity and plasticity models, the endochronic formulation is incrementally non-linear. The basic concept underlying the theory is that of intrinsic time. Intrinsic time is a non-decreasing scalar variable that depends on the increments of strains as well as time [48]. Although the theory is capable of modelling many complex phenomena, the early endochronic formulation was subjected to serious criticisms concerning uniqueness of response, stability and energy dissipation during load cycles [49,50]. These criticisms were eliminated when Bazant [51] introduced the concepts of loading surfaces and jump-kinematic hardening to give the theory features similar to that of the theory

of plasticity. Valanis [52] refined the intrinsic time in terms of plastic strain and showed that the various versions of classical plasticity theories represent particular cases of endochronic formulation.

3.3.2 Modelling of Concrete Fracture

Fracture of concrete may be classified as crushing or cracking. Under compressive stresses, the crushing type of fracture is characterised by progressive degradation of the materials internal structure. Crushing is assumed to occur when the compression deformation capacity of the material is exceeded. For multiaxial loading, the ultimate deformation level is usually modelled by a failure surface in strain space. At the instant of crushing all the stresses at a sampling point are released completely and concrete is assumed to lose its stiffness in all directions. Thus,

$$d\underset{\sim}{\sigma} = \underset{\sim}{0}\, d\underset{\sim}{\varepsilon} \tag{3.8}$$

$$\underset{\sim}{\sigma} = \underset{\sim}{0}\, \underset{\sim}{\varepsilon} \tag{3.9}$$

The cracking, tensile, type of fracture is characterised by a gradual growth and continuous propagation of micro-cracks which join ,together, eventually to form a failure plane. After crack formation only the normal and the shear stresses across the failure plane are gradually released. Because cracking is a partial and directional failure, the material parallel to the crack is assumed to be capable of carrying stress according to the prevailing uniaxial or biaxial

conditions. The onset of cracking is generally modelled by one of two fracture criteria. These are the maximum principal stress criterion and the maximum principal strain criterion. A crack is assumed to form in a plane normal to the offending principal stress (or strain) when the principal stress (or strain) exceeds its limiting value.

For the maximum principal stress criterion, the limiting tensile stress is usually expressed in terms of the uniaxial tensile strength. Unfortunately, the magnitude of the concrete tensile strength can not be determined precisely. Different values may be obtained from the modulus of rupture, the split cylinder and the direct tension tests. Furthermore, a significant scatter of results from specimens cast from the same concrete using the split cylinder test has been obtained [53]. In the application of the non-linear finite element method to reinforced concrete members, the predicted response at early stages of loading can be quite sensitive to the specified concrete tensile strength. For slab and beam analysis, reasonable predictions have been obtained using the split cylinder tensile strength [54].

3.3.3 Methods of Crack Representation

Two basically different approaches are generally used to represent the cracks for the finite analysis of concrete structures. Cracks can be modelled either as discrete individual cracks between concrete elements or as smeared cracks within the elements.

The discrete crack representation was used in the first finite element model for reinforced concrete beams proposed by Ngo and Scordelis [28]. In this method the crack is simulated by a physical separation of preselected finite elements along their boundaries. The major drawback of such an approach is that the locations and orientation of the cracks are not known in advance. Instead of using predefind cracks, Nilson [55] modified the approach by tracing the cracks individually. The finite element solution was interrupted whenever an element indicated cracking, the nodes were redefined and the element mesh topology was regenerated for the next step. Such a technique is extremely complex and computationally expensive [56]. For this reason the use of discrete crack models has received a limited acceptance in the finite analysis for general structural applications. However, for problems involving a few dominant cracks, the discrete crack model, that is where the crack is represented by a strain discontinuity, offers a more realistic simulation of those cracks [2,3].

Because of the complications involved in using discrete crack representation, most finite element models utilise the concept in which the local discontinuties are assumed to be distributed, or smeared, over the volume of the sampling point under consideration. The smeared crack approach, which was originally introduced by Rashid [57], replaces the physical crack displacements by fictiouas strains. Therefore, cracking effects can adequately be modelled in terms of local modifications to the constit tive rqlationships rather than the restructuring of finite element topology. This representation is consistent with the continuum mechanics assumptions used in the finite element formulation. Moreover, it offers automatic generation

of cracks and complete generality of possible crack direction [3].

The smeared crack representation can be divided into fixed and rotating crack categories. The former category uses a fixed orientation of the crack during the entire computational process. Concrete is assumed to behave as an orthotropic material with the local material axes being defined by the principal directions associated with the first principal stress that violates the cracking criterion. The approach has worked satisfactorily in many applications of the finite element method to reinforced concrete. However, for problems in which the axes of the principal stresses rotate after crack formation the fixed crack model can lead to a stiffer response and an overestimation of failure loads [58,59].

In order to allow for the axes of material orthotropy to coincide with the axes of principal strains, Cope and Rao [60] have suggested the rotating, or swinging, crack approach. In this approach, the crack direction is always aligned normal to the direction of maximum principal strain, and the principal stress and strain directions are assumed to coincide. Application of this model to finite element analyses of reinforced concrete structures has produced a softer behaviour when compared to the fixed crack model [59,61,62].

Cope and Rao [63] proposed a modified version of the rotating crack model. In this approach, the principal strain directions may be inclined to the initial crack axes for a number of further load stages. At some load stage at which the maximum principal tensile strain and its inclination to the initial principal directions exceed prescribed values, new cracks are assumed to form and the orthotropic

material axes are set in the new crack directions. An experimental study of the behaviour of reinforced concrete panels loaded in pure shear carried out by Vecchio and Collins [11] revealed that secondary cracks inclined to the initial cracks occurred in certain panels. These panels were reinforced with percentage of steel in the transverse direction considerably less than that provided in the longitudinal direction. It was found that the secondary cracks occurred at loading stages at which relatively large values of strain were recorded. These large strains did not occur until the transverse reinforcement had started to yield.

Recently, de Borst and Nauta [64] proposed a multi-directional smeared crack model. The fundamental concept underlying this model is the decomposition of the total strain increment into concrete strain and crack strain increments. The crack strain increment may also be decomposed into the separate contributions from a number of non-orthogonal cracks which occur at a sampling point. In this model, new cracks are assumed to initiate whenever the angle of inclination between the existing crack, or cracks, and the current direction of the major principal stress exceeds a given value, the threshold angle. In this way, a system of non-orthogonal cracks can occur at a sampling point [65,66].

3.3.4 Post-Cracking Behaviour

Cracking of plain and reinforced concrete structures is not a perfectly brittle phenomenon and experimental evidence shows that the tensile stresses normal to a cracked plane are gradually released as

the crack width increases. This response is usually modelled in the finite element analysis using either the tension-stiffening or the strain-softening concepts. The former concept is suitable for analysing reinforced concrete structures where the behaviour is characterised by the formation of closely spaced cracks. In contrast, the strain-softening concept is useful for analysing plain concrete structures where the behaviour is governed by the formation of a single macrocrack or a few dominant cracks. These concepts are discussed in the following sections.

3.3.4.1 Tension-stiffening concept

In a reinforced concrete member, primary cracks form when the concrete reaches its tensile strength. The number and extent of these cracks are controlled by the size, position and orientation of the reinforcing bars crossing the crack [3]. In the vicinity of a primary crack, the concrete stress drops to zero and the steel carries the full load. However, some of the tensile force is transferred back to the concrete between the cracks due to bond between the bar and the concrete. The ability of the concrete to retain the tension is called tension-stiffening. As the applied load increases, this ability progressively becoming weaker because of the formation of secondary systems of internal cracks around the reinforcing bar. Hence, concrete tensile stress drops. Test results for beams and one way slabs show that the effect of tension-stiffening decreases with the increase in the steel ratio and the steel strain [67].

Two different approaches have been utilised to incorporate the tension-stiffening effect in the finite element modelling of reinforced concrete structures. The first method, which was originally proposed by Scanlon [68], is characterised by assuming a descending branch for the concrete average stress-strain curve in tension. Falling branches of linear, bilinear and curved shapes have been used by many researchers [35,69,70]. The second method represents the tension-stiffening effect by increasing the steel stiffness [71]. In this case, the total tensile force carried by both the steel and the concrete between cracks is represented by the additional stress in the steel [3].

3.3.4.2 Strain-softening concept

The response of plain concrete specimens under tension is primarly controlled by the formation of micro-cracks. When the tensile peak stress is exceeded somewhere in the specimen all additional deformation due to micro-cracks will concentrate near the crack tips, i.e will localise at the fracture zone. Within a fracture zone the stress gradually decreases as the strain increases. This phenomenon is known as tensile strain-softening. Outside the fracture zone the material experiences unloading while the cracks form, which means that the micro-cracks outside the fracture zone are arrested or even closed [72,73]. Hillerborg [72] has proposed the use of stress-displacement, crack width, relationship for concrete within the fracture zone and a stress-strain relationship for the material outside the cracking zone. In smeared crack models, this stress-displacement curve has to be converted to an equivalent

stress–strain curve. To do this, the fracture energy, the energy required to create one unit area of continuous cracked surface, is taken as a material constant given by the area under the stress–displacement curve. Recently, the strain–softening concept has been used in some finite element models, for example see refs. [73,74], to express the descending branch of the post–cracking stress–strain curve.

3.3.4.3 Transfer of shear forces across the crack

After cracking, reinforced concrete retains a significant shear stiffness and is able to transfer shear forces across the cracks due to the aggregate interlock at the crack interfaces and the dowel action of reinforcing bars crossing the crack. Shear forces transferred by means of any of these mechanisms reduces as the cracks widen [75,76]. Experimental evidence reveals that there is a rapid fall in the value of shear modulus after cracking [75–78]. In smeared crack models, the interface shear transfer is presented by a reduced shear stiffness modulus, βG (with $0 \leq \beta \leq 1$), in the constitutive relation at a cracked sampling point. A constant value for the shear reduction factor, β, has been used in many finite element studies after cracking has occurred, for example see refs. [79,80]. Other studies used a gradually decreasing value for β following either a linear or a non–linear curve [77,81].

3.3.5 Compressive Strength Reduction Due to Orthogonal Cracking

In a reinforced concrete member, a significant degradation in compression strength can result due to presence of transverse tensile strain after cracking. Tests by Robinson and Demorieux [82] on panels subjected to longitudinal compressive stresses and reinforced with transverse bars revealed that the concrete may crush at a stress level considerably less than f'_c. The tensile straining of the transverse reinforcement was shown to cause a significant deterioration in both the strength and the stiffness in the longitudinal compression direction. Vecchio and Collins [11] confirmed these findings in their extensive experimental study on the behaviour of reinforced concrete panels under in-plane shear and direct stresses. They modelled the effects of the transverse cracking by modifying the commonly used parabolic uniaxial stress-strain curve given by,

$$\sigma_c = f'_c \left\{ \frac{2\epsilon_c}{\epsilon_0} - \left[\frac{\epsilon_c}{\epsilon_0} \right]^2 \right\} \qquad (3.10)$$

where σ_c and ϵ_c are the uniaxial compression stress and strain respectively and ϵ_0 is the strain at peak stress f'_c given by

$$\epsilon_0 = 2\, f'_c / E \qquad (3.11)$$

Substitution of (3.11) into (3.10) yields

$$\sigma_c = E\, \epsilon_c - \frac{E}{2\epsilon_0} \epsilon_c^2 \qquad (3.12)$$

For a cracked reinforced concrete member, the peak compression stress f'_c and the corresponding peak strain ϵ_0 are reduced to $\lambda f'_c$ and $\lambda\epsilon_0$ respectively, Fig. 3.5a. Therefore from (3.10), the modified stress–strain relationship proposed by Vecchio and Collins can be expressed as:

$$\sigma_c = f'_c \left\{ \frac{2\epsilon_c}{\epsilon_0} - \frac{1}{\lambda} \left[\frac{\epsilon_c}{\epsilon_0} \right]^2 \right\} \qquad (3.13)$$

where λ is the compression strength reduction factor. By relating the peak compressive stresses obtained from different panels to the corresponding strains, Vecchio and Collins showed that a suitable formula for the compression reduction factor is

$$\lambda = \frac{1}{0.85 + 0.27 \frac{\epsilon_t}{\epsilon_c}} \leq 1.0 \qquad (3.14)$$

where ϵ_t is the tensile strain in the transverse direction (both ϵ_t and ϵ_c are given positive values). Equations (3.13) and (3.14) indicate that the compression stresses reduce as the transverse tensile strain increases.

Cervenka [83] conducted a numerical parametric study on four of Vecchio and Collins panels using (3.13) and proposed a new expression for the compression reduction factor which is given by,

$$\lambda = 1.0 - k_1 \beta_t \qquad (3.15)$$

where

$$\beta_t = \epsilon_t / 0.005 \leq 1.00 \qquad (3.16)$$

and k_1 is a parameter to be determined from the test. Cervenka showed that the optimum value for the compression strength reduction parameter k_1 is variable in the panels considered and suggested an average value of $k_1 = 0.52$.

Recently, Vecchio and Collins [84] have proposed a new modified stress-strain relationship in the form

$$\sigma_c = \lambda f'_c \left\{ \frac{2\epsilon_c}{\epsilon_0} - \left[\frac{\epsilon_c}{\epsilon_0} \right]^2 \right\} \qquad (3.17)$$

In this model, only the peak stress f'_c is reduced to $\lambda f'_c$ while the coressponding peak strain ϵ_0 is kept free from modifications, Fig. 3.5b. The expression for the compression reduction factor is also modified to

$$\lambda = \frac{1}{0.8 + 0.34 \dfrac{\epsilon_t}{0.002}} \leq 1.0 \qquad (3.18)$$

3.4 Concrete Models Adopted in the Analysis

In view of the scatter of experimental results for concrete specimens and the variation of the material properties throughout a real reinforced concrete member, numerical material models are usually kept as simple as possible so that they can be easily

implemented in finite element programs. However, such models should accurately trace the overall behaviour of the member within engineering degrees of accuracy. The present material model is suitable for the non-linear static analysis of three-dimensional reinforced concrete structures under monotonically increasing load. The behaviour of concrete in compression is simulated by an elasto-plastic work hardening model followed by a perfectly plastic plateau, which is terminated at the onset of crushing. The plasticity model will be illustrated in terms of the following constituents:

a) the yield criterion,

b) the hardening rule,

c) the flow rule and

d) the crushing condition.

In tension, linear elastic behaviour prior to cracking is assumed. The onset of cracking is governed by a maximum principal stress criterion. A smeared crack model with fixed orthogonal cracks is adopted to represent the fractured concrete. The model will be described in terms of

a) the cracking criterion,

b) the post cracking formulation,

c) the shear retention model and

d) the modelling of compressive strength reduction in presence of orthogonal cracking.

3.4.1 Plasticity Model for Concrete in Compression

3.4.1.1 The yield criterion

A yield criterion for isotropic materials must be independent of the choice of the coordinate system in which the stress state is defined and therefore it should be a function of the stress invariants only [2,36]. Under a triaxial state of stress, the yield criterion for concrete is generally assumed to be dependent on three stress invariants. However, a yield criterion dependent on two stress invariants only has been proved to be adequate for most practical situations [3,41]. The yield criterion incorporated in the present model is of such a type and has been successfully used by many researchers [41,85-87]. It can be expressed as:

$$f(\sigma) = f(I_1, J_2) = (\alpha I_1 + 3 \beta J_2)^{\frac{1}{2}} = \sigma_0 \qquad (3.19)$$

where α and β are material parameters, I_1 is the first stress invariant given by,

$$I_1 = \sigma_x + \sigma_y + \sigma_z, \qquad (3.20)$$

J_2 is the second deviatoric stress invariant given by,

$$J_2 = \frac{1}{3} \left(\left(\sigma_x^2 + \sigma_y^2 + \sigma_z^2 \right) - \left(\sigma_x\sigma_y + \sigma_y\sigma_z + \sigma_z\sigma_x \right) \right) + \tau_{xy}^2 + \tau_{yz}^2 + \tau_{zx}^2 \qquad (3.21)$$

and $\sigma_0 > 0$ is the equivalent effective stress at the onset of plastic

deformation which can be determined from the uniaxial compression test as:

$$\sigma_0 = c_p f'_c \tag{3.22}$$

where $0 \leq c_p \leq 1.0$ is the plasticity coefficient which is used to mark the initiation of the plastic deformation.

The uniaxial compression test and the biaxial test under equal compression stresses are used to determine the material parameters α and β. For a uniaxial compression state, the yield stress (or strength) is given by,

$$\sigma_x = -\sigma_0 \tag{3.23}$$

And for the equal biaxial compression state, the yield stress (or strength) is given by,

$$\sigma_x = \sigma_y = -\gamma \sigma_0 \tag{3.24}$$

If the results obtained by Kupfer [6] for a failure envelope is employed for initial yield, the value of the constant γ is equal to 1.16. From equations (3.19-3.24) the material constants can be found to be

$$\alpha = 0.35468 \sigma_0 \quad \text{and} \quad \beta = 1.35468 \tag{3.25}$$

$$\text{Let} \qquad c = \alpha / (2\sigma_0) = 0.17734 \tag{3.26}$$

Therefore, equation (3.19) can be rewritten as,

$$f(\underline{\sigma}) = (2\ c\ \sigma_0\ I_1 + 3\ \beta\ J_2)^{\frac{1}{2}} = \sigma_0 \qquad (3.27)$$

This can be solved for σ_0 as

$$f(\underline{\sigma}) = c\ I_1 + \{\ (c\ I_1)^2 + 3\ \beta\ J_2\ \}^{\frac{1}{2}} = \sigma_0 \qquad (3.28)$$

The resultant yield criterion (3.28) is compared in Fig. 3.6 with the experimental results of Kupfer et al. [6] in the biaxial stress space for $\sigma_0 = f'_c$.

3.4.1.2 The hardening rule

When a work hardening material is stressed beyond its initial yielding surface , a hardening rule is required to describe the growth of subsequent loading surfaces during plastic deformation. In the current study an isotropic hardening rule is adopted. This rule implies a uniform expansion of the initial yield surface as the plastic deformation increases. Therefore from (3.28), the subsequent loading functions may be expressed as,

$$f(\underline{\sigma}) = c\ I_1 + \{\ (c\ I_1)^2 + 3\ \beta\ J_2\ \}^{\frac{1}{2}} = \bar{\sigma} \qquad (3.29)$$

where $\bar{\sigma}$ represents the stress level at which further plastic deformation will occur and is termed as the effective stress or the equivalent uniaxial stress. In order to define the expansion of the current loading surface, the incremental theory of plasticity implies

a relationship between the effective stress and the effective plastic strain to extrapolate the results of a uniaxial state of stress to the multiaxial states. The effective, accumulated, plastic strain, ϵ_p, can be calculated by integrating the effective plastic strain increment, $d\epsilon_p$, along the strain path as,

$$\epsilon_p = \int d\epsilon_p \tag{3.30}$$

The effective plastic strain increment may be determined using the work hardening hypothesis as

$$d\epsilon_p = \frac{dW_p}{\bar{\sigma}} = \frac{\underline{\sigma}\ d\underline{\epsilon}^p}{\bar{\sigma}} \tag{3.31}$$

In the present model, a parabolic stress-strain curve is used for the equivalent uniaxial stress-strain relationship beyond the limit of elasticity, $c_p\ f'_c$. This parabolic curve represents the work-hardening stage of behaviour. When the peak compressive stress is reached, a perfectly plastic response is assumed to occur. Fig. 3.7 shows the equivalent uniaxial stress-strain curve in the various stages of behaviour. These are given by,

a) for $\bar{\sigma} \leq c_p\ f'_c$

$$\bar{\sigma} = E\ \epsilon_c \tag{3.32}$$

b) for $c_p\ f'_c \leq \bar{\sigma} \leq f'_c$

$$\bar{\sigma} = c_p\ f'_c + E\left[\epsilon_c - \frac{c_p\ f'_c}{E}\right] - \frac{E}{2\ \epsilon'_0}\left[\epsilon_c - \frac{c_p\ f'_c}{E}\right]^2 \tag{3.33}$$

c) for $\epsilon_c \geq (2-c_p)\ f'_c/E$

$$\bar{\sigma} = f'_c \tag{3.34}$$

where ϵ'_0 is the total strain corresponding to the parabolic part of the curve given by,

$$\epsilon'_0 = 2(1-c_p)\ f'_c/E \tag{3.35}$$

A value of 0.3 is assumed for the plastic coefficient c_p in the present study and hence plastic yielding begins at a stress level equal to 0.3 f'_c. If $c_p = 1.0$ then elastic-perfectly plastic behaviour is specified, Fig. 3.7. When $c_p = 0$ equations (3.33) and (3.35) reduce to (3.12) and (3.11) respectively.

In order to derive the relationship between the effective stress and the effective plastic strain, the total strain, ϵ_c, is decomposed into its elastic and plastic components as,

$$\epsilon_c = \epsilon_e + \epsilon_p \tag{3.36}$$

where ϵ_e is the elastic strain component given by,

$$\epsilon_e = \bar{\sigma} / E \tag{3.37}$$

By substituting (3.36) and (3.37) into (3.33), the effective stress-plastic strain relation can be expressed as

$$\bar{\sigma} = c_p f'_c - E \epsilon_p + (2 E^2 \epsilon'_0 \epsilon_p)^{\frac{1}{2}} \tag{3.38}$$

The slope of the effective stress–plastic strain curve, the hardening coefficient, is used in the formulation of the elasto–plastic incremental stress–strain relationship. Therefore, by differentiation of (3.38) with respect to the effective plastic strain, the hardening coefficient, H', can be expressed as:

$$H' = \frac{d\bar{\sigma}}{d\epsilon_p} = E\left\{ \left[\frac{\epsilon_0'}{2\ \epsilon_p} \right]^{\frac{1}{2}} - 1.0 \right\} \qquad (3.39)$$

3.4.1.3 The flow rule

In plasticity theory a flow rule must be defined so that the plastic strain increment can be determined for a given stress increment. Concrete, like other granular materials, exhibits a volumetric change under state of shearing stress and therefore the direction of plastic straining is not necessarily normal to the current loading surface [88]. However, the associated flow rule has been widely used for concrete models mainly because of its simple formulation. This approach is adopted in the current model. Recalling equation (3.7), the plastic strain increment is expressed as:

$$d\underline{\epsilon}^P = d\lambda \frac{\partial f(\underline{\sigma})}{\partial \underline{\sigma}} \qquad (3.40)$$

The normal to the current loading surface ($\partial f(\underline{\sigma})/\partial \underline{\sigma}$) is termed as the flow vector. The yield function derivatives with respect to the stress components define the flow vector $\underline{a}$ as:

$$\underline{a} = \left[\frac{\partial f}{\partial \sigma_x} , \frac{\partial f}{\partial \sigma_y} , \frac{\partial f}{\partial \sigma_z} , \frac{\partial f}{\partial \tau_{xy}} , \frac{\partial f}{\partial \tau_{yz}} , \frac{\partial f}{\partial \tau_{zx}} \right]^T \qquad (3.41)$$

These derivatives can be evaluated from (3.28) with the use of (3.20) and (3.21) as,

$$\begin{aligned}
\frac{\partial f}{\partial \sigma_x} &= c + [\ 2\ (c^2+\beta)\ \sigma_x + (2c^2-\beta)\ (\sigma_y+\sigma_z)\ ]\ /\ Q \\
\\
\frac{\partial f}{\partial \sigma_y} &= c + [\ 2\ (c^2+\beta)\ \sigma_y + (2c^2-\beta)\ (\sigma_x+\sigma_z)\ ]\ /\ Q \\
\\
\frac{\partial f}{\partial \sigma_z} &= c + [\ 2\ (c^2+\beta)\ \sigma_z + (2c^2-\beta)\ (\sigma_x+\sigma_y)\ ]\ /\ Q
\end{aligned} \qquad (3.42)$$

$$\begin{aligned}
\frac{\partial f}{\partial \tau_{xy}} &= 6\ \beta\ \tau_{xy}\ /\ Q \\
\\
\frac{\partial f}{\partial \tau_{yz}} &= 6\ \beta\ \tau_{yz}\ /\ Q \\
\\
\frac{\partial f}{\partial \tau_{zx}} &= 6\ \beta\ \tau_{zx}\ /\ Q
\end{aligned}$$

where

$$\begin{aligned}
Q = 2\ [\ & (c^2+\beta)\ (\sigma_x^2+\sigma_y^2+\sigma_z^2) + (2c^2-\beta)\ (\sigma_x\sigma_y+\sigma_y\sigma_z+\sigma_z\sigma_x) \\
& + 3\beta\ (\tau_{xy}^2+\tau_{yz}^2+\tau_{zx}^2)\ ]^{\frac{1}{2}}
\end{aligned} \qquad (3.43)$$

and c and β are the material constants previously defined.

3.4.1.4 Incremental stress-strain relationship

In this section, the derivation of the incremental stress-strain relation is given for an elastic work-hardening plastic material based on the associated flow rule (3.40). During the plastic loading, both the initial yield and the subsequent stress states must satisfy the yield condition, $F(\underline{\sigma},k) = 0$. The yield function, first defined in (3.28) can be rewritten as,

$$F(\underline{\sigma},k) = f(\underline{\sigma}) + K(k) = 0 \tag{3.44}$$

where k is the hardening parameter which governs the expansion of the yield surface. By differentiating (3.44) we have,

$$dF = \frac{\partial F}{\partial \underline{\sigma}} d\underline{\sigma} + \frac{\partial F}{\partial k} dk = 0 \tag{3.45}$$

or

$$\underline{a}^T d\underline{\sigma} - A\, d\lambda = 0 \tag{3.46}$$

where

$$A = -\frac{1}{d\lambda} \frac{\partial F}{\partial k} dk \tag{3.47}$$

For the yield function adopted in the analysis, the scalar term A given by (3.47) can be proved to be equal to the slope of the effective stress-plastic strain curve, H', by using Euler's theorem for homogeneous functions and the work hardening hypothesis [2,36].

The total incremental strain vector given by (3.3) can be rewritten with the use of (3.40) as,

$$d\underline{\varepsilon} = d\underline{\varepsilon}^e + d\lambda \frac{\partial f}{\partial \underline{\sigma}} \tag{3.48}$$

The elastic strain increment is related to the stress increment by the elastic constitutive relation which is given by

$$d\underline{\sigma} = \underline{D}\, d\underline{\varepsilon}^e \tag{3.49}$$

where $\underline{D}$ is the elastic constitutive matrix given by,

$$\underline{D} = \frac{E}{(1+\nu)(1-2\nu)} \begin{bmatrix} 1-\nu & \nu & \nu & 0 & 0 & 0 \\ \nu & 1-\nu & \nu & 0 & 0 & 0 \\ \nu & \nu & 1-\nu & 0 & 0 & 0 \\ 0 & 0 & 0 & \frac{1-2\nu}{2} & 0 & 0 \\ 0 & 0 & 0 & 0 & \frac{1-2\nu}{2} & 0 \\ 0 & 0 & 0 & 0 & 0 & \frac{1-2\nu}{2} \end{bmatrix} \tag{3.50}$$

Substitution of (3.49) into (3.48) yields,

$$d\underline{\varepsilon} = \underline{D}^{-1}\, d\underline{\sigma} + d\lambda\, \underline{a} \tag{3.51}$$

Pre-multiplying both sides of (3.51) by $\underline{a}^T \underline{D}$ and eliminating $\underline{a}^T d\underline{\sigma}$ by making use of (3.46), the following expression for the plastic multiplier $d\lambda$ is obtained,

$$d\lambda = \left[\frac{\underline{a}^T \underline{D}}{H' + \underline{a}^T \underline{D}\, \underline{a}} \right] d\underline{\varepsilon} \qquad (3.52)$$

By substitution of (3.52) into (3.48) and pre-multiplying both sides by $\underline{D}$, the complete elasto-plastic incremental stress-strain relationship can be expressed as,

$$d\underline{\sigma} = \left[\underline{D} - \frac{\underline{D}\, \underline{a}\, \underline{a}^T \underline{D}}{H' + \underline{a}^T \underline{D}\, \underline{a}} \right] d\underline{\varepsilon} \qquad (3.53)$$

where the second term in the bracket represents the stiffness degradation due to the plastic deformation. The above expression is valid for infinitesimal increments of stress. If a finite sized stress increment is considered, the final stress point may depart from the loading surface. In this case the stress point can be scaled back to the loading surface by relaxing the excess stress in several stages using the technique described by Owen and Hinton [36]. This technique has been used in the present study.

3.4.1.5 The crushing condition

In the present model, the isotropic expansion of the subsequent loading surfaces is terminated when the effective stress reaches the peak compression stress. Beyond that a perfectly plastic response is

assumed to occur. This stage of behaviour is represented by a fixed loading surface in the stress space which does not depend, in any way, on the degree of plastification. The perfectly plastic flow continues until the ultimate deformation capacity of concrete is reached and the material eventually exhibits a crushing failure. After crushing, concrete stresses drop abruptly to zero and the material is assumed to lose its resistance completely against any further deformation.

The crushing type of fracture is a strain related phenomenon and it may be controlled by defining a failure surface in strain space. Due to lack of experimental data concerning the concrete ultimate deformation capacity under multiaxial loading, the crushing criterion is obtained by simply converting the yield criterion (3.28), described in terms of stresses, directly into strains [2,89]. Thus,

$$c\, I_1' + \left((c\, I_1')^2 + 3\, \beta\, J_2' \right)^{\frac{1}{2}} = \epsilon_{cu} \qquad (3.54)$$

where I_1' is the first strain invariant, J_2' is the second deviatoric strain invariant and ϵ_{cu} is the ultimate strain value that can be extrapolated from the uniaxial compression test.

3.4.2 Smeared Crack Model for Concrete in Tension

3.4.2.1 Determination of the principal stresses

At any point under a general three-dimensional state of stress, the principal stresses and their directions can be determined from the cartesian stress components. A detailed procedure for the evaluation of the principal stresses and the principal directions is described in reference [90]. The roots of the following cubic equation represent the values of the principal stresses, σ_1, σ_2 and σ_3

$$\sigma_i^3 - I_1 \sigma_i^2 + I_2 \sigma_i - I_3 = 0 \qquad (3.55)$$

where I_1 is the first stress invariant previously defined and I_2 and I_3 are the second and the third stress invariants given by,

$$I_2 = \sigma_x\sigma_y + \sigma_y\sigma_z + \sigma_z\sigma_x - \tau_{xy}^2 - \tau_{yz}^2 - \tau_{zx}^2 \qquad (3.56)$$

$$I_3 = \sigma_x\sigma_y\sigma_z - \sigma_x\tau_{yz}^2 - \sigma_y\tau_{zx}^2 - \sigma_z\tau_{xy}^2 + 2\tau_{xy}\tau_{yz}\tau_{zx} \qquad (3.57)$$

The planes on which the principal stresses act are called "principal planes"; and the directions of the outer normals to these planes are called "principal directions". For any given state of stress, the principal directions can be always be found to be a set of three matually orthogonal directions. These directions can be expressed through the direction cosines as:

$$l_i = \cos \theta_{xi}$$

$$m_i = \cos \theta_{yi} \qquad (3.58)$$

$$n_i = \cos \theta_{zi}$$

For example, the direction cosines of the major principal stress, σ_1, with respect to the x, y and z axes are l_1, m_1 and n_1 respectively. These direction cosines are given by [90],

$$l_1 = A / (A^2 + B^2 + C^2)^{\frac{1}{2}}$$

$$m_1 = B / (A^2 + B^2 + C^2)^{\frac{1}{2}} \qquad (3.59)$$

$$n_1 = C / (A^2 + B^2 + C^2)^{\frac{1}{2}}$$

where

$$A = (\sigma_y - \sigma_1) (\sigma_z - \sigma_1) - \tau_{yz}^2$$

$$B = \tau_{yz} \tau_{zx} - \tau_{xy} (\sigma_z - \sigma_1) \qquad (3.60)$$

$$C = \tau_{xy} \tau_{yz} - \tau_{zx} (\sigma_y - \sigma_1)$$

3.4.2.2 The cracking criterion

In the current model, the initiation of cracking is controlled by a maximum tensile stress criterion. For a previously uncracked sampling point, the principal stresses and their directions are calculated. If the major principal stress, σ_1, exceeds a limiting value of tensile stress a crack is assumed to form. The limiting tensile stress required to define the onset of cracking can be calculated for states of triaxial tensile stress and for combinations of tension and compression principal stresses as follows [35]:

a) for the triaxial tension zone ($\sigma_1 \geq \sigma_2 \geq \sigma_3 > 0$)

$$\sigma_i = \sigma_{cr} = f_t \qquad i = 1,2,3 \qquad (3.61)$$

b) for the tension–tension–compression zone ($\sigma_1 \geq \sigma_2 > 0,\ \sigma_3 \leq 0$)

$$\sigma_i = \sigma_{cr} = f_t \left[1 + \frac{0.75\ \sigma_3}{f'_c} \right] \qquad i = 1,2 \qquad (3.62)$$

c) for the tension–compression–compression zone($\sigma_1 > 0,\ \sigma_3 \leq \sigma_2 \leq 0$)

$$\sigma_1 = \sigma_{cr} = f_t \left[1 + \frac{0.75\ \sigma_2}{f'_c} \right] \left[1 + \frac{0.75\ \sigma_3}{f'_c} \right] \qquad (3.63)$$

where σ_{cr} is the cracking stress and both f_t and f'_c are given positive values. Equation (3.62) incorporates the fact that the compression in one direction favours the cracking in the others and thus reduces the tensile capacity of the material. Fig. 3.8 shows the tensile failure envelope resulting from (3.61-3.63) in principal

stress space.

When the major principal stress, σ_1, violates the cracking criterion, planes of failure develop perpendicular to its direction, Fig. 3.9a. The concrete behaviour is no longer isotropic, it becomes orthotropic with the direction of orthotropy coincides with the direction of σ_1. The normal and the shear stresses across the plane of failure and the corresponding normal and shear stiffnesses are reduced. However, the behaviour of the material between two adjacent failure planes remains linearly elastic, i.e concrete is assumed to be transversly isotropic with planes of isotropy being perpendicular to the direction of σ_1. Thus, the increments of strain in the local material axes (1,2,3) may be written in terms of stress increments as:

$$\begin{bmatrix} \Delta\epsilon_1 \\ \Delta\epsilon_2 \\ \Delta\epsilon_3 \\ \Delta\gamma_{12} \\ \Delta\gamma_{23} \\ \Delta\gamma_{31} \end{bmatrix} = \begin{bmatrix} \frac{1}{E_1} & \frac{-\nu'}{E_1} & \frac{-\nu'}{E_1} & 0 & 0 & 0 \\ \frac{-\nu'}{E_1} & \frac{1}{E} & \frac{-\nu}{E} & 0 & 0 & 0 \\ \frac{-\nu'}{E_1} & \frac{-\nu}{E} & \frac{1}{E} & 0 & 0 & 0 \\ 0 & 0 & 0 & \frac{1}{\beta_1 G} & 0 & 0 \\ 0 & 0 & 0 & 0 & \frac{1}{G} & 0 \\ 0 & 0 & 0 & 0 & 0 & \frac{1}{\beta_1 G} \end{bmatrix} \begin{bmatrix} \Delta\sigma_1 \\ \Delta\sigma_2 \\ \Delta\sigma_3 \\ \Delta\tau_{12} \\ \Delta\tau_{23} \\ \Delta\tau_{31} \end{bmatrix} \quad (3.64)$$

where E_1 is the reduced modulus of elasticity in the direction of σ_1, $\beta_1 G$ is the reduced shear modulus across the failure plane, i.e in the plane normal to the plane of isotropy, and ν' is Poisson's ratio characterising transverse strain reduction in the plane of isotropy

due to the tensile stress σ_1. Because of the lack of interaction between the orthogonal planes caused by the cracking, the Poisson's ratio ν' is set to zero. Therefore, the incremental stress–strain relationship in the local material axes may be expressed as,

$$\begin{bmatrix} \Delta\sigma_1 \\ \Delta\sigma_2 \\ \Delta\sigma_3 \\ \Delta\tau_{12} \\ \Delta\tau_{23} \\ \Delta\tau_{31} \end{bmatrix} = \begin{bmatrix} E_t & 0 & 0 & 0 & 0 & 0 \\ 0 & \frac{E}{1-\nu^2} & \frac{\nu E}{1-\nu^2} & 0 & 0 & 0 \\ 0 & \frac{\nu E}{1-\nu^2} & \frac{E}{1-\nu^2} & 0 & 0 & 0 \\ 0 & 0 & 0 & \beta_1 G & 0 & 0 \\ 0 & 0 & 0 & 0 & G & 0 \\ 0 & 0 & 0 & 0 & 0 & \beta_1 G \end{bmatrix} \begin{bmatrix} \Delta\varepsilon_1 \\ \Delta\varepsilon_2 \\ \Delta\varepsilon_3 \\ \Delta\gamma_{12} \\ \Delta\gamma_{23} \\ \Delta\gamma_{31} \end{bmatrix} \qquad (3.65)$$

Equation (3.65) may be written in the form:

$$\Delta\underline{\sigma} = \underline{D}_{cr}\,\Delta\underline{\varepsilon} \qquad (3.66)$$

where $\underline{D}cr$ is the material stiffness in the local axes. The elastic material between two adjacent failure planes is presented in (3.65) by a plane stress constitutive relation. The reduced modulus of elasticity, E_t, should be negative as it represents the slope of the tension–stiffening curve. However, a very small positive value is usually assigned when forming the stiffness matrix to avoid the numerical problems due to the formation of negative pivots in the stiffness matrix. An alternative method assumes a progressively decreasing value for E_t using the current secant slope of the tension–stiffening curve.

The stress increments in the global axes (x,y,z) may be obtained by using the coordinate transformation matrix such that,

$$\begin{bmatrix} \Delta\sigma_x \\ \Delta_\sigma y \\ \Delta_\sigma z \\ \Delta_\tau xy \\ \Delta_\tau yz \\ \Delta_\tau zx \end{bmatrix} = \underset{\sim}{T}^T \begin{bmatrix} E_1 & 0 & 0 & 0 & 0 & 0 \\ 0 & \frac{E}{1-\nu^2} & \frac{\nu E}{1-\nu^2} & 0 & 0 & 0 \\ 0 & \frac{\nu E}{1-\nu^2} & \frac{E}{1-\nu^2} & 0 & 0 & 0 \\ 0 & 0 & 0 & B_1 G & 0 & 0 \\ 0 & 0 & 0 & 0 & G & 0 \\ 0 & 0 & 0 & 0 & 0 & \beta_1 G \end{bmatrix} \underset{\sim}{T} \begin{bmatrix} \Delta\epsilon_x \\ \Delta\sigma_y \\ \Delta\epsilon y \\ \Delta\gamma xy \\ \Delta_\gamma yz \\ \Delta_\gamma zx \end{bmatrix} \quad (3.67)$$

Where $\underset{\sim}{T}$ is the transformation matrix expressed in terms of the direction cosines as [91]:

$$\underset{\sim}{T} = \begin{bmatrix} l_1^2 & m_1^2 & n_1^2 & l_1 m_1 & m_1 n_1 & n_1 l_1 \\ l_2^2 & m_2^2 & n_2^2 & l_2 m_2 & m_2 n_2 & n_2 l_2 \\ l_3^2 & m_3^2 & n_3^2 & l_3 m_3 & m_3 n_3 & n_3 l_3 \\ 2l_1 l_2 & 2m_1 m_2 & 2n_1 n_2 & (l_1 m_2 + l_2 m_1) & (m_1 n_2 + m_2 n_1) & (n_1 l_2 + n_2 l_1) \\ 2l_2 l_3 & 2m_2 m_3 & 2n_2 n_3 & (l_2 m_3 + l_3 m_2) & (m_2 n_3 + m_3 n_2) & (n_2 l_3 + n_3 l_2) \\ 2l_3 l_1 & 2m_3 m_1 & 2n_3 n_1 & (l_3 m_1 + l_1 m_3) & (m_3 n_1 + m_1 n_3) & (n_3 l_1 + n_1 l_3) \end{bmatrix} \quad (3.68)$$

For the tension–tension–compression and the triaxial tension states of stress, the cracking criterion may be violated by the major principal stress, σ_1, and the second principal stress, σ_2, simultaneously. Thus, two sets of orthogonal failure planes develop. These planes are perpendicular to the principal axes 1 and 2

respectively. In this case, Poisson's ratio is set to zero in all directions and the constitutive matrix in the local material axes becomes a diagonal matrix,

$$\underset{\sim}{D}_{cr} = \begin{bmatrix} E_1 & 0 & 0 & 0 & 0 & 0 \\ & E_2 & 0 & 0 & 0 & 0 \\ & & E & 0 & 0 & 0 \\ & & & \beta_1 G & 0 & 0 \\ & & \text{sym.} & & \beta_2 G & 0 \\ & & & & & \beta_1 G \end{bmatrix} \qquad (3.69)$$

In the fixed crack model, the rotation of the principal stresses after the formation of the first crack is ignored. However, if the second crack initiates at a subsequent stage of loading, rotation of the principal stresses within the planes perpendicular to direction of σ_1 may be taken into account. Magnitudes and directions of the new second and minor principal stresses, σ_2' and σ_3', may be calculated from the original principal stresses σ_2 and σ_3 and the shear stress τ_{23} accumulated during loading stages beyond the formation of the first crack. Thus,

$$\sigma_i' = \frac{\sigma_2 + \sigma_3}{2} \pm \left[\left(\frac{\sigma_2 - \sigma_3}{2} \right)^2 + \tau_{23}^2 \right]^{\frac{1}{2}} \qquad i = 2,3 \qquad (3.70)$$

For tension–tension–compression states, the onset of the second crack is expressed in terms of the new principal stresses as:

$$\sigma_2' = \sigma_{cr} = f_t \left[1 + \frac{0.75\ \sigma_3'}{f_c'} \right] \qquad (3.71)$$

Failure planes corresponding to the second crack are assumed to be perpendicular to the direction of the second principal stress σ_2', Fig. 3.9b. The angle between the original and the new in-plane sets of principal directions, θ_p, may be calculated as:

$$\theta_p = \frac{1}{2} \tan^{-1} \frac{2\tau_{23}}{\sigma_2 - \sigma_3} \tag{3.72}$$

After the formation of the second crack, the local in-plane constitutive matrix with respect to the new principal directions (2',3') is expressed as:

$$\underline{D}_{cr} = \begin{bmatrix} E_2 & 0 & 0 \\ 0 & E & 0 \\ 0 & 0 & \beta_2 G \end{bmatrix} \tag{3.73}$$

This matrix may be transformed to the original principal directions (2,3) using the in-plane coordinate transformation matrix. Therefore, the in-plane incremental stress-strain relationship in the original principal directions can written as:

$$\begin{bmatrix} \Delta\sigma_2 \\ \Delta\sigma_3 \\ \Delta\tau_{23} \end{bmatrix} = \underline{T}_p^T \begin{bmatrix} E_2 & 0 & 0 \\ 0 & E & 0 \\ 0 & 0 & \beta_2 G \end{bmatrix} \underline{T}_p \begin{bmatrix} \Delta\epsilon_2 \\ \Delta\epsilon_3 \\ \Delta\gamma_{23} \end{bmatrix} \tag{3.74}$$

where $\underline{T}_p$ is the in-plane transformation matrix given by

$$\underline{T}_p = \begin{bmatrix} C^2 & S^2 & CS \\ S^2 & C^2 & -CS \\ -2CS & 2CS & C^2-S^2 \end{bmatrix} \tag{3.75}$$

where $C = \cos \theta_p$ and $S = \sin \theta_p$.

In the current model, a maximum of three sets of cracks are allowed to form at each sampling point, Fig. 3.9c. For triaxial tension states, a third crack may occurred when the minor principal stress, σ_3 (or σ_3') exceeds the uniaxial tensile strength f_t.

3.4.2.3 Post-cracking models

The gradual release of tensile stresses normal to the cracked plane is represented by an average stress-strain curve. In the current study, such a relationship may be obtained using either the tension-stiffening or the strain-softening models

3.4.2.3.1 Tension-stiffening model

Test data on tension-stiffening exhibits considerable scatter because of the nature of the phenomenon and method of calculating tensile stresses in concrete. Therefore, simple models are usually suggested for such phenomenon. In the present work, the tensile stress contributed by the concrete between the cracks is expressed as:

a) for $\epsilon_{cr} \leq \epsilon_n \leq \alpha_1 \epsilon_{cr}$

$$\sigma_n = \alpha_2 \sigma_{cr} \frac{\left[\alpha_1 - \frac{\epsilon_n}{\epsilon_{cr}} \right]}{\left[\alpha_1 - 1.0 \right]} \tag{3.76}$$

b) for $\epsilon_n \geq \alpha_1 \epsilon_{cr}$

$$\sigma_n = 0.0 \tag{3.77}$$

where σ_n and ϵ_n are the stress and strain normal to the cracked plane, ϵ_{cr} is the cracking strain assoicated with the cracking stress σ_{cr} and α_1 and α_2 are the tension-stiffening parameters. α_1 represents the rate of stress release as the crack widens; α_2 represents the sudden loss of stress at instant of cracking, Fig. 3.10.

An experimental relationship between concrete force due to tension-stiffening and steel strains in reinforced concrete beams and slabs has been obtained by Clark and Speirs [67]. In non-linear finite element slab analysis, Cope [54] used an average stress-strain curve with $\alpha_1 = 15$ which gave good predictions of the results of Clark and Speirs. Values in the ranges of 5-25 and 0.2-1.0 have been used for α_1 and α_2 respctively by many workers [89,92-94]. A numerical study on the effect of tension-stiffening parameters on the non-linear behaviour of reinforced concrete deep beams has been performed by Al-Manaseer and Phillips [95]. Results of the analysis show that the best load deflection curve was obtained when $\alpha_1 = 10$ and $\alpha_2 = 0.6$. The variation of these parameters also influences the

load displacement behaviour, crack propagation and the ultimate load, and significantly affects the total number of iterations required to achieve a converged solution.

An estimate for the value for α_1 may be derived by assuming that $\alpha_1\ \epsilon_{cr}$ is equal the yield strain of the reinforcement. This is likely to be a reasonable estimate if the crack is perpendicular to the steel. However, if cracks do not intersect the reinforcement perpendicularly this is a rather severe restriction. Determination of the value of α_1 is discussed in more detail in section 6.2.3.

In the finite element analysis of reinforced concrete structures, average strains are considered at the sampling points. Therefore the tension-stiffening curve can be mesh independent for reasonable values of α_1 and mesh dimensions. Cope [69] suggested the ideal spacing of sampling points to be approximately equal the average spacing between cracks.

3.4.2.3.2 Strain-softening model

In the finite element modelling of plain concrete, the post-cracking stresses are calculated from average strains at discrete sampling points according to an equivalent stress-strain relationship. To improve the realism of the model and to obtain solutions insensitive to the size of the finite elements, it is necessary to take sampling point spacing into account when specifying the equivalent post-cracking stress-strain curve [96]. To do this, the fracture energy which represents the area under the stress-crack

width curve is assumed to be a constant for the material considered. Thus,

$$G_f = \int \sigma(w)\, dw \tag{3.78}$$

where w is the crack width which may be expressed in the smeared crack representation in terms of the tensile strain normal to the cracked plane as

$$w = \left[\frac{V}{S} \right] \epsilon_n = l_c \epsilon_n \tag{3.79}$$

where V is the volume of concrete represented by the cracked sampling point and S is the area of the cracked plane. The ratio V/S can be identified as the characteristic crack length, l_c, of the sampling point, the gauge length in an experiment. The characteristic length may be approximated in three-dimensional problems as the cubic root of the volume associated with sampling point. Thus,

$$l_c = (V)^{0.33} \tag{3.80}$$

By making use of (3.78) and assuming the same linear equivalent post-cracking stress-strain relationship of (3.76), Fig .3.10, the parameter α_1 may be expressed in terms of the fracture energy as

$$\alpha_1 = \frac{2\, G_f}{\alpha_2\, \sigma_{cr}\, \epsilon_{cr}\, l_c} - \frac{1}{\alpha_2} + 1.0 \tag{3.81}$$

Equation (3.81) demonstrates the mesh dependence of the strain-softening model via the inclusion of the crack characteristic length. Expermental tests indicate that the average characteristic

crack length is of the same order as the maximum size of aggregate [97]. Experimental results to determine the fracture energy exhibit considerable scatter. However for normal weight concrete, the fracture energy may be taken to be in the range 200 f_t^2/E - 400 f_t^2/E N/m [69].

3.4.2.4 Closing and re-opening of cracks

Unloading of a cracked sampling point may occur as a result of the stress redisribution at neigbouring points. For a closing crack it is assumed that the orthotropy of the sampling point under consideration is maintained. Unloading and re-loading are assumed to follow a secant path, Fig. 3.10. The secant modulus, E_i, can be evaluated from the previously stored maximum strain developed normal to the cracked plane. This secant modulus may be used to calculate the retained stress as:

$$\sigma_n = E_i \epsilon_n \tag{3.82}$$

When the crack is completely closed, the effects of any residual strains are neglected.

3.4.2.5 Shear retention model

The shear stiffness at a cracked sampling point becomes progressively smaller as the crack widens. In the present study, a reduced shear modulus, βG, has been used across the cracked plane.

Before cracking, a value of unity is assigned to the shear reduction factor, β. As the cracks propagate, the shear reduction factor is taken as a linearly decreasing function of the strain normal to the cracked plane, which represents the crack width. When the cracks have sufficiently opened, a constant value is assigned to β to account for dowel action. The shear retention model is shown in Fig. 3.11 and is given by

a) for $\epsilon_n < \epsilon_{cr}$

$$\beta = 1.0 \tag{3.83}$$

b) for $\epsilon_{cr} \leq \epsilon_n \leq \gamma_1 \epsilon_{cr}$

$$\beta = \frac{\gamma_2 - \gamma_3}{\gamma_1 - 1} \left[\gamma_1 - \frac{\epsilon_n}{\epsilon_{cr}} \right] + \gamma_3 \tag{3.84}$$

c) for $\epsilon_n > \gamma_1 \epsilon_{cr}$

$$\beta = \gamma_3 \tag{3.85}$$

where γ_1, γ_2 and γ_3 are shear retention parameters. γ_1 represents the rate of decay of shear stiffness as the crack widens; γ_2 represents the sudden loss in shear stiffness at the instant of cracking and γ_3 represents the residual shear stiffness due to the dowel action. In cases when a crack is totally closed, it is assumed that the original shear modulus is retained and a value of unity is assigned to the shear reduction factor.

3.4.2.6 Modelling the compressive strength reduction due to orthogonal cracks

The deterioration of compressive strength due to orthogonal cracking may be taken into account using the proposals presented in section 3.3.5. In a plasticity based model, effects of transverse tensile strains on the yield criterion and the evolution of subsequent loading surfaces can be simulated by scaling the equivalent uniaxial stress-strain relationships given by (3.32-3.34) according to the current value of the compression reduction factor. The necessary modifications required for equations (3.14, 3.15 and 3.18) to be suitable for three-dimensional analysis are described in this section. Three different models have been incorporated in the current study based on the proposals of Cervenka [83] and Vecchio and Collins [11,84]. These models are illustrated in the following sections.

a) Model A

Cervenka's [83] proposed the use of the reduction factor to reduce both the peak stress and the corresponding strain. Therefore from (3.32-3.35), the modified stress strain relationships may be written as:

a) for $\bar{\sigma} \leq \lambda\, c_p\, f'_c$

$$\bar{\sigma} = \lambda\, E\, \epsilon_c \tag{3.86}$$

b) for $\lambda\ c_p\ f'_c \leq \bar{\sigma} \leq \lambda\ f'_c$

$$\bar{\sigma} = \lambda\ c_p\ f'_c + E\left[\ \epsilon_c - \frac{\lambda\ c_p\ f'_c}{E}\ \right] - \frac{E}{2\epsilon'_0}\left[\ \epsilon_c - \frac{\lambda\ c_p\ f'_c}{E}\ \right]^2 \qquad (3.87)$$

c) for $\epsilon_c \geq (2-c_p)\ \lambda\ f'_c/E$

$$\bar{\sigma} = \lambda\ f'_c \qquad (3.88)$$

where

$$\epsilon'_0 = 2(1-c_p)\ \lambda\ f'_c/E \qquad (3.89)$$

Consequently, the effective stress–plastic strain relation (3.38) can be modified as

$$\bar{\sigma} = \lambda\ c_p\ f'_c - E\ \epsilon_p + (\ 2\ E^2\ \lambda\ \epsilon'_0\ \epsilon_p\ )^{\frac{1}{2}} \qquad (3.90)$$

And hence, the hardening parameter can be expressed as:

$$H' = \frac{d\bar{\sigma}}{d\epsilon_p} = E\left\{\ \left[\ \frac{\lambda\ \epsilon'_0}{2\ \epsilon_p}\ \right]^{\frac{1}{2}} - 1.0\ \right\} \qquad (3.91)$$

For a singly cracked sampling point, the compression reduction factor is given by,

$$\lambda = 1.0 - k_1\ \frac{\epsilon_1}{0.005} \leq 1.0 - k_1 \qquad (3.92)$$

where ϵ_1 is the transverse tensile strain in principal direction 1, the strain normal to the cracked plane. And, for a doubly cracked

sampling point the expression may be taken as:

$$\lambda = 1.0 - k_1 \frac{(\epsilon_1^2 + \epsilon_2^2)^{\frac{1}{2}}}{0.005} \leq 1.0 - k_1 \qquad (3.93)$$

where ϵ_2 is the tensile strain normal to the second crack.

b) Model B

Based on the model proposed by Vecchio and Collins [11], the reduction factor used in (3.86-3.91) may be calculated for a singly cracked point as,

$$\lambda = \frac{1}{0.85 + 0.27 \frac{\epsilon_1}{c_1\ \epsilon_{eq}}} \leq 1.0 \qquad (3.94)$$

where ϵ_{eq} is a strain equivalent to the state of strain of the material within the plane of isotropy which may be calculated using (3.54) as:

$$\epsilon_{eq} = c\ I_1' + ((c\ I_1')^2 + 3\ \beta\ J_2')^{\frac{1}{2}} \qquad (3.95)$$

and c_1 is a constant which may evaluated from (3.14) to be

$$c_1 = \epsilon_c / \epsilon_{eq} \qquad (3.96)$$

By substituting the state of uniaxial compression stress and setting Poisson's ratio to be 0.2, the constant c_1 can be calculated from (3.95) to be equal to 0.7725.

The reduction factor of a doubly cracked sampling point may be taken as,

$$\lambda = \frac{1}{0.85 + 0.27 \dfrac{(\epsilon_1^2 + \epsilon_2^2)^{\frac{1}{2}}}{\epsilon_3}} \leq 1.0 \qquad (3.97)$$

where ϵ_3 is the compressive strain in the local principal direction 3 taken as a positive value.

c) Model C

According to the modified proposal of Vecchio and Collins [84], the effect of the reduction factor results in reducing the peak stress only. Therefore, the modified equivalent stress-strain relationships may be given as:

a) for $\bar{\sigma} \leq \lambda\, c_p\, f'_c$

$$\bar{\sigma} = \lambda\, E\, \epsilon_c \qquad (3.98)$$

b) for $\lambda\, c_p\, f'_c \leq \bar{\sigma} \leq \lambda\, f'_c$

$$\bar{\sigma} = \lambda \left\{ c_p\, f'_c + E \left[\epsilon_c - \frac{c_p\, f'_c}{E} \right] - \frac{E}{2\epsilon'_0} \left[\epsilon_c - \frac{c_p\, f'_c}{E} \right]^2 \right\} \qquad (3.99)$$

c) for $\epsilon_c \geq (2-c_p)\, f'_c/E$

$$\bar{\sigma} = \lambda f_c' \tag{3.100}$$

where

$$\epsilon_0' = 2(1-c_p)\, f_c'/E \tag{3.101}$$

Hence, the effective stress–plastic strain relation may be written as:

$$\bar{\sigma} = \lambda \left\{ c_p f_c' - E \epsilon_p + \left(2 E^2 \epsilon_0' \epsilon_p \right)^{\frac{1}{2}} \right\} \tag{3.102}$$

And, the hardening parameter can be expressd as:

$$H' = \frac{d\bar{\sigma}}{d\epsilon_p} = \lambda E \left\{ \left[\frac{\epsilon_0'}{2\ \epsilon_p} \right]^{\frac{1}{2}} - 1.0 \right\} \tag{3.103}$$

In this model, the reduction factor for a singly cracked point is expressed using (3.18) as:

$$\lambda = \frac{1}{0.80 + 0.34\ \dfrac{\epsilon_1}{0.002}} \leq 1.0 \tag{3.104}$$

And for double cracks,

$$\lambda = \frac{1}{0.80 + 0.34\ \dfrac{\left(\epsilon_1^2 + \epsilon_2^2 \right)^{\frac{1}{2}}}{0.002}} \leq 1.0 \tag{3.105}$$

3.4.2.7 Treatment of the compressive behaviour of cracked concrete

In the previous section, the equivalent uniaxial stress-strain curves and the corresponding effective stress-plastic strain relations are described as functions of the compression strength reduction factor λ. Thus, for a cracked sampling point the evolution of the subsequent loading surfaces can be described by a family of equivalent uniaxial curves depending on the current value of the factor λ, Fig. 3.12. Consider the situation existing for the i^{th} iteration of any particular loading increment where $\Delta\sigma_e$ represents the elastic increment of equivalent uniaxial stress corresponding to the strain increment $\Delta\epsilon$. Let points A and C represent the state of stresses at the end of the $i-1^{th}$ and the i^{th} iterations respectively. The path followed during the i^{th} iteration to reach point C is illustrated in Fig. 3.12c. The state of stress is assumed to transfer from point A, on the curve $\lambda = \lambda_1$, to point B, on the curve $\lambda = \lambda_2$, without changing the value of the current effective plastic strain, i.e elastic loading, Figs. 3.12b and 3.12c. Because of the variation in the value of λ, the portion of the stress increment, $R\Delta\sigma_e$, to be included in the residual force vector is represented in the figure by the segment CF. However, for the case of no change in the value of λ this portion is given by the segment DF.

Because cracking is a partial and directional failure, the material within the planes of isotropy, planes perpendicular to the direction of the maximum principal tensile stress, can still sustained compressive stresses in directions parallel to the cracks. In the presence of a single set or two orthogonal sets of cracks at a sampling point, see Figs. 3.9a and 3.9b,the plasticity formulation is

assumed to apply for the concrete between the cracked planes using the relevant biaxial or uniaxial state of stress.

3.5 Modelling of Reinforcement

Compared to concrete, steel is a much simpler material to represent. Its strain-stress behaviour can be assumed to be identical in tension and compression. In reinforced concrete members, reinforcing bars are normally long and relatively slender and therefore they can be generally assumed to be capable of transmitting axial forces only. A typical uni-axial stress-strain curve for a steel specimen loaded monotonically in tension is shown in Fig. 3.13. In the current study, the uniaxial stress-strain behaviour of reinforcement is simulated by an elastic linear work hardening model, Fig. 3.14.

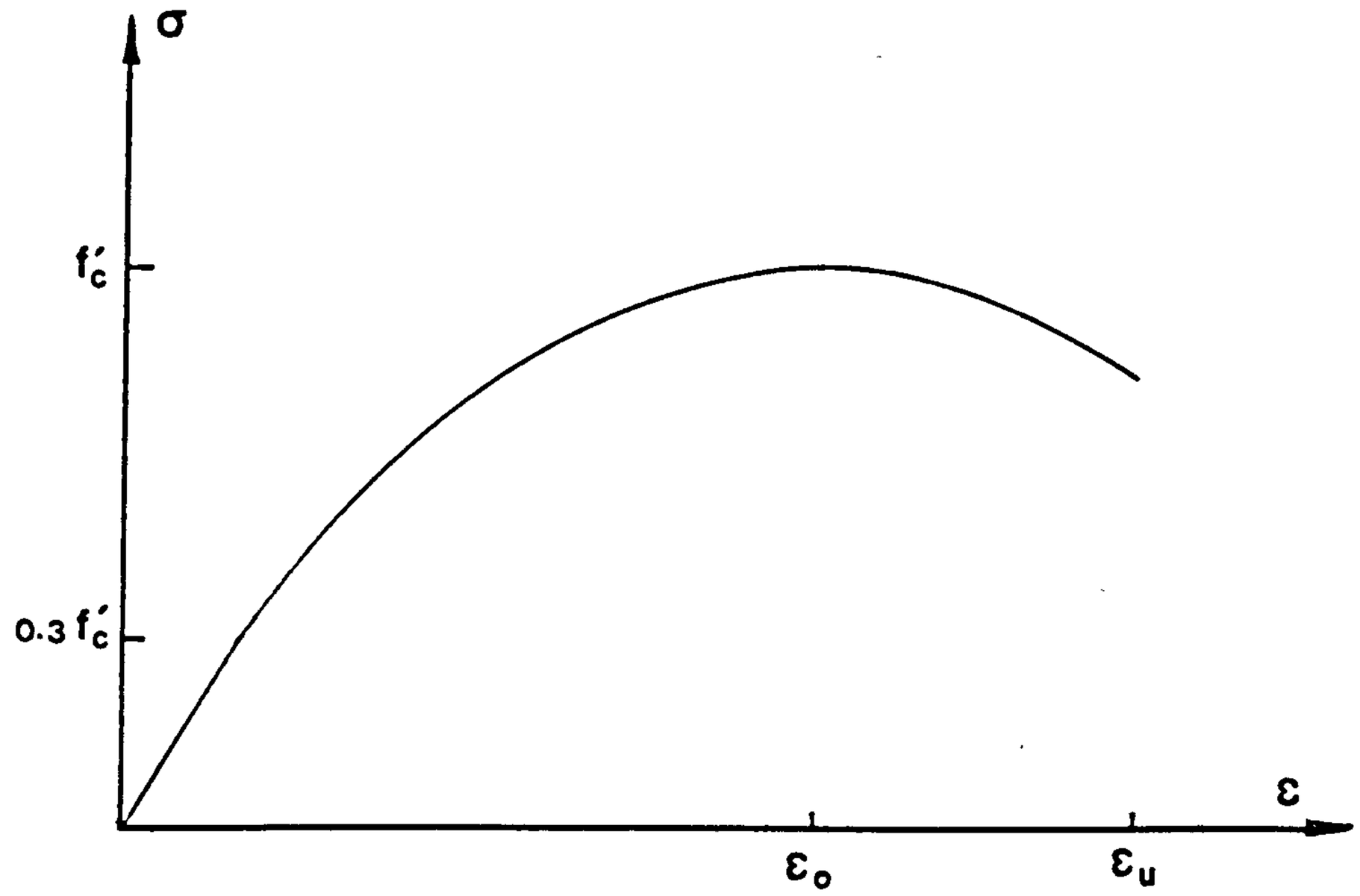

Fig. 3.1 Typical uniaxial stress–strain curve for concrete in compression.

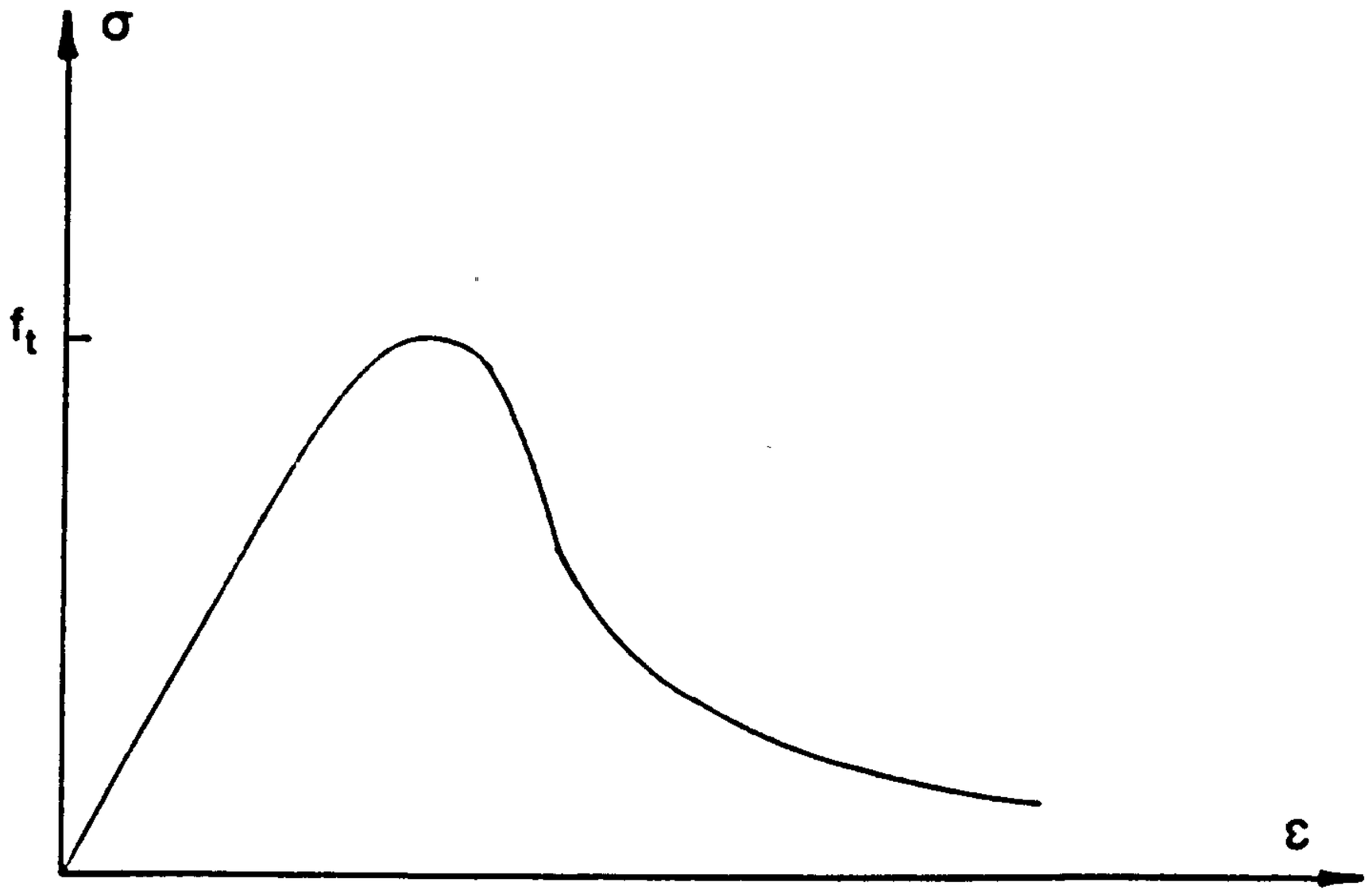

Fig. 3.2 Typical uniaxial stress–strain curve for concrete in tension.

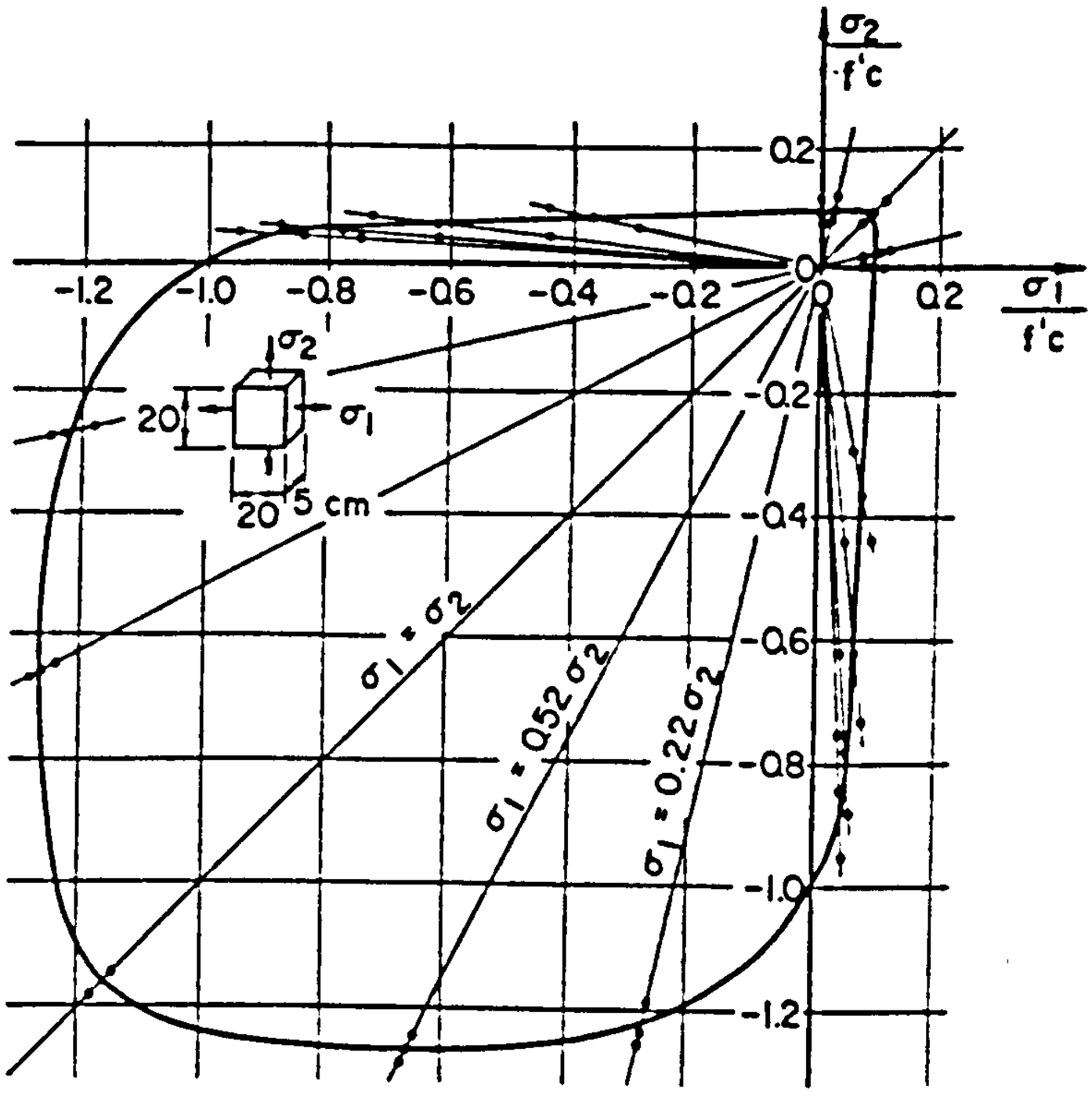

Fig. 3.3 Failure envelope of plain concrete in biaxial stress space, (Kupfer el al. [6]).

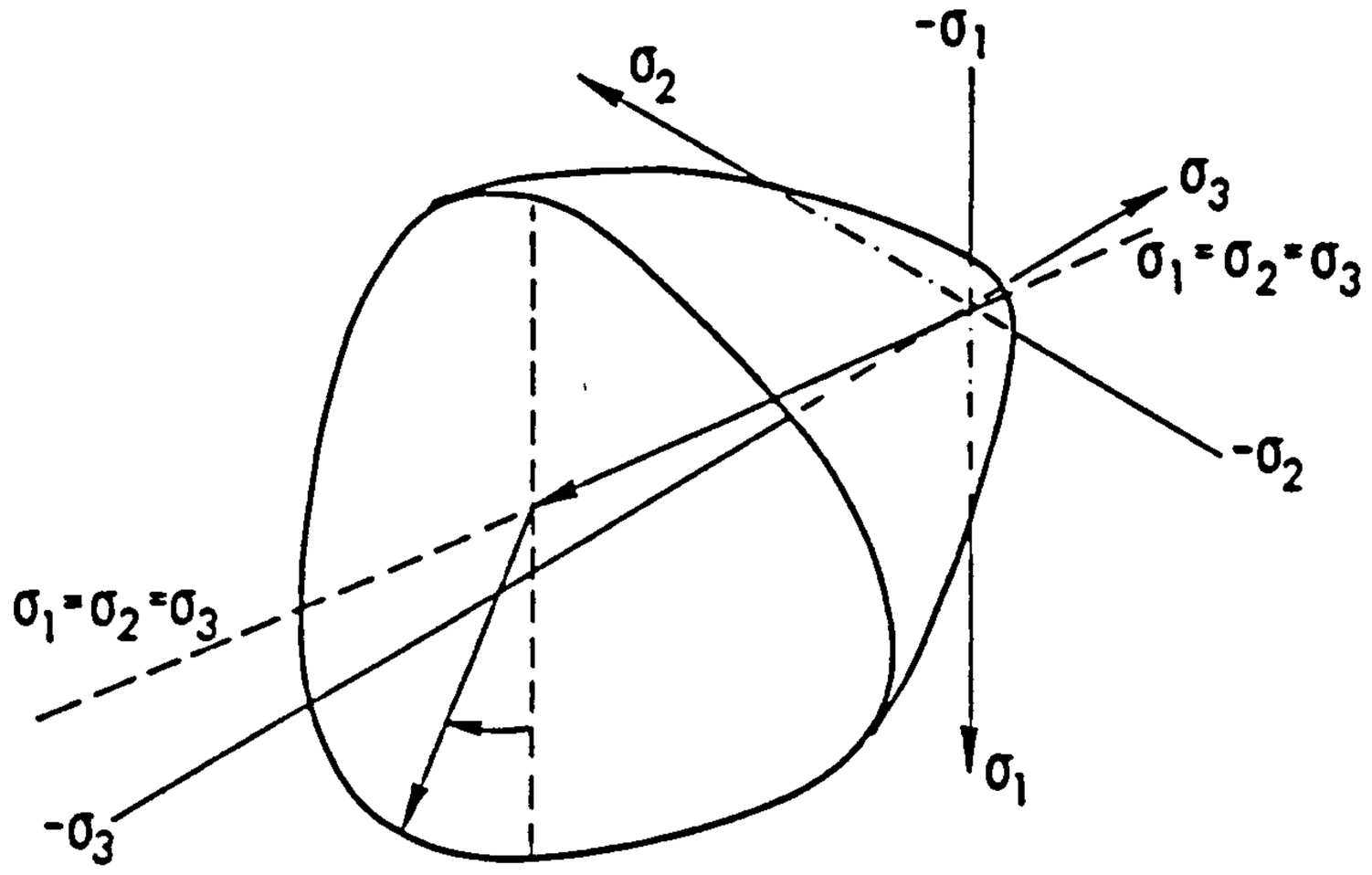

Fig. 3.4 Typical triaxial failure envelope of concrete, (Ref. 3).

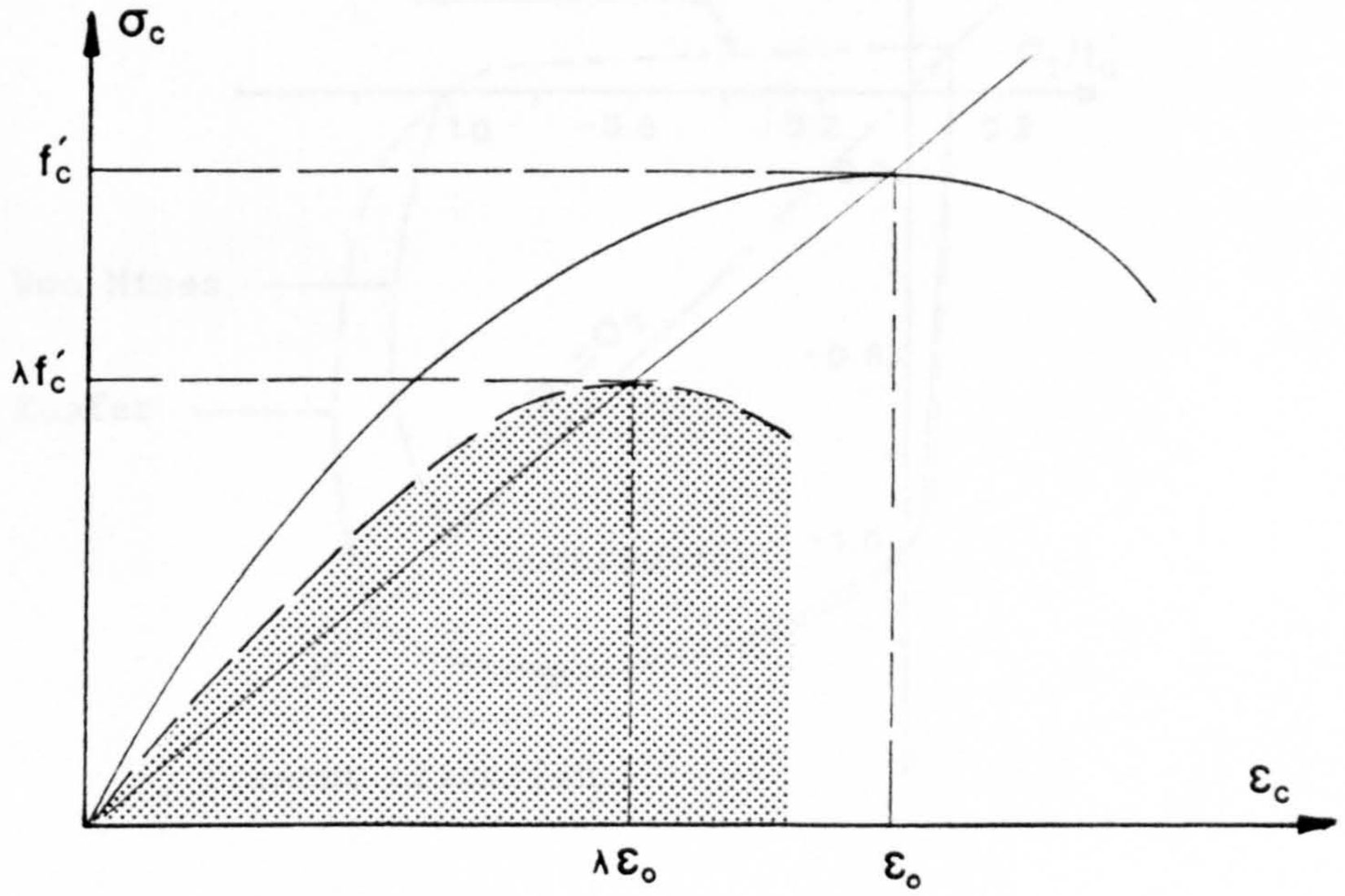

a) Vecchio and Collins model.

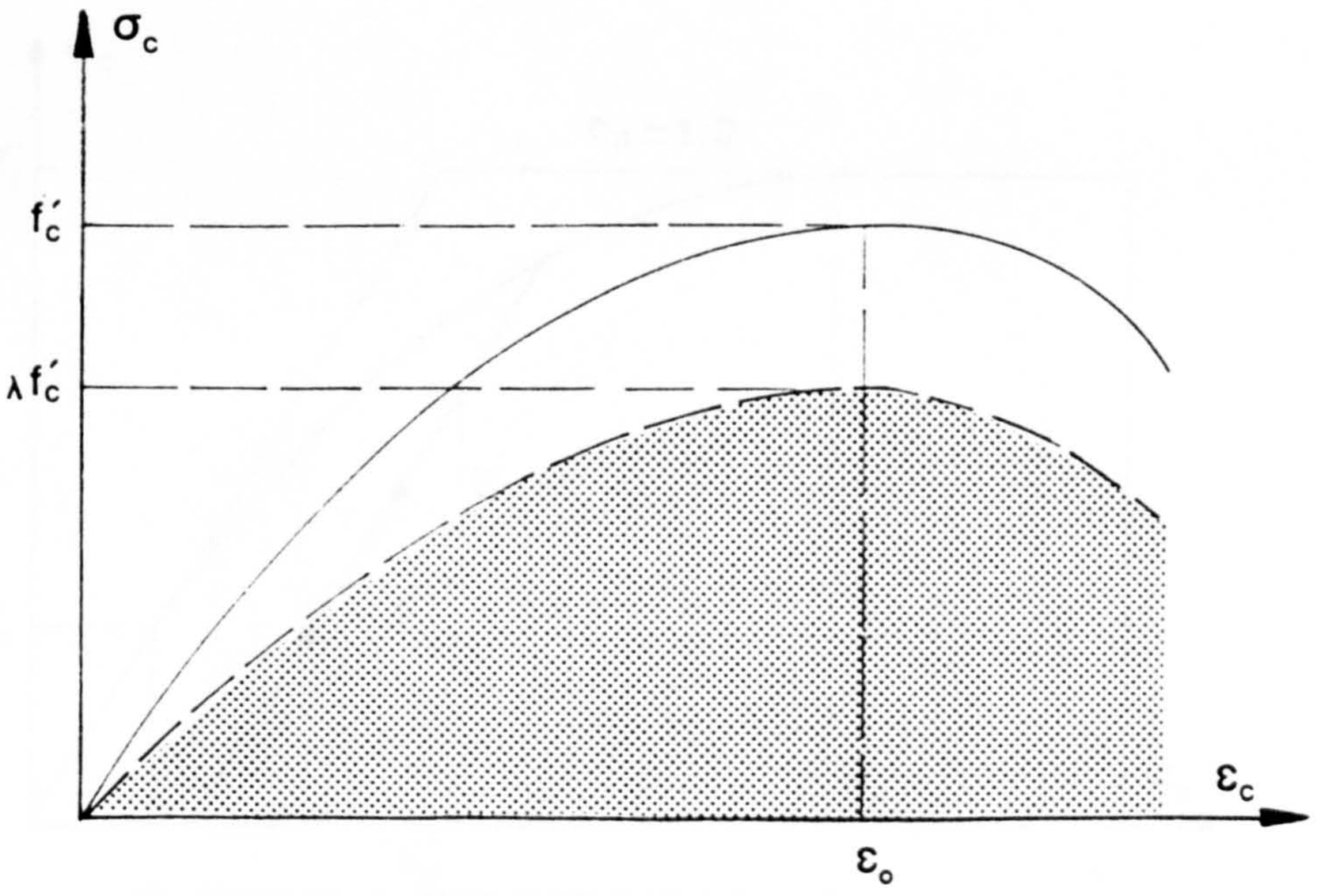

b) Modified Vecchio and Collins model.

Fig. 3.5 Uniaxial compressive stress–strain relationship for cracked concrete.

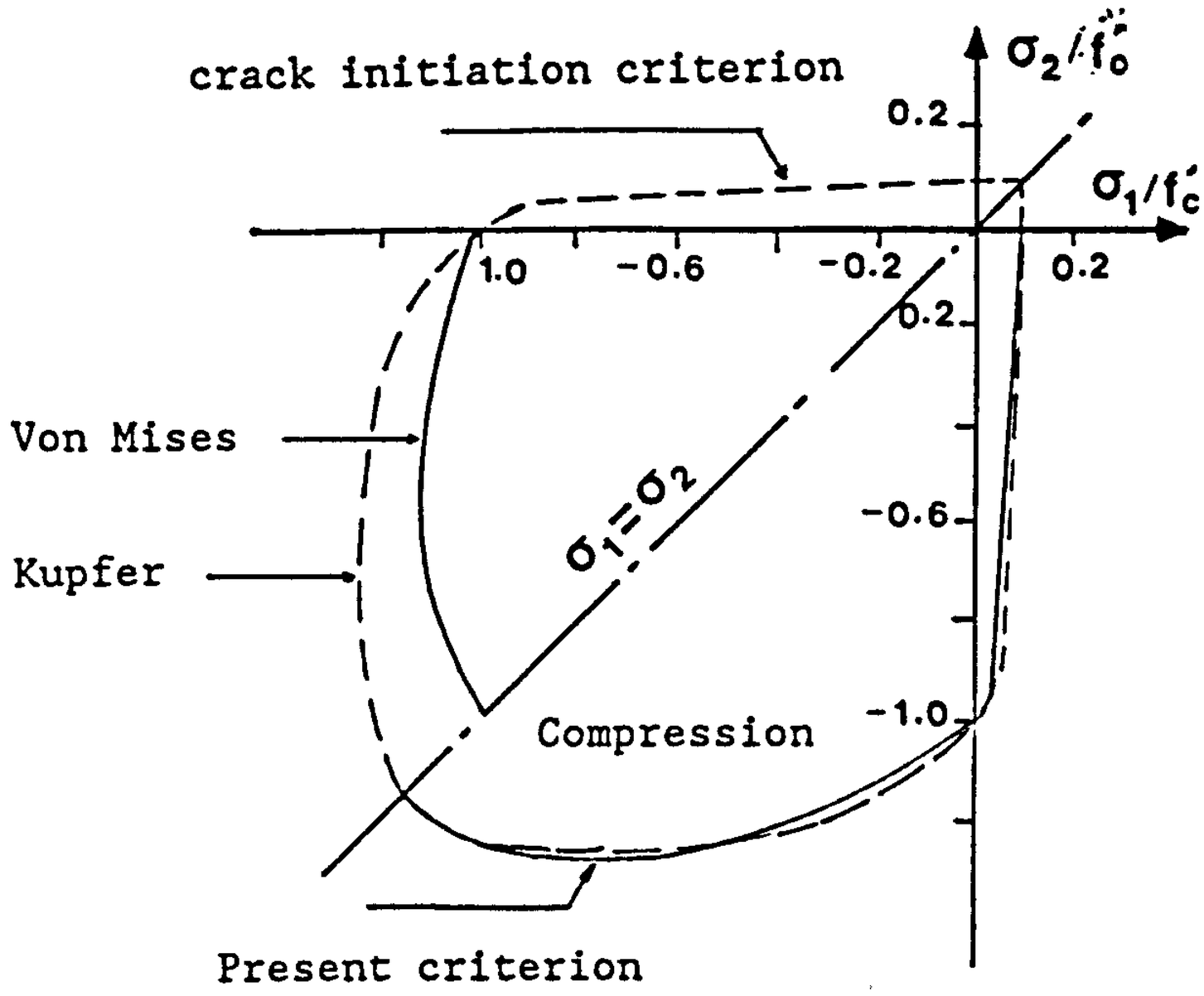

Fig. 3.6 Failure envelope adopted in current model compared to Kupfer results and Von Mises criterion.

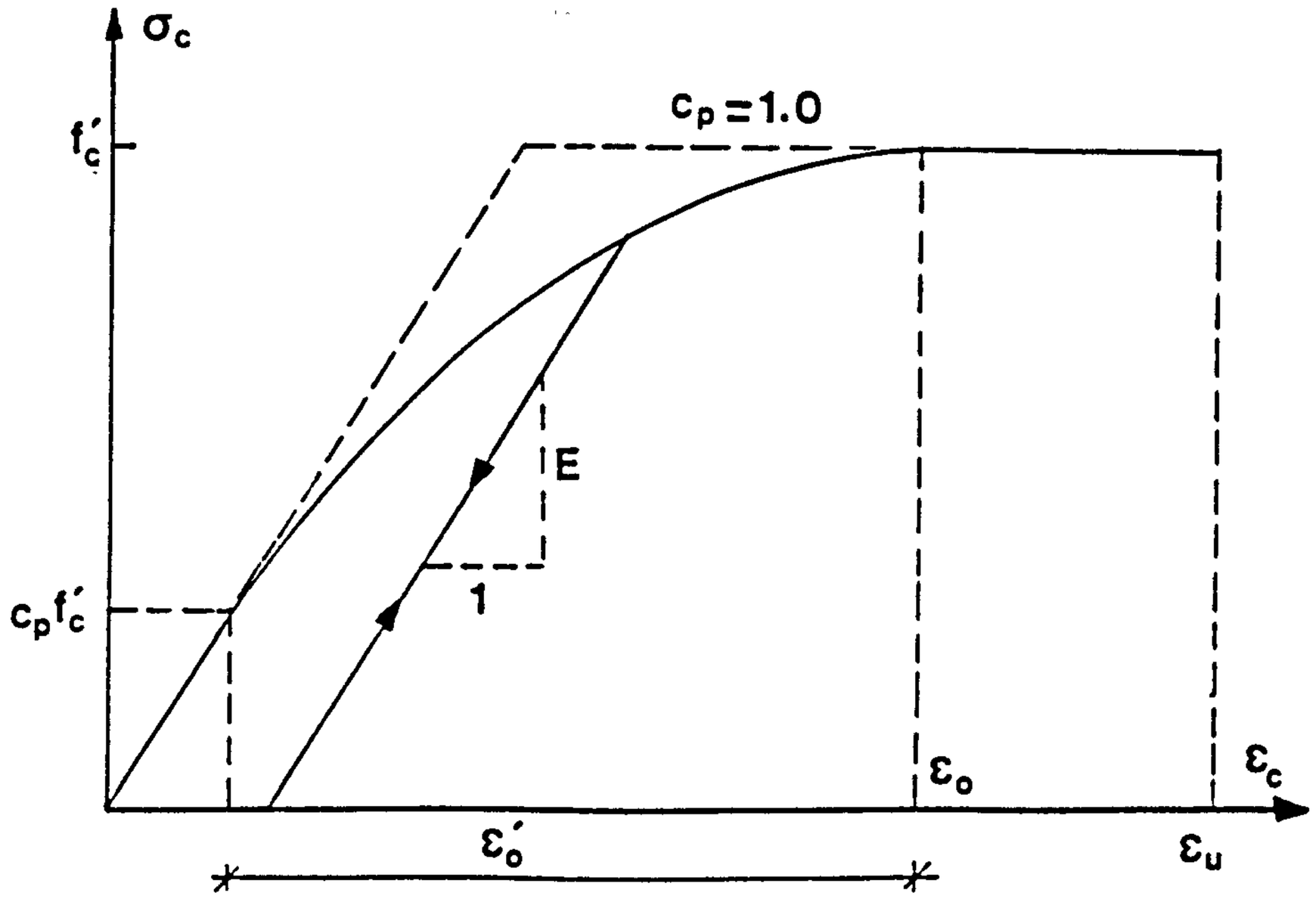

Fig. 3.7 Uniaxial stress-strain curve for concrete.

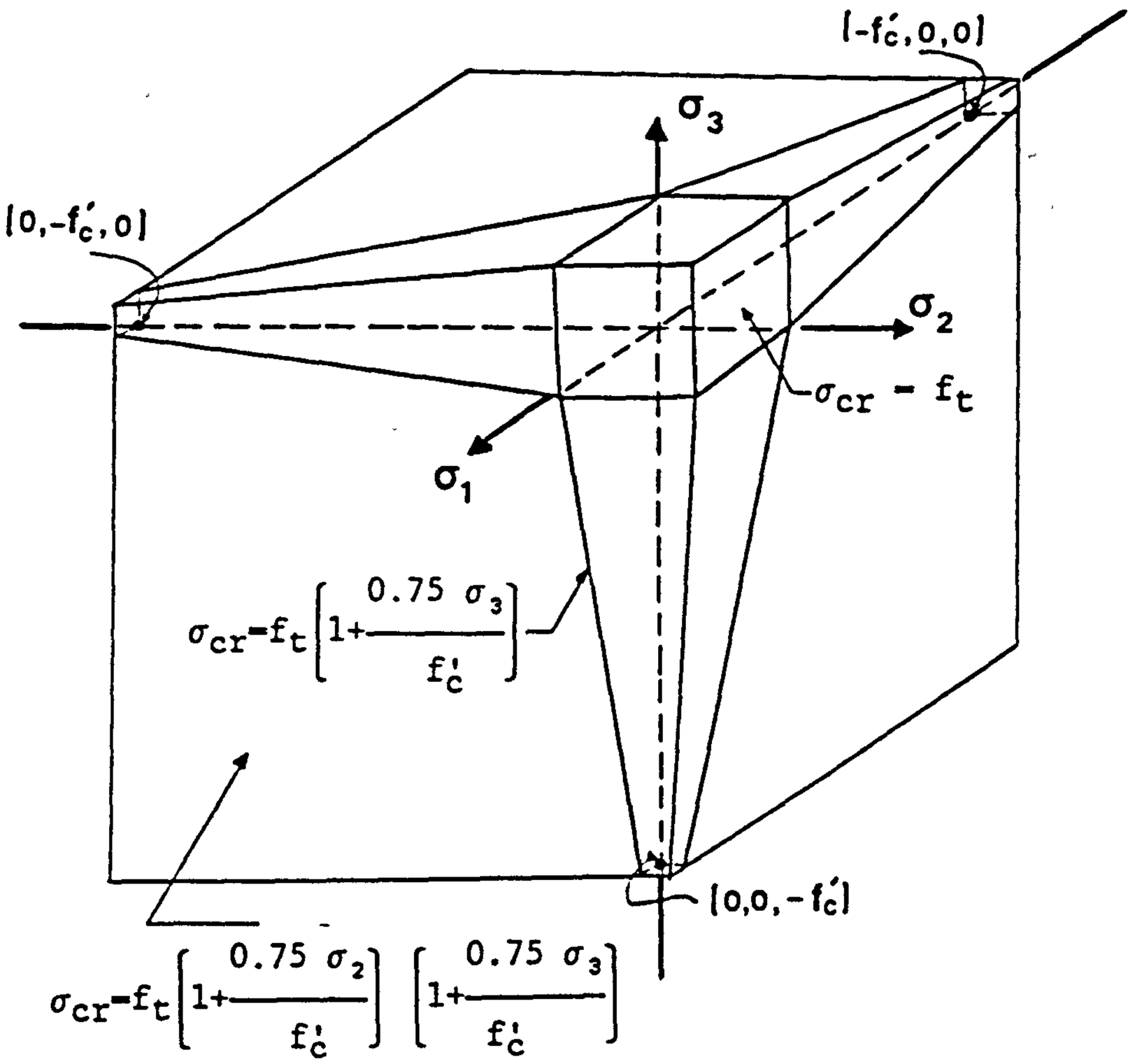

Fig. 3.8 Triaxial tensile failure , cracking, envelope of concrete.

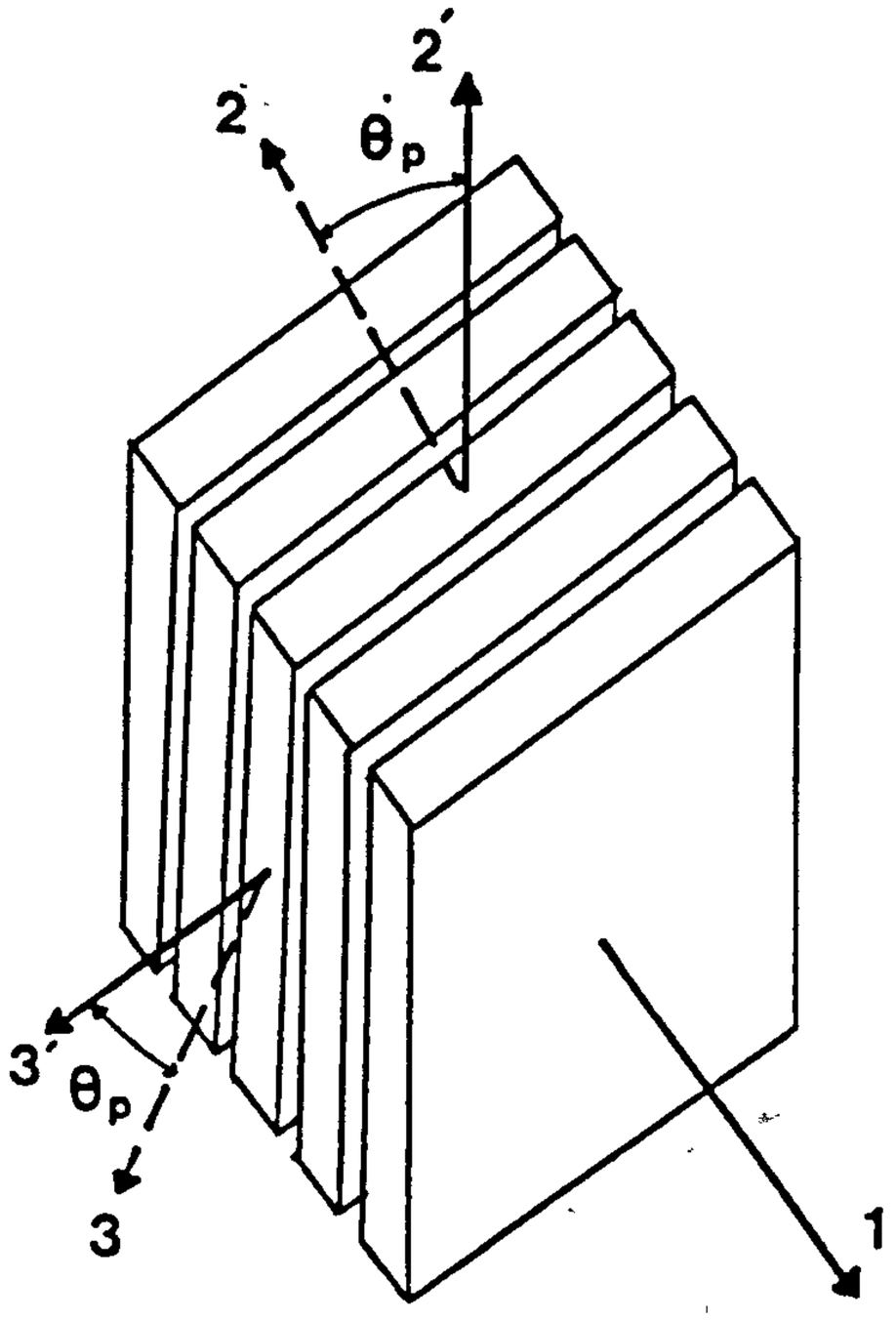

a) Single crack.

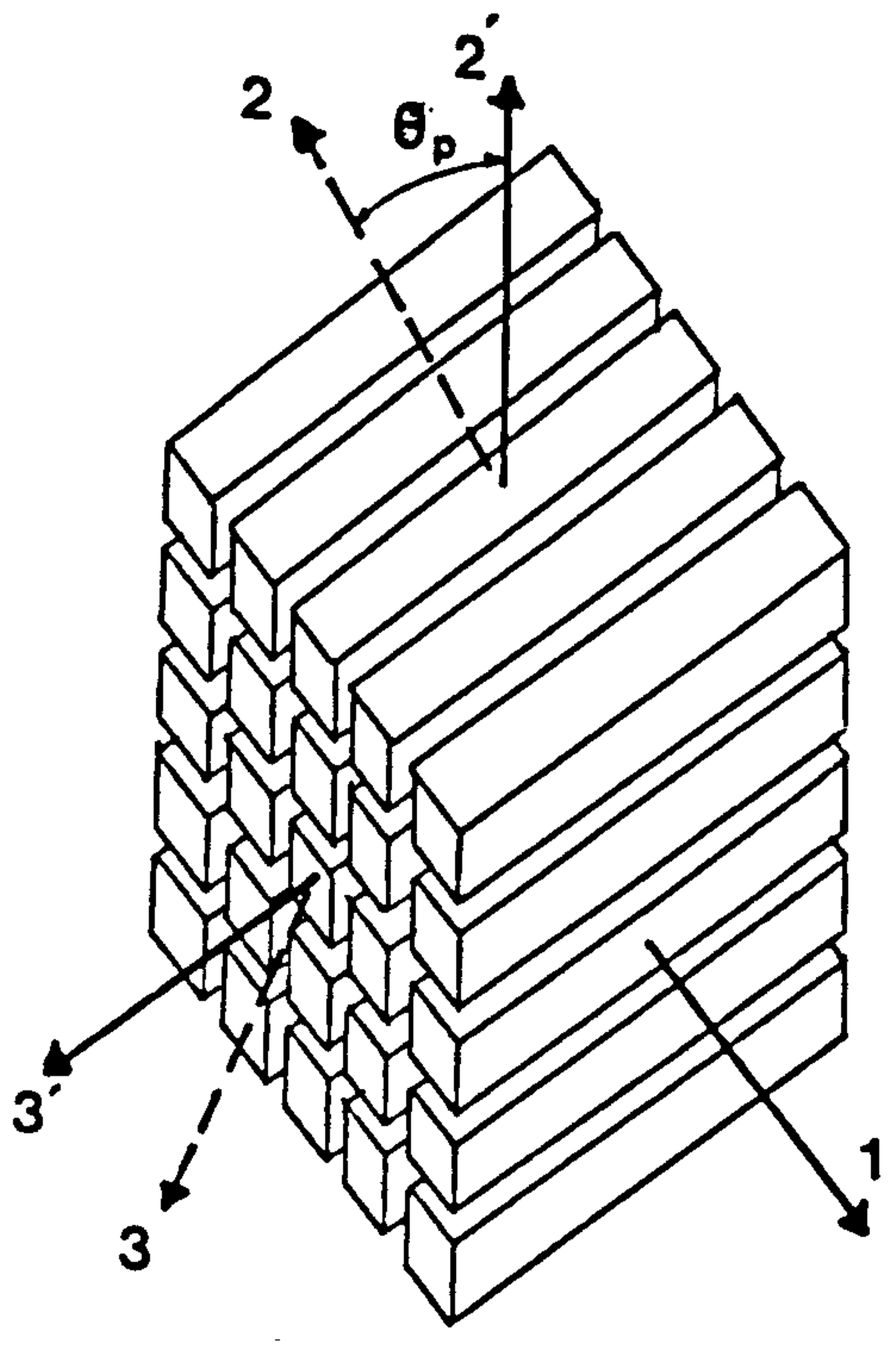

b) Double cracks.

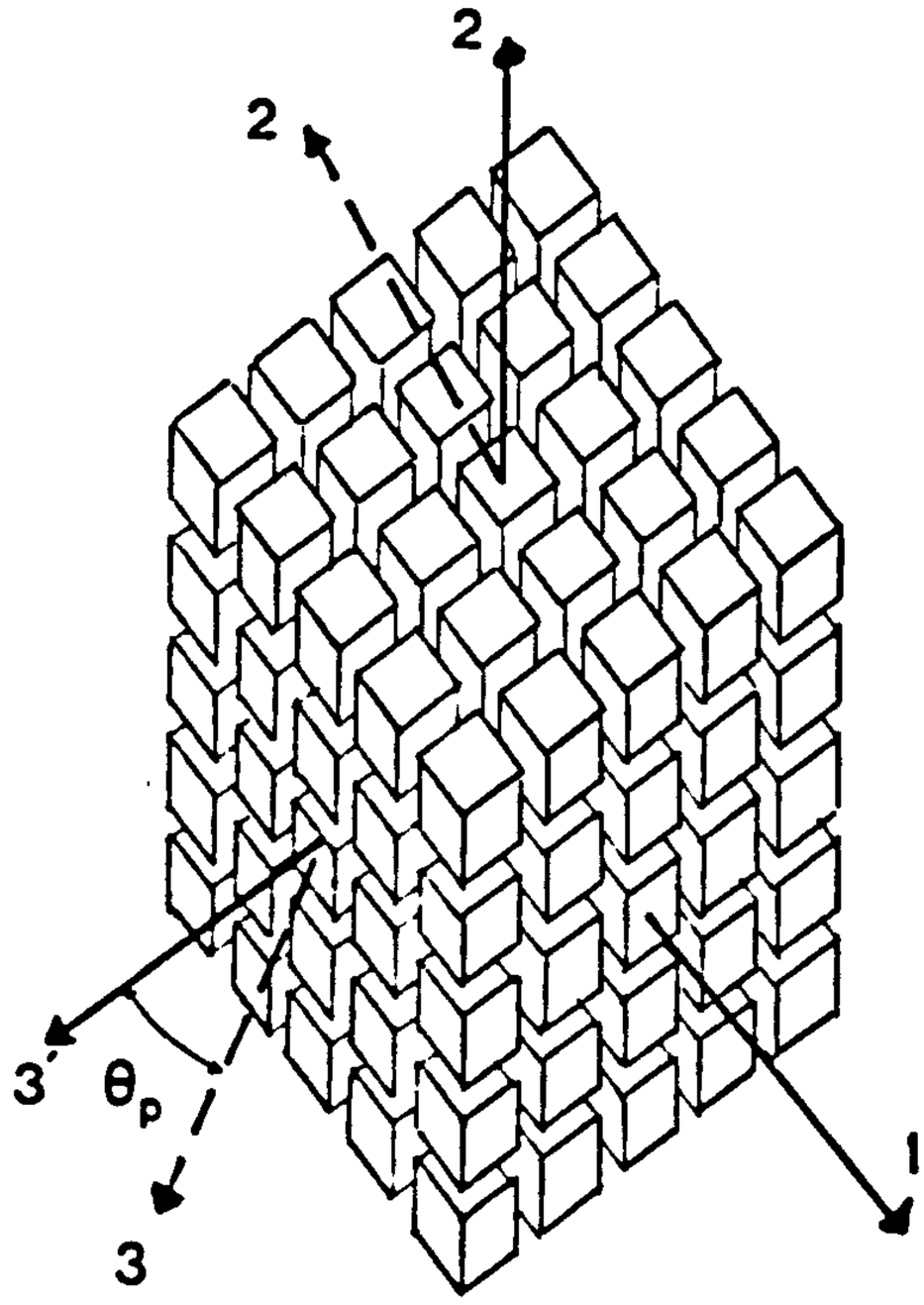

c) Triple cracks.

Fig. 3.9 Crack patterns in local material axes.

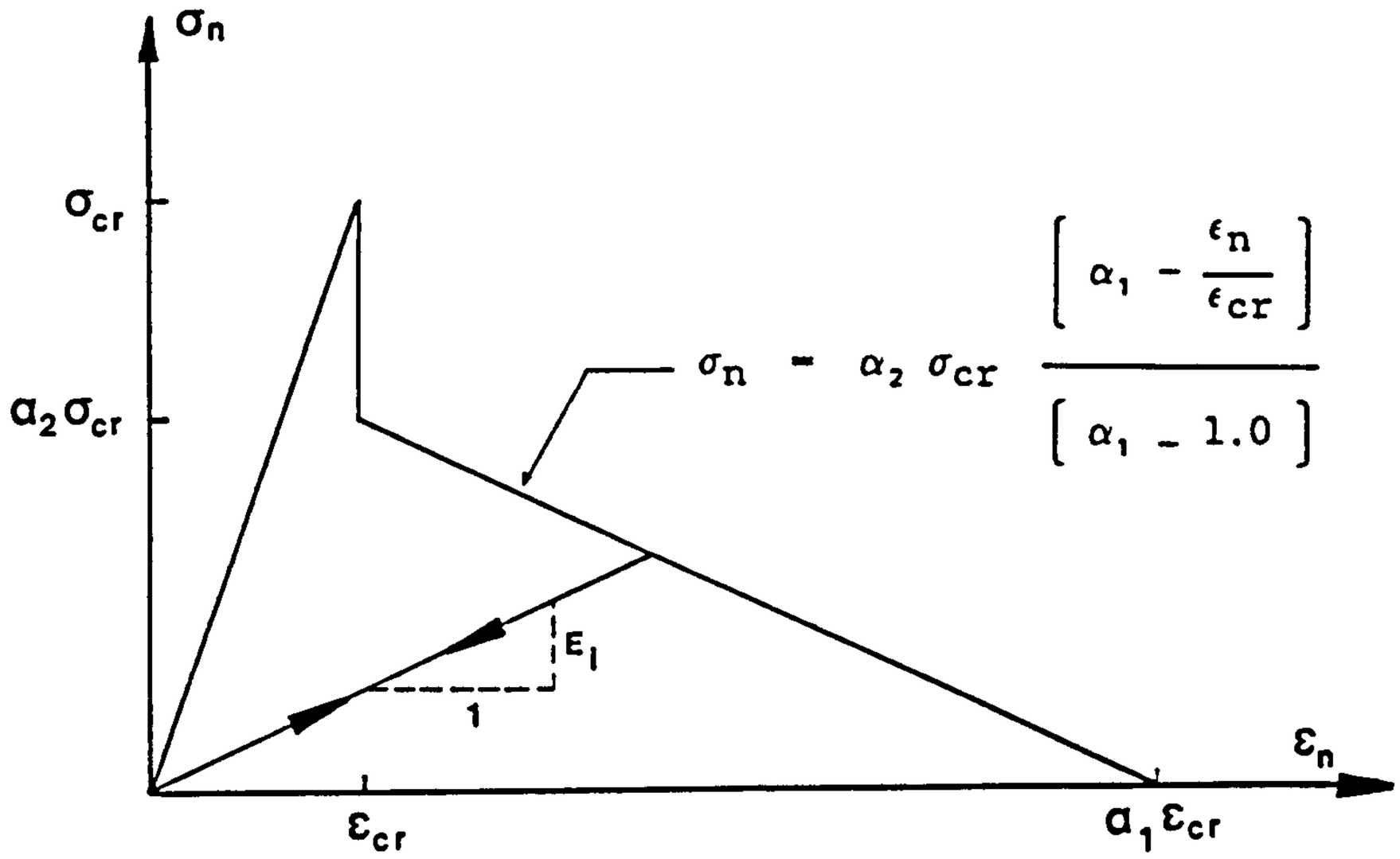

Fig. 3.10 Post-cracking model for concrete.

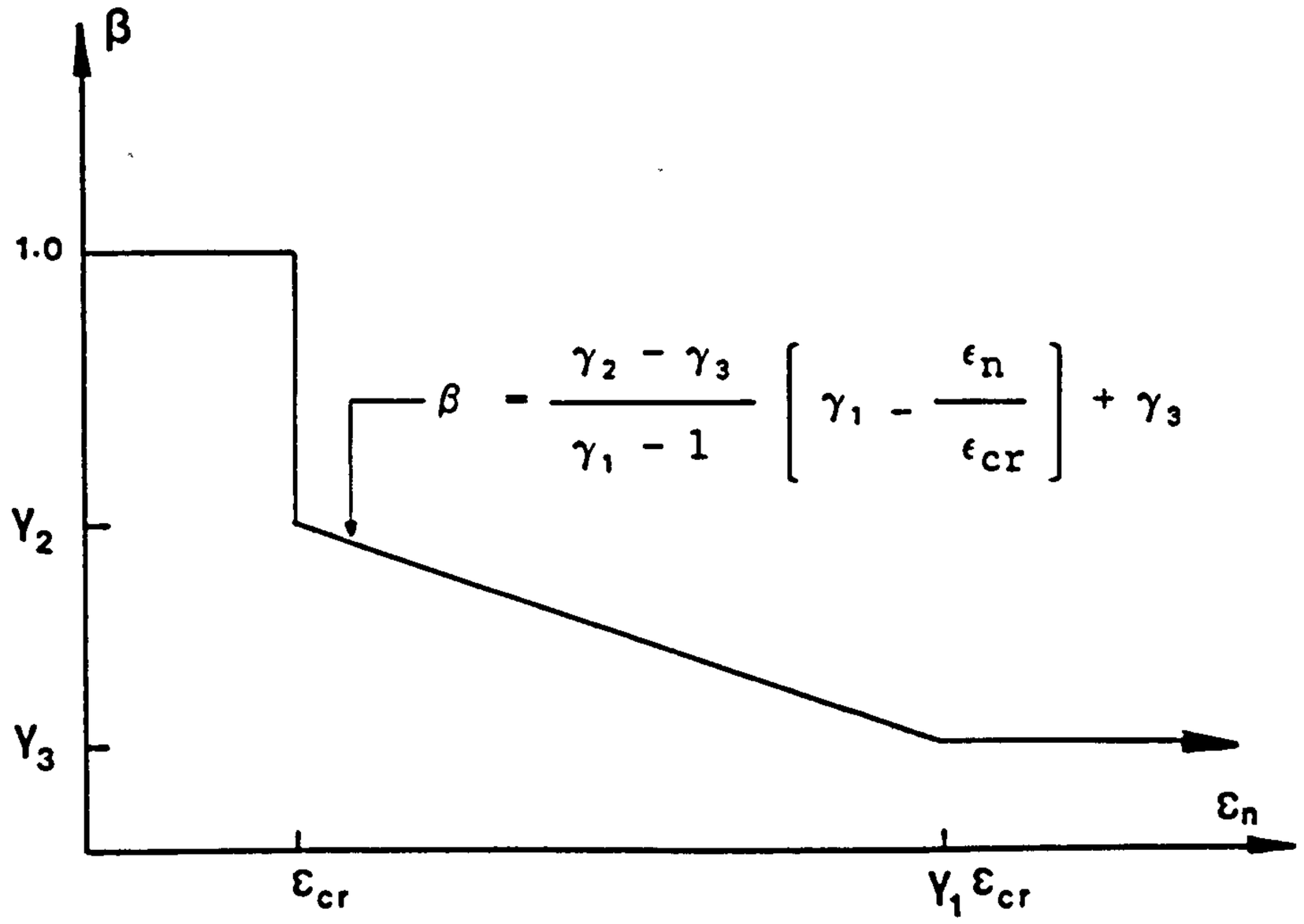

Fig. 3.11 Shear retention model for concrete.

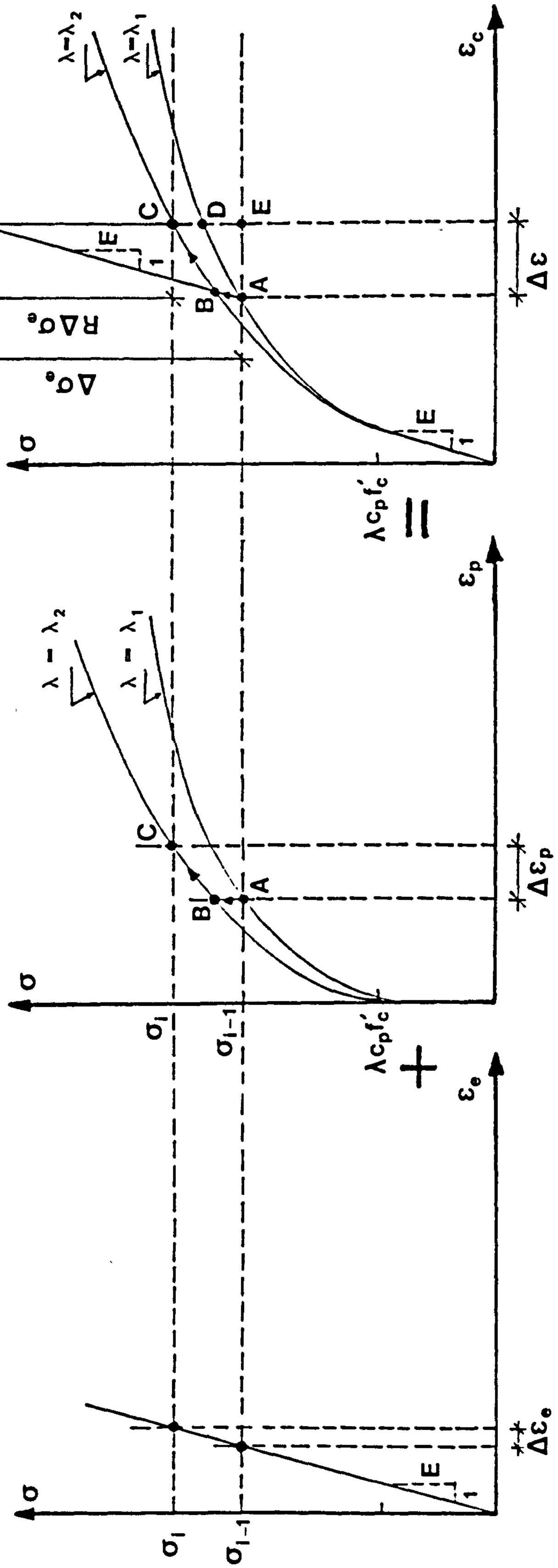

a) Stress–elastic strain relation b) Stress–plastic strain relation c) Stress–strain relationship for cracked concrete.

Fig. 3.12 Equivalent uniaxial compressive stress–strain relation for cracked concrete.

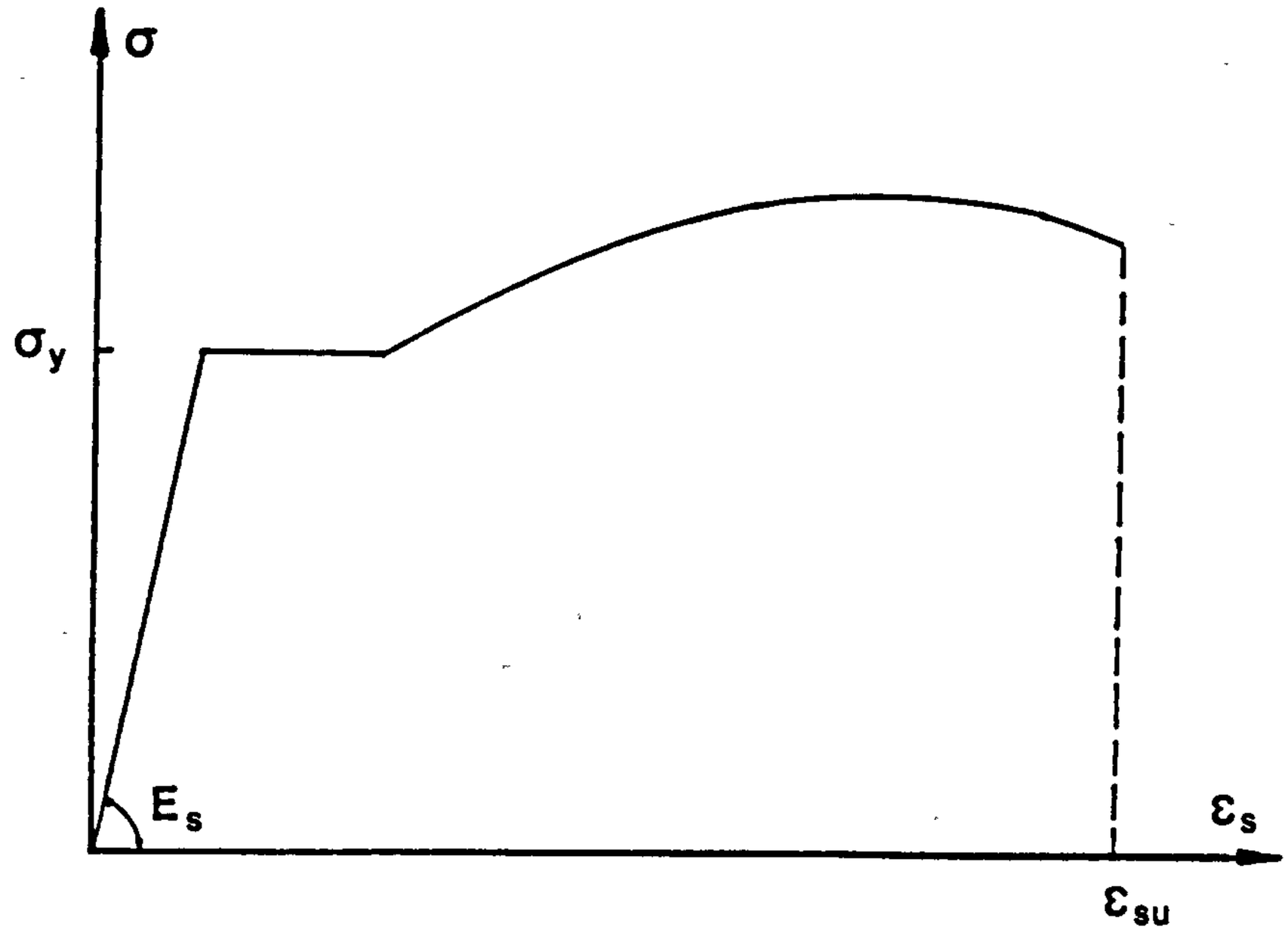

Fig. 3.13 Typical stress-strain curve for steel bars.

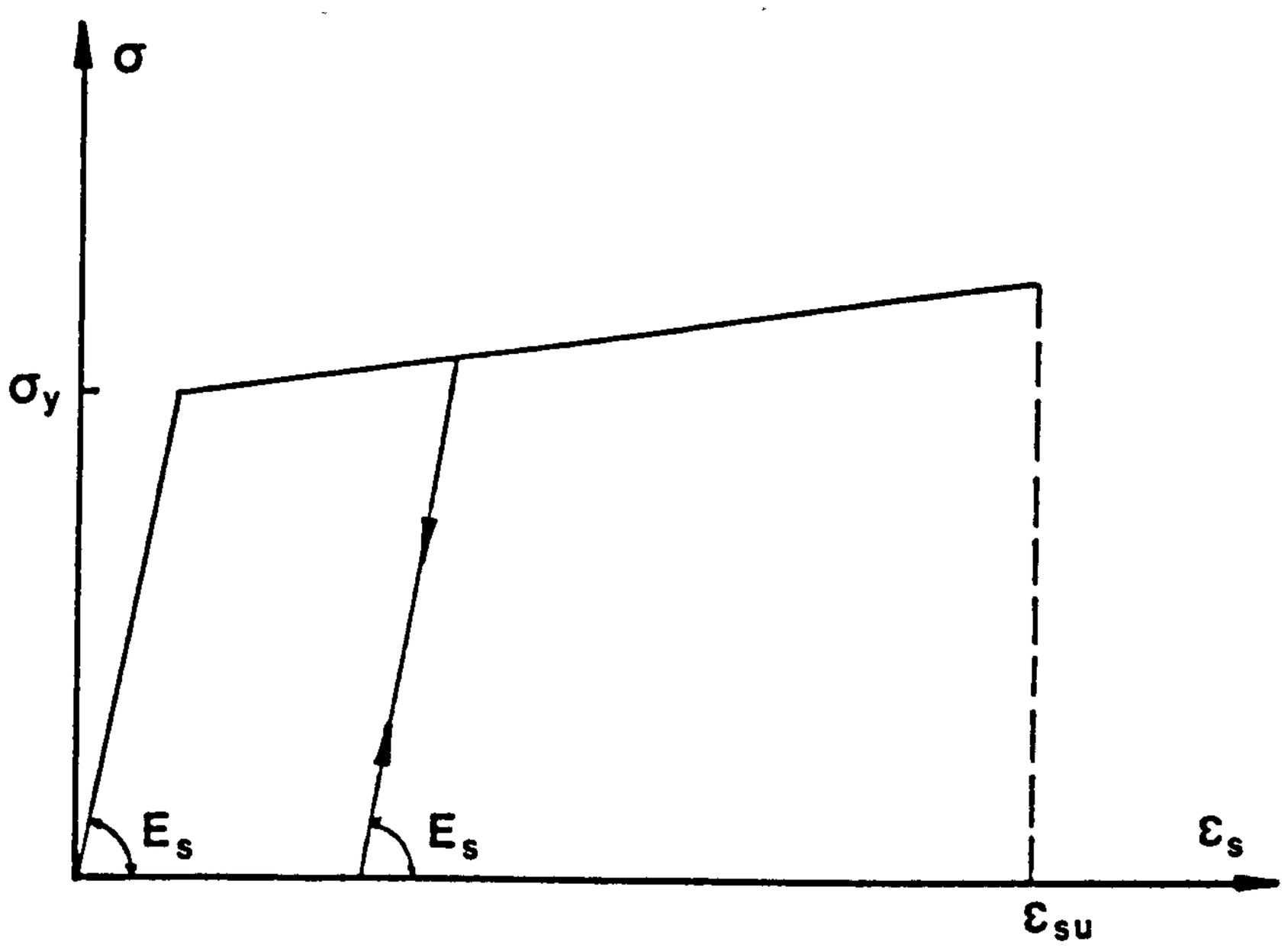

Fig. 3.14 Stress-strain relationship of steel bars used in the analysis.

REFERENCES

1. Naville, A.M. and Brooks, J.J., "Concrete Technology", Longman Scientific and Techincal, U.K, 1987.

2. Chen, W.F., "Plasticity in Reinforced Concrete", McGraw-Hill, 1982.

3. ASCE Committee on Concrete and Masonry Structures, " A State of the Art Reoprt on the Finite Element Analysis of Reinforced Concrete", Task Committee on Finite Element Analysis of Reinforced Concrete Structures, ASCE Spec. Publ., 1981.

4. Shah, S.P. and Winter, G.M., "Inelastic Behaviour and Fracture of Concrete", J. of the Amer. Conc. Inst., Vol. 63, No. 9, 1966, pp. 925-930.

5. Karsan, I.K and Jirsa, J.O., "Behaviour of Concrete under Compressive Loading", J. of the Struct. Div., ASCE, Vol. 95, No. ST12, December 1969, pp. 2543-2563.

6. Kupfer, H., Hilsdorf, H.K. and Rüsch, H., "Behaviour of Concrete under Biaxial Stresses", J. of the Amer. Conc. Inst., Vol. 66, No. 8, August 1969, pp. 656-666.

7. Liu, T.C.Y., Nilson, A.H. and Slate, F.O., "Biaxial Stress-Strain Relations for Concrete", J. of the Struct. Div., ASCE, Vol. 98, No. ST5, May 1972, pp. 1025-1034.

8. Nelissen, L.J.M., "Biaxial Testing of Normal Concrete", HERON, Vol. 18, No. 1, 1972.

9. Kupfer, H.B. and Gerstle, K.H., "Behaviour of Concrete under Biaxial Stresses", J. of the Eng. Mech. Div., ASCE, Vol. 99, No. EM4, August, 1973, pp. 852-866.

10. Tasuji, M.E., Slate, F.O. and Nilson, A.H., " Stress-Strain Response and Fracture of Concrete in Biaxial Loading", J. of the Amer. Conc. Inst., Vol. 75, No. 7, July 1978, pp.306-312.

11. Vecchio, F. and Collins, M.P., "The Response of Reinforced Concrete to In-Plane Shear and Normal Stresses", Publication No. 82-03, University of Toronto, Canada, 1982.

12. Maekawa, K. and Okamura, H., "The Deformational Behaviour and Constitutive Equation of Concrete Using the Elasto-Plastic and Fracture Model", J. of the Faculty of Engineering, University of Tokyo (B), Vol. XXXVII, No. 2, 1983.

13. Willam, K.J., Sture, S., Brcanic, N., Christensen, J. and Hurlbut, B., "Identification of Strain-softening Properties and Computational Predictions of Localised Fracture", Structural Research Series No. 8404, University of Colorado, Boulder, 1984.

14. Van mier, J.G.M., "Fracture of Concrete under Complex Stress", HERON, Vol. 31, No. 3, 1986.

15. Popovics, S., "A Review of Stress-Strain Relationships for Concrete", J. of the Amer. Conc. Inst., Vol. 67, No. 3, March 1970, pp. 243-248.

16. Gerstle, K.H. et al., "Behaviour of Concrete under Multiaxial Stress State", J. of the Eng. Mech. Div., ASCE, Vol. 106, No. EM6, December 1980, pp. 1383-1403.

17. ACI (318-77), "Building Code Requirements for Reinforced Concrete", ACI Committee 318, Amer. Conc. Inst., Detroit, 1977.

18. Darwin, D. and Pecknold, D.A., "Inelastic Model for Cyclic Biaxial Loading of Reinforced Concrete", Civ. Eng. Studies, SRS No. 409, University of Illinois at Urbana-Champaign, Urbana, Ill., July, 1974.

19. Hughes, B.P. and Chapman, G.P., "The Deformation Concrete and Microconcrete in Compression and Tension with Particular Reference to Aggregate Size", Magazine of Concrete Research, London, Vol. 18, No. 54, March 1966, pp. 19-24.

20. Reinhardt, H.W., "Fracture Mechanics of an Elastic Softening Material Like Concrete", HERON, Vol. 29, No. 2, 1984.

21. Carino, N.J. and Slate, F.O., "Limiting Tensile Strain Criterion for Failure of Concrete", J. of the Amer. Conc. Inst., Vol. 73, No. 3, March 1976, pp. 160-165.

22. Balmer, G.G., "Shearing Strength of Concrete under High Triaxial State-Computation of Mohr's Envelope as a Curve", Struct. Res. Lab. Rep. SP-23, Denever, Colo., October, 1949.

23. Gerstle, K.H., Linse, D.H., et al, "Strength of Concrete under Multiaxial Stress States", Proc., Douglas and McHenry Int. Symp. on Conc. and Conc. Struct., ACI Publ. SP-55, Amer. Conc. Inst., Detroit, 1978, pp. 103-131.

24. Cedolin, L., Crutzen, Y.R.J. and Die Poli, S., "Triaxial Stress-Strain Relationship for Concrete", J. of the Eng. Mech. Div., ASCE, Vol. 103, No. EM3, June 1977, pp. 423-439.

25. Chen, W.F. and Saleeb, A.F., "Constitutive Equations for Engineering Materials", Vol. 1, "Elasticity and Modelling", 1981, Vol. 2, "Plasticity and Modelling", 1982, John Willey and Sons, New York.

26. Kotsovos, M.D. and Newman, J.B., "Generalised Stress-Strain Relationship for Concrete", J. of the Eng. Mech. Div., ASCE, Vol. 104 No. EM4, August 1978, pp. 845-856.

27. Mills, L.L., and Zimmerman, R.M., "Compressive Strength of Plain Concrete Under Multiaxial Loading Conditions", J. of Amer. Conc. Inst., Vol 67, No. 10, October 1970, pp. 802-807.

28. Ngo, D. and Scordelis, A.C., "Finite Element Analysis of Reinforced Concrete Beams", J. of the Amer. Conc. Inst., Vol. 64, No. 3, March 1967, pp. 152-163.

29. Chen, W.F. and Ting, E.C., "Constitutive Models for Concrete Structures", J. of the Eng. Mech. Div., ASCE, Vol. 106, No. EM1, February 1980, pp. 1-19.

30. Cope, R.J. and Rao, P.V., "Nonlinear Response of Reinforced Concrete Skewed Slab Bridges", Res. Rep., Dept. Civ. Eng., University of Liverpool, 1981.

31. Gerstle, K.H., " Simple Formulation of Biaxial Concrete Behaviour", J. of the Amer. Conc. Inst., Vol. 78, No.1, September 1981, pp. 62-68.

32. Darwin, D. and Pecknold, D.A., "Analysis of RC Shear Panels under Cyclic Loading", J. of the Struct. Div., ASCE, Vol. 102, No. ST2, February 1976, pp. 355-369.

33. Darwin, D. and Pecknold, D.A., "Non-linear Biaxial Stress-Strain Law for Concrete", J. of the Eng. Mech. Div., ASCE, Vol. 103, No. EM2, April 1977, pp. 229-241.

34. Elwi, A.A., and Murray, D.W., "A 3D Hypoelastic Concrete Constitutive Relationship", J. of the Eng. Mech. Div., ASCE, Vol. 105, No. EM4, August 1979, pp. 623-641.

35. Bathe, K.J. and Sundberg, J.A., "A Concrete Material Model", In the Computational Modelling of Reinforced Concrete Structures, Eds. Hinton, E. and Owen, R., Pineridge Press, Swansea, U.K., 1986, pp. 101-121.

36. Owen, D.R.J. and Hinton, E., "Finite Elements in Plasticity Theory and Applications", Pineridge Press, Swansea, U.K, 1980.

37. Buyukozturk, O., "Non-Linear Analysis of Reinforced Concrete Structures", Comput. Struct., Vol. 7, 1977, pp. 149-156.

38. Chen, A.C.T., and Chen, W.F., "Constituitive Relations for Concrete", J. of the Eng. Mech. Div., ASCE, Vol. 101, No. EM4, August 1975, pp. 465-481.

39. Owen, D.R.J. and Figueiras, J.A., "Ultimate Load Analysis of Reinforced Concrete Plate and Shell Including Geometric Non-Linear Effects", In Finite Element Software for Plates and Shells, Eds. Hinton, E. and Owen D.R.J., Pineridge Press, Swansea, U.K, 1984.

40. Imbabi, M.S. and Cope, R.J., "An Equivalent Elasto-Plastic Constitutive Model for Biaxially Loaded Concrete", Proc. Int. Conf. on Computer Aided Analysis and Design of Conc. Struct., Eds. Damjanic et al., Vol. I, Split, Yogoslavia, September 1984, pp. 275-288.

41. Cervera, M. and Hinton, E., "Non-Linear Aanlysis of Reinforced Concrete Plates and Shells Using a Three Dimensional Model", In the Computational Modelling of Reinforced Concrete Structures, Eds. Hinton, E. and Owen, R., Pineridge Press, Swansea, U.K., 1986, pp. 327-370.

42. Drucker, D. C., "A More Fundamental Approach to Plastic Stress-Strain Relations, Proc., 1st. U.S. National Congress on Applied Mechanics, 1951, PP. 487-491.

43. Bazant, Z.P. and Kim, S.S., "Plastic-Fracturing Theory for Concrete", J. of the Eng. Mech. Div., ASCE, Vol. 105, June 1979, pp. 407-428 with Errata in Vol. 106.

44. Hsieh, S.S., Ting, E.C. and Chen, W.F., "A Plastic-Fracture Model for Concrete", Int. J. of Solids and Struct., Vol. 18, No. 3, 1982, pp. 181-197.

45. Glemberg, R. and Samuelsson, A., "A General Constitutive Model for Concrete Structures", Proc. Int. Conf. on Computer Aided Analysis and Design of Conc. Struct., Eds. Damjanic et al., Vol. I, Split, Yogoslavia, September 1984, pp. 119-132.

46. Valanis, K.C., "A Theory of Viscoplasticity without a Yield Surface - Theory and Application", Archives of Mechanics, Vol. 23, No. 4, 1971, pp. 517-551.

47. Bazant, Z.P., and Bhat, P., "Endochronic Theory of Inelasticity and Failure of Concrete", J. of the Eng. Mech. Div., ASCE, Vol. 102, No. EM4, August 1976, pp. 701-722.

48. Reddy, D.V. and Gopal, K.R., "Endochronic Constitutive Modelling of Marine Fiber Reinforced Concrete", In the Computational Modelling of Reinforced Concrete Structures, Eds. Hinton, E. and Owen, R., Pineridge Press, Swansea, U.K., 1986, pp. 154-186.

49. Sandler, I.S., "On the Uniquness and Stability of Endochronic Theories of Material Behaviour", J. of Appl. Mech., Vol. 45, No. 2, June 1978, pp. 263-266.

50. Rivlin, R.S., "Some Comments on the Endochronic Theory of Plasticity", Int. J.of Solids and Struct., Vol. 17, 1981, pp. 231-248.

51. Bazant, Z.P., "Endochronic Inealsticity and Incremental Plasticity", Int. J. of Solids and Struct., Vol. 14, 1978, pp. 691-714.

52. Valanis, K.C., "Fundamental Consequences of a New Intrinsic Time Measure-Plasticity as a Limit of the Endochronic Theory", Archives of Mechanics, Vol. 32, No. 1, 1980, pp. 171-191.

53. Mirza, S.A., Hatzinikdas, M. and MacGregor, J.G., "Statistical Descriptions of Strength in Concrete", J. of the Struct. Div., ASCE, Vol. 105, No. ST6, June 1979, pp. 1021-1037.

54. Cope, R.J., "Material Modelling of Real Reinforced Concrete Slabs", Proc. Int. Conf. on Computer Aided Analysis and Design of Conc. Struct., Eds. Damjanic et al., Vol. I, Split, Yogoslavia, September 1984, pp. 85-117.

55. Nilson, A.H., "Non-Linear Analysis of Reinforced Concrete by the Finite Element Method", J. of the Amer. Conc. Inst., Vol. 65, No.9, September 1968, pp. 757-766.

56. Ngo, D., "A Network-Topological Approach to the Finite Element Analysis of Progressive Crack Growth in Concrete Members", Ph.D. Thesis, University of California, Berkeley, 1975.

57. Rashid, Y.R., "Analysis of Prestressed Concrete Pressure Vessels", Nuclear Engineering and Design, Vol. 7, No. 4, April 1968, pp. 334-355.

58. Cope, R.J. and Rao, P.V., "Moment Redistribution in Skewed Slab Bridges", Proc. Instn. Civ. Engrs., Vol. 75, 1983, pp. 419-452.

59. Gupta, A.K. and Akber, A., "Cracking in Reinforced Concrete Analysis", J. of the struct. Div., ASCE, Vol. 110, 1984, pp. 1735-1746.

60. Cope, R.J. and Rao, P.V., "Non-Linear Finite Element Analysis of Concrete Slab Structures", Proc. Instn. Civ. Engrs., Vol. 63, 1977, pp. 159-179.

61. Milford, R.V. and Schnobrich, W.C., "Numerical Model for Cracked Reinforced Concrete", Proc. Int. Conf. on Computer Aided Analysis and Design of Conc. Struct., Eds. Damjanic et al., Vol. I, Split, Yogoslavia, September 1984, pp. 71-84.

62. Crisfield, M.A. and Wills, J., "Numerical Comparisons Involving Different 'Concrete-Models'", IABSE Colloquium on Numerical Modelling of Reinforced Concrete, Delft, 1987, pp. 177-187.

63. Cope, R.J., Rao, P.V., Clark, L.A. and Norris, P., "Modelling of Reinforced Concrete Behaviour for Finite Element Analysis of Bridge Slabs", Numerical Methods for Non-Linear Problems, Vol. 1, Pineridge Press, Swansea, 1986, pp. 457-470.

64. De Borst, R. and Nauta, P., "Smeared Crack Analysis of Reinforced Concrete Beams and Slabs Failing in Shear", Proc. Int. Conf. on Computer Aided Analysis and Design of Conc. Struct., Eds. Damjanic et al., Vol. I, Split, Yogoslavia, September 1984, pp. 261-274.

65. De Borst, R., "Computational Aspects of Smeared Crack Analysis", In the Computational Modelling of Reinforced Concrete Structures, Eds. Hinton, E. and Owen, R., Pineridge Press, Swansea, U.K., 1986, pp. 44-83.

66. Rots, J.G, "Computational Modelling of Concrete Fracture", Ph.D. Thesis, University of Technology, Delft, 1988.

67. Clark, L.A. and Speirs, D.M., "Tension Stiffening in Reinforced Concrete Beams and Slabs under Short Term Loads", Tech. Rep.42-521, Cement and Conc. Ass., London, 1978.

68. Scanlon, A., "Time Dependent Deflections of Reinforced Concrete Slabs", Ph.D. Thesis, University of Alberta, Edmonton, Alberta, Canada, 1971.

69. Cope, R.J., "Non-Linear Analysis of Reinforced Concrete Slabs", In the Computational Modelling of Reinforced Concrete Structures, Eds. Hinton, E. and Owen, R., Pineridge Press, Swansea, U.K.,

1986, pp. 3-43.

70. Abdel-Rahman, H.H., "Computational Models for the Non-Linear Analysis of Reinforced Concrete Flexural Slab Systems", Ph.D. Thesis, University of Wales, Swansea, U.K.

71. Gilbert, R.I. and Warner, R.F., "Non-Linear Analysis of Reinforced Concrete Slabs with Tension Stiffening", UNICIV Rep. No. R-167, University of New South Wales, Kensington, Australia, January 1977.

72. Hillerborg, A., "The Influence of Tensile Toughness of Concrete on the Behaviour of Reinforced Concrete Structures", Proc., 9th Congress of the FIP, Stockholm, Vol. 1, 1982, PP. 157-164.

73. Rots, J.G., Nauta, P., Kusters, G.M.A. and Blaauwendraad, J., "Smeared Crack Approach and Fracture Localisation in Concrete", HERON, Vol 30, No. 1, 1985, PP.1-48.

74. Glemberg, R., Oldenburg, M., Nelisson, L. and Samuelsson, A., "A General Constitutive Model for Concrete", In the Computational Modelling of Reinforced Concrete Structures, Eds. Hinton, E. and Owen, R., Pineridge Press, Swansea, U.K., 1986, pp. 84-100.

75. Millard, S.G., "Shear Transfer in Cracked Reinforced Concrete", Ph.D. Thesis, University of Warwick, 1983.

76. Millard, S.G. and Johanson, R.P., "Shear Transfer Across Cracks in Reinforced Concrete Due to Aggregate Interlock and Dowel Action", Magazine of Concrete Research, Vol. 37, No. 130, 3-15, 1985.

77. Al-Mahaidi, R.S.H., "Non-Linear Finite Element Analysis of Reinforced Concrete Deep Members", Res. Rep. 79-1, Dept. of Struct. Eng., Cornell University, January 1979.

78. Gerstle, K.H., "Material Modelling of Reinforced Concrete", IABSE Colloquium on Advanced Mechanics of Reinforced Concrete, Delft, 1981, PP.41-62.

79. Phillips, D.V., "Non-Linear Analysis of Structural Concrete by Finite Element Method", Ph.D. Thesis, University of Wales, Swansea, 1972.

80. Hand, F.R., Pecknold, D.A. and Schnobrich, W. C., "Non-Linear Layered Analysis of RC Plates and Shells", J. of the Struct. Div., ASCE, Vol. 99, No. ST7, July 1973, PP. 1491-1505.

81. Cedolin, L. and Dei Poli, S., "Finite Element Studies of Shear Critical Reinforced Concrete Beams", J. of the Eng. Mech. Div., ASCE, Vol. 103, No. EM3, June 1977.

82. Robinson, J.R. and Demorieux, J.M., "Essais de Traction-Compression sur Models d'ame de Poutre en Béton Armé," Institut de Recherches Applliquées du Béton Armé (IRABA), Part 1, June 1968 and Part 2, May 1972.

83. Cervenka, V., "A Constitutive Model for Reinforced Concrete", J. of the Amer. Conc. Inst., Vol. 82, November-December 1985, pp. 877-882.

84. Vecchio, F.J. and Collins M.P., "The Modified Compression-Field Theory for Reinforced Concrete Elements Subjected to Shear", J. of the Amer. Conc. Inst., March-April 1986, pp. 219-230.

85. Figueiras, J.A. and Owen, R.J., "Non-Linear Analysis of Reinforced Shell Structures", Proc. Int. Conf. on Computer Aided Analysis and Design of Conc. Struct., Eds. Damjanic et al., Vol. I, Split, Yogoslavia, September 1984, pp. 509-532.

86. Kent, A.J, "Finite Element Models for the Analysis of Reinforced Concrete Shell Structures with Geometric and Material Non-Linearites, Ph.D. Thesis, University of Wales, Swansea, 1987.

87. Naji, J.H., "Non-linear Finite Element Analysis of Reinforced Concrete Panels and Infilled Frames under Monotonic and Cyclic Loading", Ph.D. Thesis, University of Bradford, 1989.

88. De Borst, R., "Non-linear Analysis of Frictional Materials", Rep. for Inst. T.N.O. for Building Materials and Building Struct., Delft, 1986.

89. Figueiras, J.A., "Practical Approach for Modelling the Non-Linear Response of RC Shells", In the Computational Modelling of Reinforced Concrete Structures, Eds. Hinton, E. and Owen, R., Pineridge Press, Swansea, U.K., 1986, pp. 217-253.

90. Durelli, A.J., Phillips, E.A. and Taso, C.H., "Introduction to the Theoretical and Experimental Analysis of Stress and Strain, McGraw Hill, 1956.

91. Cook, R.D., "Concepts and Applications of Finite Element Analysis", 2nd. Ed., John Wiely and Sons, New York, 1981.

92. Hinton, E., Abdel-Rahman, H.H., and Zienkiewicz, O.C., "Computational Models for Reinforced Concrete Slab Systems", IABSE Colloquium on Advanced Mechanics of Reinforced Concrete, Delft, June 1981, PP. 303-313.

93. Al-Manaseer, A.A., "A Non-Linear Finite Element Study of Reinforced Concrete Beams", Ph.D. Thesis, University of Glasgow, 1983.

94. Crisfield, M.A., "Difficulties with Concrete Numerical Models for Reinforced Concrete and Some Tentative Solutions", Proc. Int. Conf. on Computer Aided Analysis and Design of Conc. Struct., Eds. Damjanic et al., Vol. I, Split, Yogoslavia, September 1984, pp. 331-357.

95. Al-Manaseer, A.A. and Phillips, D.V., "Numerical Study of Some Post-Cracking Material Parameters Affecting Non-Linear Solutions in Reinforced Concrete Deep Beams", Canadian J. of Civ. Eng., Vol. 14, No. 5, 1987, pp. 655-666.

96. Bazant, Z.P., and Oh, B.H., "Spacing of Cracks in Reinforced Concrete", J. of the Struct. Eng. Div., ASCE, Vol. 109, No. 9, September 1983, pp. 2066-2085.

97. Petersson, P. E., "Crack Growth and Development of Fracture Zone in Plain Concrete and Similar Materials", Rep. TVBM - 1006, Divison of Building Materials, Lund Inst. of Technoloy, Sweden, 1981.

CHAPTER FOUR

NON-LINEAR SOLUTION TECHNIQUES

4.1 Introduction

One of the main objectives of the finite element analysis of reinforced concrete structures is to determine the response under loading. Fig. 4.1 shows a typical load deformation curve for a monotonically loaded member where the behaviour is essentially linear up to point A. Beyond this point a non-linear load deformation response occurs. Such a response is due to either non-linear material behaviour, material non-linearity, or large deformations in the structure, geometrical non-linearity, or a combination of both.

In the analysis of reinforced concrete structures, the effect of large deformations can be neglected for the majority of cases. This is due to the early onset of material non-linearity, with large deformations occurring only close to structural collapse [1]. The sources of material non-linearity considered in the present study are:

1. cracking of concrete,
2. crushing of concrete,
3. yielding of reinforcement and
4. plastic deformation of concrete and reinforcement.

At the linear stage of behaviour, the solution of the discretised

system of the equilibrium equations can be achieved in a direct manner. However, at the non-linear stage it is not possible to solve the governing equations directly. Therefore resort has to be made to more sophisticated solution strategies. A combined incremental-iterative solution technique is usually used. In the present work, Newton-Raphson incremental-iterative solution algorithms have been implemented to trace the response of the structures up to failure. The solution techniques adopted are operated under a load control incrementation scheme.

This Chapter describes the numerical solution algorithms used in this study. Section 4.2 summarises the iterative and incremental methods which are usually used to solve non-linear problems. A full description of the solution techniques adopted is given in section 4.3. Section 4.4 deals with the schemes incorporated to accelerate the convergence of the solution. The convergence criteria and the analysis termination criteria are presented in sections 4.5 and 4.6 respectively. An outline of the computer program developed is given in section 4.7.

4.2 Solution Techniques for Non-Linear Equations

For a non-linear structural response, the discretised system of algebraic equations can generally be written in the form,

$$\underset{\sim}{r}(\underset{\sim}{a}) = \underset{\sim}{p}(\underset{\sim}{a}) - \underset{\sim}{f} \qquad (4.1)$$

where $\underset{\sim}{r}$ is the out of balance, residual, force vector, $\underset{\sim}{a}$ is the

vector of nodal displacements, $\underset{\sim}{f}$ is the vector of externally applied nodal loads and p is the internal nodal load vector given by,

$$p(\underset{\sim}{a}) = \int_V B^T \underset{\sim}{\sigma} \, dV \tag{4.2}$$

Solution of the equilibrium equations (4.1) is based upon obtaining a balance between the external and internal loads vectors such that the residual forces are zero. Three basic solution techniques are usually used in this context. These are the iterative, incremental and combined incremental-iterative approaches. The approaches are diagrammatically illustrated in Fig. 4.2 for a one degree of freedom case.

The purely iterative techniques imply the application of the total load in a single increment, Fig. 4.2a. An initial estimate of the vector of unknown nodal displacements $\underset{\sim}{a}_1$ is obtained. The stresses corresponding to the predicted initial solution are calculated using the relevant constitutive relations. These stresses are used to calculate the internal force vector p and then the out of balance force vector $\underset{\sim}{r}$. The out of balance forces are successively applied to the structure in order to obtain progressively improved solutions $\underset{\sim}{a}_2$, $\underset{\sim}{a}_3$ .... . The total displacement is taken as the sum of the accumulated displacements from each iteration. The iterative corrections continue until the out of balance forces become negligibly small. This type of technique is not suitable for tracing the entire non-linear equilibrium path because it fails to produce information about the intermediate stages of loading. For such cases the incremental techniques are essential.

The purely incremental techniques, Fig. 4.2b, are usually carried out by applying the external loads as a sequence of sufficiently small increments. Within each increment of loading, linear constitutive relationships are generally assumed. Because the purely incremental techniques does not account for the redistribution of forces during the application of loading increments, they suffer from a progressive and uncorrected tendency to drift from the true equilibrium path. The drift depends on the degree of non-linearity and the size of loading increments.

The combined incremental-iterative techniques, Fig 4.2c, imply the subdivision of the total external load into smaller increments. Within each increment of loading iterative cycles are performed in order to obtain a converged solution corresponding to the stage of loading under consideration. In practice the progress of the iterative procedure is monitored with reference to a specified convergence criterion.

At present, the incremental-iterative method is the most commonly used technique for solving non-linear finite element problems. The standard and the modified Newton-Raphson methods [2-4] are usually used with this regard. More recently the quasi-Newton methods [5-7] and the secant-Newton methods [8-10] have also been used in the finite element structural analysis. The computer program described incorporates the standard Newton-Raphson method and its modified versions. These methods are described in the following section.

4.3 Standard and Modified Newton–Raphson Methods

In these methods the external load is applied inrementally and a series of iterations are performed within each increment of load in order to eliminate the out of balance forces $\underset{\sim}{r}$, such that:

$$\underset{\sim}{r}(\underset{\sim}{a}) = \underset{\sim}{0} \tag{4.3}$$

If an approximate solution to $\underset{\sim}{a}$ such as $\underset{\sim}{a}_i^n$ exists, note that the subscripts i and n correspond to the number of the current iteration and current loading increment respectively, an improved solution can be achieved using a truncated Taylor series of the form

$$\underset{\sim}{r}(\underset{\sim}{a}_{i+1}^n) = \underset{\sim}{r}(\underset{\sim}{a}_i^n) + \left.\frac{\partial \underset{\sim}{r}(\underset{\sim}{a})}{\partial \underset{\sim}{a}}\right]_{\underset{\sim}{a}_i^n} \delta \underset{\sim}{a}_i^n \tag{4.4}$$

In the above expression , the term

$$\left.\frac{\partial \underset{\sim}{r}(\underset{\sim}{a})}{\partial \underset{\sim}{a}}\right]_{\underset{\sim}{a}_i^n} = \underset{\sim}{K}_T(\underset{\sim}{a}_i^n) \tag{4.5}$$

represents the tangential stiffness matrix at iteration i of increment n. If the approximation $\underset{\sim}{a}_{i+1}^n$ is used in (4.3) instead of $\underset{\sim}{a}$ then equation (4.4) can be written as:

$$\underset{\sim}{r}(\underset{\sim}{a}_i^n) + \underset{\sim}{K}_T(\underset{\sim}{a}_i^n)\ \delta \underset{\sim}{a}_i^n = 0 \tag{4.6}$$

from which the iterative displacement $\delta \underset{\sim}{a}_i^n$ can be found as,

$$\delta \underset{\sim}{a}_I^n = - \underset{\sim}{K}_T(\underset{\sim}{a}_I^n)^{-1} \underset{\sim}{r}(\underset{\sim}{a}_I^n) \tag{4.7}$$

The improved approximation $\underset{\sim}{a}_{I+1}^n$ can be expressed as,

$$\underset{\sim}{a}_{I+1}^n = \underset{\sim}{a}_I^n + \delta \underset{\sim}{a}_I^n \tag{4.8}$$

Equations (4.7) and (4.8) constitute the standard Newton–Raphson algorithm for the solution of (4.3). The procedure using (4.7) and (4.8) continues and for each iteration a new system of linearised equations has to be solved for $\delta \underset{\sim}{a}_I^n$ until the solution converges. The solution process is illustrated diagrammatically in Fig. 4.3a for the case of a one degree of freedom system.

In the standard, or full, Newton–Raphson method, the tangential stiffness matrix is updated and a new system of equations is solved for each iteration. This is an expensive computational procedure, particularly if the size of loading increments is small. To overcome this, the algorithm can be modified by only updating the stiffness matrix occasionally.

4.3.1 Modified Newton–Raphson Methods

The most commonly used modified forms of the standard Newton–Raphson method are those in which the stiffness matrix is updated only once for each increment of loading. Figs. 4.3b and 4.3c illustrate two possible modifications. In Fig 4.3b the stiffness matrix is updated at the begining of the first iteration of each increment, the KT1 method. While in Fig. 4.3c the stiffness matrix

is calculated at the begining of the second iteration, the KT2 method, so that the non-linear effects are more accurately represented in the stiffness matrix.

These methods are generally more economical than the full Newton-Raphson method since they involve fewer stiffness matrix reformulations. However, the convergence is slower and a large number of iterations is required to achieve converged solution. This is particularly true for an increment of loading at which a sudden softening may occur due to cracking, yielding or substantial non-linear behaviour of concrete in compression. In order to make the modified methods more effective at loading stages at which slow convergence occurs, the stiffness matrix may be updated more than once within the increment. The developed program incorporates a modified Newton-Raphson method, KT2a method, in which the stiffness matrix is updated at 2nd, 12th, 22nd....etc iterations of each increment of loading.

Another difficulty which can occur with the modified Newton-Raphson methods arises due to elastic unloading when stress redistribution takes place during an increment of loading. A possible divergence of the solution may then occur as a result of the elastic unloading [1]. A practical solution may be provided by using the initial elastic constitutive relations throughout the entire analysis.

4.3.1.1 The initial stiffness method

This method is a version of the modified Newton–Raphson methods in which the initial elastic stiffness matrix is maintained throughout the entire analysis. The method was introduced by Zienkiewicz et al [11] for the solution of elasto–plastic problems. It offers a practical solution to some of the problems associated with the modified Newton–Raphson methods such as those that occur due to elastic unloading and the development of ill–conditioned stiffness matrices close to ultimate load.

Because the stiffness matrix is formulated only once for the analysis, the computation cost per iteration is significantly reduced. However, the solution requires many more iterations compared with those required by the previous methods. The relative computational efficiency of the initial stiffness method with respect to the standard and other modified Newton–Raphson methods depends to a large extent on the degree of non–linearity inherent in the problem under consideration.

4.4 Acceleration Schemes

The onvergence characteristics of the modified Newton–Raphson methods can be substantially improved by the inclusion of a suitable acceleration technique. Several schemes have been proposed and introduced for finite element analyses. One such acceleration scheme is Aitken's method [12]. This approach introduces a diagonal matrix, $\underset{\sim}{\alpha}_I^n$, containing acceleration factors. The iterative displacements are

multiplied by the acceleration factors at every other iteration, such that

$$\underset{\sim}{a}^{n}_{i+1} = \underset{\sim}{a}^{n}_{i} + \underset{\sim}{\alpha}^{n}_{i} \quad \delta\underset{\sim}{a}^{n}_{i} \tag{4.9}$$

The acceleration factor for each degree of freedom j is given by

$$\alpha_{i,j} = \frac{\delta a_{i-1,j}}{\delta a_{i-1,j} - \delta a_{i,j}} \tag{4.10}$$

Irons and Tuck [13] proposed a modification to Atiken's scheme in which the acceleration is applied at every iteration. Jennings [14] proposed replacing the diagonal acceleration matrix by scalar which applies equally to all terms of the iterative displacement. Cope et al [15] used the modified Atiken's method proposed by Jennings in the analysis of reinforced concrete slabs and concluded that the procedure did not significantly speed up the convergence of the analysis.

Recently, line searches have been introduced to accelerate convergence for non-linear finite element analyses [10,16-20]. Crisfield [17] showed that the line search techniques can significantly improve the performence of both the modified Newton-Raphson and, to a lesser extent, the secant-Newton methods particularly for problems involving the cracking of concrete. Similar conclusions have been obtained by others for finite element analysis of reinforced concrete structures [1,21-23]. This technique has been incorporated in the present work and a formulation similar to that given by Crisfield [16] is presented in the following

section.

4.4.1 Line Searches

For an increment of loading n, the iterative displacement vector $\delta \underset{\sim}{a}_i$ can be premultiplied by a variable scalar, η_i, termed the step length. Therefore, equation (4.8) may be modified to,

$$\underset{\sim}{a}_{i+1} = \underset{\sim}{a}_i + \eta_i \, \delta \underset{\sim}{a}_i \tag{4.11}$$

If no line search has been activated then the step length parameter is taken as unity.

The idea of applying such a variable step length has long been established in the mathematical programming literature. The concept of the line search is to find the optimum or near optimum value of η_i. Effectively the procsess tries to obtain a stable equilibrium state by choosing a value of η_i such that the residual forces in the next iteration are zero. If a potential energy formulation is used, then the out of balance force vector $\underset{\sim}{r}$ represents the gradient of the total potential energy, Φ,

$$\underset{\sim}{r}(\underset{\sim}{a}) = \frac{\partial \Phi(\underset{\sim}{a})}{\partial \underset{\sim}{a}} \tag{4.12}$$

If $\delta \underset{\sim}{a}_i$ and $\underset{\sim}{a}_i$ of (4.11) are held fixed, an optimum scalar η_i may be obtained by seeking a stationary value of the total potential energy $\Phi_{i+1}(\underset{\sim}{a}_{i+1})$ with respect to the variations in the scalar η_i. Hence by making use of (4.11) and (4.12),

$$\frac{\partial \Phi_{i+1}}{\partial \eta_i} = \frac{\partial \Phi_{i+1}}{\partial \underset{\sim}{a}_{i+1}} \frac{\partial \underset{\sim}{a}_{i+1}}{\partial \eta_i} = \underset{\sim}{r}(\underset{\sim}{a}_{i+1})^T \, \delta \underset{\sim}{a}_i - s_i(\eta_i) = 0 \qquad (4.13)$$

The above expression can be satisfied by recalculating the residual force vector $\underset{\sim}{r}(\underset{\sim}{a}_{i+1})$ for various values of η_i. This is a rather expensive procedure since it requires frequent recalculations of the out of balance forces for each trial. Therefore instead of obtaining the exact solution of (4.13), it is more desirable to satisfy the approximate condition

$$| \, s_j(\eta_{i,j}) \, | \; < \; \psi \; | \, s_0(\eta_{i,0}) \, | \qquad (4.14)$$

where

$$s_0 = s_0(\, \eta_{i-0} \,) = \delta \underset{\sim}{a}_i^T \, \underset{\sim}{r}(\underset{\sim}{a}_i) \qquad (4.15)$$

In the above expression, $\underset{\sim}{r}(\underset{\sim}{a}_i)$ is the out of balance force vector at the end of the previous iteration, i and j refer to the global solution iteration and line search trial numbers respectively and ψ is a tolerance given by,

$$0.0 \; < \; \psi \; < \; 1.0 \qquad (4.16)$$

It is expected that when a small value of ψ is used, the number of line search trials will increase and the number of iterations decreases. Crisfield [16] has indicated that a relatively slack tolerance ($\psi \cong 0.8$) is optimum, in terms of computation time, for the modified Newton–Raphson methods.

The approximate criterion (4.14) is likely to be satisfied by the

first trial value of the step length factor, $\eta_{i,1}$, which is usually taken as unity. However if equation (4.14) is not immediately satisfied, subsequent trials are performed to evaluate the step length using a linear interpolation (or extrapolation) of the form

$$\frac{\eta_{i,j+1}}{\eta_{i,j}} = \frac{-s_0}{s_j - s_0} \tag{4.17}$$

If $\eta_{i,j+1}$ is greater than $\eta_{i,j}$ the procedure involves extrapolation which may lead to an overestimation of the displacements. A maximum value of 10 has been used for the step length in the present work. On the other hand, if $\eta_{i,j+1}$ was very small the change in the displacement would also be small and this will prevent the iterative procedure from making any progress. A minimum value of 0.1 has therefore been adopted for the step length throughout the present study [16]. The maximum number of line search trials allowed in an iteration is three, after which the line search routine is abandond for the current iteration. The analysis then proceeds to the next iteration.

4.5 Convergence Criteria

In the incremental iterative solution strategy, the progress of the iterative procedure is monitored with reference to a specified convergence criterion. Convergence is assumed to occur when the difference between the external and internal forces has reached an acceptably small value and the iterative process is then terminated. Accuracy of the approximate solution is usually specified by

selecting a suitable convergence tolerance. If the convergence tolerance is too loose, inaccurate results may obtained and if the tolerance is too tight, additional computation effort is spent to obtain needless accuracy.

For non-linear structural analyses, several convergence criteria can be used to monitor equilibrium. These criteria are usually based on out of balance forces, displacements or internal energy. Details of various kinds of criteria are reviewed in [1]. The convergence criteria adopted are based on the Euclidean norm and may generally written in the form

$$\frac{\| \underset{\sim}{x} \|}{\| \underset{\sim}{y} \|} \times 100\% \leq \text{TOLER} \tag{4.18}$$

where

$$\| \underset{\sim}{x} \| = (\underset{\sim}{x}^T \underset{\sim}{x})^{\frac{1}{2}}, \tag{4.19}$$

$$\| \underset{\sim}{y} \| = (\underset{\sim}{y}^T \underset{\sim}{y})^{\frac{1}{2}} \tag{4.20}$$

and TOLER is a specified convergence tolerance. For the force based criterion, the norms refer to the out of balance force and the external applied load vectors such that

$$\underset{\sim}{x} = \underset{\sim}{r}_i \tag{4.21}$$

$$\underset{\sim}{y} = \underset{\sim}{f} \tag{4.22}$$

while for the displacement based criterion they refer to the displacement vectors as,

$$\underset{\sim}{x} = \delta \underset{\sim}{a}_i \tag{4.23}$$

$$y = \underset{\sim}{a}_i \tag{4.24}$$

An internal energy based convergence criterion was introduced by Bathe and Cemento [24] and was used by Cope and Rao [25] in the analysis of reinforced concrete slabs. In this criterion, the amount of work done during an iteration by the residual forces and the iterative displacements can be compared with the initial value of that particular increment. Thus, convergence can be assumed to occur when

$$\frac{| \underset{\sim}{r}_i^T \delta \underset{\sim}{a}_i |}{| \underset{\sim}{r}_1^T \delta \underset{\sim}{a}_1 |} \times 100\% \leq \text{TOLER} \tag{4.25}$$

In the present work, a force convergence criterion has been adopted. This type of criterion is favored because it monitors directly the redistribution of the out of balance forces. Accuracy of the solution is specified by setting the convergence tolerance to an acceptable limit. Convergence tolerances ranging form 1% to 5% have been used for the different numerical examples presented in the following three Chapters.

4.6 Analysis Termination Criteria

The non-linear finite element analysis must be provided with criteria to detect failure of the solution. In the physical tests under load control, collapse of a structure takes place when no further loading can be sustained. This is usually indicated in the numerical tests by successively increasing iterative displacements and a continuous growth in the dissipated energy. Hence, convergence of the iterative procedure can not be achieved and therefore it is necessary to specify suitable criteria to terminate the analysis and save wasting computation effort.

Several criteria have been suggested to terminate the numerical analysis [1] for example setting a limiting value to the maximum deflection, specifing the maximum number of iterations, setting a limit to the growth of the dissipated energy or the use of the current stiffness parameter proposed by Bergan et al [26]. Satisfaction of any of these criteria indicates the failure of the non-linear solution procedure rather than the failure of the structure being analysed. In some cases, careful study of the numerical results by comparing them with any available theoretical or experimental results is necessary. When the numerical solution indicates unrealistic results, it may be useful to restart the analysis using a refined or a different solution strategy.

In the present study, the non-linear analysis is terminated when the stiffness matrix is no longer positive definite, a steel bar has fractured, excessive concrete crushing at sampling points has taken place, the number of loading increments exceeds a preselected number

or the number of iterations is greater than the specified maximum number. The later criterion is not always sufficient to indicate failure because the specified maximum number of iterations may be exceeded while the solution is converging slowly. This may take place when a sudden softening has occurred due to extensive cracking or yielding, a very tight convergence tolerance has been selected or a large increments of loading has been used. In these situations, an adequately large maximum number of iterations must be selected.

4.7 Outline of the Computer Program

One of the aims of the present work was to develop a numerical tool suitable for three dimensional-finite element analysis of reinforced concrete structures under monotonically increasing loads. The computer program 3DNFEA has been written for this purpose. The program makes use of some of the standard NAGFE level 0 [27] subroutines. The main aspects of the program are given below. A more detailed description is available in reference [28].

1. Main objective

The main objective of the computer program 3DNFEA is to analyse non-linear reinforced concrete, or steel, members under general three-dimensional states of loading up to failure. A special emphasis is given to the analyses of beams under torsion.

2. Concrete representation

Concrete is simulated by brick elements. The following isoparametric elements are incorporated in the program

(a) The 8 noded linear element.

(b) The 20 noded quadratic element.

(c) The 32 noded cubic element.

3. Reinforcement representation

Reinforcing bars are simulated as axial members embedded in the brick elements. It should be noted that the discrete representation of reinforcement is a special case of the embedded representation in which the bars are embedded along the boundaries of the brick elements.

4. Integration rules used

The following integration rules have been implemented in the program

(a) The 27 (3x3x3) Gauss-quadrature rule.

(b) The 8 (2x2x2) Gauss-quadrature rule.

(c) The 14 sampling Gauss type point rule.

(d) The 15a sampling Gauss type point rule.

(e) The 15b sampling Gauss type point rule.

5. Material non-linearites

The material non-linearites considered in the program are due to cracking and crushing of concrete, yielding of reinforcement bars and the plastic deformation of the concrete and the reinforcement. A special emphasis is placed in modelling the reduction of the concrete compressive strength in the presence of orthogonal cracking.

6. Non-linear solution algorithms

The following incremental iterative solution algorithms are incorporated in the program

(a) The standard Newton-Raphson method.

(b) The modified Newton-Raphson method in which the stiffness matrix is updated at the first iteration of each increment of loading, the KT1 method.

(c) The modified Newton-Raphson method in which the stiffness matrix is updated at the second iteration of each increment of loading, the KT2 method.

(d) The modified Newton-Raphson method in which the stiffness matrix is updated at the 2nd, 12th, 22nd..... iterations of each increment of loading, the KT2a method.

(e) The initial stiffness method.

Line searches may be optionally activated in each of the solution algorithms considered. The solution of the banded set of algebraic equilibrium equations is carried out using the Cholesky factorisation technique [27].

7. Loading schemes

The computer program employs a load incrementation scheme with the size of loading increment being specified by the user. In finite element analyses, the external loads are simulated by a set of equivalent nodal forces. For simple cases of loading such as gravity load or uniformly distributed loads, the equivalent nodal forces can be easily determined. However for complex loading, for example torsion, the nodal loads should be distributed amongst the nodes of the loaded section in a proper manner. The proportions of the nodal loads must represent the same configuration of shear stresses those induced by the original torque. An iterative scheme has been developed to predict the proper distribution of the nodal loads equivalent to an elastic torque. The scheme is described in section 5.4. A special subroutine has been written for this purpose.

8. Convergence criteria

The following criteria are available in the program to monitor convergence of iterative procedure.

(a) Force convergence criterion.

(b) Displacement convergence criterion.

The former criterion has been used for the numerical examples carried out in this work.

9. Termination of the analysis

The finite element analysis is terminated when any of the following criteria is satisfied.

(a) The stiffness matrix is no longer positive definite.

(b) A reinforcing bar has been fractured.

(c) Excessive concrete crushing takes place.

(d) The number of increments exceeds a maximum specified number.

(e) The number of iterations exceeds a maximum specified number.

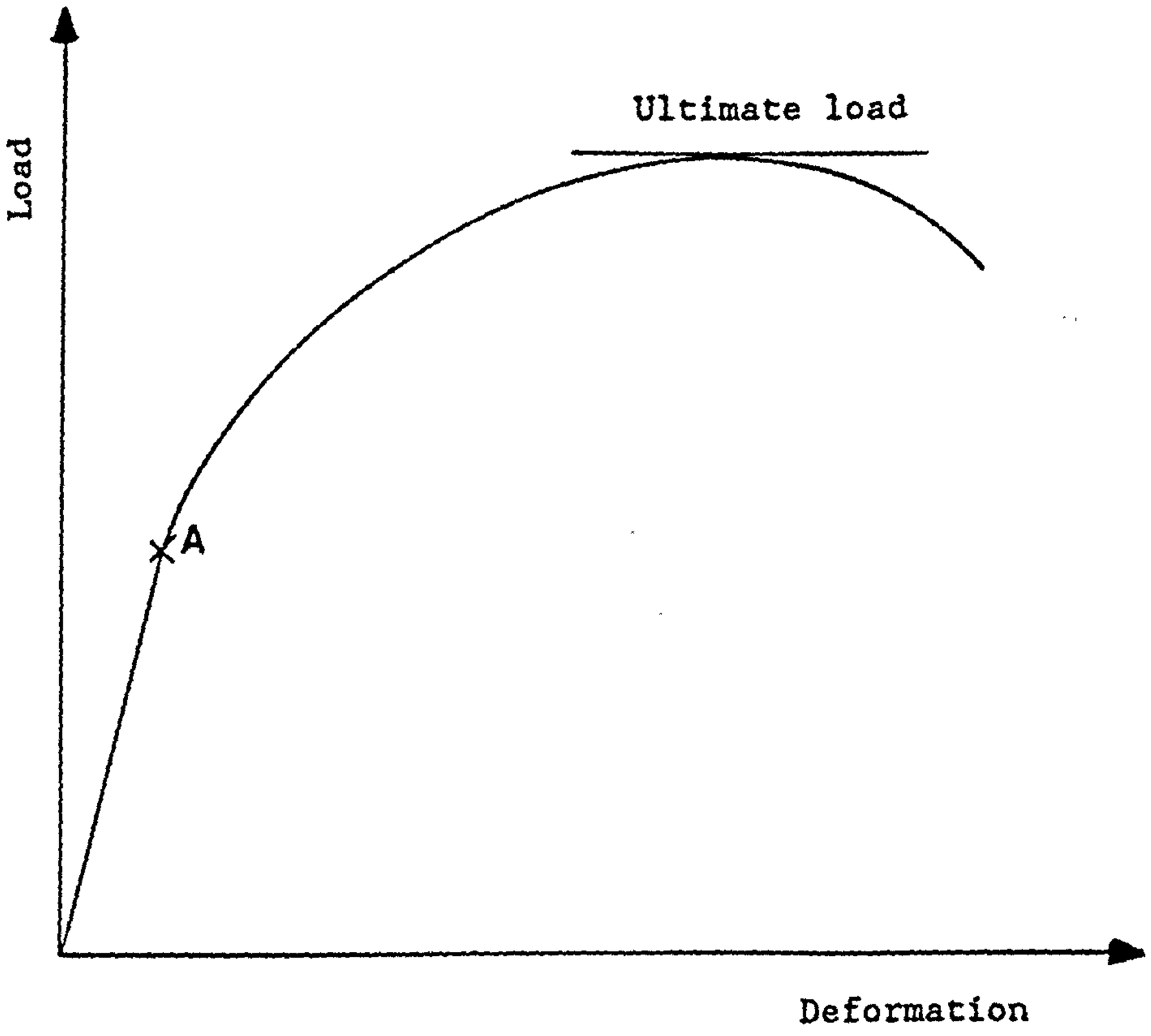

Fig. 4.1 Typical structural response of a reinforced concrete member.

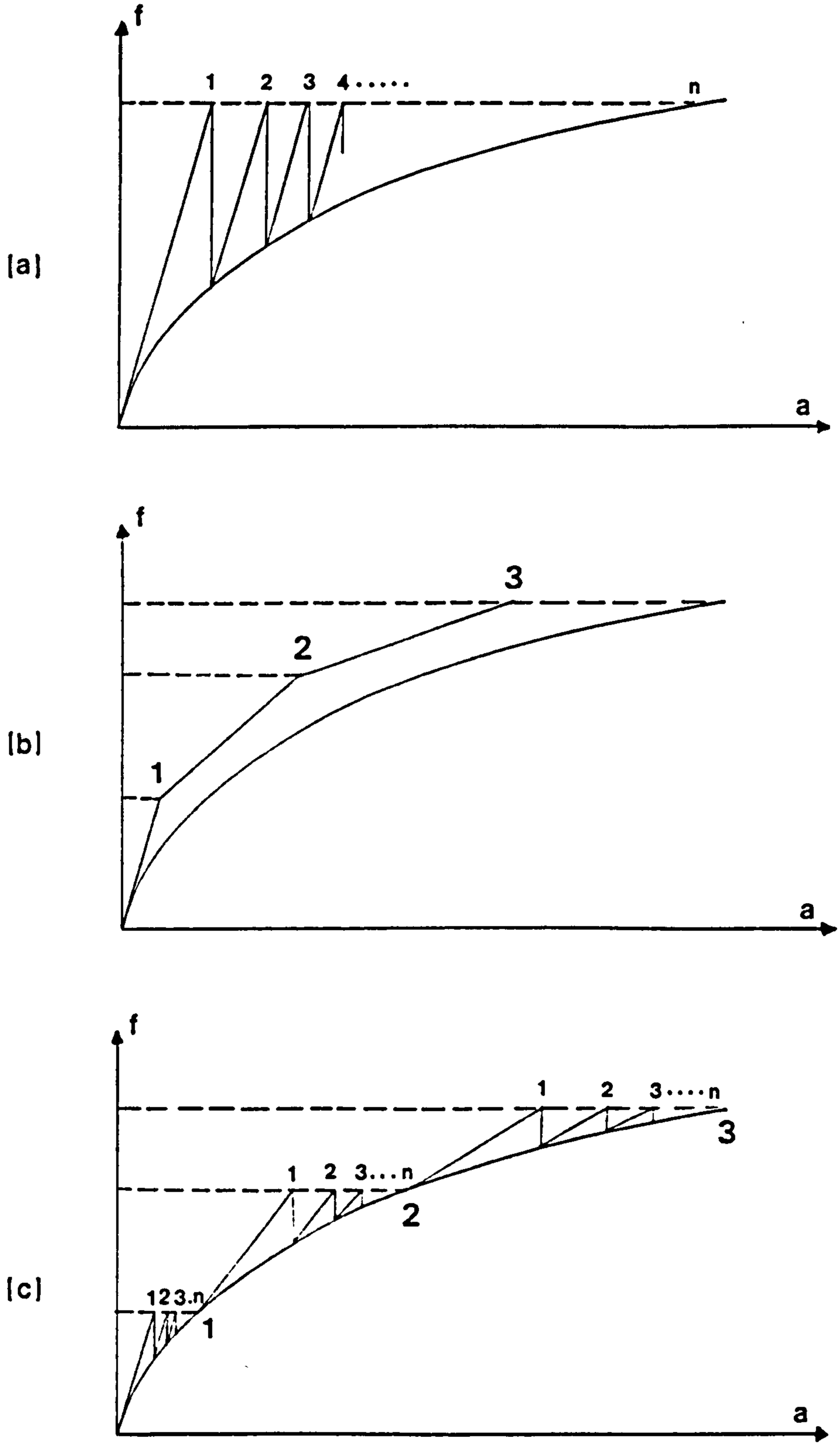

1,2,3.. Iterations 1,2,3.. Increments

Fig. 4.2 Basic techniques for the solution of non-linear equations: a)Iterative, b)Incremental, c)Incremental -iterative.

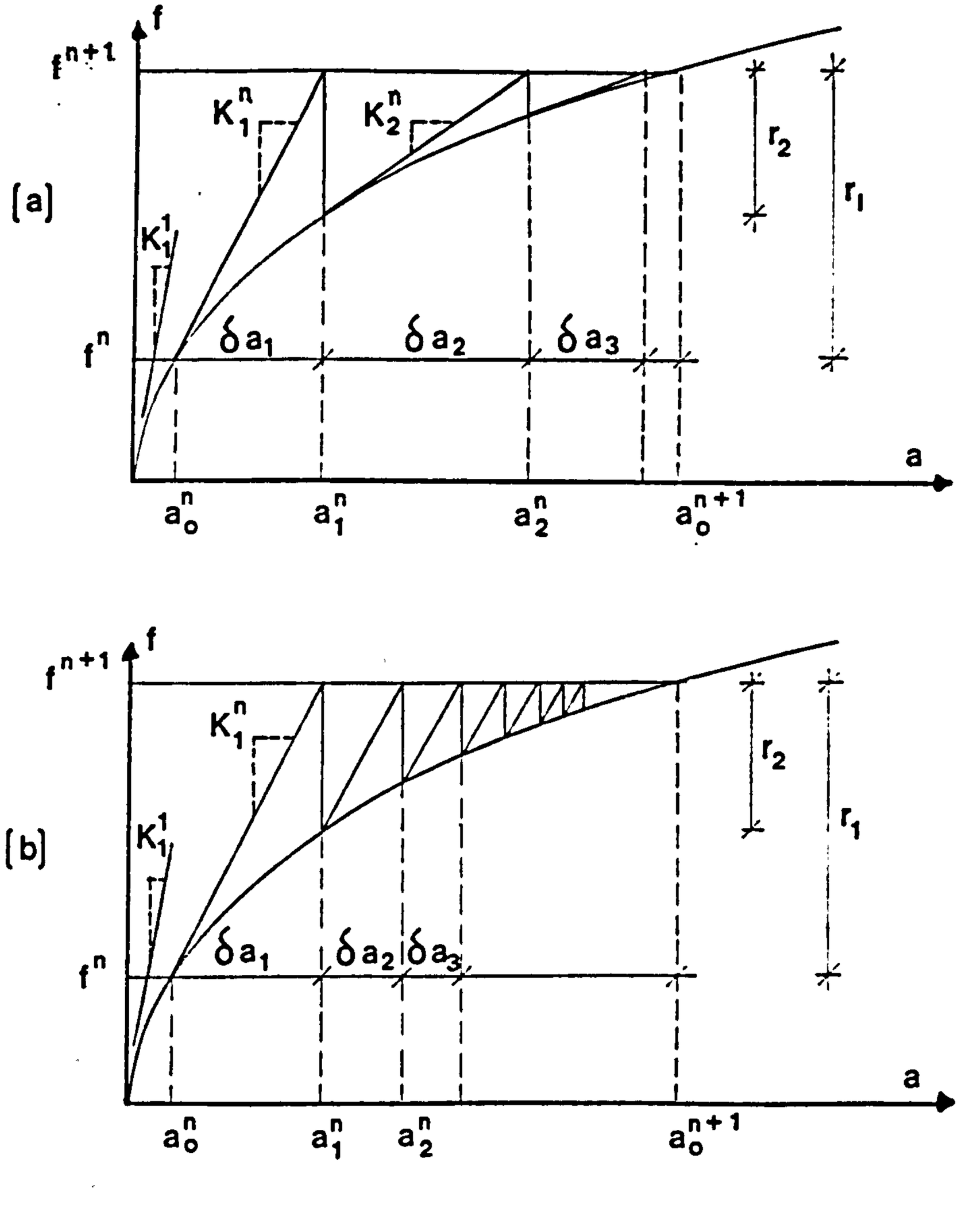

Fig. 4.3 Standard and modified Newton–Raphson procedures, one degree of freedom case: a) Standard Newton–Raphson method, b) M.N.R method (KT1), c) M.N.R method (KT2).

REFERENCES

1. Abdel-Rahman, H.H., "Computational Models for Non-Linear Analysis of Reinforced Concrete Flexural Slab Systems", Ph.D. Thesis, University of Wales, Swansea, 1982.

2. Zienkiewicz, O.C., "The Finite Element Method", McGraw-Hill Book Company, New York, 1977.

3. Owen, D.R.J. and Hinton, E., "Finite Elements in Plasticity-Theory and Practice", Pineridge Press, Swansea, 1980.

4. Bathe, K.J., "Finite Element Procedures in Engineering Analysis", Prentice-Hall, Inc, 1982.

5. Broyden, C.G., "Quasi-Newton Methods and their Application to Function Minimisation", Maths. Comput., Vol. 21, 1967, pp. 368-381.

6. Dennis, J.E and More, J., "Quasi-Newton Methods - Motivation and Theory", SIAM Rev., Vol. 19, 1977, pp. 46-89.

7. Matthies, H. and Strang, G., "The Solution of Non-Linear Finite Element Equations", Int. J. for Num. Meth. in Eng., Vol. 14, 1979, pp. 1613-1626.

8. Crisfield, M.A., "Iterative Solution Procedures for Linear and Non-Linear Structural Analysis", TRRL Report LR900, Transport and Road Research Laboratory, Crowthorne, England, 1979.

9. Crisfield, M.A., "A Faster Modified Newton-Raphson Iteration", Comput. Meth. in Appl. Mech. and Eng., Vol. 20, 1979, pp. 267-278.

10. Crisfield, M.A., "Incremental/Iterative Solution Procedures for Non-Linear Structural Analysis", Numerical Methods for Non-Linear Problems, Vol. 1, Eds. Taylor, C., Hinton, E., and Owen, D.R.J., Pineridge Press, Swansea, 1980, pp. 261-290.

11. Zienkiewicz, O.C., Vallippan, S. and King, I.P., "Elasto-Plastic Solutions of Engineering Problems 'Initial Stress' Finite Element Approach", Int. J. for Num. Meth. in Eng., Vol. 1, 1969, pp. 75-100.

12. Aitken, A.C., "On the Iterative Solution of System of Linear Equations", Proc. Royal. Soc. Edinburgh Vol. 63, 1950, pp. 52-60.

13. Irons, B. and Tuck, R., "A Version of the Aitken Acceleration for Computer Iteration", Int. J. for Num. Meth. in Eng., Vol 1, 1969, pp. 275-277.

14. Jennings, A., "Accelerating the Convergence of Matrix Iterative Processes", J. Inst. Math. Appls., Vol. 8, 1971, pp. 99-110

15. Cope, R.J., Rao, P.V. and Edwards, K.R., "Non-Linear Finite Element Analysis Techniques for Concrete Slabs", Numerical

Methods for Non-linear Problems, Vol. 1, Eds. Taylor, C., Hinton E. and Owen D.R.J., Pineridge Press, Swansea, 1980, PP. 445-456.

16. Crisfield, M.A., "Variable Step-Lengths for Non-linear Structural Analysis", TRRL Report. LR1049, Transport and Road Research Laboratory, Crowthorne, England, 1982.

17. Crisfield, M.A., "Acceleration Solution Techniques and Concrete Cracking, Comput. Meth. in Appl. Mech. and Eng., Vol. 33, 1982, pp. 585-607.

18. Hinton, E. and Abdel Rahman, H.H., "Non-Linear Solution Algorithms for Reinforced Concrete Plates", Proc. of the 6th Int. Conf. on Struct. Mech. in Reactor. Tech., Paris, M3/4, 1981.

19. Irons, B. and Elsawaf, A.F., "The Congjugate-Newton Algorithm for Solving Finite Element Equations", Proc. U.S.-German Symp. on Formulations and Algorithms in the Finite element Analysis, Eds. Bathe, K.J., Oden, J.T. and Wunderlich, W., MIT, 1977, pp. 656-672.

20. Elsawaf, A.F., "The Conjugate-Newton Method for Non-Linear Finite Element Problems", Ph.D. Thesis, University of Calgary, Canada, 1979.

21. Ganaba, T.H., "Non-Linear Finite Element Analysis of Plates and Slabs", Ph.D. Thesis, University of Warwick, 1985.

22. Kent, A.J., "Finite Elements for the Analysis of Reinforced Concrete Shell Structures with Geometric and Material Non-Linearities", Ph.D. Thesis, University of Wales, Swansea, 1987.

23. Naji, J.H., "Non-Linear Finite Element Analysis of Reinforced Concrete Panels and Infilled Frames under Monotonic and Cyclic Loading", Ph.D. Thesis, University of Bradford, 1989.

24. Bathe, K.J. and Cimento, A.P., "Some practical Procedures for Solution of Non-Linear Finite Element Equations", Comput. Meth. in Appl. Mech. and Eng., Vol. 22, 1980, pp. 59-85.

25. Cope, R.J. and Rao, P.V., "Non-Linear Response of Reinforced Concrete, Skewed, Slab Bridges, Research Report, Dept. Civil Eng., University of Liverpool, 1981.

26. Bergan, P.G., "Solution Algorithms for Non-Linear Structural Problems", Computer and Structures, Vol. 12, 1980, pp. 497-510.

27. NAGFE Library, Level 0, The Science and Engineering Research Council, Documentation, 1980.

28. Al-Shaarbaf, I.A.S and May, I.M., "3DNFEA, A Non-Linear Finite Element Program for Three-Dimensional Analysis of Reinforced Concrete Structures, Research Report No. 34, Dept. of Civil and Struct. Eng., University of Bradford, 1990.

CHAPTER FIVE

ANALYSIS OF ELASTO-PLASTIC TORSION OF HOMOGENEOUS MEMBERS

5.1 Introduction

This Chapter deals with the problem of torsion of homogeneous solid members with an elasto-plastic material constitutive relationship. For such members, the following three stages of behaviour occur as the torque is increased [1,2].

1. The elastic stage in which all the material in any typical cross-section of the member is elastic.
2. The elasto-plastic stage in which part of the cross-section is plastic and the remainder is elastic.
3. The plastic stage in which all the material in the cross-section can be assumed to deform plastically.

In the elasto-plastic stage of behaviour, the positions of the boundaries between the elastic and the plastic zones of a typical cross-section move with changes in the magnitude of the torque and therefore theoretical torque-twist relationships are difficult to obtain. For this reason, the exact expressions and the approximate analytical solutions have only been obtained for prismatic members with relatively simple cross-sections [1]. Thus, it is necessary to resort to numerical methods for other cases and this Chapter describes the implementation of the finite element method for elasto-plastic members under torsion. Therefore, the main objectives

of this study are:

1. To investigate the validity and accuracy of the proposed three-dimensional finite element model for the elasto-plastic behaviour of members subjected to pure and warping torsion.
2. To conduct some numerical tests for problems in which the comparisons with the analytical solutions are possible in order partly to test the Author's computer program.
3. To carry out parametric studies to investigate the effects of warping restraint, different types of finite elements, different integration rules and mesh refinement.

Although the numerical examples analysed are prismatic beams of simple cross-sections subjected to torsion, the computer program could be used for non-prismatic members of irregular as well as regular cross-sections subjected to general states of loading.

The available exact solutions for members under pure torsion which are related to the selected tests are outlined in section 5.2. In section 5.3 the numerical examples chosen for investigation are summarised. An iterative scheme has been proposed to predict an improved distribution of the external applied nodal loads equivalent to the required torque. This scheme is illustrated in section 5.4. In section 5.5, numerical results for members under pure torsion are compared against the analytical solutions. A comparison of the accuracy and efficiency of different integration rules has been made and the performance of different isoparametric brick elements has been examined. Results of numerical tests carried out for I-section

cantilever beams with and without warping restraint are illustrated.

5.2 Theoretical Relationships for Pure Torsion

In the case of a prismatic bar subjected to pure torsion, Fig. 5.1, one end of the member is assumed to be restrained against rotation in the xy plane and the other end is acted upon by a couple to produce the required torque. Both ends are free to move in the z direction. For a typical cross-section of the twisted bar, the displacements in the elastic and the inelastic regions are assumed to consist of a rotation of the cross-section about the z-axis which will be directly proportional to its distance from the restrained end, and a longitudinal warping of the section which will be same for every cross-section. Therefore, the displacements of the twisted bar take the form:

$$u = -\theta\, y\, z$$

$$v = \theta\, x\, z \qquad (5.1)$$

$$w = \theta\, \psi(x,y)$$

where θ is the angle of twist per unit length of the member and $\psi(x,y)$ is the warping function.

For the elastic stage of behaviour, the torque-rotation relationship and the warping displacement expression have been obtained for various cross-sections using Saint-Venant's semi inverse

method. However, such a relationship has been only obtained for circular and narrow rectangular cross-sections for the elasto-plastic stage of behaviour [1]. The fully plastic torque of the cross-sections may be easily calculated using the sand heap analogy.

5.2.1 Elastic Torsion

For elastic pure torsion of prismatic members of different solid cross-sections, exact torque-twist relationship and the expression of the warping displacement, w, may be found in many texts [3-5]. These relationships for a member of rectangular cross-section are:

$$T_e = \frac{G\theta b^3 h}{3}\left\{1 - \frac{192b}{\Pi^5 h}\sum_{n=1,3,5,..}^{\infty}\frac{1}{n^5}\tanh\frac{n\Pi h}{2b}\right\} \qquad (5.2)$$

where T_e is the applied elastic torque and b and h are the width and the depth of the cross-section, and

$$w = \theta\left\{xy - \frac{8b^2}{\Pi^3}\sum_{n=1,3,5,..}^{\infty}(-1)^{(n-1)/2}\sin\frac{n\Pi x}{b}\frac{\sinh\frac{n\Pi y}{b}}{n^3\cosh\frac{n\Pi h}{2b}}\right\} \qquad (5.3)$$

For a circular member, the theoretical torque-rotation relationship is given by [1],

$$T_e = \frac{\Pi\, r^4\, G\, \theta}{2} \qquad (5.4)$$

where r is the radius of the cross-section.

5.2.2 Elasto-Plastic Torsion

The exact elasto-plastic torque-rotation relationship of a twisted member has been obtained for a circular shaft [6]. By using the Von-Mises yield criterion and assuming a linear work hardening material, the elasto-plastic torque, T_{ep}, can be expressed as:

$$T_{ep} = \frac{2G\sigma_y r^3}{E} \left\{ \frac{\Pi\beta}{4} - \sqrt{3}\,\Pi \left[\frac{A}{4}(1-\rho^4) + \frac{B}{3}(1-\rho^3) \right] \right\} \qquad (5.5)$$

where $$\beta = \frac{\theta\, r\, E}{\sigma_y}, \qquad (5.6)$$

$$A = \frac{\sqrt{3}\,\beta\, E}{3+2(1+\upsilon)H'}, \qquad (5.7)$$

$$B = -\frac{2(1+\upsilon)E}{3+2(1+\upsilon)H'} \text{ and} \qquad (5.8)$$

$$\rho = \frac{2(1+\upsilon)}{\sqrt{3}\,\beta} \qquad (5.9)$$

where σ_y is the yield stress

5.2.3 Fully Plastic Torsion

The collapse torque of cross-sections with a perfectly plastic material can be calculated using the sand heap analogy. For a rectangular cross-section the fully plastic torque, T_p, is given by:

$$T_p = \left\{ \frac{1}{2} - \frac{b}{6h} \right\} b^2 h \frac{\sigma_y}{\sqrt{3}} \qquad (5.10)$$

And for an I-section, the collapse torque is expressed as:

a) when $b_w \leq h_f$

$$T_p = \left\{ 2h_f^2 b \left[\frac{1}{2} - \frac{h_f}{6b} \right] + \frac{1}{2} b_w^2 \left[h - 2h_f + \frac{b_w}{3} \right] \right\} \frac{\sigma_y}{\sqrt{3}} \qquad (5.11)$$

b) when $b_w \geq h_f$

$$T_p = \left\{ b_w^2 h \left[\frac{1}{2} - \frac{b_w}{6h} \right] + h_f^2 \left[b - b_w \right] \right\} \frac{\sigma_y}{\sqrt{3}} \qquad (5.12)$$

where h_f and b_w are the thicknesses of the flange and the web respectively, b is the width of the flange and h is the hight of the section

5.3 Numerical Examples

Prismatic segments of square, rectangular, circular and I cross-section have been analysed. The various characteristics and the

variables isolated for each beam segment are listed in Tables 5.1 and 5.2. The equivalent uniaxial stress–strain relationships used in the numerical tests for both tension and compression stresses are presented in Fig. 5.2. The different finite element meshes of the beam segments are shown in Figs. 5.3 and 5.4.

In beams subjected to pure torsion, all the nodes at one end are assumed to be fully restrained in the x and the y directions and the nodes along the centre lines of the cross section are also restrained in the z direction. These boundary conditions are consistent with the requirements of equations (5.1). The other end of the member is loaded by a set of equivalent nodal loads which produce the required external torque. An iterative procedure, described in the next section, has been proposed to determine the proper distribution of the applied loads on the nodes at the free end prior to the analysis [7]. By making use of symmetry, only one quarter of the beam has to be analysed. The boundary and the symmetry conditions imposed at the fixed end and at a typical cross–section are shown in Fig. 5.5 for beam S1.

For the beams with warping restraint, similar boundary, symmetry and loading conditions have been implemented apart from the condition that all the nodes at the fixed end are fully restrained in all directions.

All the numerical tests have been carried out using the modified Newton–Raphson method in which the stiffness matrix is updated at the second iteration of each increment of loading. A convergence tolerance of 1% has been adopted. Line searches have been

Table 5.1 Outline of numerical tests for square members

Cross-section	Beam Designation	Finite element mesh	Integration rule	Type of element	Variables isolated				
					Mesh refinement	Integration rule	Segment lenght	Aspect ratio	Element type
Square	S1	1	27	20 noded quadratic	*	*	*	*	*
	S2	2	27		*				
	S3	1	14			*			
	S4	1	15a			*			
	S5	1	15b			*			
	S6	1	8			*			
	S7	3	27				*		
	S8	4	27					*	
	S9	1	27	8 noded linear					*
	S10	5	27						*
	S11	1	27	32 noded cubic					*

Table 5.2 Outline of numerical tests for rectangular, circular and I members

Cross-section	Beam Designation	Finite element mesh	Integration rule	Type of element	Variables isolated		
					Mesh refinement	Integration rule	Fixed end boundary conditions
Circle	C1	8	27	20 noded quadratic	*		
	C2	9	27		*		
Rectangle	R1	6	27		*		
	R2	7	27		*		
I	I1	10	27			*	pure torsion
	I2	11	15b			*	warping torsion
	I3	10	27			*	pure torsion
	I4	11	15b			*	warping torsion

implemented in all the numerical tests to accelerate convergence. The Von-Mises yield criterion has been used to monitor the stress level at the onset of plastic deformations. It should be noted that this yield criterion represents a special case of equation (3.19) in which $\beta = 1.0$ and $\alpha = 0.0$ such that

$$(3 J_2)^{\frac{1}{2}} = \sigma_0 \qquad (5.13)$$

5.4 Equivalent Nodal Loads for Elastic Pure Torque

In a finite element analysis, general states of loading have to be represented by an equivalent set of nodal forces. In the case of an external torque these forces should be distributed amongst the nodes of the free end in such a way as to provide the same configuration of shear stresses as those induced by the original torque. In an analysis in which the loading is simple, for example a gravity load or a uniformly distributed load, the equivalent nodal forces can be easily determined [8,9]. However, in the case of torsion and other complex loadings it is difficult to do this. In the torsion case, the distribution of shear stresses at the loaded section, the free end, is a function of the assumed displacement field, number and position of elements within the section and the displacement values at their nodes. Hence, the relative distribution of nodal loads amongst the nodes of the loaded section is difficult to obtain. Applying the nodal loads in proportions other than the correct ones will lead to an incorrect distribution of stresses especially in the region adjacent to the loaded section. If the member modelled is reasonably long, the distribution of stresses at

sections away from the loaded end will depend only on the magnitude of the torque, and tend to be correct. In contrast, if only a small segment of the beam is considered in the finite element analysis, in order to minimise the computation time and the memory requirements, the proper simulation of nodal loads becomes of great importance.

An iterative scheme has been used in the present work to determine the proper distribution of nodal loads corresponding to elastic pure torque. The procedure is based on the fact that the restrained end represents a section remote from the loaded end, therefore the reaction forces at the nodes of the restrained end are a better estimate of the correct loads than the corresponding nodal loads at the free end. When the applied loads are correct then the corresponding reaction forces at the restrained end will have the same magnitude and opposite directions. The iterative scheme is illustrated by the following steps.

a) A set of nodal loads is applied at the free end such that the resulting torque equals the required applied torque. In general the distribution of the nodal loads will not be the correct one.

b) The reactions corresponding to the above loading at the fixed end are determined using the finite element analysis.

c) The reactions are then used as a new set of nodal loads at the free end.

d) Steps b and c are then repeated until the difference between each nodal force and the corresponding reaction is negligibly small.

The scheme has been carried out for each beam analysed prior to the non-linear finite element analysis and the resulting set of nodal loads are then applied as the external torque. As an example, three different sets of nodal loads for the external applied couple for beam S1 are shown in Figs. 5.6a, 5.6b and 5.6c. All these models converge, after applying the iterative scheme, to the proportions shown in Fig. 5.6d. Figs. 5.7a and 5.7b show the variation of the ratio of the computed angle of twist to the theoretical elastic angle of twist, equation (5.2), along the beam length for each of the loading patterns considered. The result for model D, Fig. 5.6d, coincides with the exact elastic solution in which the angle of twist per unit length is constant throughout the beam length.

5.5 Numerical Results

Numerical tests involving beam segments with simple shapes subjected to torsion were conducted to check the validity of the proposed finite element model. The outline of the numerical tests is illustrated in Tables 5.1 and 5.2. The numerical results and the parametric study carried out are discussed in sections 5.5.1 and 5.5.2 for the cases of pure and warping torsion respectively.

5.5.1 Elasto-Plastic Pure Torsion

In members under pure torsion, the stress distribution is constant along the beam length and hence a small segment of the beam is adequate to conduct the analysis provided that the relative

distribution of the applied nodal loads at the loaded end is correct. Discussion of the numerical results and the effects of the different parameters considered in the finite element analyses are illustrated in the following sections.

5.5.1.1 Effect of mesh refinement

The finite element solutions are shown in Figs. 5.8 and 5.9 for the square and the rectangular beam segments respectively. The ratio of the applied torque to the theoretical maximum elastic torque is plotted against the ratio of the computed angle of twist to the theoretical maximum elastic angle of twist. The analytical solution proposed by Smith and Sidebottom [1] is indicated in the figures as a solid line; the fully plastic torque obtained by Nadai's sand heap analogy, equation (5.10), is also indicated. All the numerical results are in a good agreement with the analytical solution. The relatively better result, with a softer response, in the elasto-plastic stage of behaviour is achieved by using a more refined mesh, beams R2 and S2, Figs. 5.8 and 5.9. In these beams the position of the outer row of sampling points is closer to the beams surface, and hence the onset of yielding is picked up at an earlier stage than in beams S1 and R1.

Finite element analyses have also been carried out for a circular shaft with a linear work hardening material. The numerical results plotted in Fig. 5.10 for beams C1 and C2 coincide with the exact torque-twist relationships expressed by equations (5.4) and (5.5) for the elastic and the elasto-plastic stages respectively. The effect

of the mesh refinement is insignificant in this particular case because no warping displacement occurs in a circular cross-section.

5.5.1.2 Effect of the integration rule

The accuracy of the different integration rules is shown in Fig. 5.11. Results for the 27 sampling point rule and the three 15 sampling point rules are in a good agreement with the analytical solution. When the 8 sampling point rule was used, the beam S6 remained elastic until the applied torque was about 1.4 times the maximum elastic torque, Fig. 5.11a, because of the positions of the sampling points. Then, because yielding took place at a large number of sampling points in the same increment of loading, a sudden change in torque-rotation relationship occurred. Better results could be achieved by using a finer mesh. The relative CPU. times were 4.4, 2.2, 2.8, 2.5 and 1.0 for the 27, 14, 15a, 15b and the 8 point rules respectively. In order to make the comparison as accurate as possible, CPU time of each test has been recorded at the end of the last converged increment of loading. The difference in CPU. times between the 14 and the 15a point rule is because the later rule has sampling points on the element surface and hence the non-linear behaviour was picked up at a relatively early stage and hence an increase in the run time occurred.

5.5.1.3 Effect of the segment length

To study the influence of the segment length used in the pure

torsion tests, the total length of beam S1, mesh 1, is doubled in the segment S7, mesh 3. The numerical results ploted in Fig. 5.12 for both beams are almost the same. Therefore, the small segment of beam S1 is adequate to simulate the problem and carrying out the finite element analyses. This is due to the use of the proper representation of the nodal loads illustrated in section 5.4. Although the distribution of the applied loads is referred to an elastic torsion, the torque-rotation curve during the elasto-plastic stage of behaviour is still close to the analytical solution, Fig. 5.12.

5.5.1.4 Effect of the aspect ratio

The influence of the element aspect ratio has been studied by comparing the torque-twist relationships of beam S1 and beam S8. The ratio of the element dimensions of the former beam is 1:1:2, mesh 1, and for the later the ratio is 1:1:4, mesh 4. Numerical results for both beams are almost identical, Fig. 5.13. This is because the angle of twist per unit length of the beam is constant and the distribution of the warping displacement is the same for all the cross-sections of the segment considered in the analysis.

5.5.1.5 Effect of the element type

In order to study the performance of the 20 noded quadratic brick element used throughout the present study, numerical tests using the 32 noded cubic brick element and the 8 noded linear brick

element also have been conducted. Details of the shape functions for these elements can be found in most finite element texts [9,10]. The finite element solutions for a square segment using the same finite element mesh, mesh 1, are shown in Fig. 5.14 for each type of element. The torque–rotation relationship obtained for both the cubic element, beam S11, and the quadratic element, beam S1, are similar and are in good agreement with the analytical solution when compared with the over stiff behaviour of the linear element, beam S9.

In beam S9, all the nodes within a typical cross-section are located at points where the value of the warping displacement is zero. Therefore, this beam deformed as if it was restrained against the warping displacement. To demonstrate this argument, the distribution of the elastic warping along the edge of a typical cross-section of the square segment considered is shown in Fig. 5.15 for each type of element together with the exact expression given by equation (5.3).

A comparison between the performance of the 20 noded element and the 8 noded element based on an approximately equal total number of degrees of freedom has been made. The segments considered in the study were beam S1, mesh 1, and beam S10, mesh 5, Fig 5.3. In the former segment two quadratic elements have been used and in the later eight linear elements have been used. The torque–twist curves and the distribution of the elastic warping along the edges of a typical cross-section are shown in Figs. 5.16 and 5.17 respectively. It may be noted that the behaviour of the linear elements is improved by using a more refined mesh, Figs. 5.14 and 5.16. However, results

obtained for beam S1 is still closer to the analytical solutions than that of beam S10. Moreover the relative CPU times are 1.0 and 1.14 for beams S1 and S10 respectively.

5.5.1.6 Effect of solution algorithm and line searches

All the numerical tests have been carried out using the modified Newton-Raphson method in which the stiffness matrix is updated at the second iteration of each increment of loading. In order to study the efficiency of this algorithm, the initial stiffness method has been used for a second run of beam S2. The relative CPU times for the modified and initial stiffness methods were 1 and 1.1 respectively. In both runs the line searches have been implemented.

To investigate the influence of the line searches on speeding up the convergence, two runs for beam S2 have been conducted with and without line searches. The initial stiffness method has been used for both runs. Results show a considerable reduction in the CPU time when line searches are used. The relative CPU times of this study were 1.0 and 2.23.

5.5.1.7 Variation of the warping displacement

The variation of the warping displacement over a typical cross-section for both the elastic and the elasto-plastic stages of behaviour is shown in Figs. 5.18a and 5.18b for beam S2 and Figs. 5.19a and 5.19b for beam R2. The distribution of the warping

displacement, w, along the edges of the cross-section during both stages of behaviour is illustrated in Figs. 5.18c, 5.19c and 5.19d. Results obtained from the finite element model during the elastic stage of behaviour coincide with the exact solution given by equation (5.3).

5.5.1.8 Progress of the plastic Regions

The progress of the plastic regions in typical square and rectangular cross-sections is shown in Figs. 5.20 and 5.21 for beams S2 and R2 respectively. As the applied torque is increased, the yielding starts at the middle of the wider face of the cross-section and propagates inside the section and towards the corners, Figs 5.20 and 5.21.

5.5.2 Elasto-Plastic Warping Torsion

In beams with warping restraint, the stress distributions are not constant along the beam length. Therefore, it is necessary to analyse the entire length of the member. Numerical tests for thick I-section cantilever beams with warping restraint have been carried out to check the validity of the proposed finite element model for the case of warping torsion. The parameters considered in this study were the warping restraint and the integration rule.

5.5.2.1 Effect of the warping restraint

The torque-rotation relationships of the I-beams with warping restraint, beams I2 and I4, have been compared with the pure torsion cases, Beams I1 and I3. The finite element solutions for all beams are shown in Fig. 5.22, where the ratio of the applied torque to the maximum elastic pure torque computed from the relevant pure torsion case, because no analytical solution is available for thick I-section, have been plotted against the ratio of the angle of twist to the maximum computed elastic angle of twist obtained from the finite element analysis of the relevant pure torsion case.

The plastic collapse warping torque, calculated by the method proposed by Dinno and Merchant [11], and the fully plastic pure torque obtained by Nadai's sand heap analogy, equation (5.11) are indicated in the figure. The approximate collapse torque for an I-section cantilever beam restrained against the warping displacement at its fixed end is given by:

$$T_o = T_p + \frac{(h-h_f)}{l} \sigma_y \frac{h_f b^2}{4} \qquad (5.14)$$

where T_o is the fully plastic torque in presence of warping restraint, T_p is the sand heap torque given by equation (5.11) and l is the length of the cantilever.

Results from the finite element model show that the warping restraint at the fixed end increases the ultimate torsion capacity of the beam. The plastic collapse torques obtained from the present

work and the study by Baba and Kajita [12] converge to Merchant's upper bound value, equation (5.14), however the experimental value reported by Dinno and Gill [13] for the same beam is higher than Merchant's upper bound solution by 33 per cent. A stiffer torque-rotation relationship in both the elastic and the elasto-plastic stages of behaviour compared with the pure torsion case is obtained. Similar results have been reported by Baba and Kajita [12], however a direct comparison with their results is not possible due to the lack of information in their paper.

5.5.2.2 Effect of the integration rule

Fig. 5.22 shows that the differences in the results using the 15b rule and the 27 point rule are negligible. However, the ratio of the CPU time for the 15b and 27 point rule for pure torsion case is 1:1.7 and for warping torsion case the ratio is 1:1.8. These ratios are similar to those obtained for the same integration rules for a rectangular section subjected to pure torque as discussed earlier in section 5.5.1.2.

5.5.2.3 Variation of the angle of twist

Fig. 5.23 shows the variation of the angle of twist for beam I2 at different stages of loading. In this figure, the angle of twist per unit length divided by the maximum computed elastic angle of twist per unit length in pure torsion is plotted against the ratio of the distance from the fixed end to the total beam length. The

results show that the angle of twist per unit length increases at a decreasing rate as the distance from the fixed end increases, and that the rate of change of the angle of twist per unit length at an arbitrary cross-section increases with increasing applied torque.

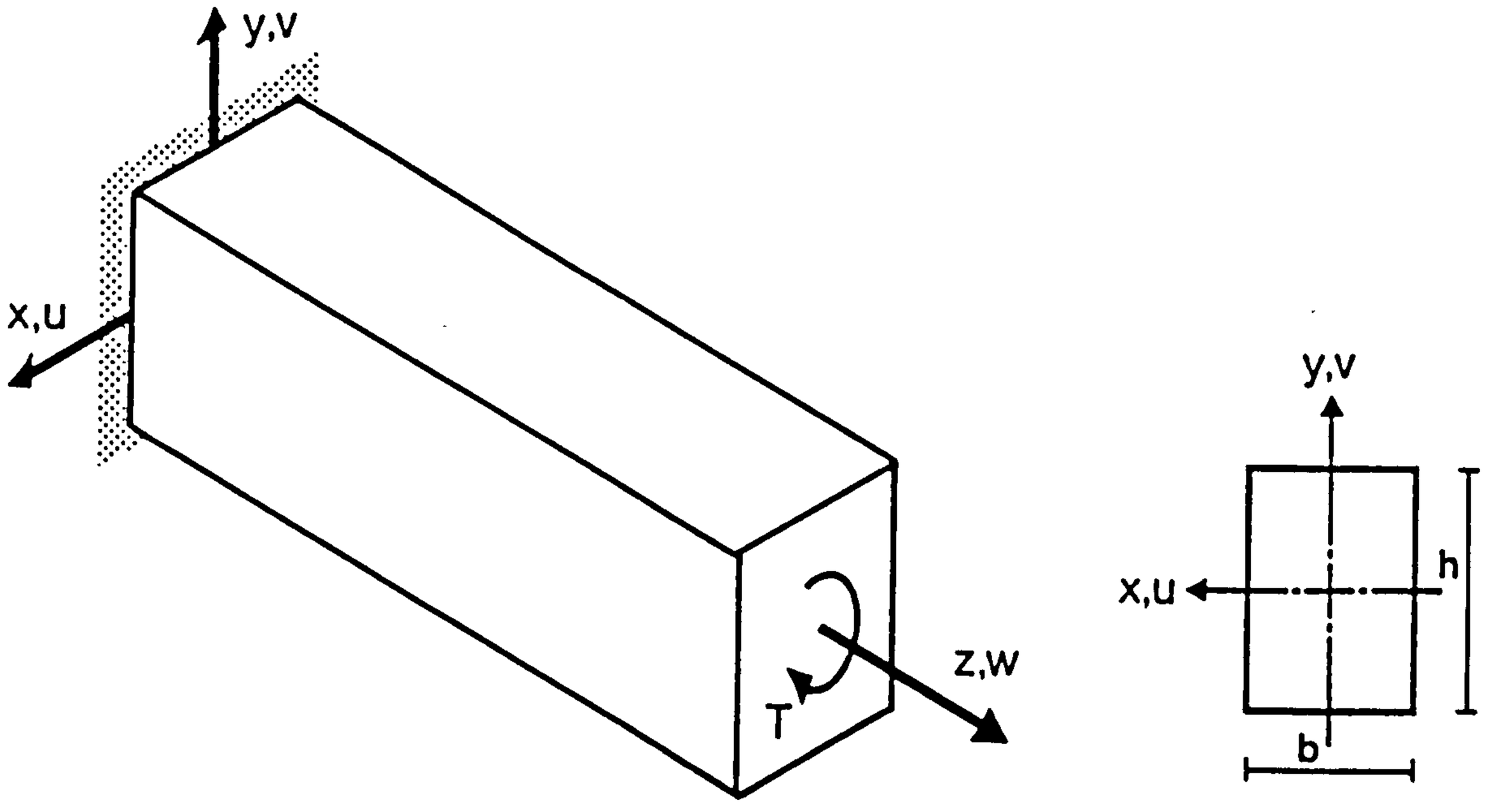

Fig. 5.1 Torsion of prismatic bars.

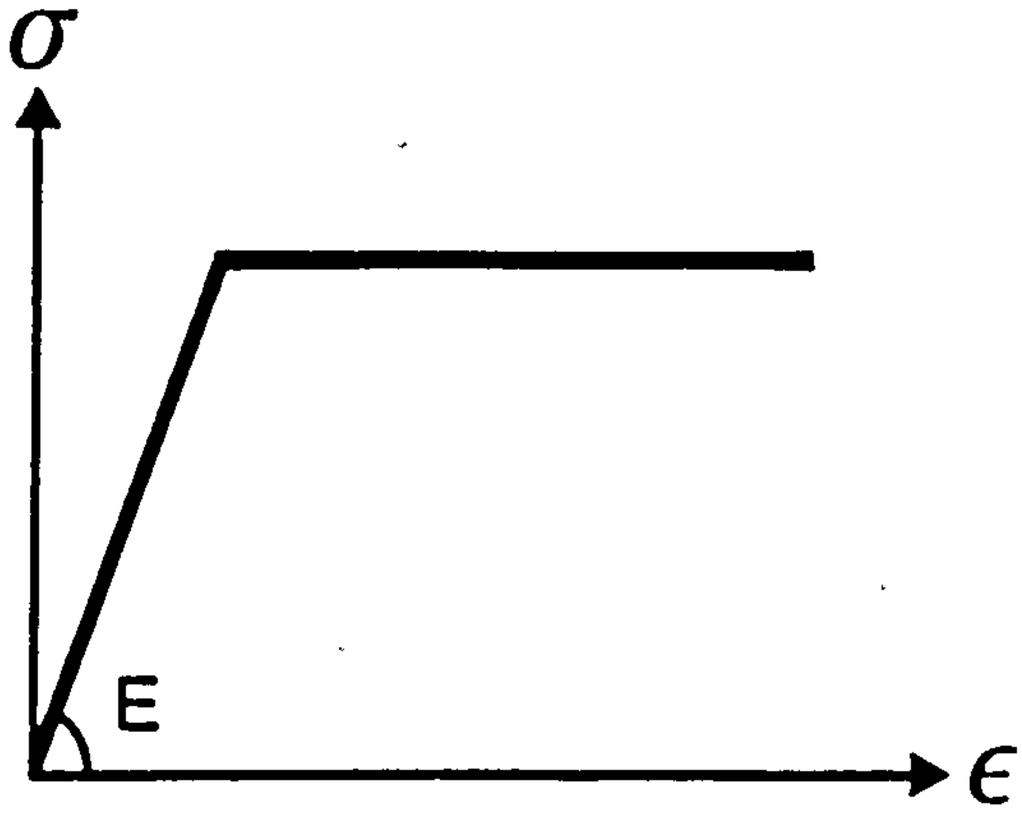

Hardening parameter = 0.0

a) For square, rectangular and I beams.

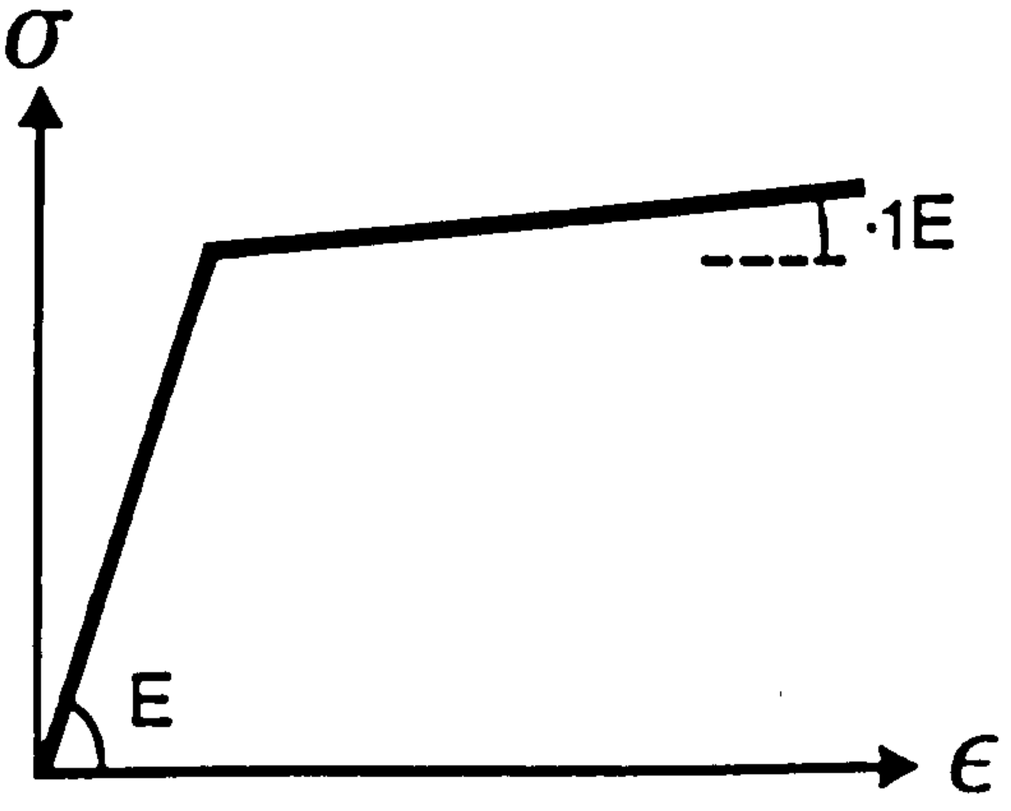

Hardening parameter = 0.111

b) For circular beams.

Fig. 5.2 Equivalent uniaxial stress-strain relationships.

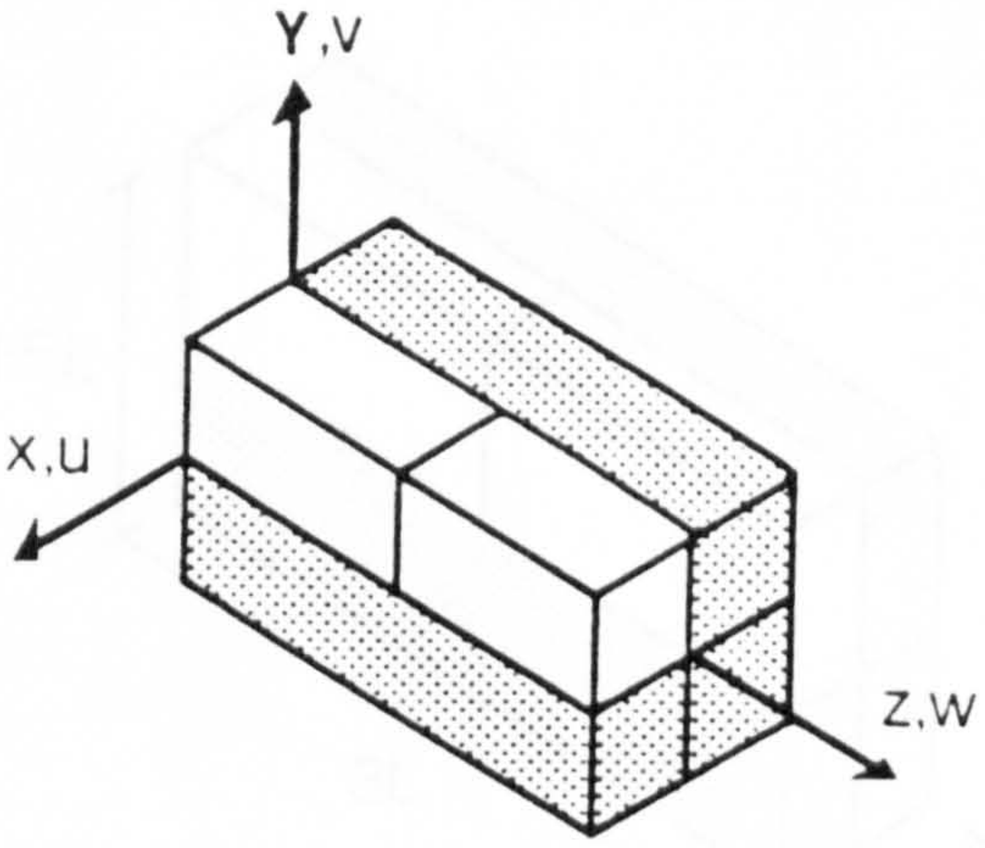

Mesh 1

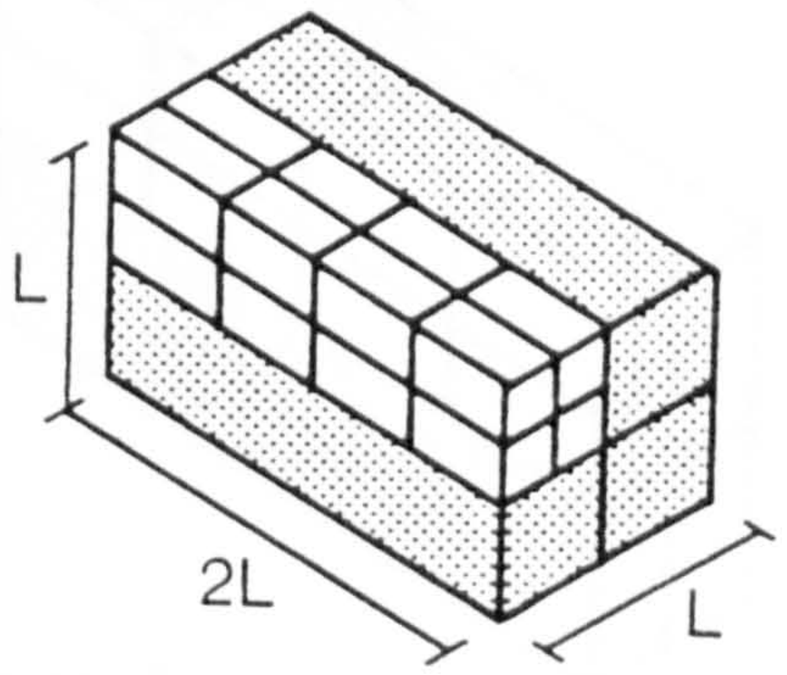

Mesh 2

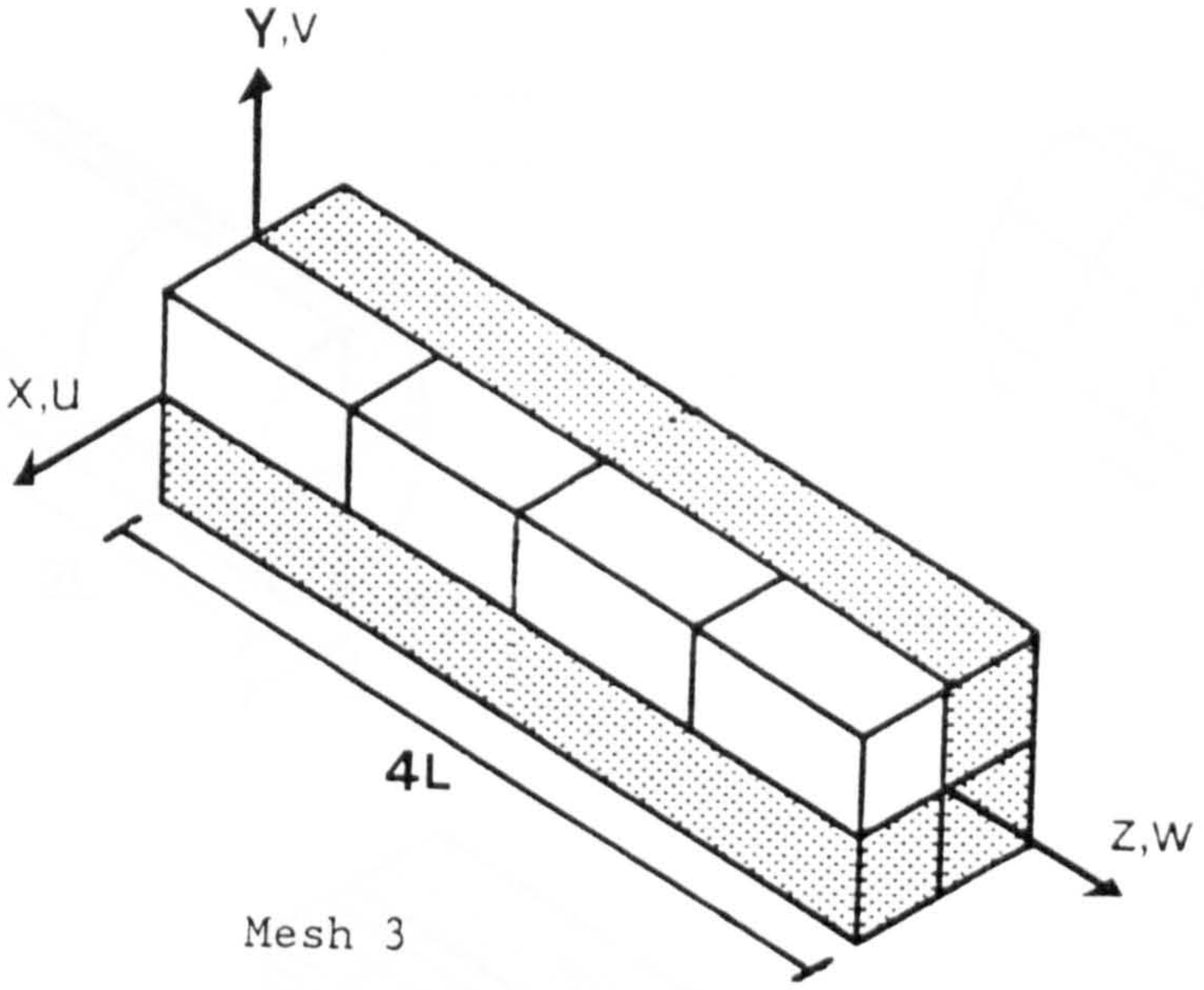

Mesh 3

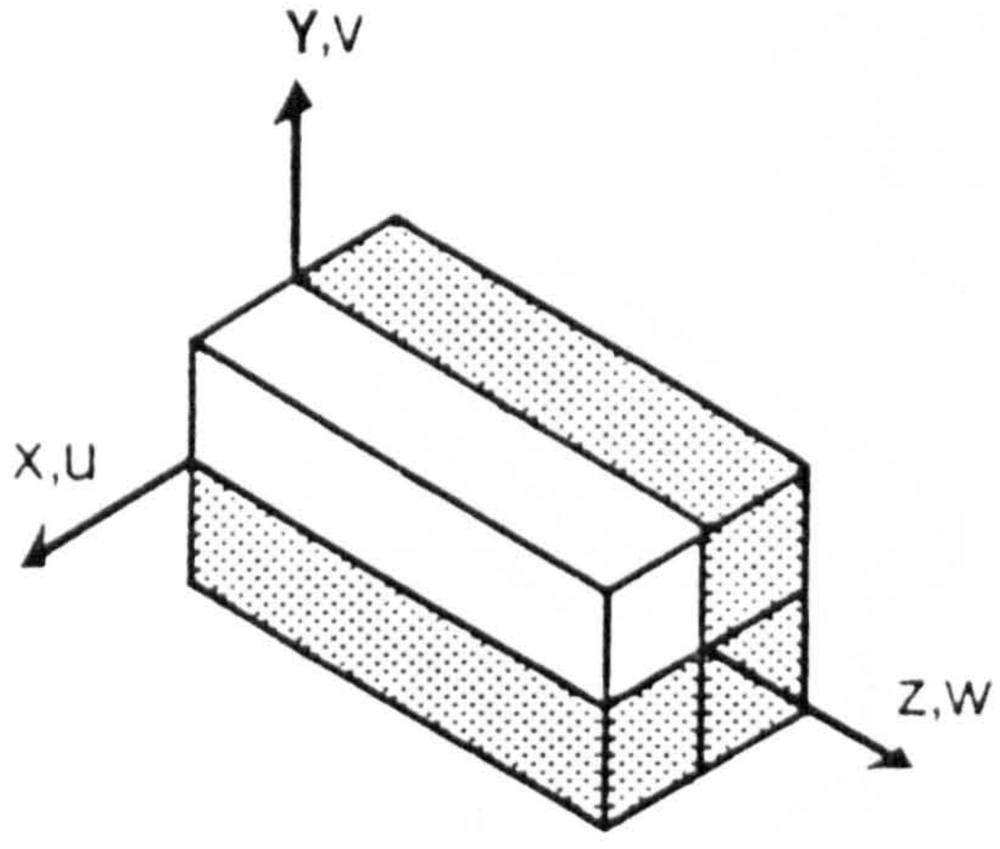

Mesh 4

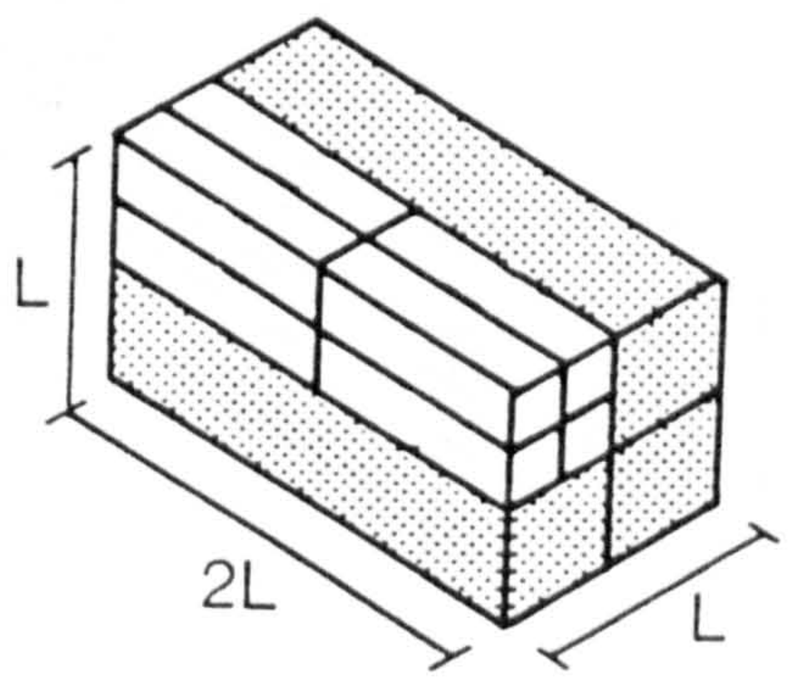

Mesh 5

Fig. 5.3 Finite element meshes for square members.

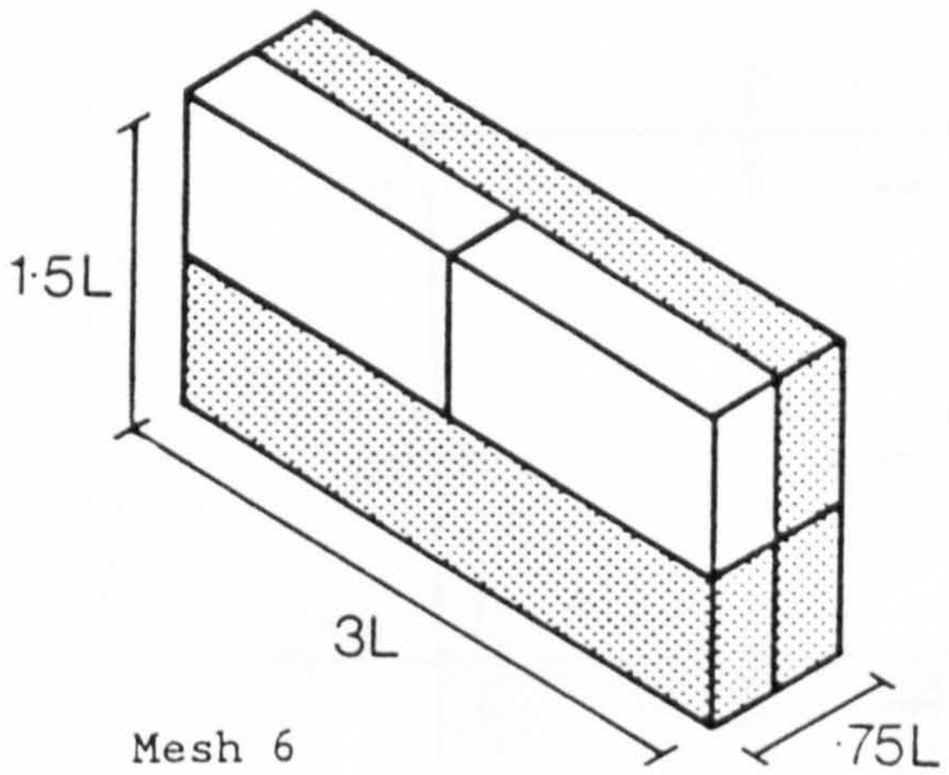

Mesh 6

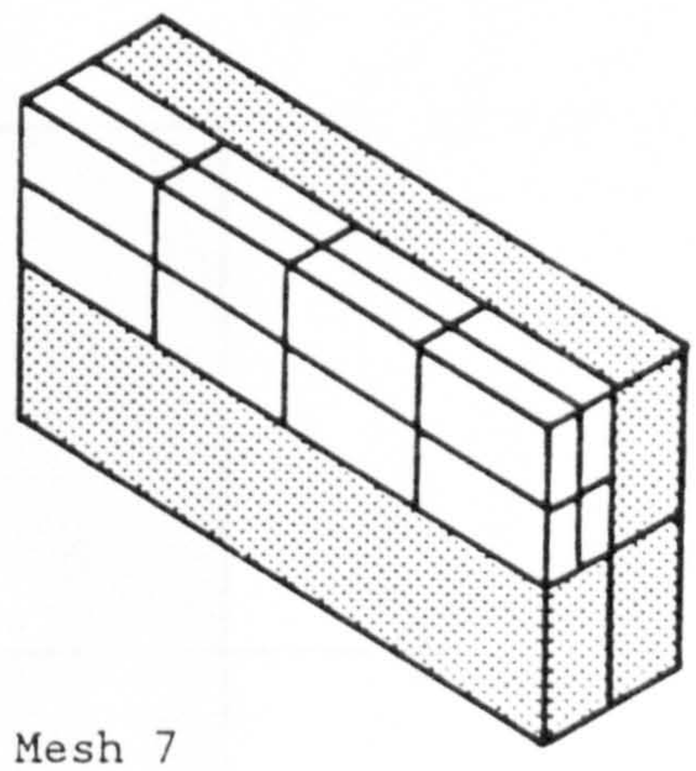

Mesh 7

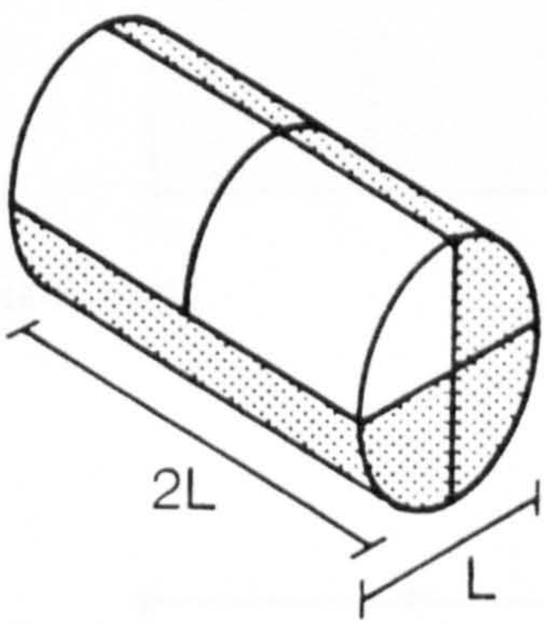

Mesh 8

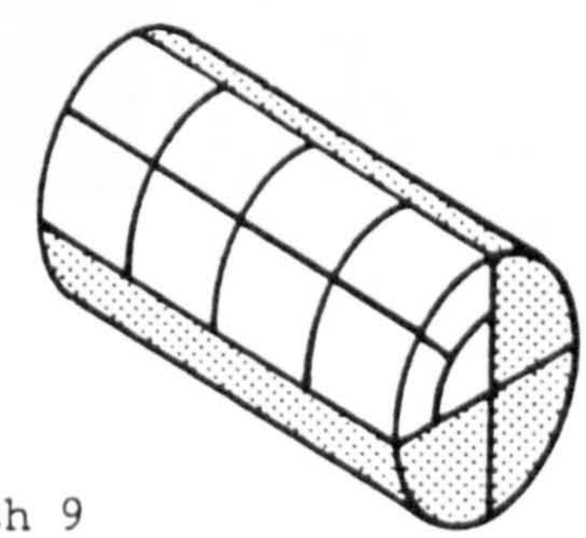

Mesh 9

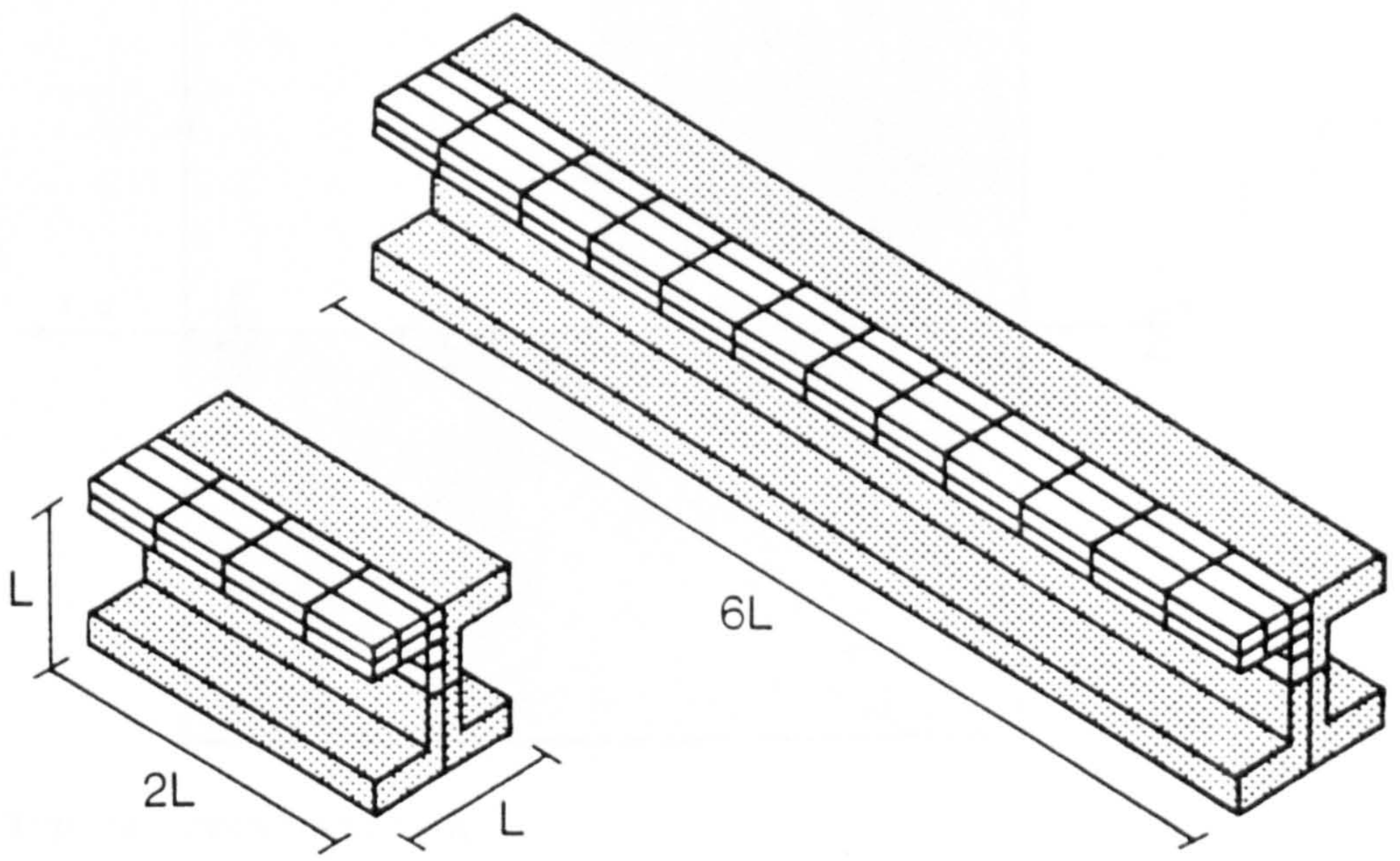

Mesh 10

Mesh 11

Fig. 5.4 Finite element meshes for rectangular, circular and I members.

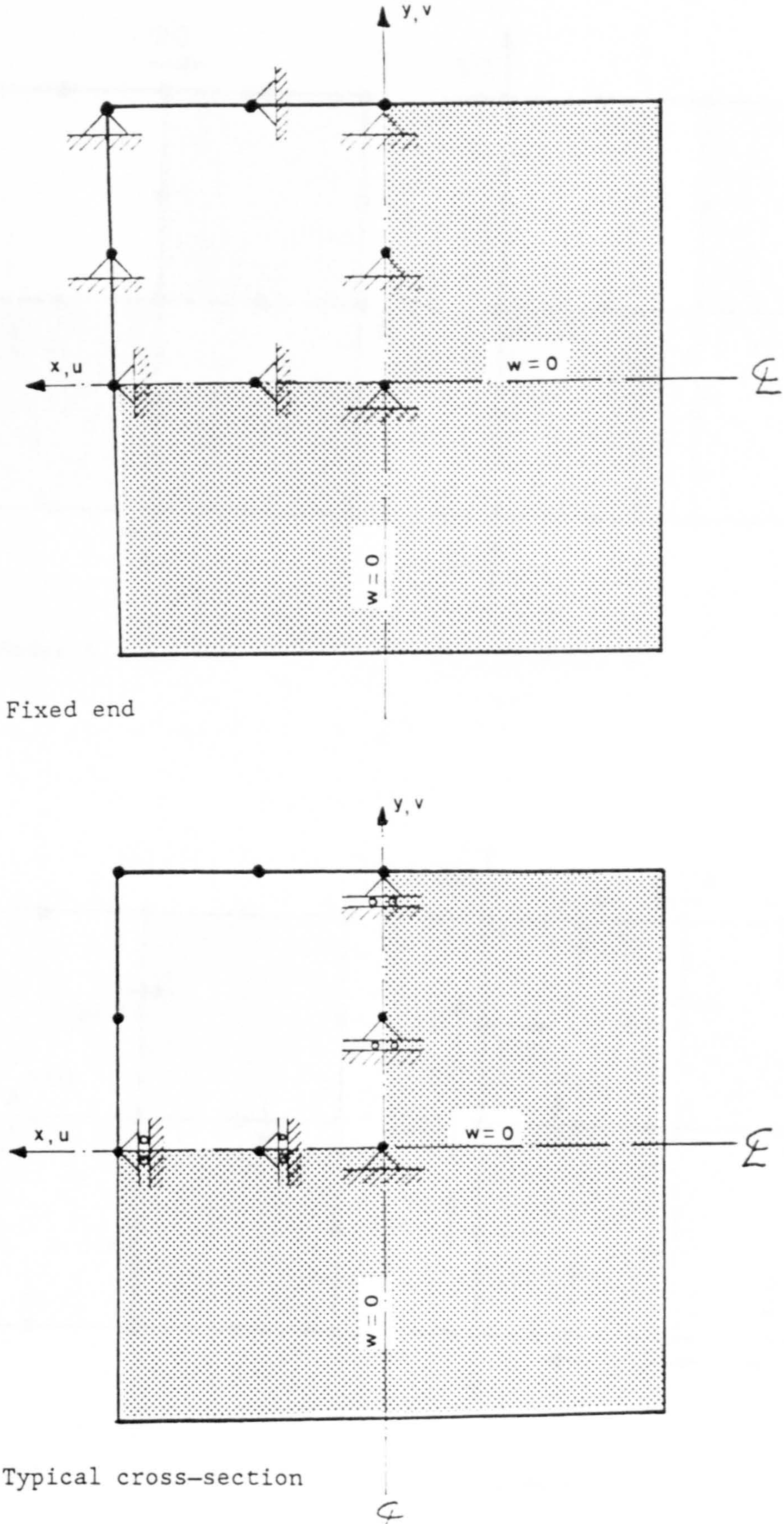

Fig. 5.5 Boundary conditions at the fixed end and at a typical cross-section of beam S1.

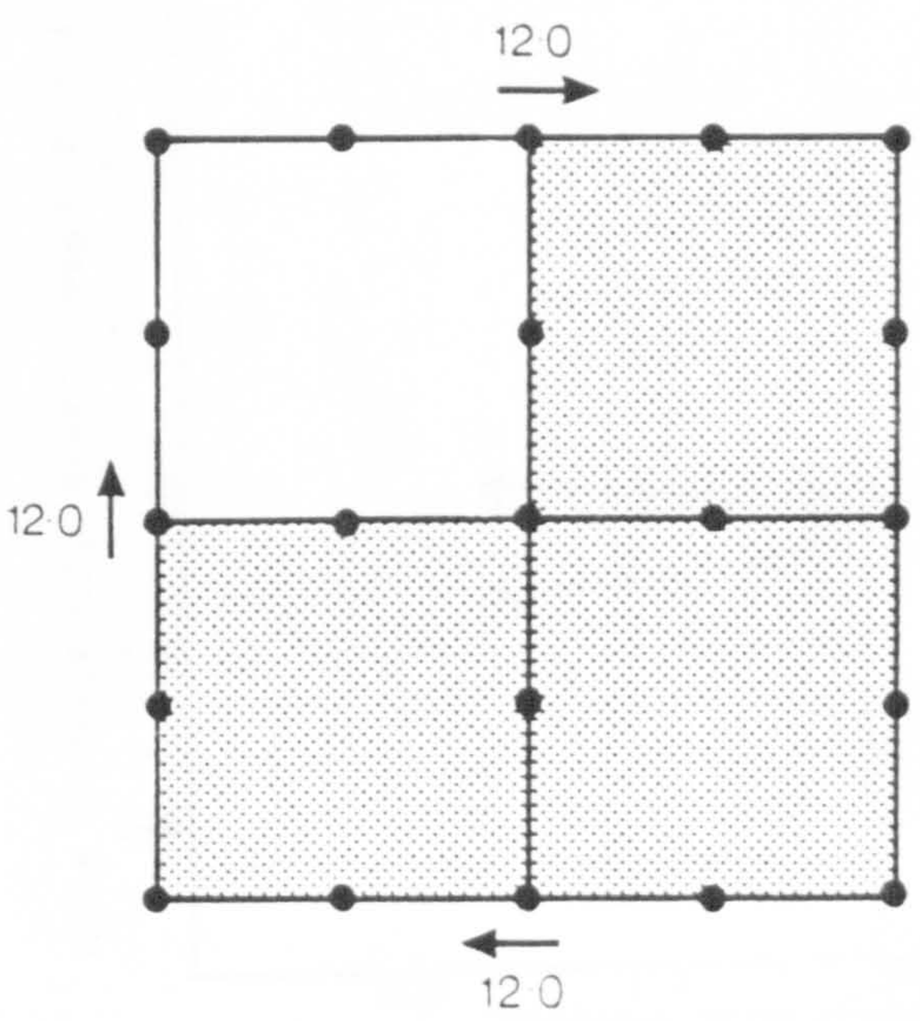

a) Model A

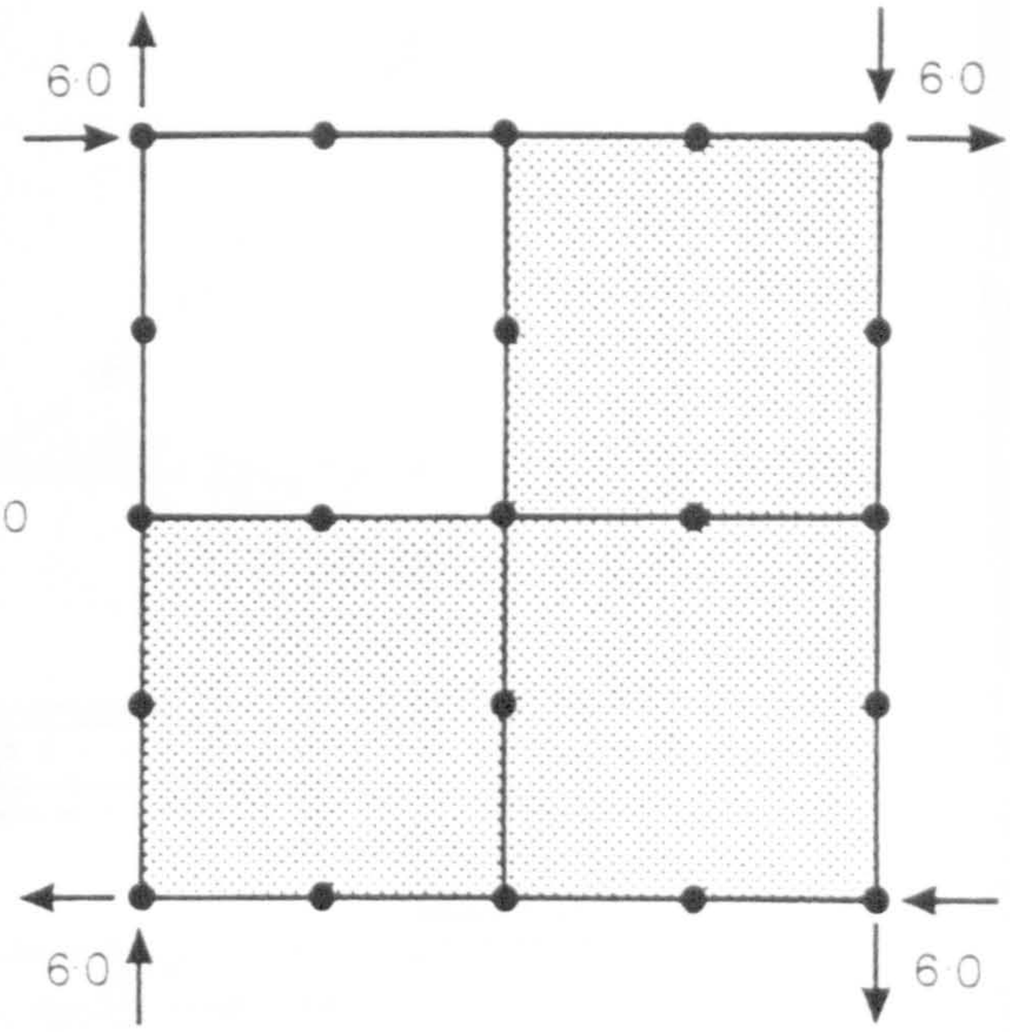

b) Model B

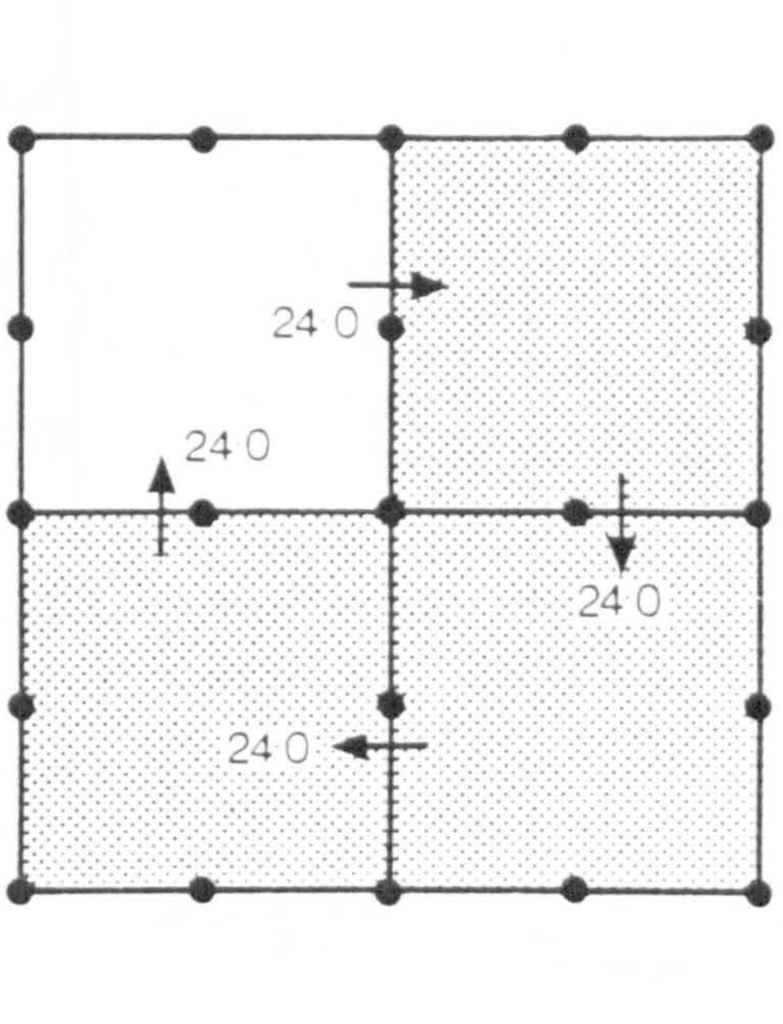

c) Model C

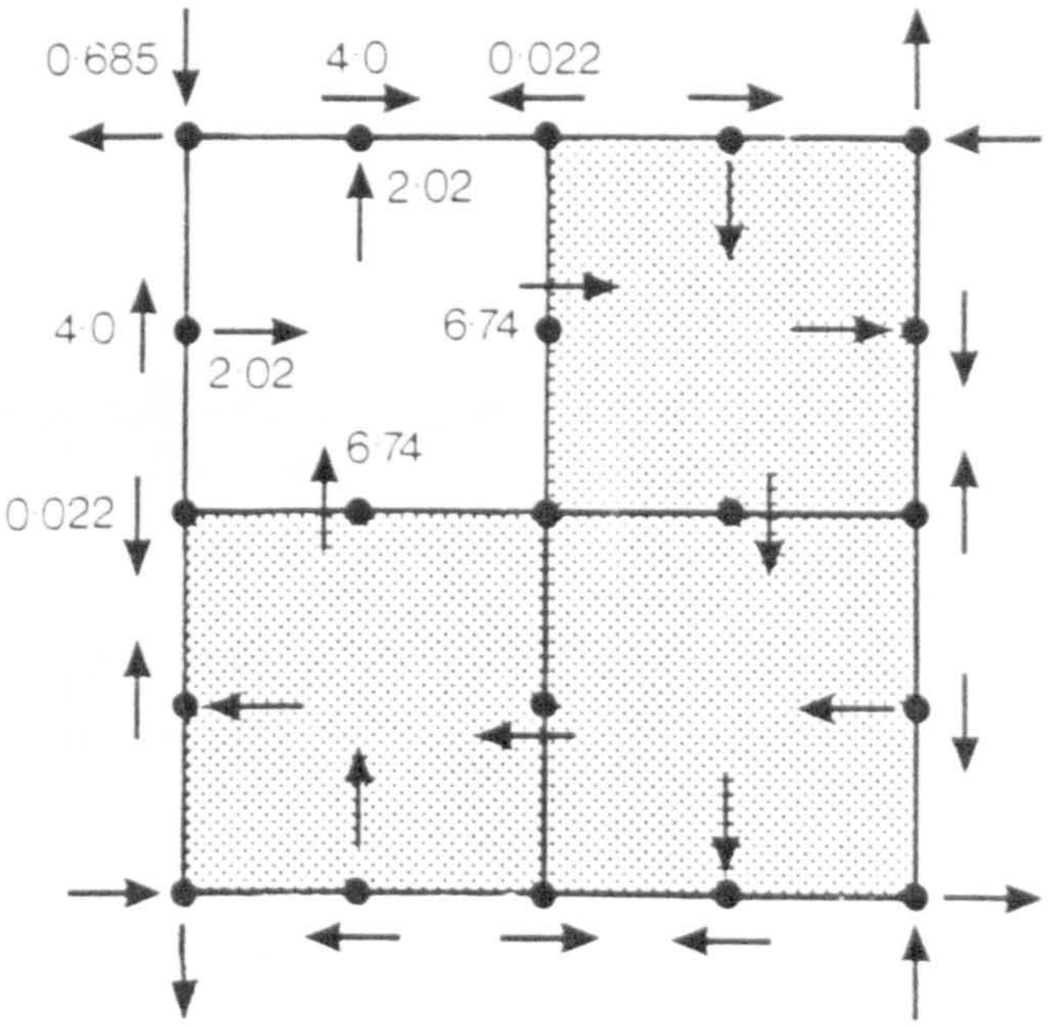

d) Model D

Fig. 5.6 Modelling of external applied torque at the free end.

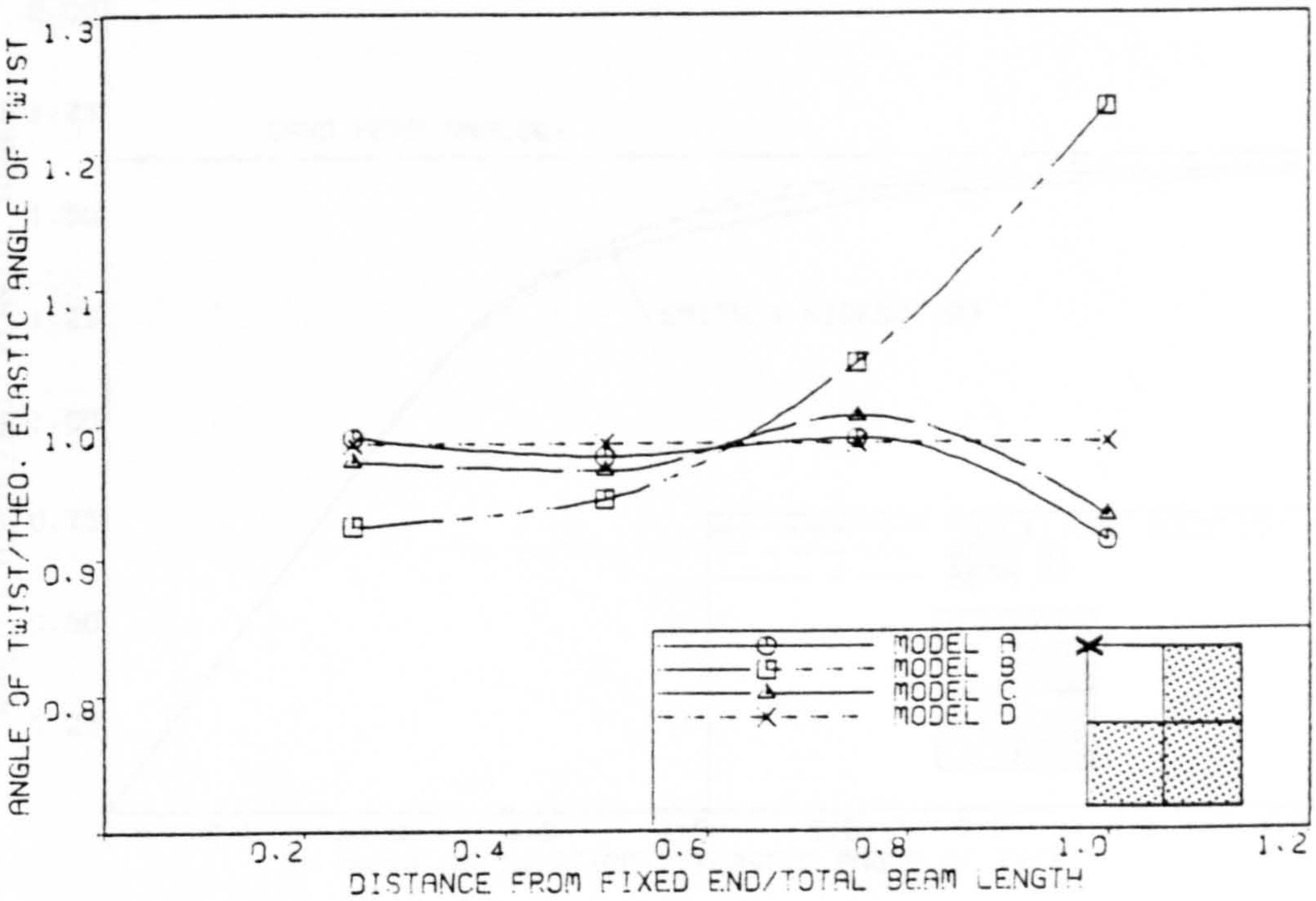

a) Angle of twist computed at the corner of the cross-section.

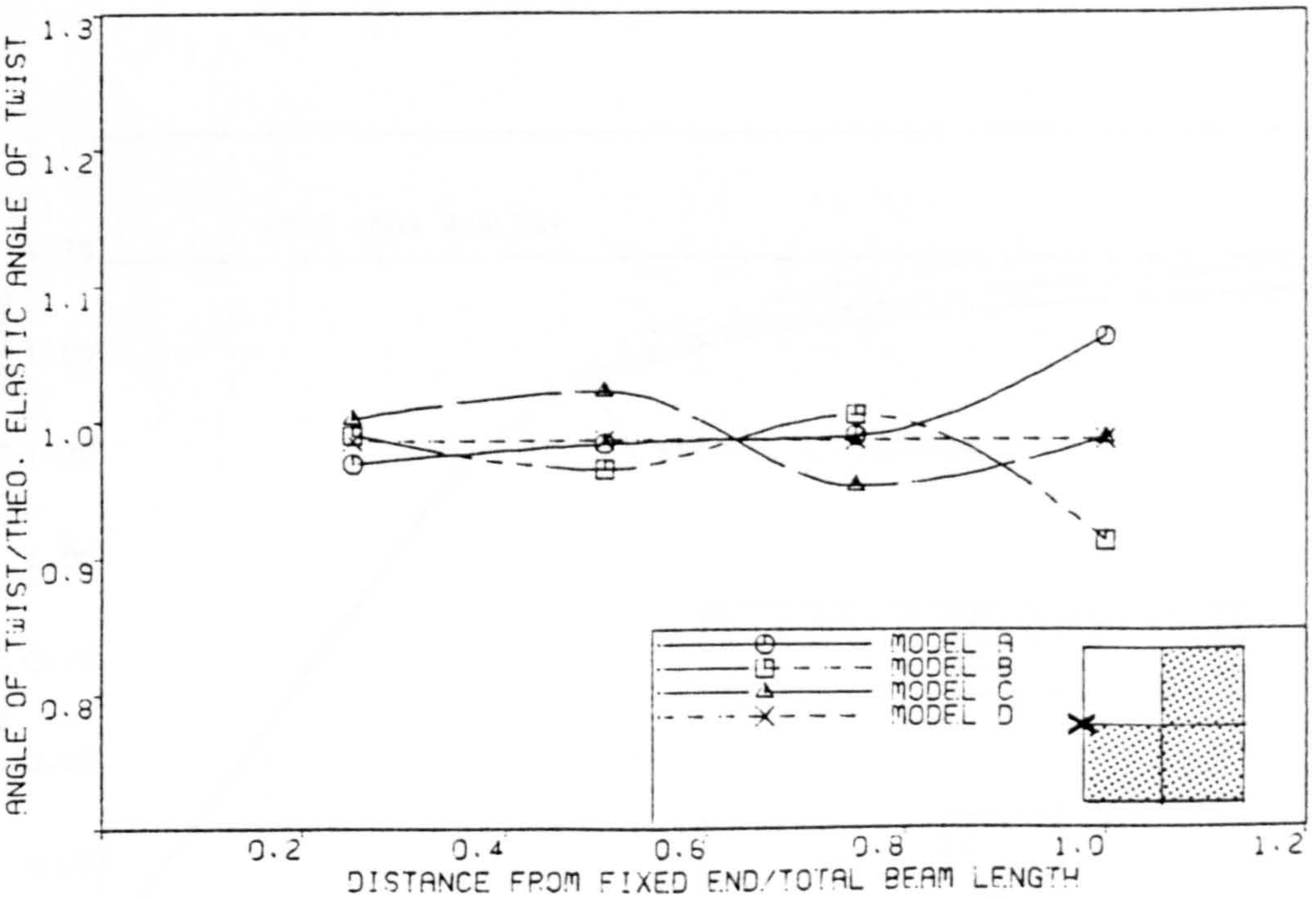

b) Angle of twist computed at the middepth of the cross-section.

Fig. 5.7 Variation of computed angle of twist along beam length.

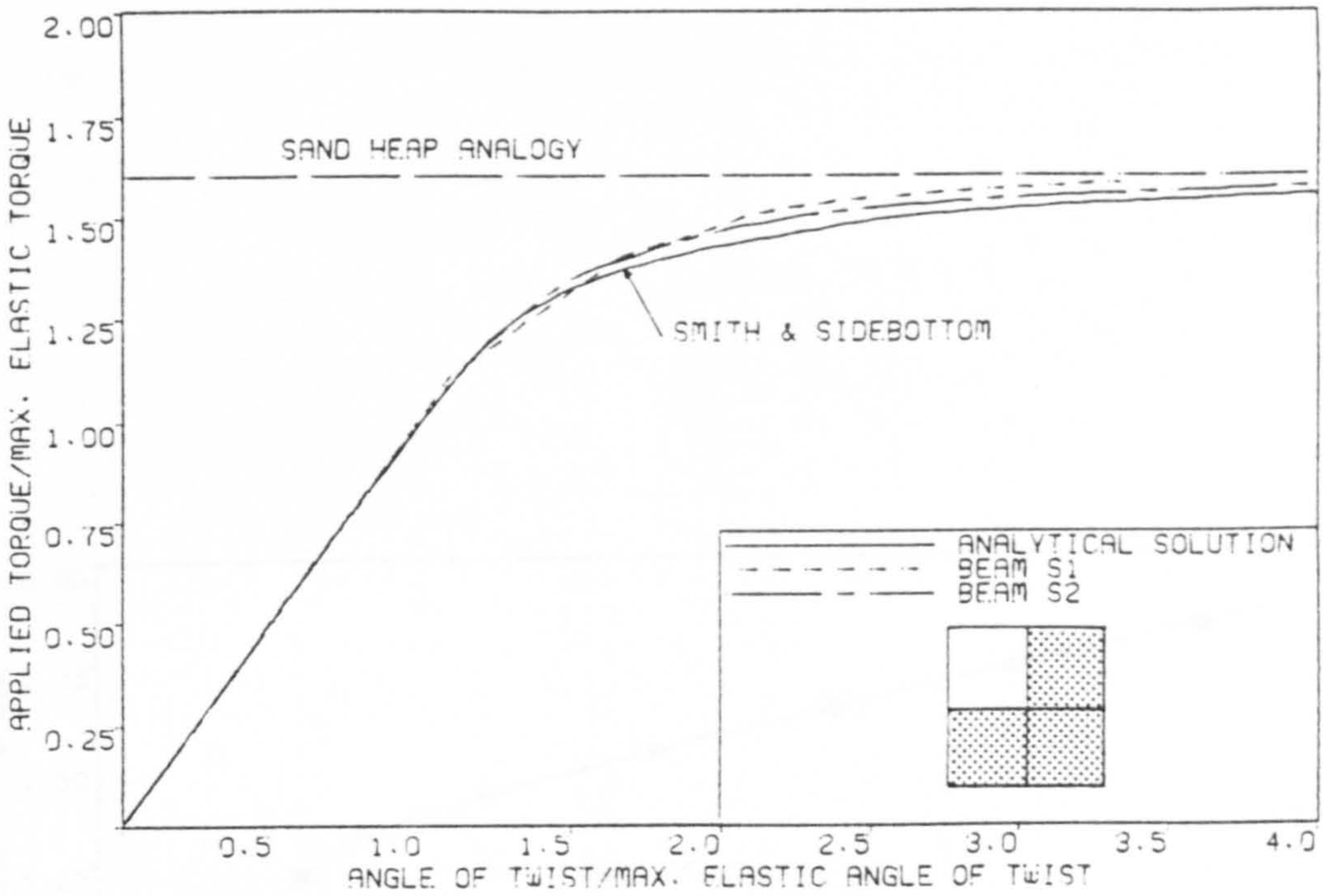

Fig. 5.8 Elasto-plastic pure torque-rotation relationship for a member of square cross-section.

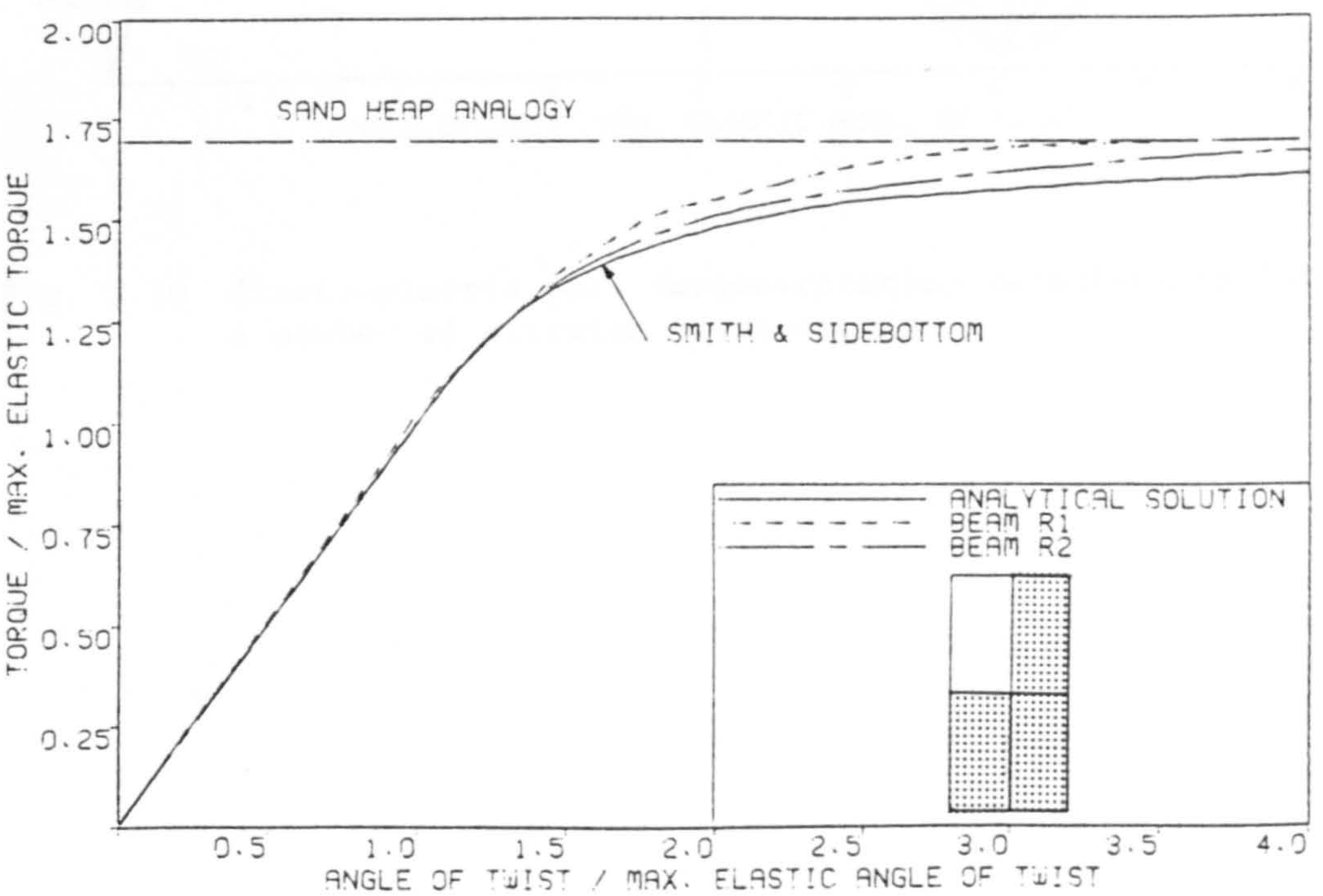

Fig. 5.9 Elasto-plastic pure torque-rotation relationship for a member of rectangular cross-section.

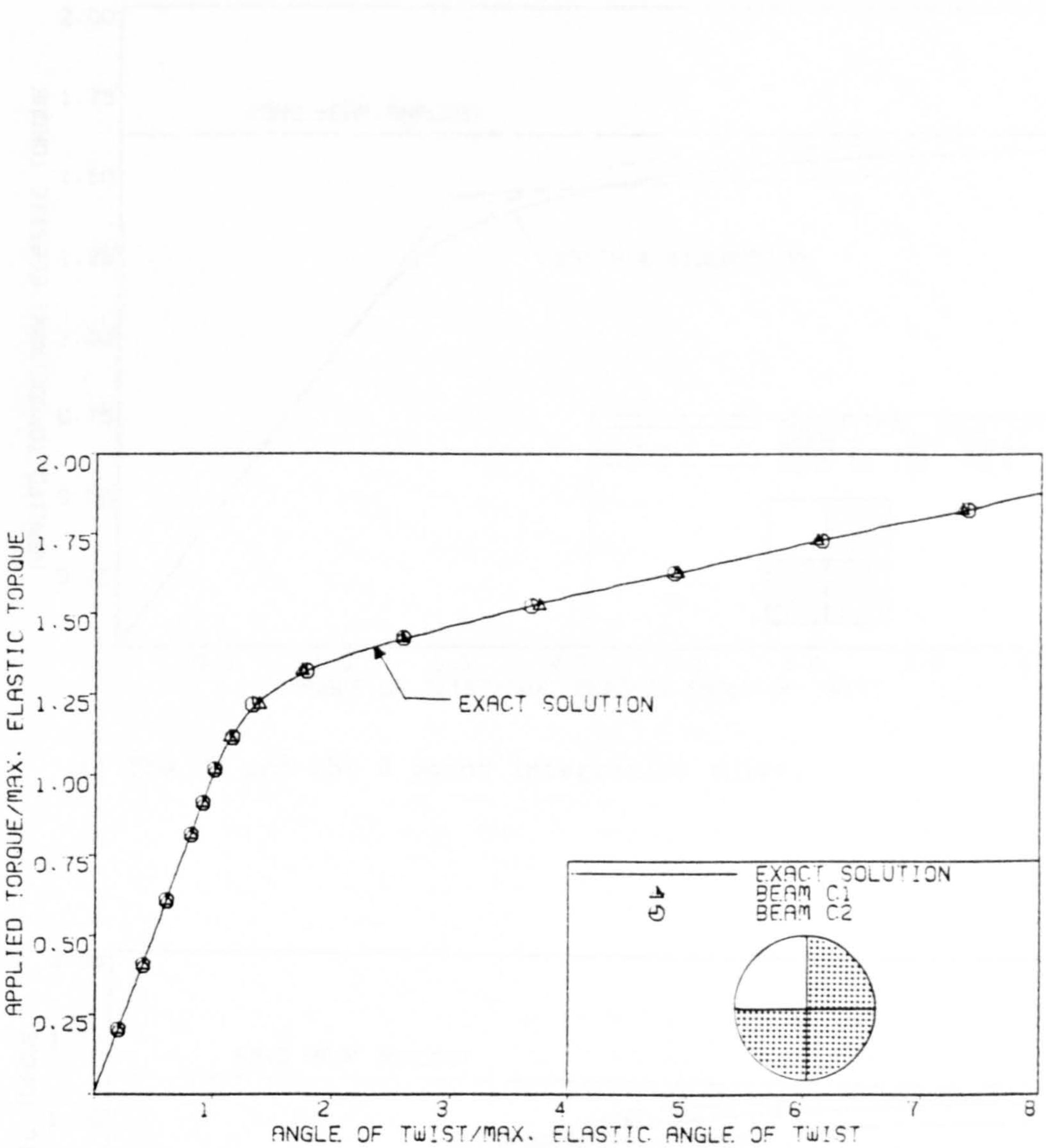

Fig. 5.10 Elasto-plastic pure torque-rotation relationship for a member of circular cross-section.

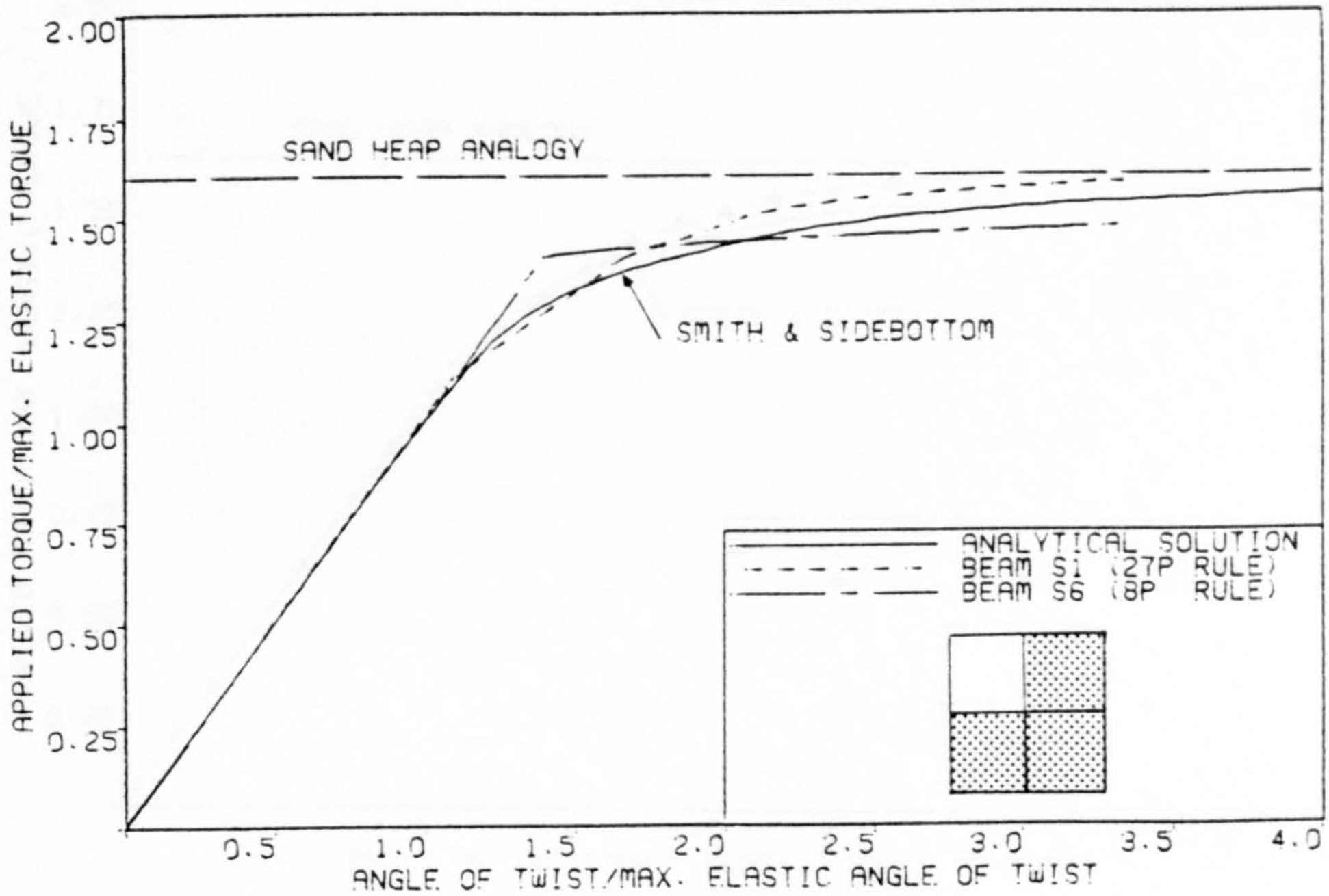

a) The 27 and the 8 point integration rules.

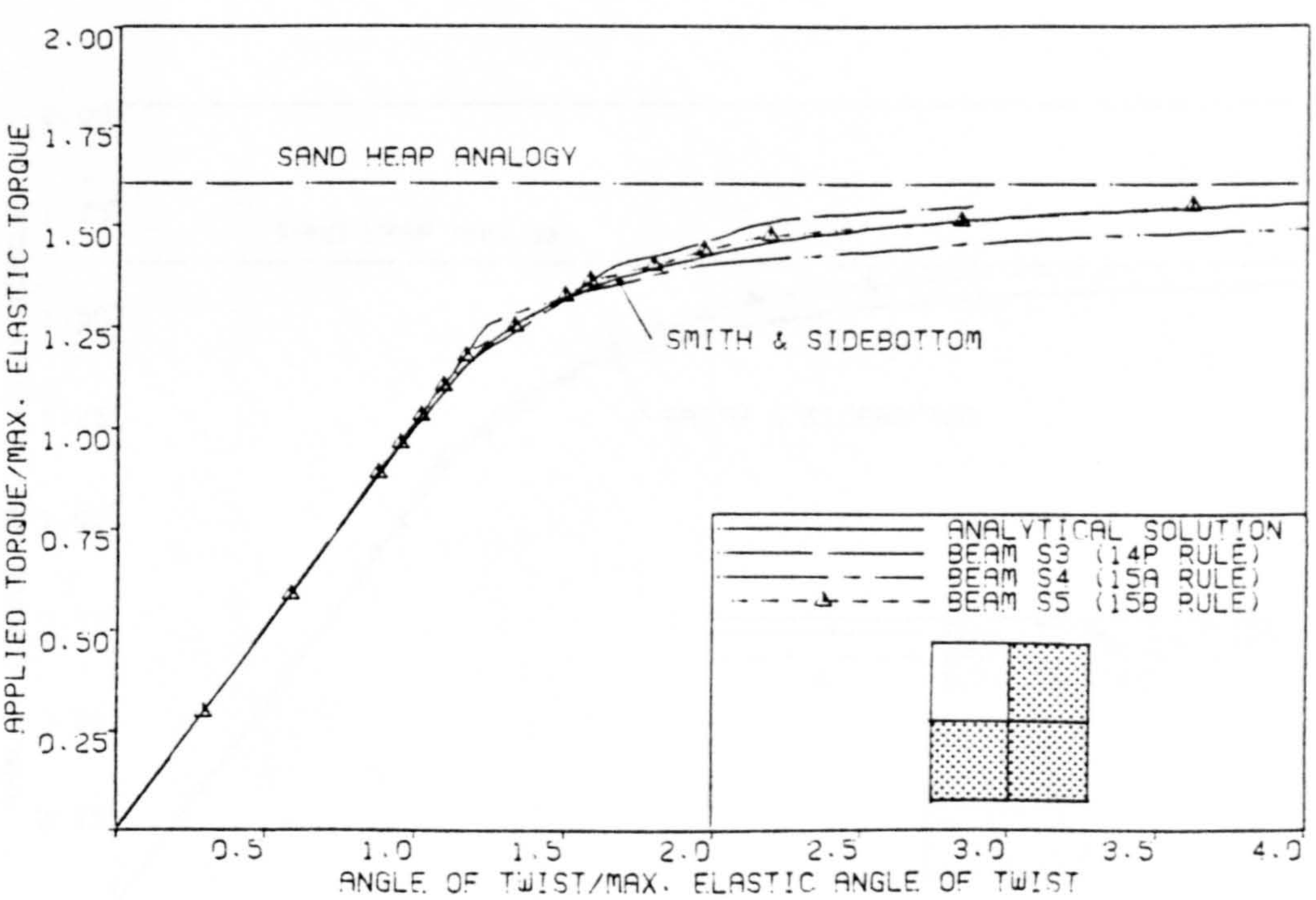

b) The 15 point integration rules.

Fig. 5.11 Effect of integration rules on the elasto-plastic pure torsion in a member of square cross-section.

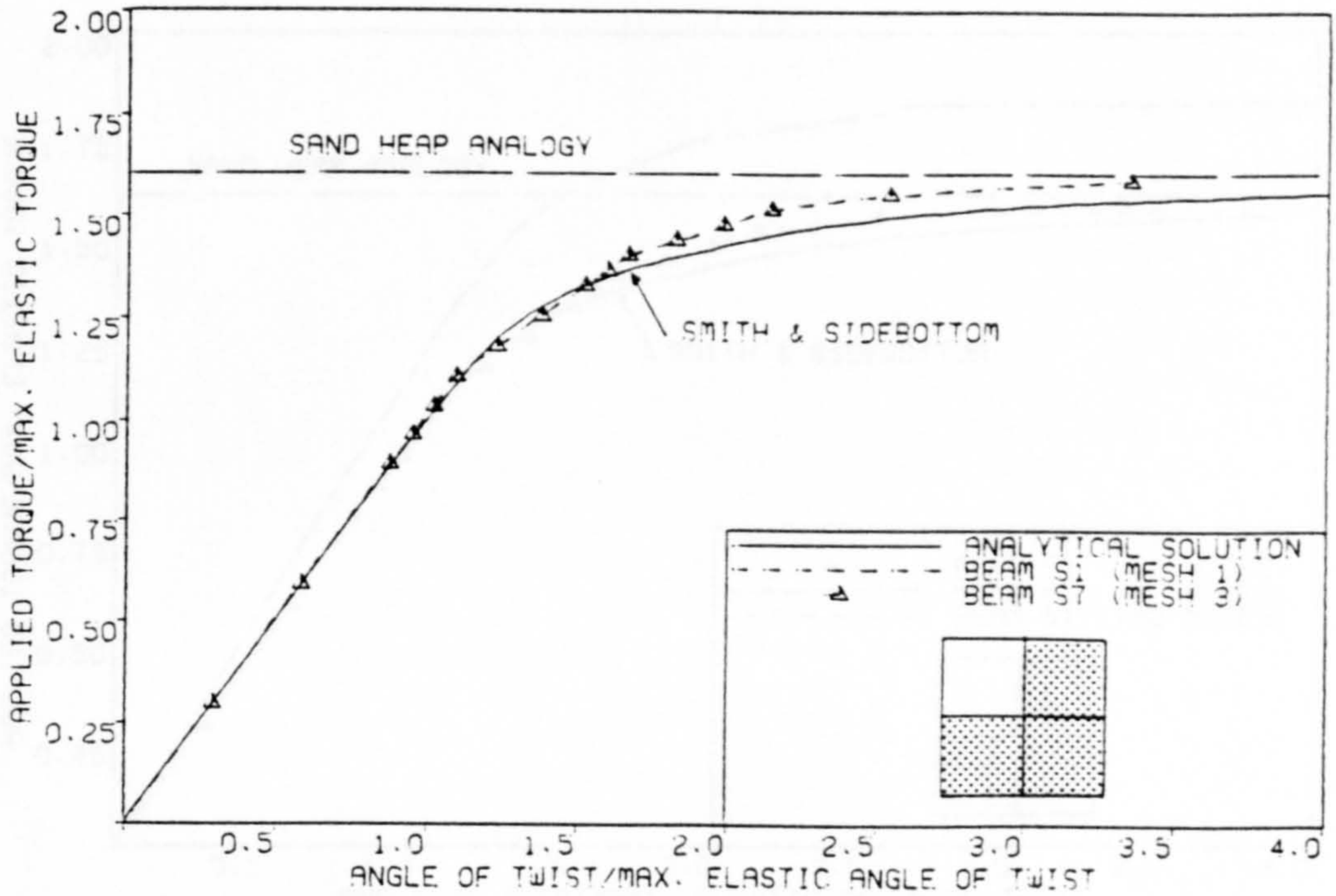

Fig. 5.12 Effect of segment length on the elasto-plastic pure torsion in a member of square cross-section.

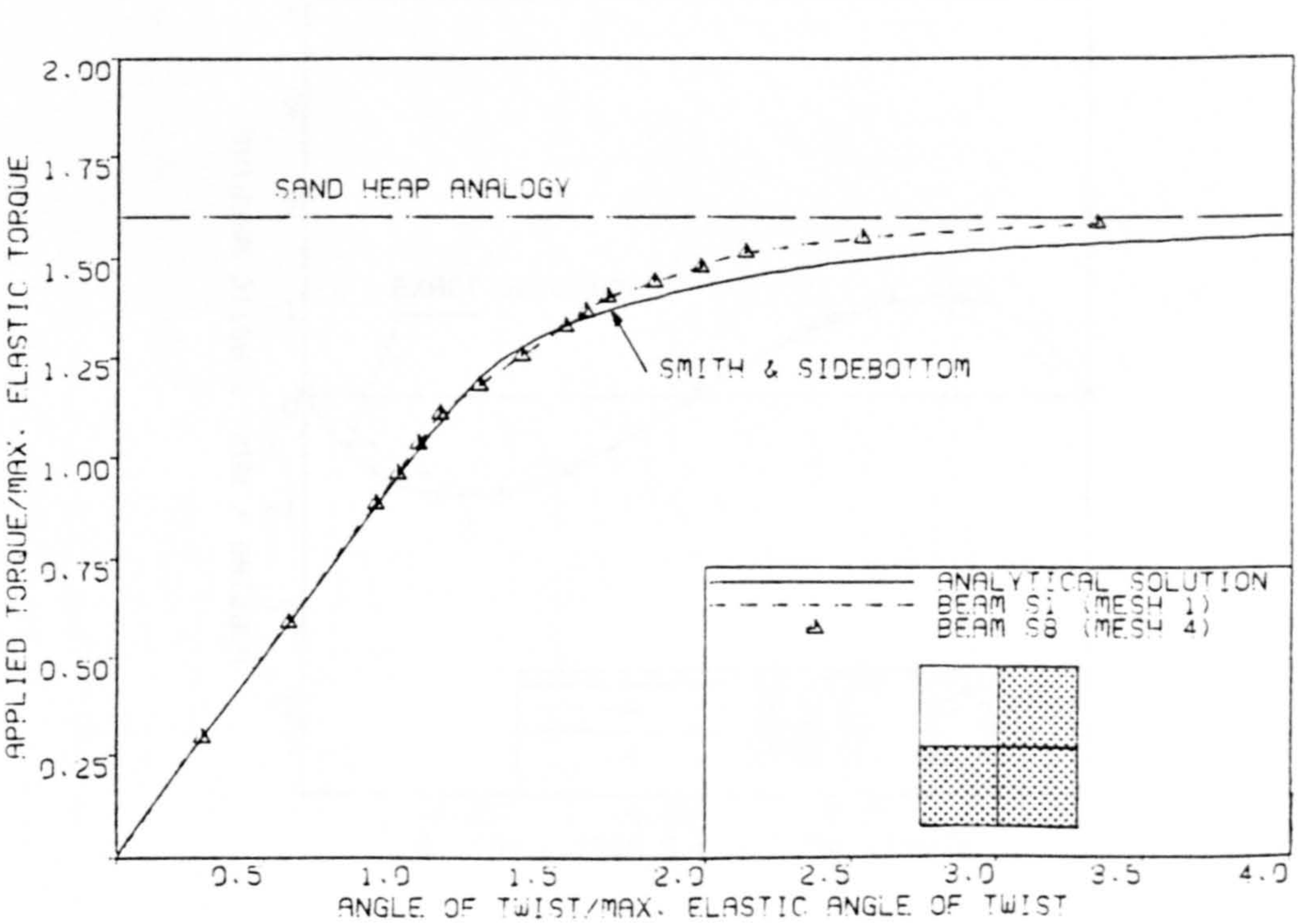

Fig. 5.13 Effect of element aspect ratio on the elasto-plastic pure torsion in a member of square cross-section.

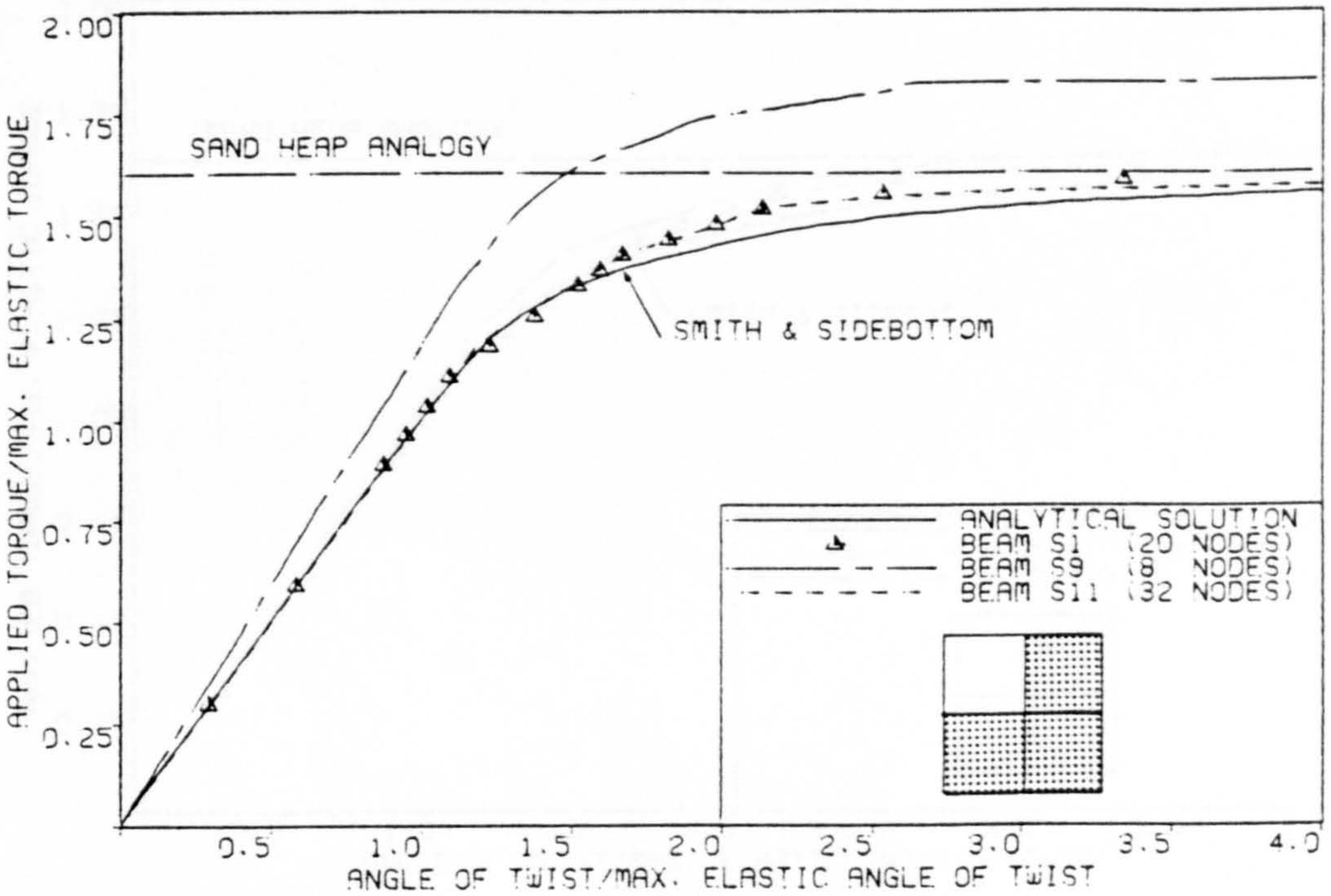

Fig. 5.14 Effect of element type on the elasto-plastic pure torsion in a member of square cross-section.

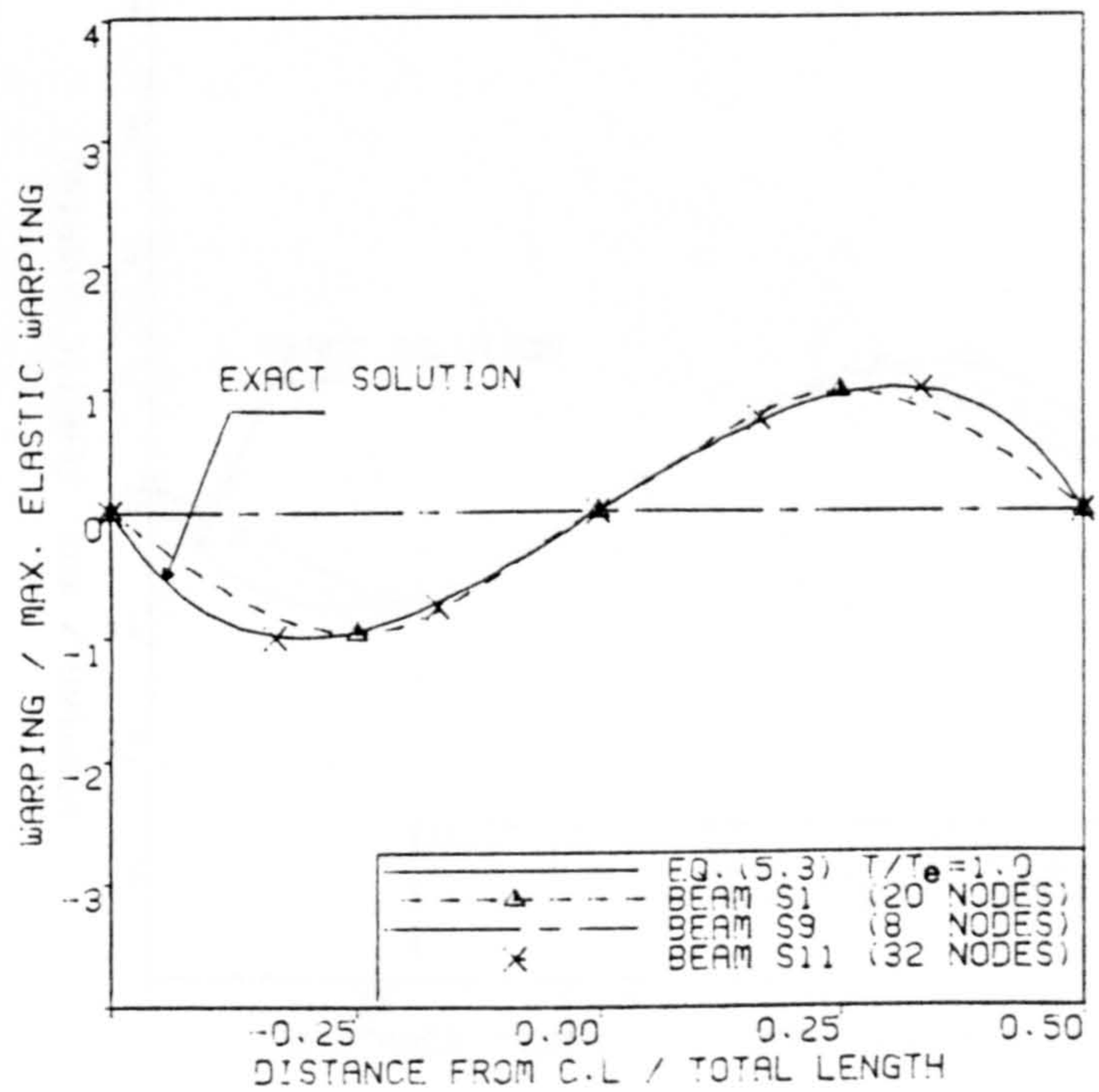

Fig. 5.15 Distribution of warping displacement along the edges of a member of square cross-section at the elastic stage.

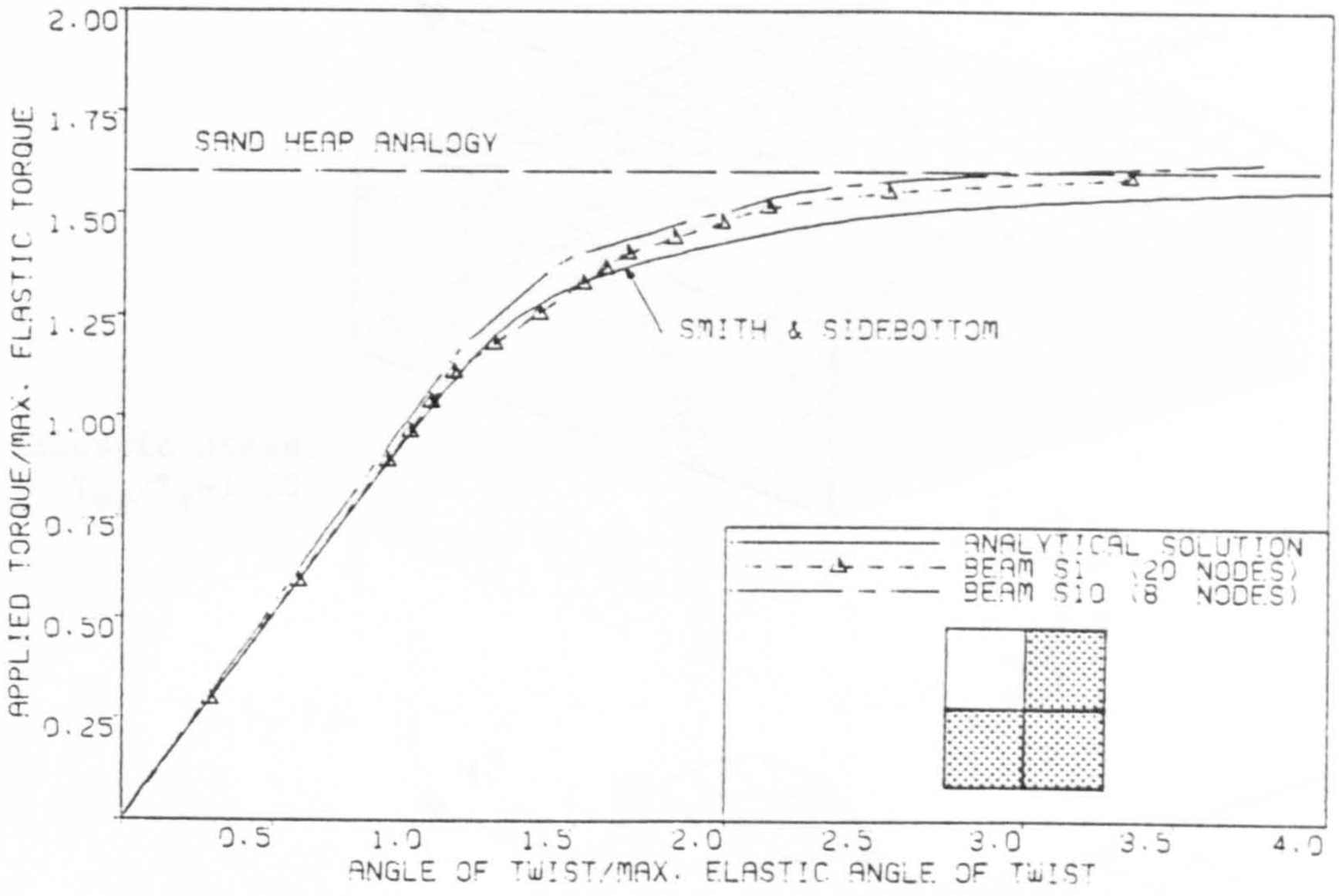

Fig. 5.16 Effect of element type on the elasto–plastic pure torsion in a member of square cross–section.

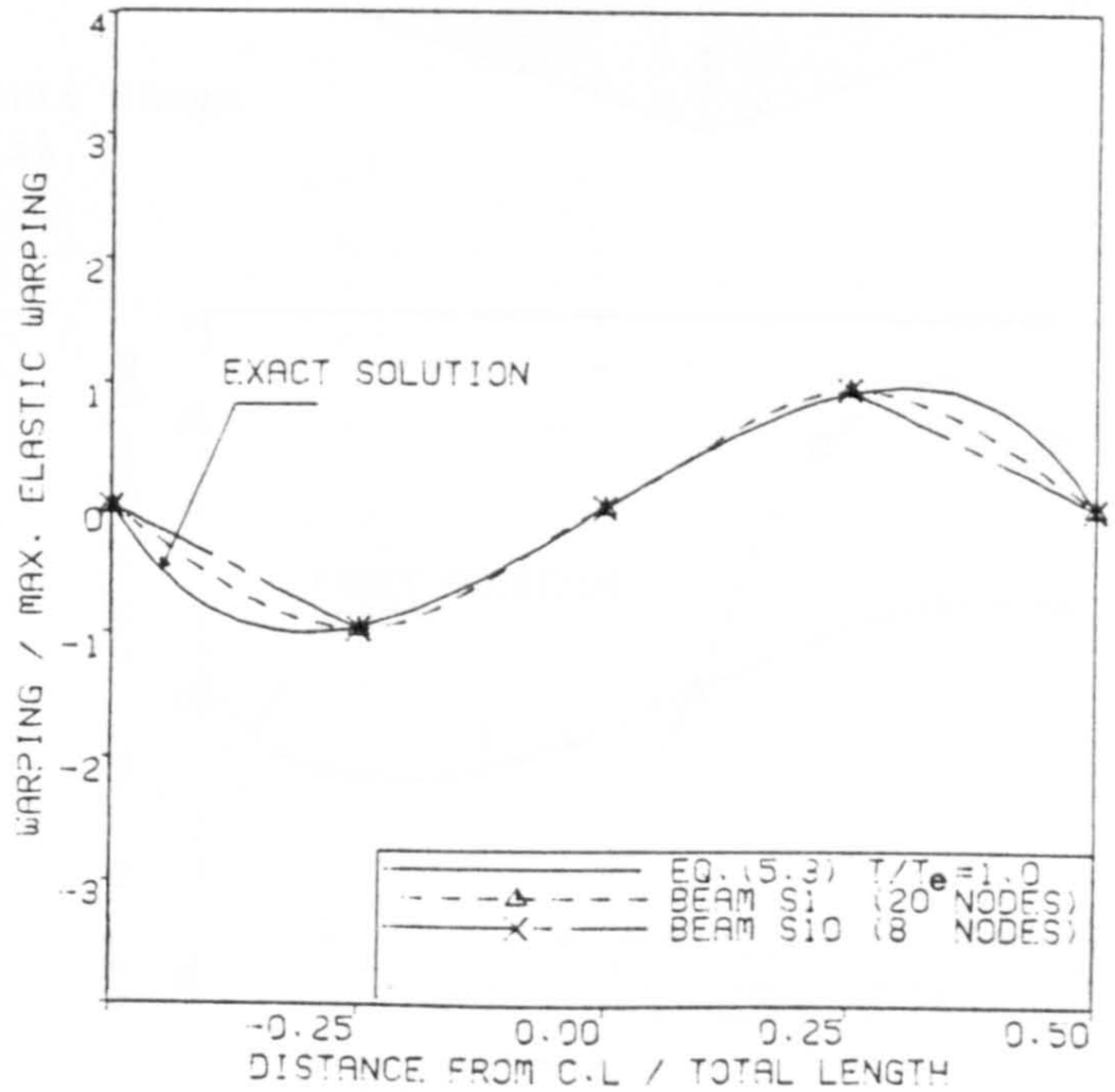

Fig. 5.17 Distribution of warping displacement along the edges of a member of square cross–section at the elastic stage.

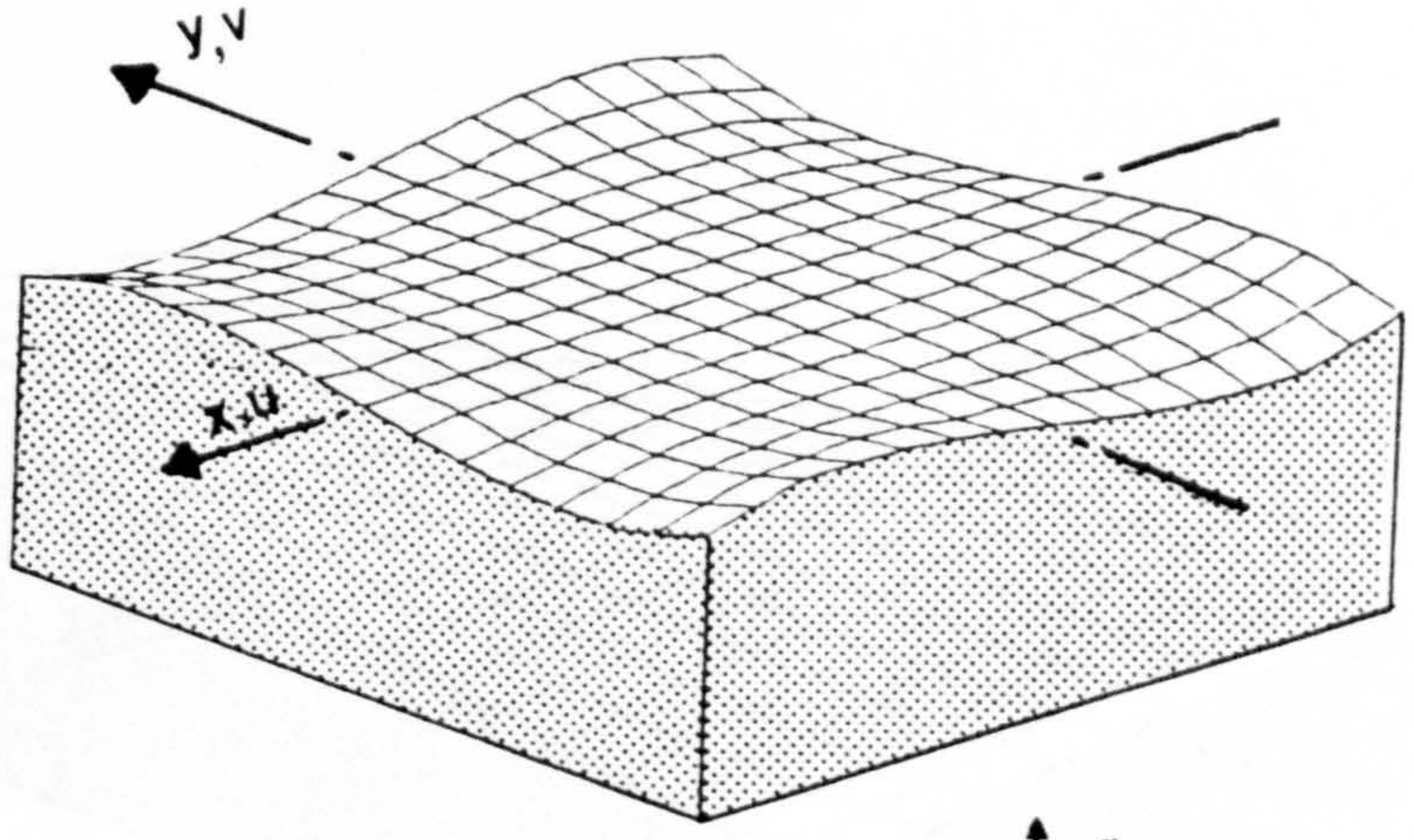

a) Elastic stage,
T_{ep}/T_e=1.00

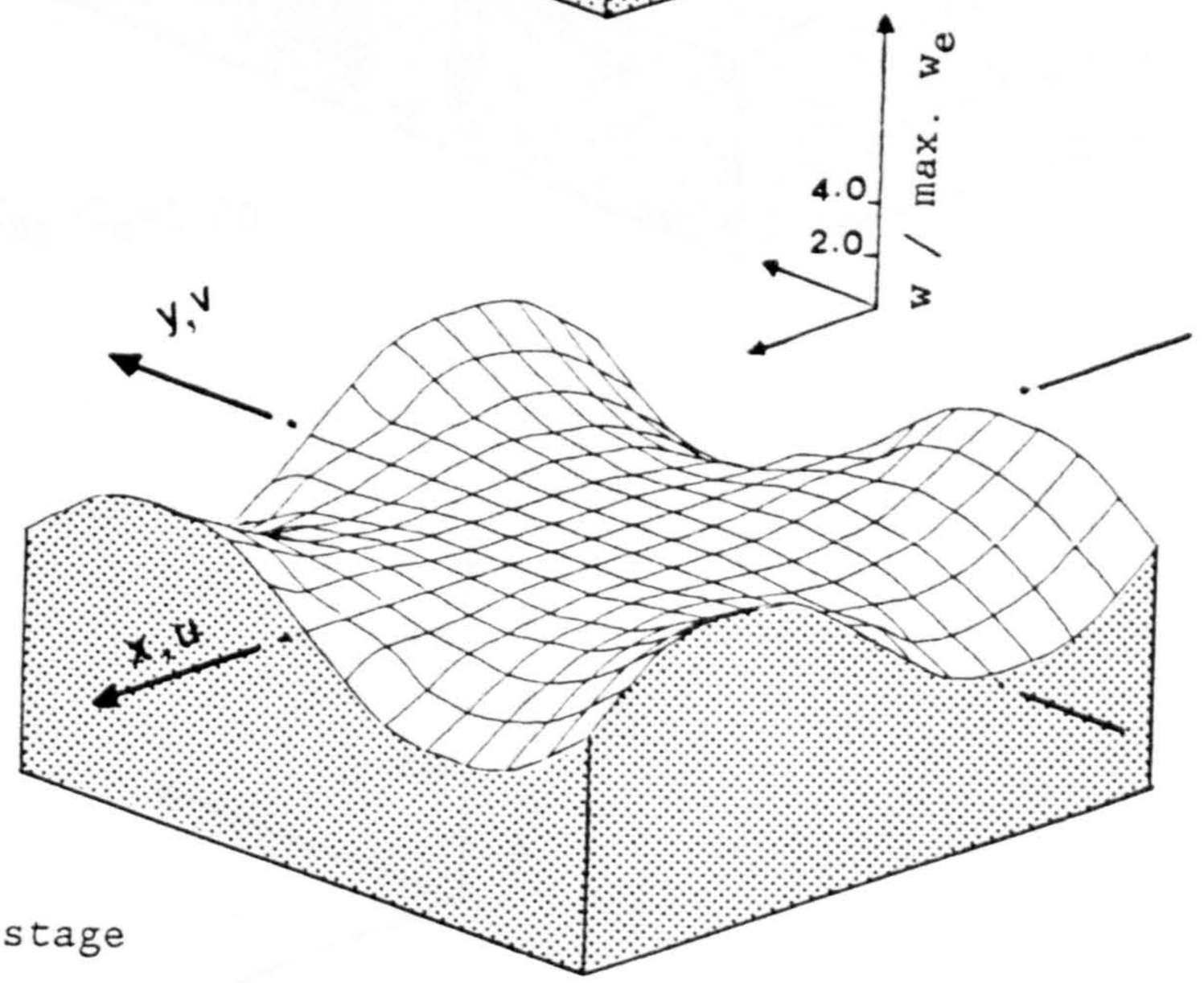

b) Elasto-plastic stage
T_{ep}/T_e=1.51

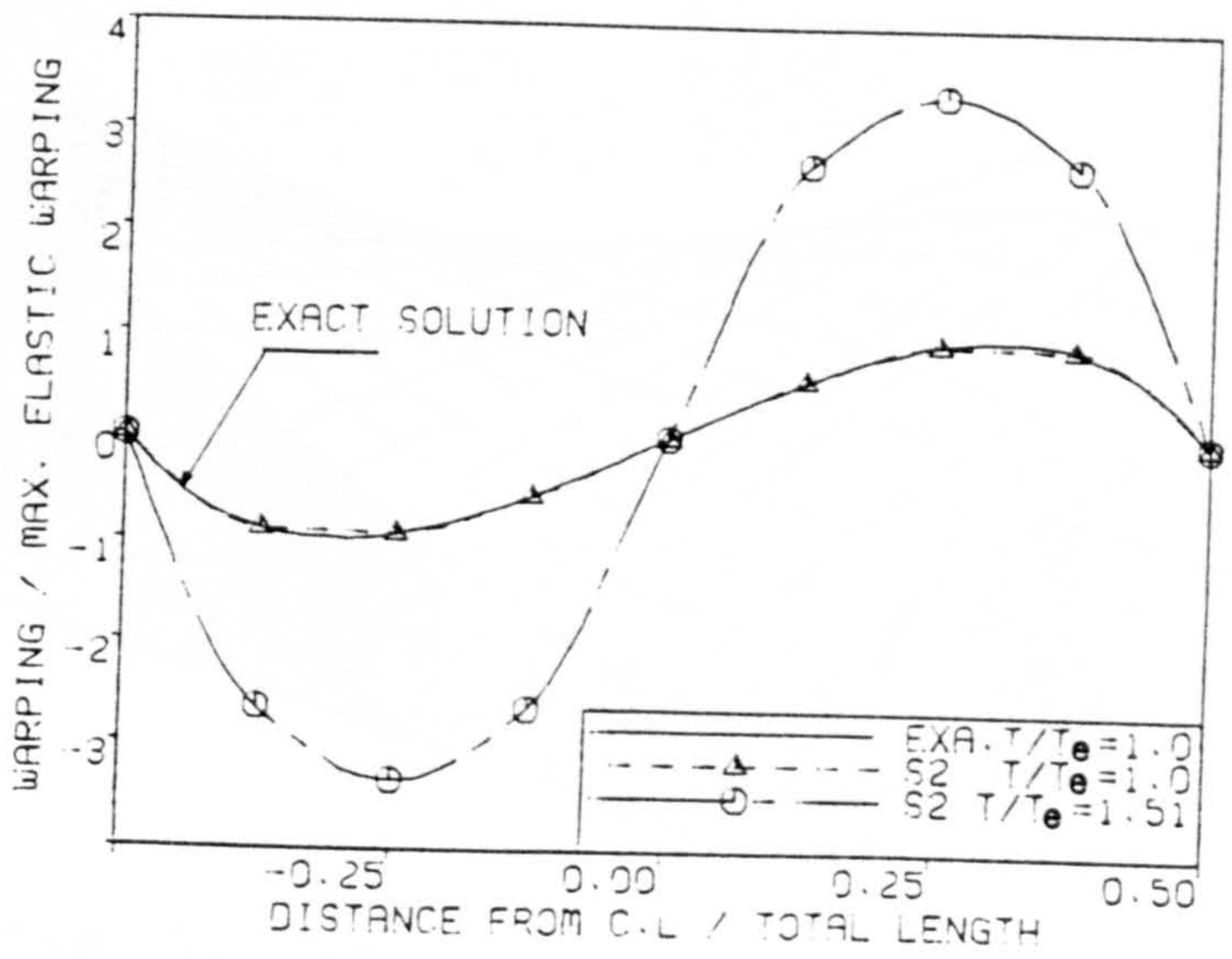

c) Distribution of warping displacement along the edges of the cross-section.

Fig. 5.18 Variation of the warping displacement in a member of square cross-section (beam S2).

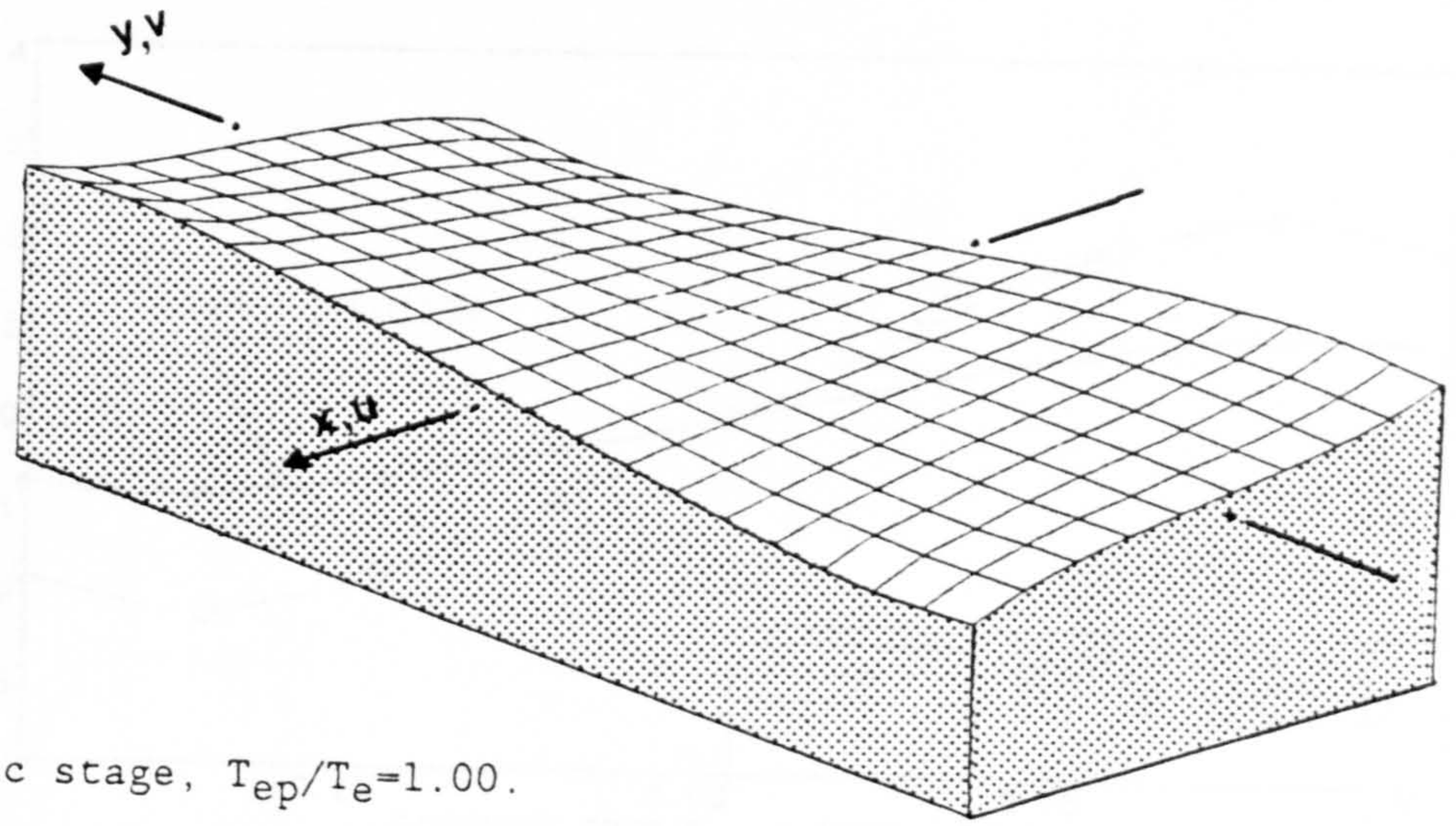

a) Elastic stage, T_{ep}/T_e=1.00.

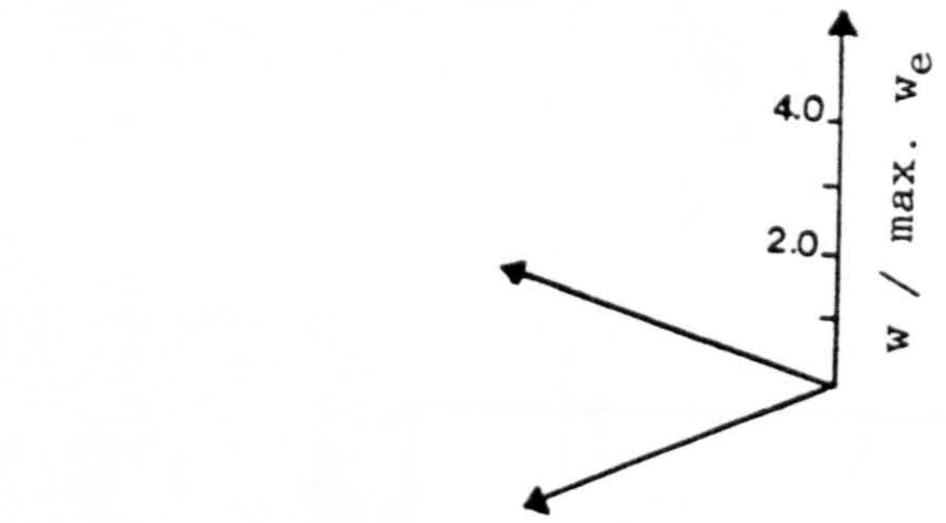

b) Elasto-plastic stage, T_{ep}/T_e=1.52.

Fig. 5.19 (cont.)

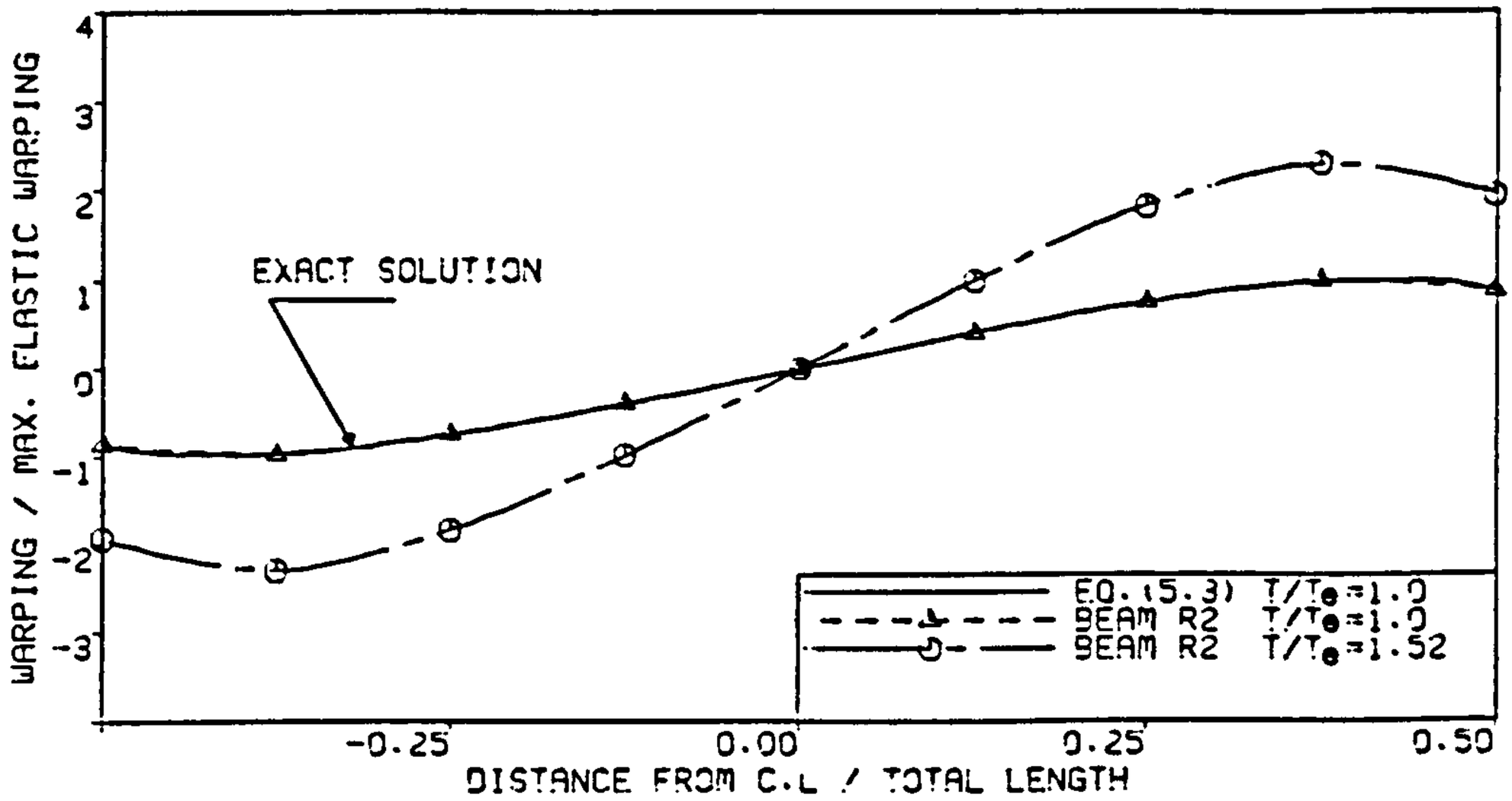

c) Distribution of warping displacement along the longer edge of the cross-section.

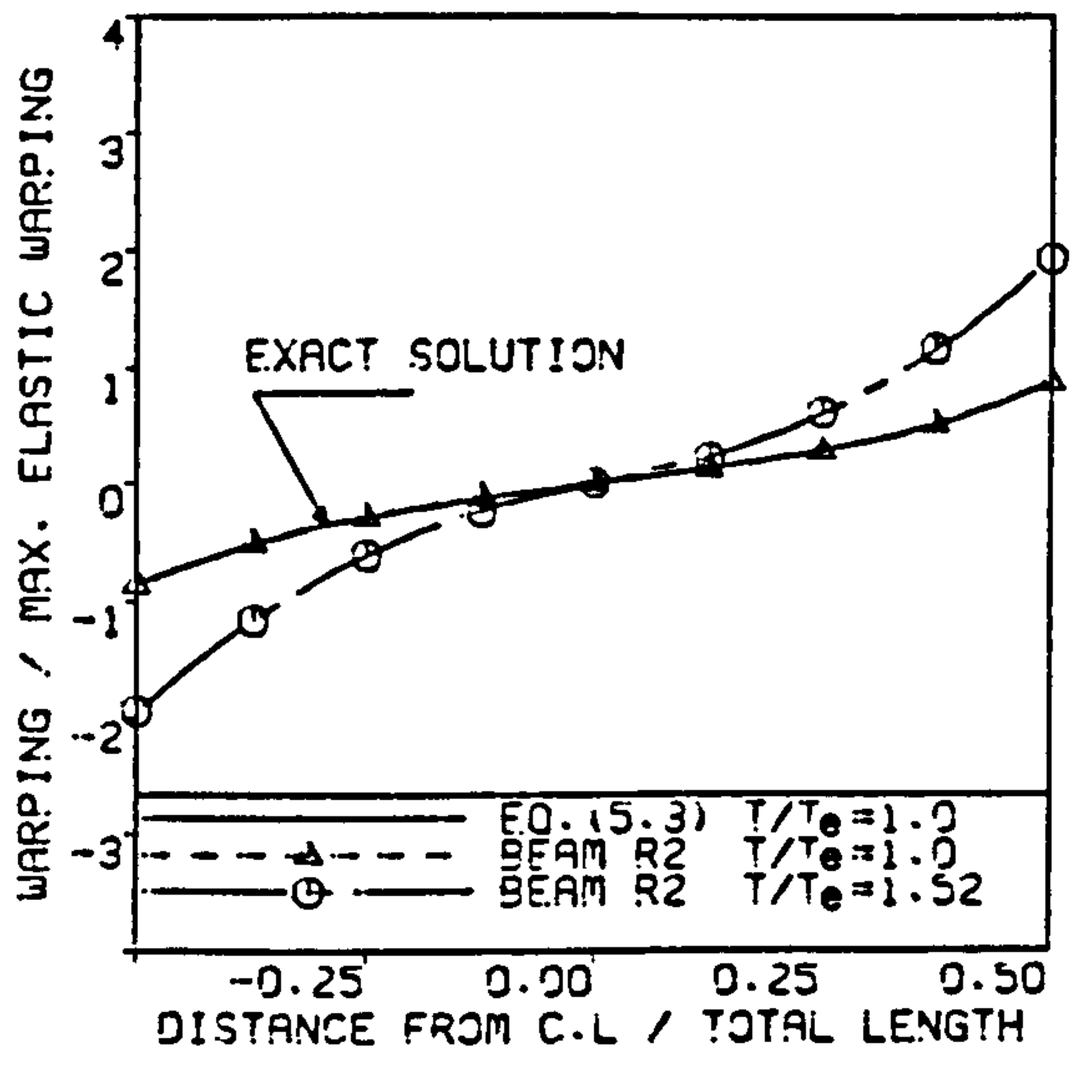

d) Distribution of warping displacement along the shorter edge of the cross-section.

Fig. 5.19 Variation of the warping displacement in a member of rectangular cross-section (beam R2).

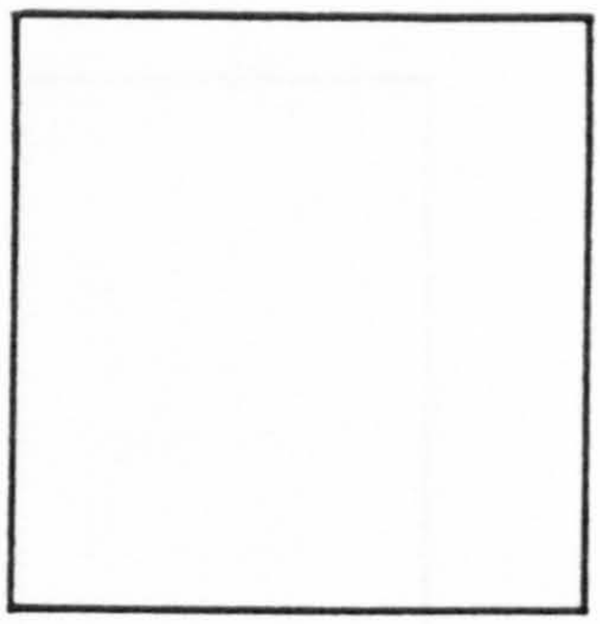

T_{ep}/T_e=1.00

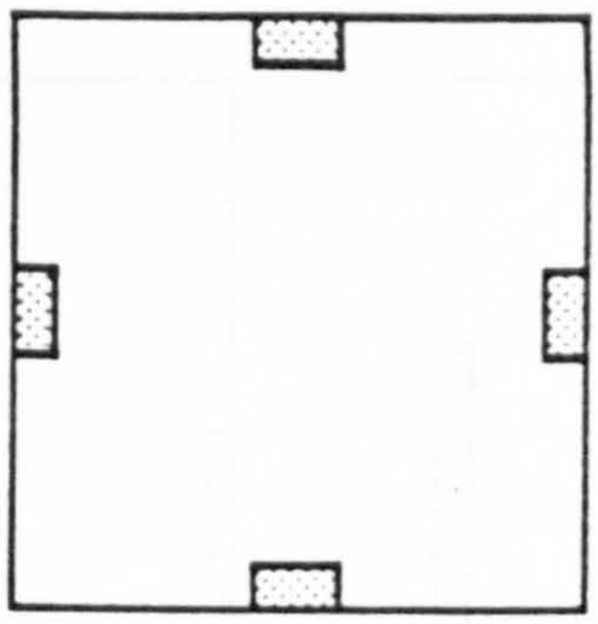

1.10

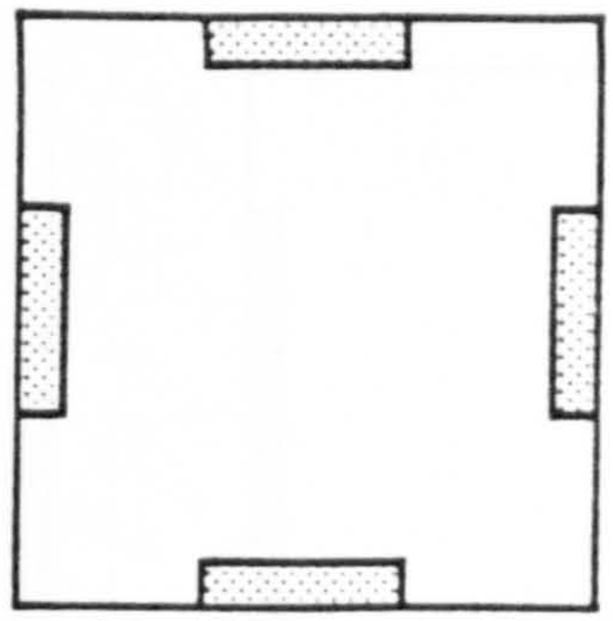

1.18

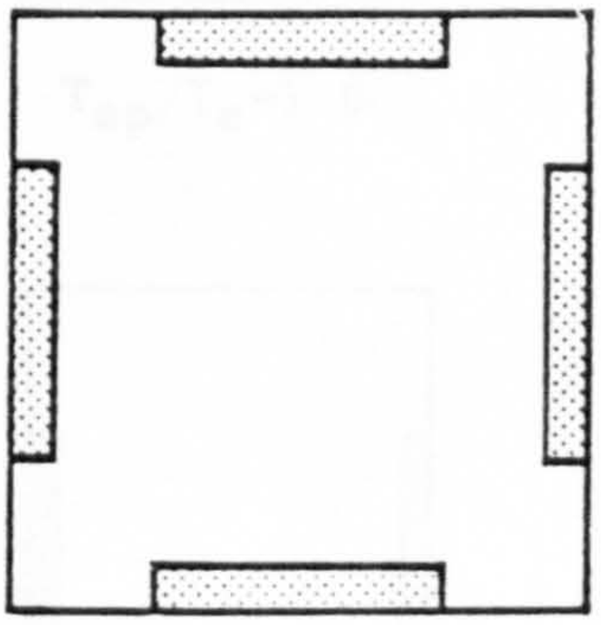

1.26

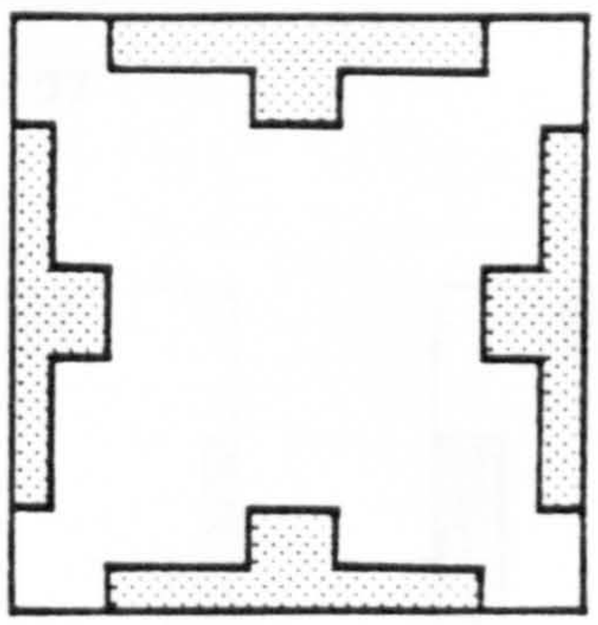

1.33

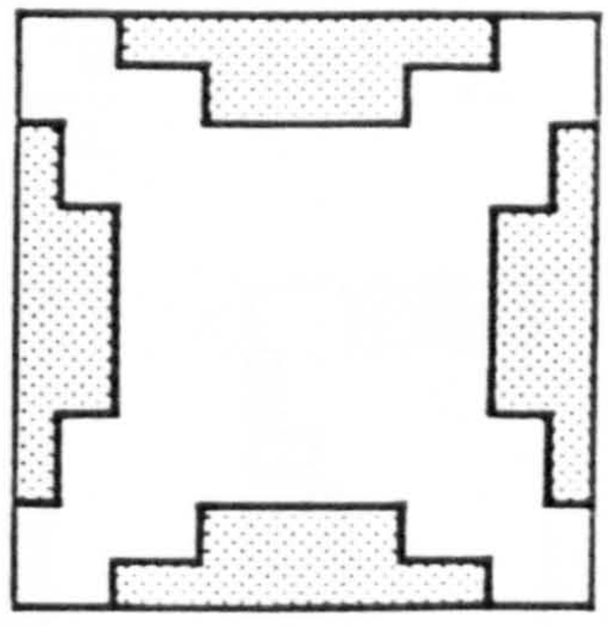

1.40

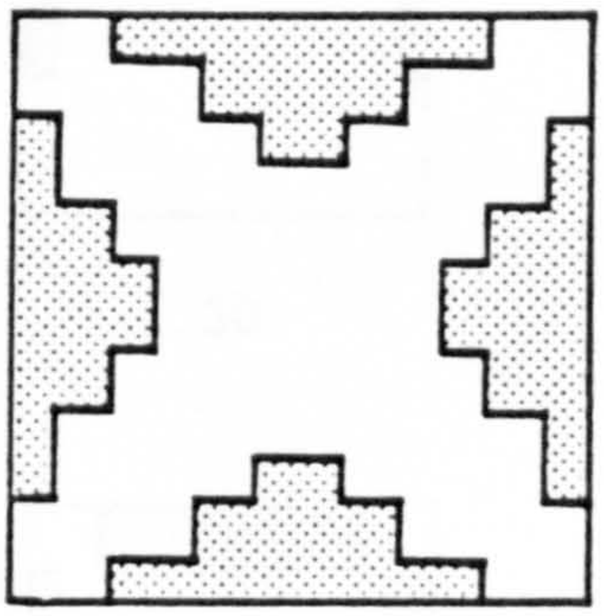

1.48

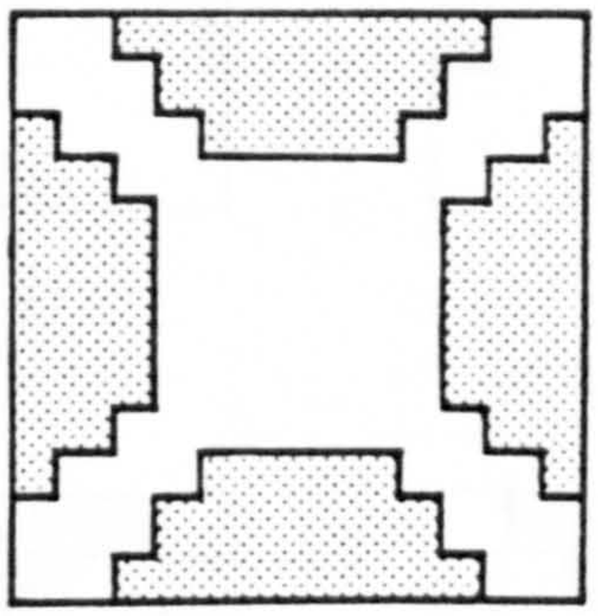

1.51

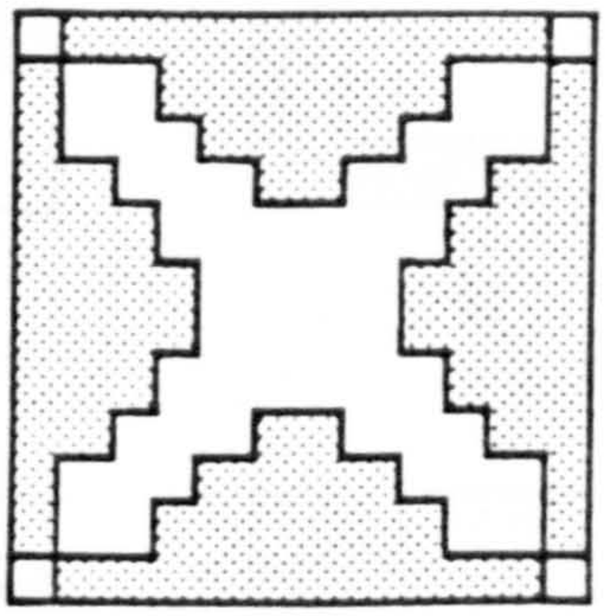

1.55

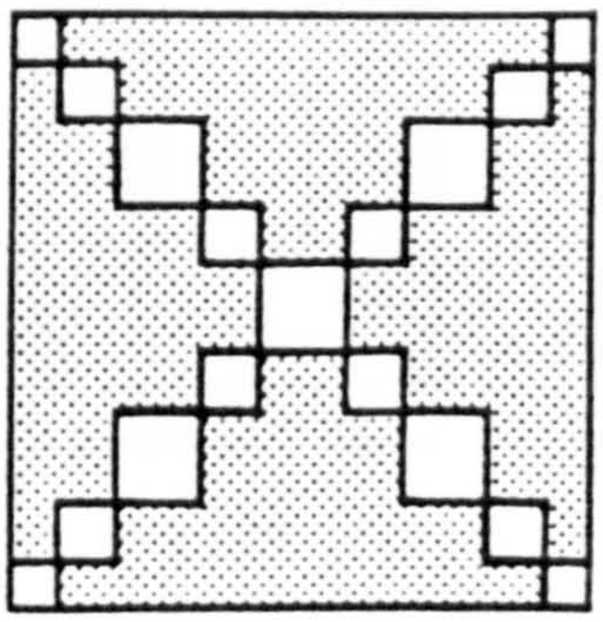

1.59

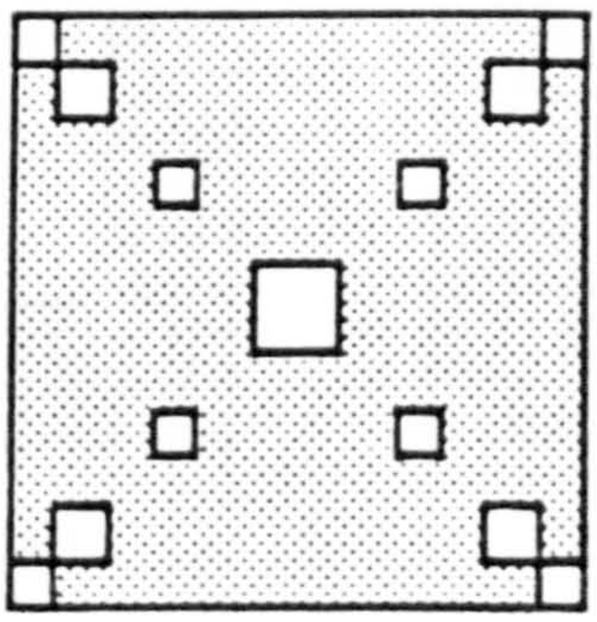

1.60

Fig. 5.20 Progress of the plastic regions in pure torsion for a member of square cross-section (beam S2).

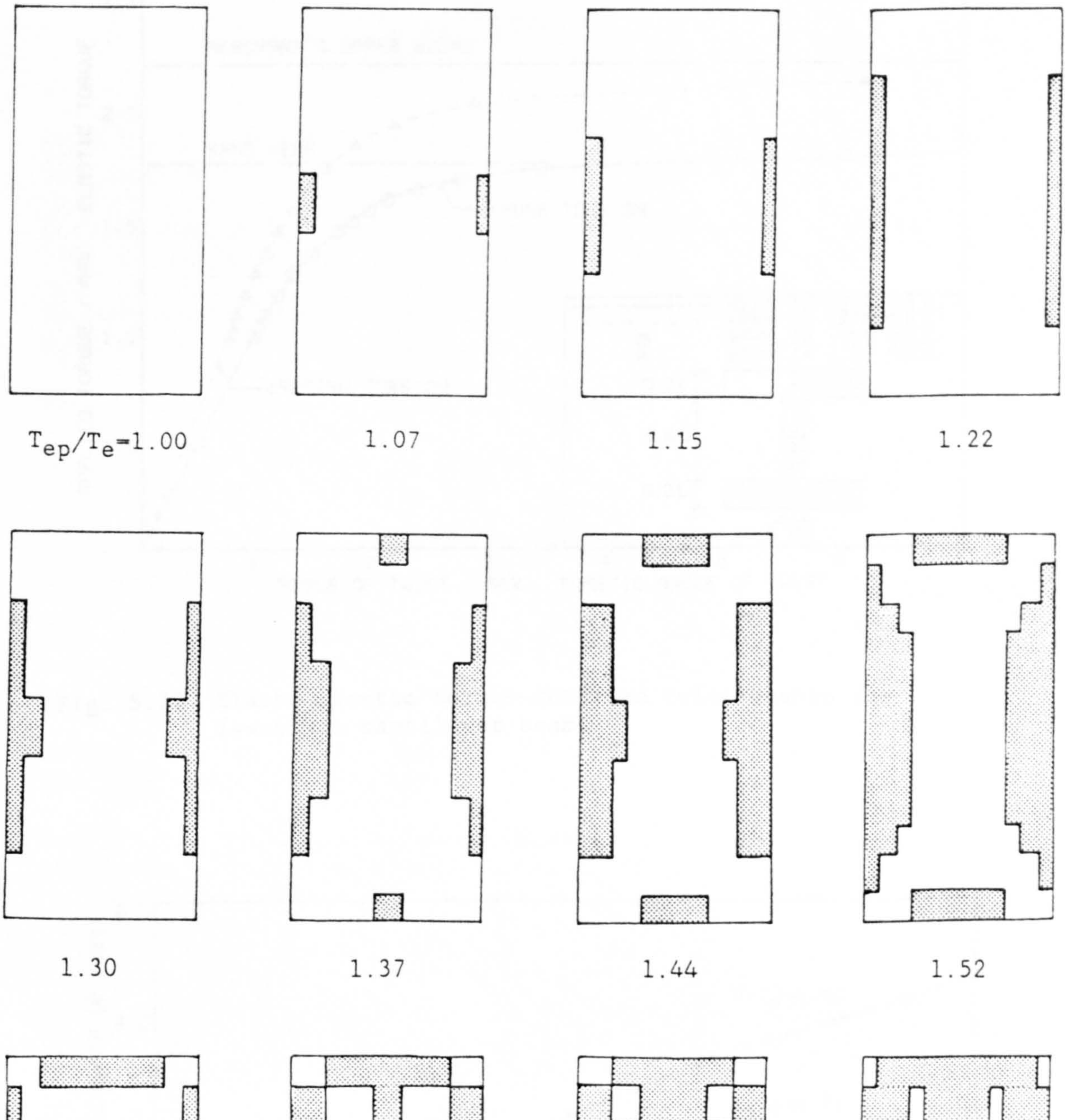

Fig. 5.21 Progress of the plastic regions in pure torsion for a member of rectangular cross-section (beam R2).

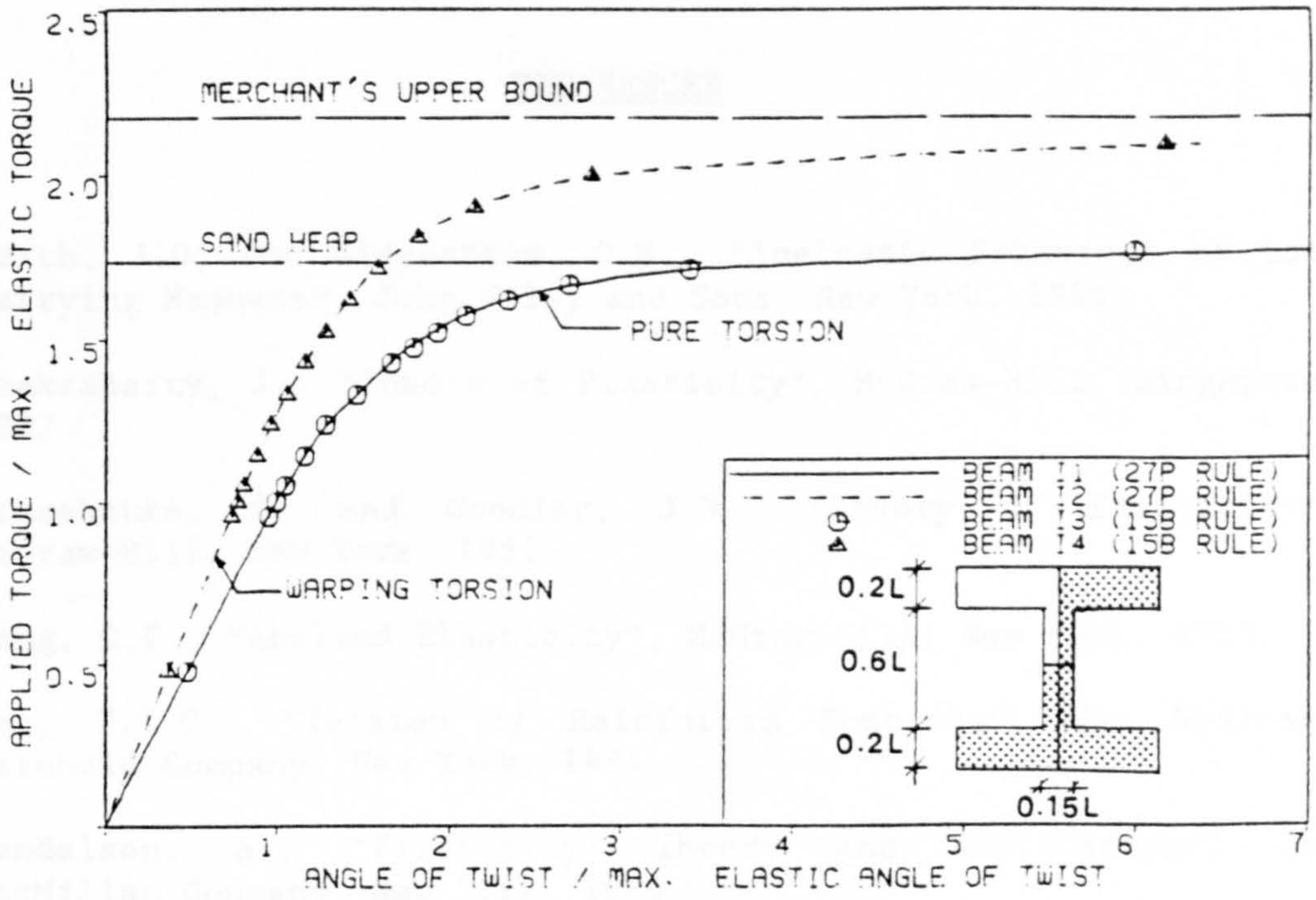

Fig. 5.22 Elasto-plastic torque-rotation relationship for I-section cantilever beams.

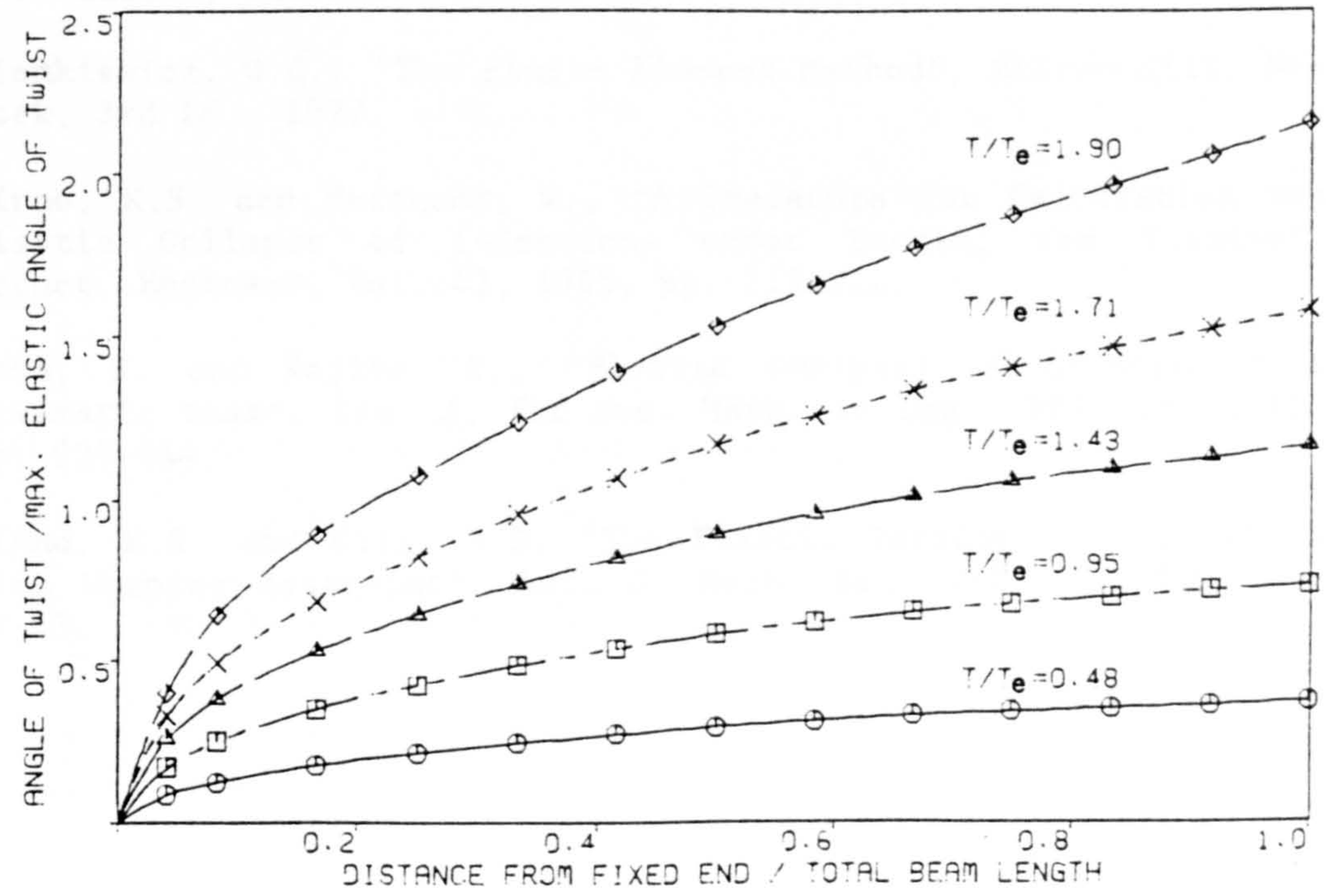

Fig. 5.23 Variation of the angle of twist per unit length for beam I2 for different stages of loading.

REFERENCES

1. Smith, J.O. and Sidebottom, O.M., "Inelastic Behaviour of Load Carrying Members", John Wiley and Sons, New York, 1965.

2. Chakrabarty, J., "Theory of Plasticity", McGraw-Hill, Singapore, 1987

3. Timoshenko, S. and Goodier, J.N., "Theory of Elasticity", McGraw-Hill, New York, 1951.

4. Wang, C.T., "Applied Elasticity", McGraw-Hill, New York, 1953.

5. Hsu, T.T.C., "Torsion of Reinforced Concrete", Van Nostrand Reinhold Company, New York, 1984.

6. Mendelson, A., "Plasticity: Theory and Application", The MacMillan Company, New York, 1968.

7. May, I.M. and Al-Shaarbaf, I.A.S., "Elasto-Plastic Analysis of Torsion Using a Three-Dimensional Finite Element Model", Comput. and Struct., Vol. 33, No. 3, 1989, pp. 667-678.

8. Hinton, E. and Owen D.R.J., "Finite Element Programming", Academic Press, London, 1977.

9. Dawe, D.J., "Matrix and Finite Element Displacement Analysis of Structures", Clarendon Press, Oxford, 1984.

10. Zienkiewicz, O.C., "The Finite Element Method", McGraw-Hill, New York, 3rd Ed., 1977.

11. Dinno, K.S. and Merchant, W., "A Procedure for Calculating the Plastic Collapse of I-Sections under Bending and Torsion", Struct. Engineer. Vol. 43, 1965, pp. 219-221.

12. Baba, S. and Kajita, T., "Plastic Analysis of Torsion of a Prismatic Beam", Int. J. for Num. Meth. in Eng., Vol. 18, 1982, pp. 927-944.

13. Dinno, K.S. and Gill, S.S, "The Plastic Torsion of I-Sections with Warping Restraint", Int. J. Mech. Sci. Vol. 6, 1964, pp. 27-43.

CHAPTER SIX

ANALYSIS OF REINFORCED CONCRETE PANELS IN SHEAR AND VOIDED SLAB STRIPS IN BENDING

6.1 Introduction

In this Chapter applications to test the computer program developed in the course of this study are presented. Two sets of problems have been analysed, reinforced concrete panels loaded in pure shear and voided slab strips under pure bending.

The ability of the constitutive model to simulate the behaviour of reinforced concrete subjected to longitudinal compression coupled with transverse tension is demonstrated through the analyses of panels tested by Vecchio and Collins [1]. The models described in Chapter 3 to reduce concrete compressive strength in presence of orthogonal cracking have been used and compared. Parametric studies to investigate the effects of shear retention, tension-stiffening and other important parameters are also presented.

All numerical tests were carried out on Amdahl 5980-300E computer. Finite element solutions have been compared with the results of experimental tests. A brief description of the tests is given, further details can be found in the references given in the text.

6.2 Reinforced Concrete Panels under Pure Shear

An extensive experimental study of the behaviour of reinforced concrete panels under in-plane shear and normal stresses has been carried out by Vecchio and Collins [1]. Results of this study revealed that deterioration of the concrete compressive strength is dependent on the transverse tensile strain after cracking. These findings can be used to substantially improve the capability of finite element models to predict the ultimate load of reinforced concrete members which fail in shear or torsional modes. Two of the panels, PV27 panel PV19, which were subjected to pure shear have been chosen for the present study. Both panels were tested under proportional monotonic in-plane shear up to failure. Panel PV27 experienced crushing of the concrete prior to yielding of the steel, while in panel PV19 the transverse reinforcement yielded before failure.

6.2.1 Description of the Panels

The panels were 890 mm. square by 70 mm. thick, symmetrically reinforced with two layers of wire mesh of 50 mm. grid. The steel wires were aligned parallel to the sides of the panel. A clear cover of 6 mm was provided between faces of the panel and the outer layers of the reinforcement. The reinforcing meshes were heat-treated and exhibited a very ductile response. The steel ratios used for panel PV27 were 0.01785 in both longitudinal and transverse directions. For panel PV19, the ratios were 0.01785 and 0.00713 in the longitudinal and transverse directions respectively. Two separate

concrete mixes were used for each panel. A relatively strong concrete was cast in the band around the perimeter of the panel; a weaker mix was cast in the central regions. This was done to assure that the ultimate failure of the panel was initiated away from the load transfer regions. The dimensions and loading arrangement of a typical panel are shown in Fig. 6.1.

The panels were tested in a specially designed loading rig capable of applying in-plane shear and direct tension or compression loading. The specimens were loaded by forces applied to shear keys uniformly distributed around the perimeter of the panel. If the applied forces were slightly inclined to the plane of the rig, they would have tended to push the panel out of the testing plane. Hence, a lateral support frame was provided to resist any out-of-plane forces and therefore the displacement perpendicular to the plane of the rig was restrained along the perimeter of the panel.

6.2.2 Test Observations

During testing of panel PV27, initial cracks inclined at 45 degrees with the horizontal axis were formed at a shear stress level of 2.04 N/mm^2. The crack direction did not change, nor did the steel reinforcement yield throughout the test. At a shear stress level of 5.24 N/mm^2, the first signs of crushing were observed. The concrete was extensively damaged at 6.24 N/mm^2 and ultimately a sliding shear failure of the panel took place at a stress of 6.35 N/mm^2.

When panel PV19 was tested, initial cracks formed, also at 45

degrees, at a shear stress level of 2.07 N/mm². No noticeable change in crack direction was observed until a stress level of 3.11 N/mm² above which the cracks began to change direction. At 3.45 N/mm², the transverse steel yielded and evidence of crushing and spalling of concrete was observed. Ultimately, a sliding shear failure of concrete occurred at 3.95 N/mm².

6.2.3 Finite Element Idealisation and Material Properties

Because the stresses are uniformly distributed throughout the specimen, generally only the central region of the panel has been considered in the finite element analyses. This region has been modelled using four quadratic brick elements with the reinforcing wires being placed in their correct positions. The finite element mesh, boundary conditions and loading arrangement used in the analyses are shown in Figs. 6.2 and 6.3. The material properties and the additional material parameters adopted for the numerical tests are listed in Table 6.1 for both panels considered.

The shear stresses have been applied, initially, in equal increments of 0.5 N/mm². Smaller increments were used at stress levels near the ultimate load. Except where otherwise stated, the 8 (2x2x2) point integration rule and a convergence tolerance of 2% have been used for the analyses. The modified Newton-Raphson method in which the stiffness matrix is updated at the 2nd, 12th, 22nd .... etc. iterations of each increment of loading has been adopted.

Table 6.1 Material properties and additional material parameters of Vecchio and Collins panels

Concrete	Panel PV27	Panel PV19
Young's modulus, E (N/mm^2)	20000	20000
Comp. strength, f'_c (N/mm^2)	20.5	19.0
Tensile strength, f_t (N/mm^2)	2.40	2.40
Poisson's ratio, ν	0.2	0.2
Uniaxial crushing strain	0.003	0.003
Steel		
Young's modulus, E_s (N/mm^2)	200000	200000
Longitudinal steel		
Steel ratio, ρ_h	0.01785	0.01785
Yield stress, f_y (N/mm^2)	442.0	458.0
Transverse steel		
Steel ratio, ρ_v	0.01785	0.00713
Yield stress, f_y (N/mm^2)	442.0	229.0
Hardening parameter, H'	0.00	0.00
Tension-stiffening parameters		
α_1	65.0	45.0
α_2	1.0	1.0
Shear retention parameters		
γ_1	10.0	10.0
γ_2	0.50	0.50
γ_3	0.10	0.10
Comp. strength reduction, Model A		
Comp. reduction parameter, k_1	0.50	0.55

Note: Where different material parameters have been used these are given in the text.

For panel PV27, the tension-stiffening parameter α_1 may be calculated from the experimental values of the principal tensile and compressive strains obtained by Vecchio and Collins [1]. Because equal percentages of steel have been used in both directions, cracks do not change direction during loading and they cross the reinforcement at 45 degrees. Thus, the tensile strain in the steel bars, ϵ_s, may be calculated for this particular panel from the principal values obtained from Mohr's circle for strains, Fig. 6.4, as

$$\epsilon_s = (\epsilon_1 + \epsilon_2)/2 \qquad (6.1)$$

From the experimental results given in [1], the ratio between the compressive and tensile principal strains for the last three stages of loading were -0.301, -0.333 and -0.328 respectively. Therefore, the principal compressive strain can be taken as,

$$\epsilon_2 = - \epsilon_1 / 3 \qquad (6.2)$$

Substitution of (6.2) into (6.1) yields,

$$\epsilon_s = \epsilon_1 / 3 \qquad (6.3)$$

When the steel wires yield, the tensile stress carried by the concrete between the cracks is assumed to fall to zero. From Fig. 3.10, the corresponding principal tensile strain may be expressed as,

$$\epsilon_1 = \alpha_1 \epsilon_{cr} \qquad (6.4)$$

Therefore, equation (6.3) may be rewritten as,

$$\epsilon_s - \epsilon_y = \alpha_1 \epsilon_{cr} / 3 \qquad (6.5)$$

where ϵ_y is the yield strain of the reinforcement given by,

$$\epsilon_y = f_y / E_s \qquad (6.6)$$

and ϵ_{cr} is the cracking strain of concrete given by,

$$\epsilon_{cr} = \sigma_{cr} / E \qquad (6.7)$$

Substitution of (6.6) and (6.7) into (6.5) yields,

$$\alpha_1 = 3 E f_y / E_s \sigma_{cr} \qquad (6.8)$$

By making use of the material properties given in Table 6.1 and taking the experimental value of the cracking stress, 2.04 N/mm², the tension-stiffening parameter α_1 is found from (6.8) to be equal to 65.

6.2.4 Results of the Analyses, Panel PV27

Graphs of the experimental and numerical shear stress-shear strain relationship for panel PV27 are shown in Fig. 6.5. The finite element solution is in good agreement with the experimental results throughout the entire behaviour of the panel. In the numerical test, the compressive strength has been reduced according to Cervenka's proposal, Model A. As in the experimental test, cracks occurred at

45 degrees with the horizontal axis at a shear stress level just above 2.0 N/mm². The predicted collapse stress was 6.25 N/mm² which is very close to the experimental value, 6.35 N/mm², and the predicted failure mode was crushing of concrete prior to yielding of the reinforcement.

To study the effect of reducing the compressive strength on the prediction of the collapse stress, a second analysis has been carried out with the compression strength reduction factor, λ, was set to unity, i.e $k_1 = 0.0$. The predicted failure stress was 8.0 N/mm² which is about 26% higher than the experimental value, Fig. 6.5. Milford and Schnobrich [2] analysed some of the panels tested by Vecchio and Collins using a rotating crack model. No attempt was made to model the degradation in compressive strength due to orthogonal cracking. However, results obtained by the Author and other researchers [3,4] for panel PV27, in which the principal directions did not change with increasing load, indicate that the inclusion of a compression strength reduction model is necessary to improve the finite element solutions, Fig. 6.5.

6.2.4.1 Effect of the boundary conditions

The numerical tests presented in the previous section have been carried out by considering the central region of the panel, Fig. 6.2. In these tests, the nodes along the perimeter of the finite element model were kept free to allow movement in the z-direction, Fig. 6.3. In order to simulate the effect of the lateral support frame used in the experimental work, the whole panel has been analysed using 16

quadratic brick elements, Fig. 6.6, with the nodes along the perimeter being restrained in the z–direction, w=0. As in the experimental work, a stronger concrete with a compressive strength of 31.2 N/mm² has been assumed for the elements in the outer band. The compressive strength for the inner four elements was 20.5 N/mm².

Results of this analysis are compared with the experimental work and the finite element analysis of the central region, Fig. 6.7. The figure shows that the effect of restraining the nodes along the perimeter in the z–direction may be neglected and therefore the rest of the finite element analyses can be carried out by only considering the central region of the panel.

6.2.4.2 Effect of the compression reduction parameter, k_1

The reduction in compressive strength due to transverse tensile strain has been taken into account using model A. In this model, the compression reduction factor λ is dependent on the parameter k_1 according to equation (3.15). Cervenka [4] showed that the value of k_1 which gave the best fit varied in the panels analysed and suggested an average value of 0.52. Three tests have been conducted in the present study with different values of k_1, Fig. 6.8. The predicted failure stresses were, 6.5, 6.25 and 6.0 N/mm² for k_1 equal to 0.45, 0.50 and 0.55 respectively. Results of the analyses confirm Cervenka's conclusion that the variation of the parameter k_1 has a negligible effect on the overall behaviour of the panel and only affects the collapse stress, Fig. 6.8.

6.2.4.3 Effect of compression strength reduction models

Three different models for reducing the compressive strength have been incorporated in the current study. These models are described in sections 3.3.5 and 3.4.2.6. Fig. 6.9 shows the finite element solutions obtained using Cervenka's proposal [3], model A with k_1 equal to 0.5, Vecchio and Collins's model [1], model B, and the modified Vecchio and Collins's model [5], model C. The predicted failure stresses for models A ,B and C were 6.25, 7.0 and 6.5 N/mm^2 respectively. The shear stress-shear strain curves obtained using models A and C are similar and in good agreement with the experimental results compared with the softer response obtained from model B.

Graphs of the compression reduction factor λ versus the applied shear stress are presented in Figs. 6.10, 6.11 and 6.12 for models A, B and C respectively. For each model, the numerical results are compared against the corresponding graphs obtained by substituting the experimental principal strains listed by Vecchio and Collins into the expression for the reduction factor. Figs. 6.10 and 6.12 show that the compression reduction factor of models A and C decreases almost linearly as the applied shear stress increases. This is because the reduction factor is a decreasing function of the tensile strain which increases with increasing shear stress, equations (3.15) and (3.18). For model B, the reduction factor decreases at a decreasing rate for shear stresses less than 4.0 N/mm^2. Above this level of stress, the reduction factor increases slightly as the applied stress increases, Fig. 6.11. This is because the reduction factor expressed by (3.14) is a function of the ratio between the

tensile and compression strains rather than the tensile strain only.

6.2.4.4 Effect of integration rule and element size

The central region of the panel shown in Fig. 6.2 has been analysed using the 27 (3x3x3) point integration rule. Because the stresses are uniformly distributed throughout the panel, the shear stress-shear strain curve obtained is very close to that of the 8 point rule, Fig. 6.13. When the size of the brick elements used was reduced from 200x200x70 mm. to 100x100x70 mm., see Fig. 6.14, the results obtained for both rules are also similar and in good agreement with experimental results, Fig. 6.15.

6.2.5 Results of the Analyses, Panel PV19

The finite element solutions obtained for panel PV19 are compared with the experimental results in Fig. 6.16. The finite element mesh and the additional material parameters adopted are shown in Fig. 6.2 and given in Table 6.1 respectively. Good agreement with the experimental results has been obtained throughout the entire behaviour. As in the experimental test, initial cracks formed at 45 degree at an applied stress level just above 2.0 N/mm^2. The transverse reinforcement yielded at a stress level between 3.5 and 3.75 N/mm^2 which is close to the experimental value, 3.45 N/mm^2. Although a fixed crack model has been used in the present work, the collapse stress can be reasonably predicted by reducing the concrete compressive strength according to model A. The failure stresses

obtained from the numerical tests were 4.05 and 4.25 N/mm² for a compression reduction parameter k_1 of 0.55 and 0.5, Fig. 6.16. These values were higher than the experimental collapse stress, 3.95 N/mm², by 3% and 8% respectively. When k_1 was set to 0.0, λ = 1.0, the failure stress was 5.0 N/mm² which is higher than the actual value by about 27%. In all cases, ultimate failure of the panel occurred due to concrete crushing.

In all the numerical tests, the variation of the parameter k_1 has a negligible effect on the behaviour before and during yielding of the transverse reinforcement, Fig. 6.16. Following yielding of the transverse reinforcement, the shear strain increased significantly with small changes in shear stress. At the end of this stage, the panel started to carry additional load. Finally, a crushing failure of concrete took place at a load level dependent on the value of the parameter k_1, Fig. 6.16. This stage of behaviour only occurred in the numerical tests probably because a fixed crack model has been used in the study. In the physical tests, the crack directions changed after yielding [1].

6.2.5.1 Effect of the tension-stiffening parameter, α_1

For panel PV19, an analysis similar to that presented in section 6.2.3 for panel PV27 to calculate the tension-stiffening parameter α_1 is not possible because the principal strain direction varies after cracking. Therefore, a relationship between the tensile strains in the reinforcement and the principal strains can not be precisely determined. In order to select a suitable value for α_1, four

numerical tests have been carried out with values of α_1 ranging from 40 to 55. The finite element solutions are compared with the experimental results in Fig. 6.17. A response softer than the experimental results has been obtained for α_1 = 40 and the collapse stress was smaller than the experimental value. A stiffer behaviour has been obtained for α_1 = 55. A value of α_1 = 45 represents a reasonable estimation, Fig 6.17.

It is worth noting that the tension-stiffening parameter α_1 may affect the reduction factor λ. When α_1 decreases, the tensile strain increases and therefore the compression reduction factor will decrease correspondingly, equations (3.15) and (3.16).

6.2.5.2 Effect of the shear retention parameters

All the numerical tests described up to this point have been conducted by setting the values of the parameters γ_1, γ_2 and γ_3 to 10.0, 0.5 and 0.1 respectively, Table 6.1. Because the principal directions of the strains and stresses can change after cracking, panel PV19 has been chosen to study the effects of these parameters. Therefore, numerical tests with different values for the shear retention parameters were conducted. One parameter is considered to vary in each test, the other two parameters being set constant in order to isolate the effects of the parameter considered.

Fig. 6.18 shows that the variation of the parameter γ_1, which represents the rate of decay of shear stiffness, from 10 to 20 has negligible effect on the behaviour of the panel. At a stress level

of 3.5 N/mm², just before yielding of steel, the tensile strain was found to be greater than twenty times the cracking strain. Therefore for both values of γ_1 considered, the value of the shear reduction factor β was 0.1. A similar conclusion can be drawn from Fig. 6.19 for the variation of the parameter γ_2, which represents the sudden loss in shear stiffness at the instant of cracking, from 0.5 to 1.0.

To study the effects of the parameter γ_3, which represents the residual shear stiffness due to dowel action, three tests have been carried out with γ_3 equal to 0.2, 0.1 and 0.01. Results of the analyses are shown in Fig. 6.20. A relatively stiffer response has been obtained for γ_3 = 0.2. When γ_3 was set to 0.01 a premature failure occurred at applied stress level of 3.3 N/mm². This failure was due to the inadequacy of the assumed residual shear stiffness to provide enough stress to equilibrate the external shear forces.

For panel PV27, the variation of the parameter γ_3 has a negligible effect on the overall behaviour of the panel. Fig. 6.21 shows that all the finite element solutions are similar for the values of γ_3 considered. The collapse load is the same, even for a value of γ_3 equal to 0.01, because the principal directions did not change after cracking.

6.3 Reinforced Concrete Voided Slab Strips under Pure Bending

Concrete slabs containing longitudinal circular voids to reduce self weight are a common form of construction for bridges , and are also used in buildings. The structural response of such slabs and

the stiffening effect of concrete between major cracks have been investigated experimentally by Oduyemi and Clark [6,7]. A total of fifteen 1 to 3.33 scale model simply supported slab strips have been tested. Each of these strips, which represents a single internal cell of a bridge section, had a centrally placed circular void running in the longitudinal direction. The main variables considered in the investigation were the steel percentage, the void ratio, diameter and spacing of reinforcing bars and minimum cover to the reinforcement [8].

Although the strips were subjected to uniaxial bending, a full three-dimensional finite element idealisation is required to model the strip because of the presence of the circular void. Three strips have been chosen for this study. The selected strips which were designated as L9, L10 and L11 had the same dimensions, void ratio, bar diameter and concrete cover. They only differed with each other in the amount of reinforcement provided.

6.3.1 Description of the Strips and Test Observations

The strips had a 300 mm. square cross-section and were 3400 mm. long. The voids were formed from 1500 mm. long polystyrene cylinders. Each strip was tested under a four point loading system which gave a constant moment zone of 1200 mm. and two shear spans of 975 mm. each. The reinforcement consisted of longitudinal bars and closed stirrups uniformly distributed over the shear spans. There were no stirrups in the pure bending zone. The minimum clear cover to the main bars was 16 mm and the reinforcing steel was hot-rolled

deformed bars. The dimensions, loading arrangement and reinforcement details for a typical strip, L9, are given in Fig. 6.22.

The strips were tested in an inverted position to facilitate crack width measurements on the tension face. The load was applied to a spreader beam by means of hydraulic jack. The spreader beam applied the loads by way of rollers at the two points shown in Fig. 6.22. Concrete surface strains were measured, within the constant zone only, on the tension face and at two levels on each side of the strip. The strains were measured over a 101.6 mm. (4 in.) gauge length using a Demec mechanical gauge.

The data from the experimental tests carried out have revealed that the distribution of the average strains across the cross-section is linear and the actual neutral axis depth, with reference to the compression face, decreases after cracking as the applied load increases. Before cracking, the moment-curvature curves obtained for all strips were approximately linear and the experimental curvature increased faster when cracking occurred [8].

6.3.2 Finite Element Idealisation and Material Properties

By taking advantage of symmetry, only one quarter of the strip has been used in the finite element analyses. The quarter considered was modelled using twenty quadratic brick elements. The finite element mesh, boundary and symmetry conditions and loading arrangement used are shown in Fig. 6.23. The external forces and the corresponding reactions were modelled as line loads uniformly

distributed across the width of the strip. The material properties and the additional material parameters adopted in the analyses are given in Table 6.2.

The external loads have been applied in equal increments. The resulting increment of moment, at the constant bending zone, was 5 kN.m. The numerical tests have been carried out using the 15b point rule. A convergence tolerance of 5% and the modified Newton-Raphson method in which the stiffness matrix is updated at the 2nd, 12th, 22nd ... etc. iterations of each loading increment have been adopted. Line searches have been implemented in all tests to speed up convergence.

6.3.3 Results of the Analyses

The numerical moment-curvature relations obtained for strip L9, L10 and L11 are compared with test results in Figs. 6.24, 6.25 and 6.26 respectively. The figures show that both the initial and post-cracking stiffnesses are reasonably predicted. As in the experimental tests, the predicted moment-curvature relations were approximately linear before cracking and the curvature increased faster after the cracking moment is exceeded. The computed failure moment for all the strip considered was only slightly higher than the experimental one. For strips L9 and L10, where amount of reinforcement was relatively small, the numerical tests show that the reinforcement bars have yielded at failure. However, for strip L11, which was heavily reinforced, the predicted mode of failure was crushing of concrete prior to yielding of reinforcing steel.

Table 6.2 Material properties and additional material parameters of Oduyemi and Clark voided slab strips.

Concrete	Strip L9	Strip L10	Strip L11
Young's modulus, E (N/mm^2)	24500	26500	25800
Comp. strength, f'_c (N/mm^2)	26.3	29.9	29.4
Tensile strength, f_t (N/mm^2)	2.55	3.16	2.90
Poisson's ratio, ν	0.2	0.2	0.2
Uniaxial crushing strain	0.003	0.003	0.003
Steel			
Young's modulus, E_s (N/mm^2)	201000	201000	201000
Tension reinforcement			
Bar diameter, mm	16	16	16
No. of bars	2	3	8
Yield stress, f_y (N/mm^2)	502.0	502.0	502.0
Area of steel, mm^2	402.0	603.0	1608.0
Compression reinforcement			
Bar diameter, mm	–	–	8
No. of bars	–	–	2
Yield stress, f_y (N/mm^2)	–	–	491.0
Area of steel, mm^2	–	–	100.0
Hardening parameter, H'	0.00	0.00	0.00
Tension-stiffening parameters			
α_1	15.0	15.0	15.0
α_2	0.6	0.6	0.6
Shear retention parameters			
γ_1	10.0	10.0	10.0
γ_2	0.50	0.50	0.50
γ_3	0.10	0.10	0.10
Comp. strength reduction, Model A			
Comp. reduction parameter, k_1	0.55	0.55	0.55

Note: Where different material parameters have been used these are given in the text.

All the numerical results have been obtained with the compression reduction parameter k_1 set to 0.55. To investigate the effect of reducing the compressive strength of concrete on the post-cracking behaviour and predicting the ultimate moment, numerical tests with k_1 was set to 0.0 have also been carried out. As expected for members under pure bending, results of the analyses revealed that the reduction of concrete compressive strength has a negligible effect on the overall behaviour and collapse moment, Figs. 6.24 - 6.26.

Variation of the compression zone depth after cracking has been analytically investigated for the three strips considered. Fig. 6.27 show that the neutral axis shifts at a decreasing rate towards the compression face as the applied moment increases. It can be also seen that the depth of compression zone decreases with decreasing amount of reinforcement.

In reinforced concrete flexural members, variation of the tension-stiffening parameter α_1 can strongly affect the predicted post-cracking response. To investigate this effect, numerical tests have been carried out for strips L9 and L10 with values of α_1 equal to 10, 15, 20 and zero. In these tests, α_2 was set to 0.6. Results of the analyses show that the variation of the parameter α_1 can considerably affect the behaviour at early post-cracking stages, Figs. 6.28 and 6.29. A response softer than the experimental moment-curvature relation has been obtained for α_1 equal to zero, i.e the no tension-stiffening case. When α_1 was set to 20, the behaviour was relatively stiff compared with the experimental results. The finite element solutions show that as the curvature increases, the tension-stiffening effect becomes progressively insignificant and can be neglected at very high curvatures, Figs. 6.28 and 6.29.

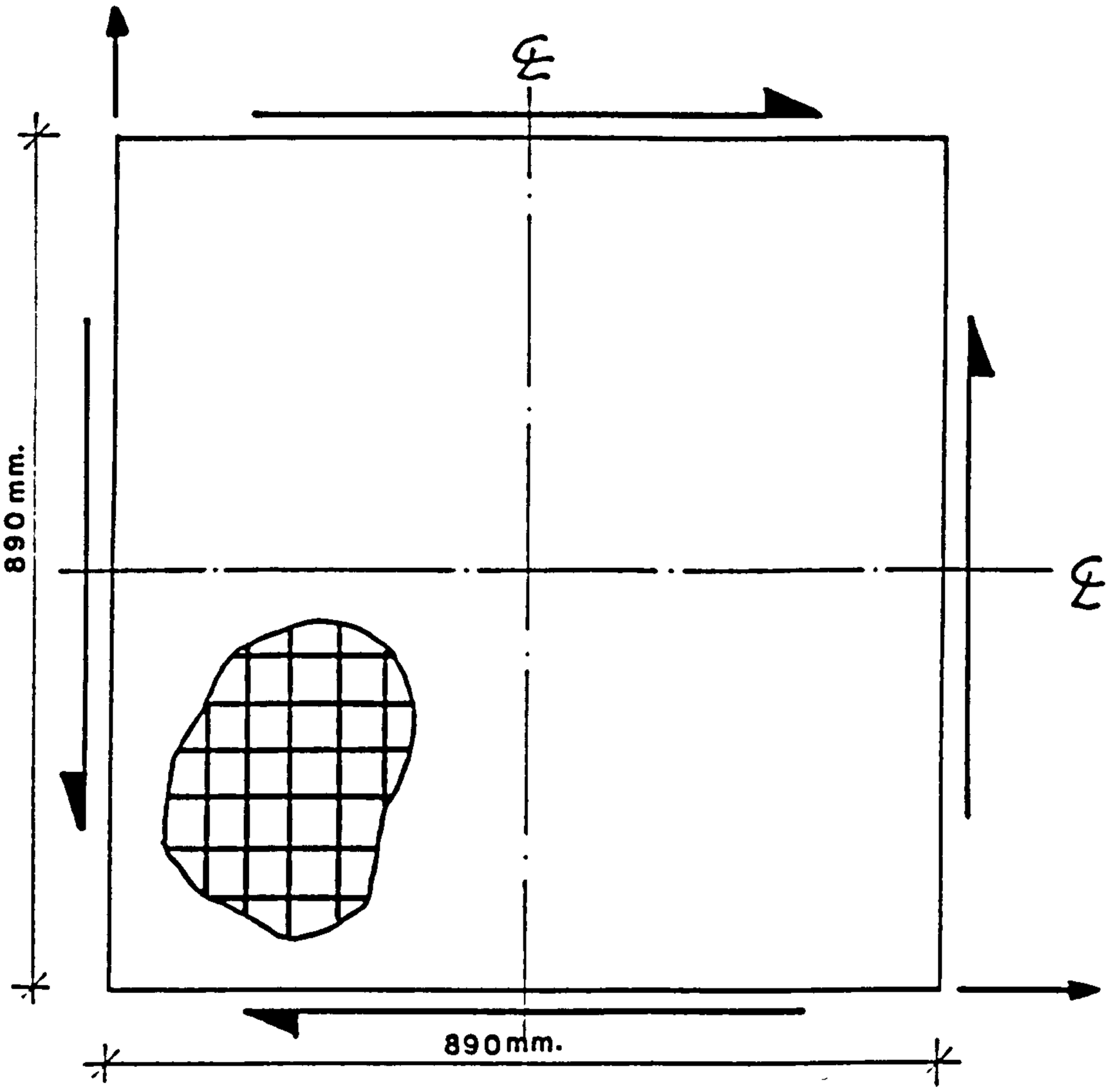

Fig. 6.1 Dimensions and loading arrangement of a typical Vecchio and Collins panel.

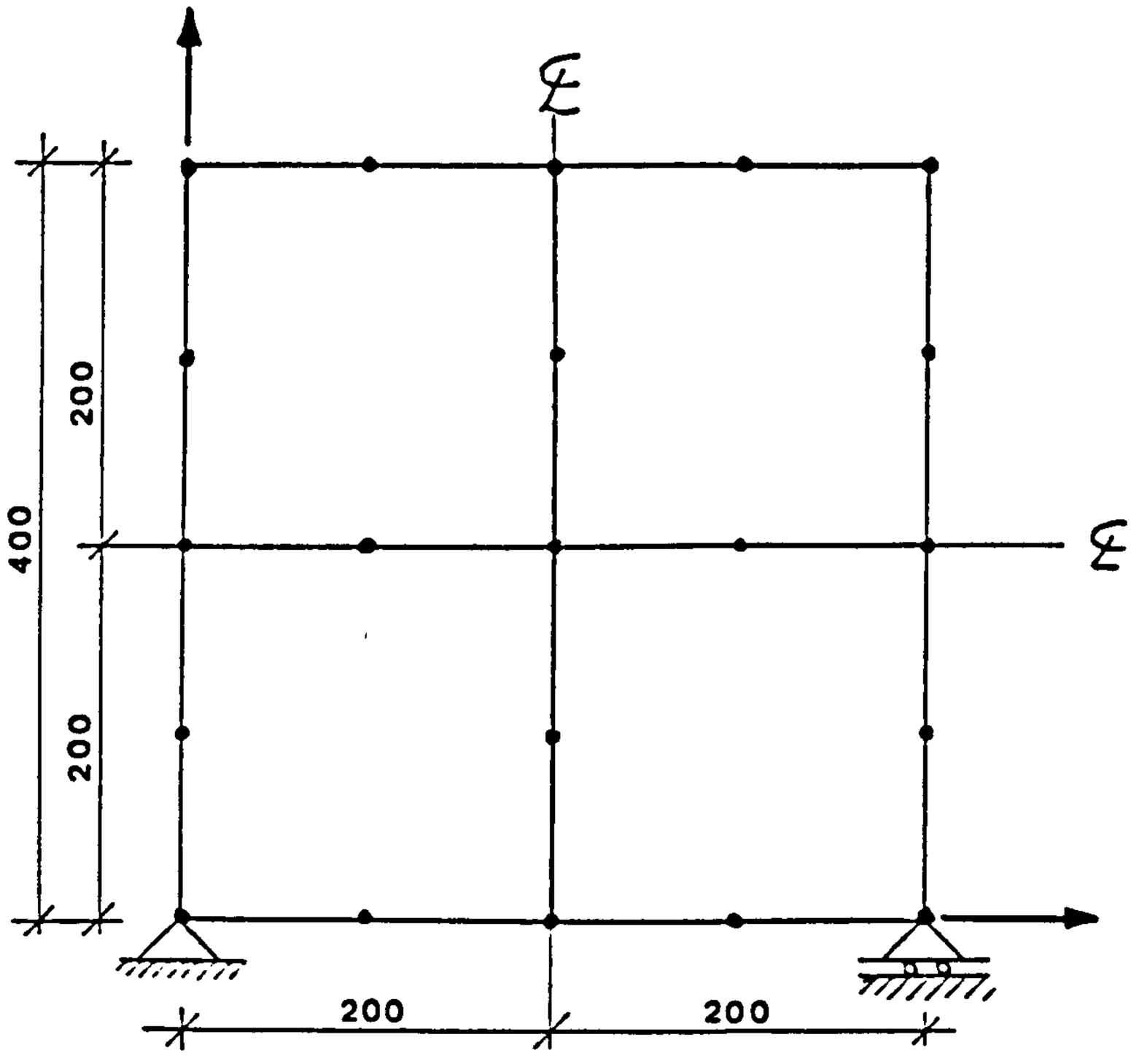

Fig. 6.2 Finite element mesh and boundary conditions used for Vecchio and Collins panels.

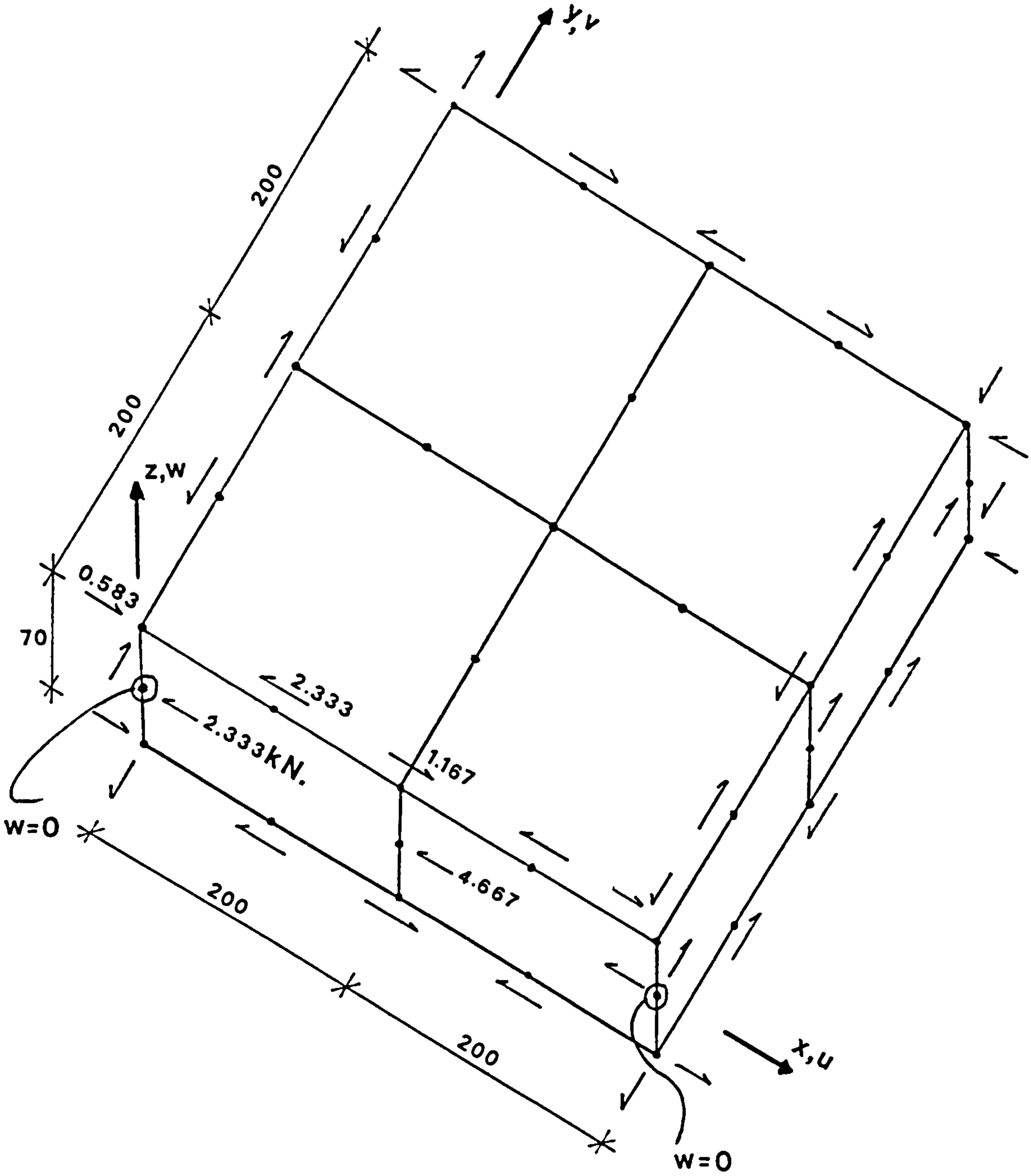

Fig. 6.3 Finite element mesh and nodal forces for an applied shear stress of 0.5 N/mm².

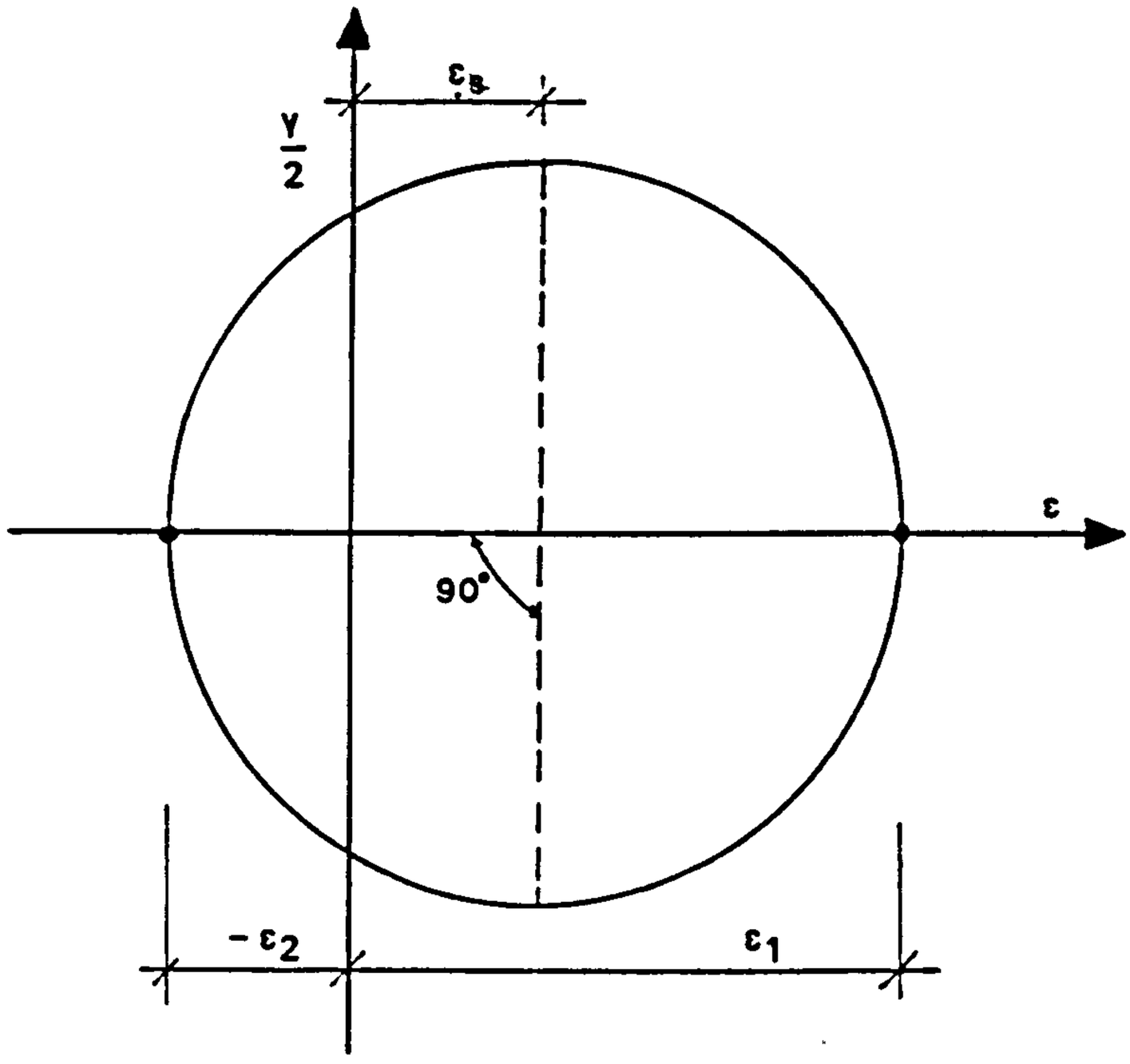

Fig. 6.4 Mohr's circle for average strains.

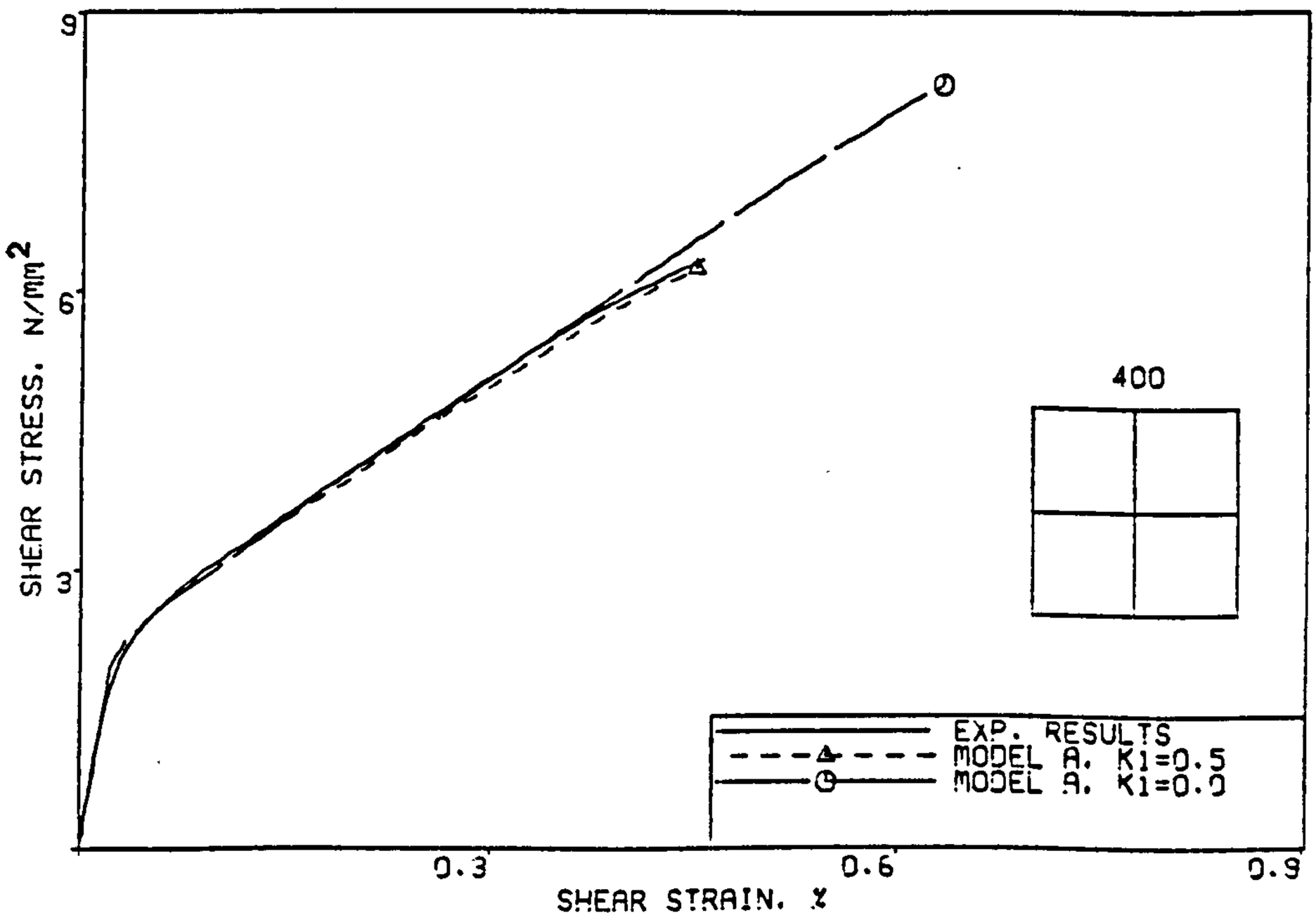

Fig. 6.5 Effect of the compressive strength reduction factor, λ, on the behaviour of panel PV27.

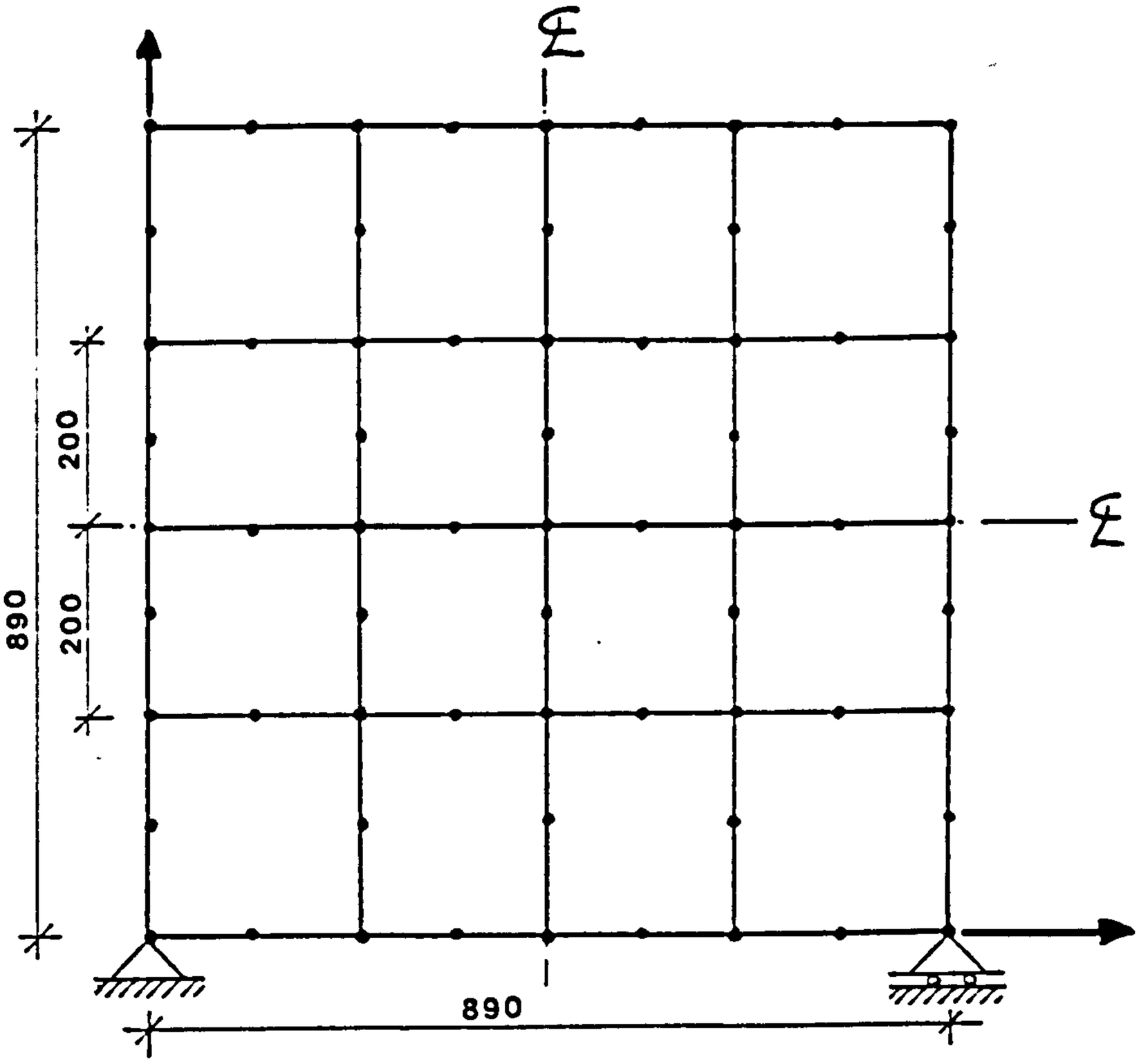

Fig. 6.6 Finite element mesh and boundary conditions for panel PV27.

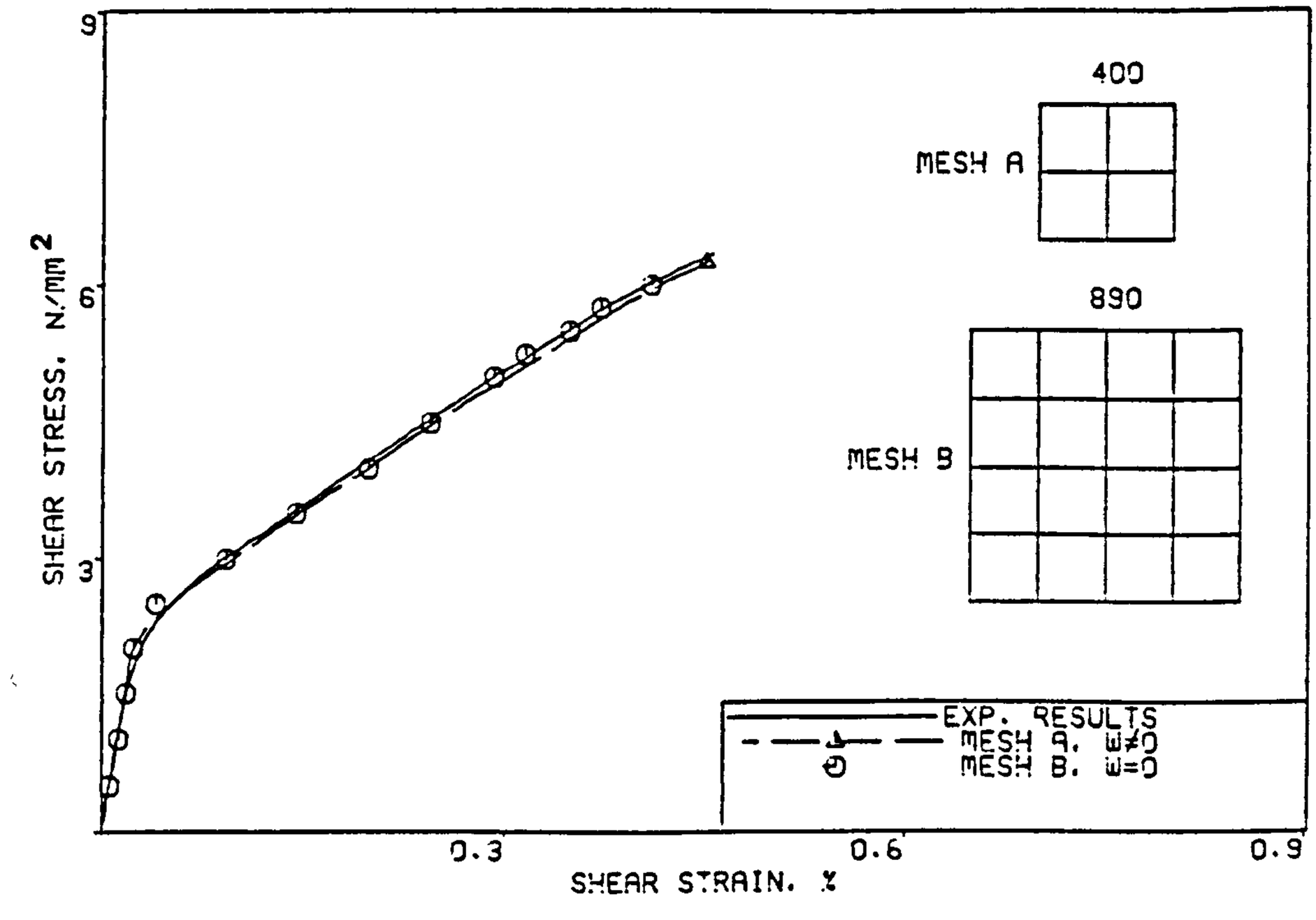

Fig. 6.7 Effect of the boundary conditions on the behaviour of panel PV27.

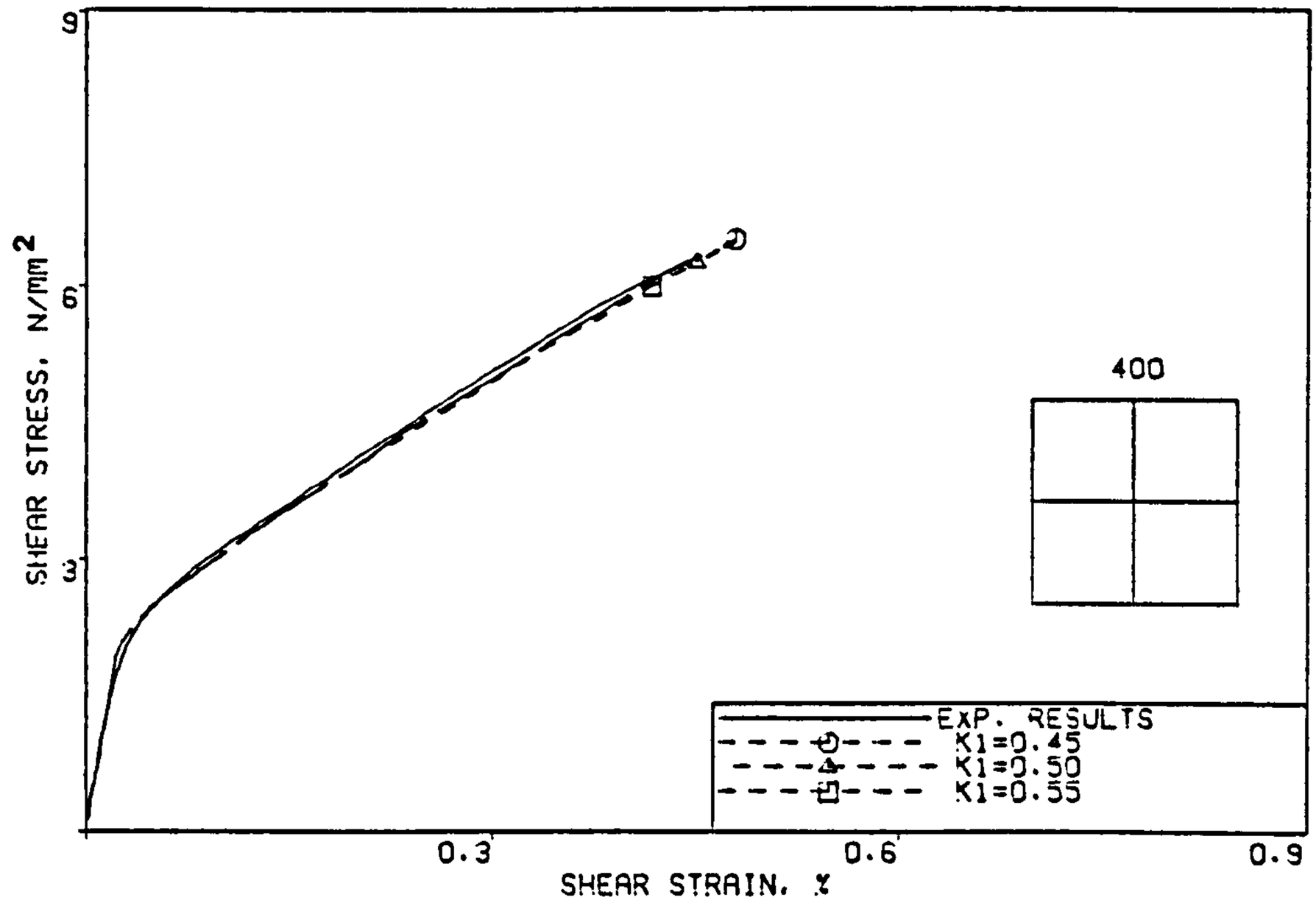

Fig. 6.8 Panel PV27 - Effect of the compression reduction parameter, k_1.

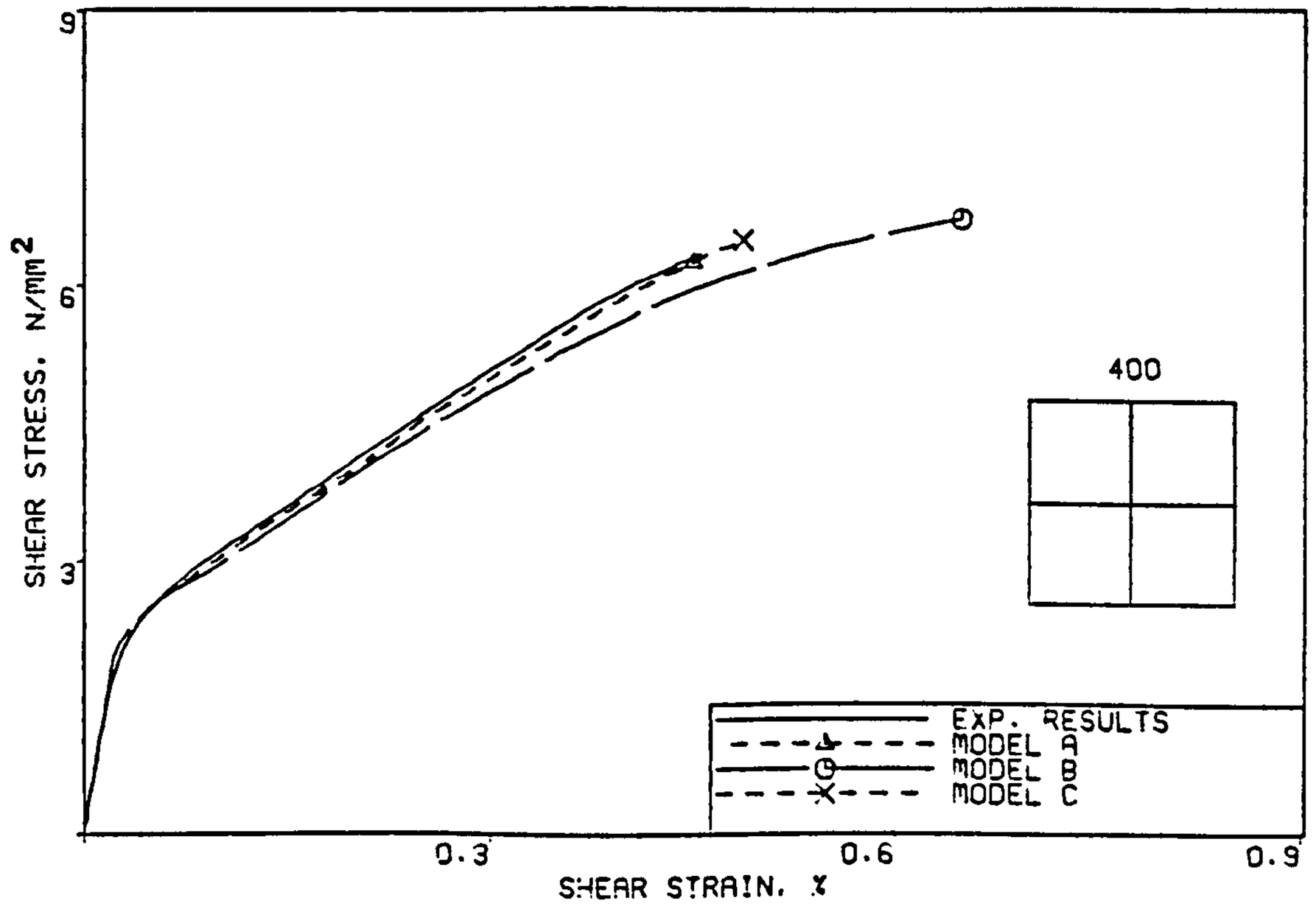

Fig. 6.9 Panel PV27 - Effect various models used to reduce the compressive strength

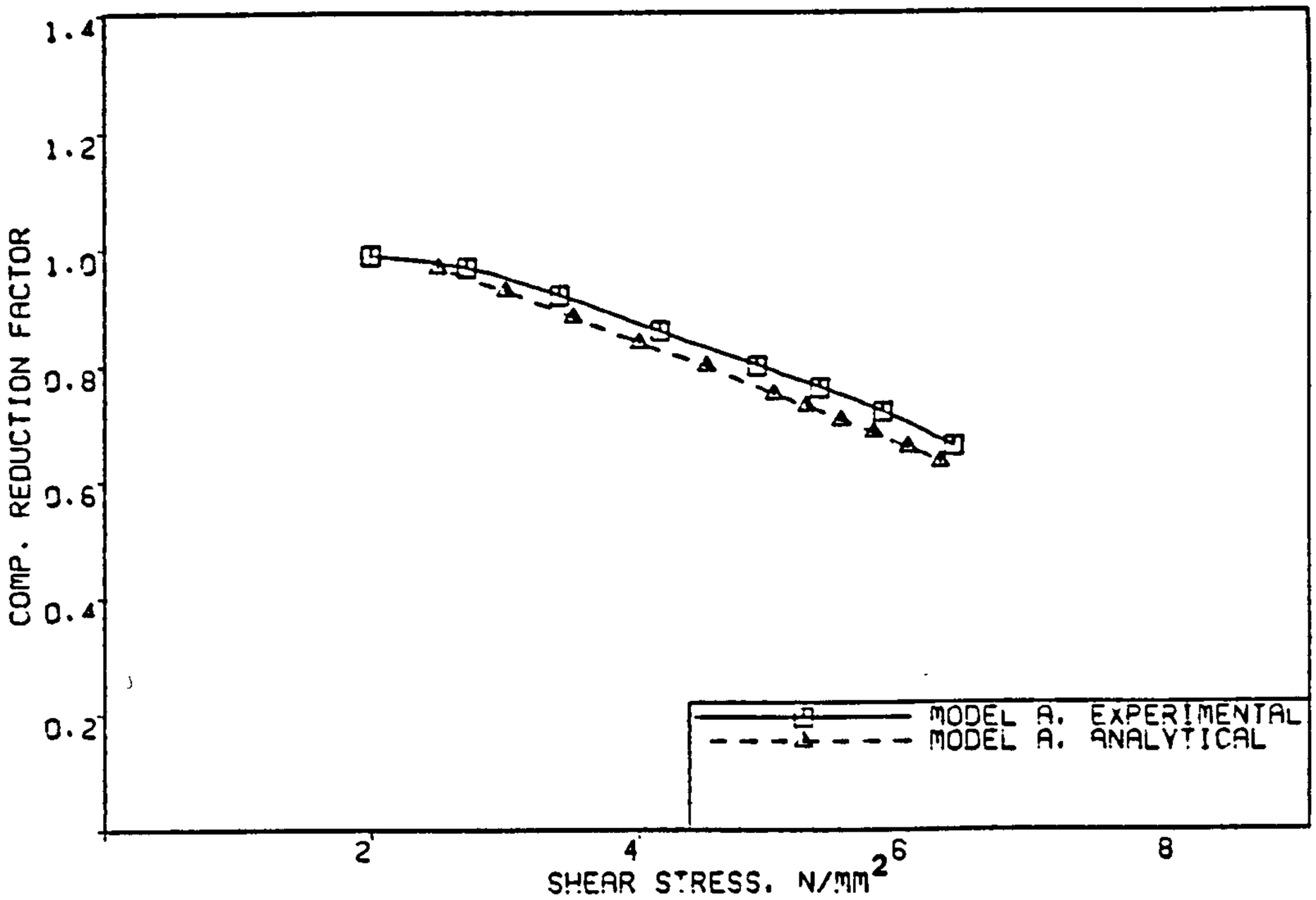

Fig. 6.10 Panel PV27 - Variation of the compression reduction factor, λ, according to model A.

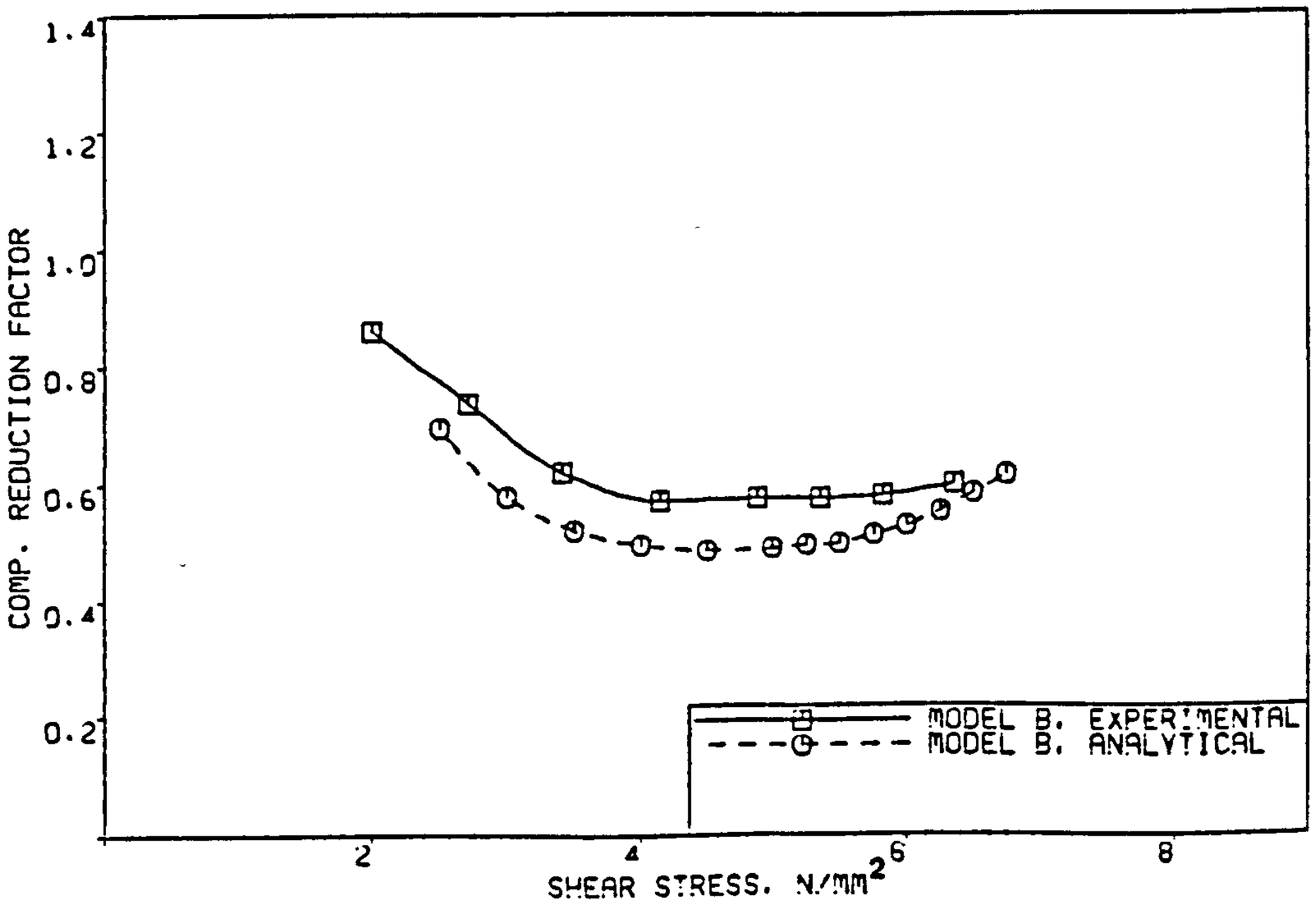

Fig. 6.11 Panel PV27 - Variation of the compression reduction factor, λ, according to model B.

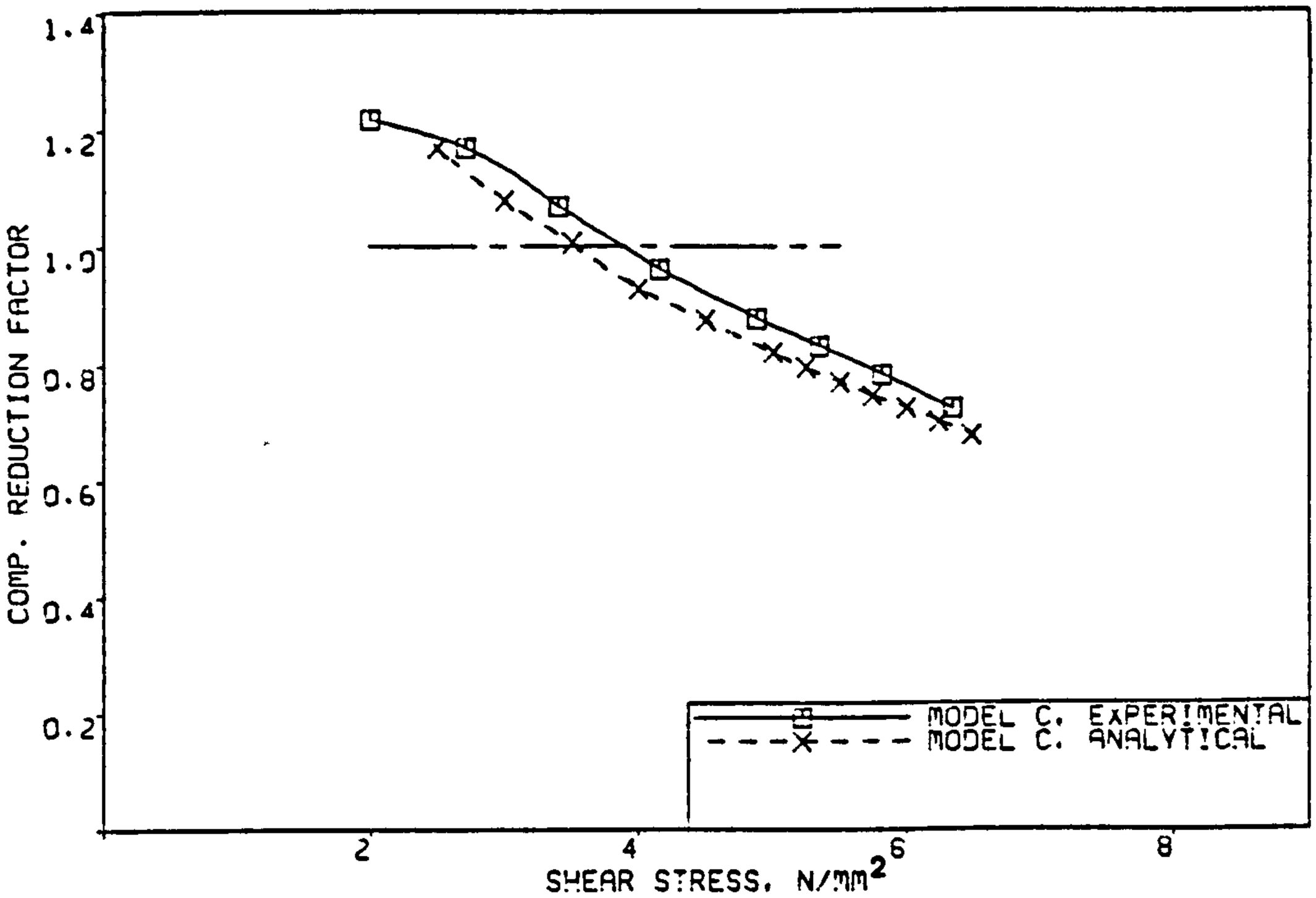

Fig. 6.12 Panel PV27 - Variation of the compression reduction factor, λ, according to model C.

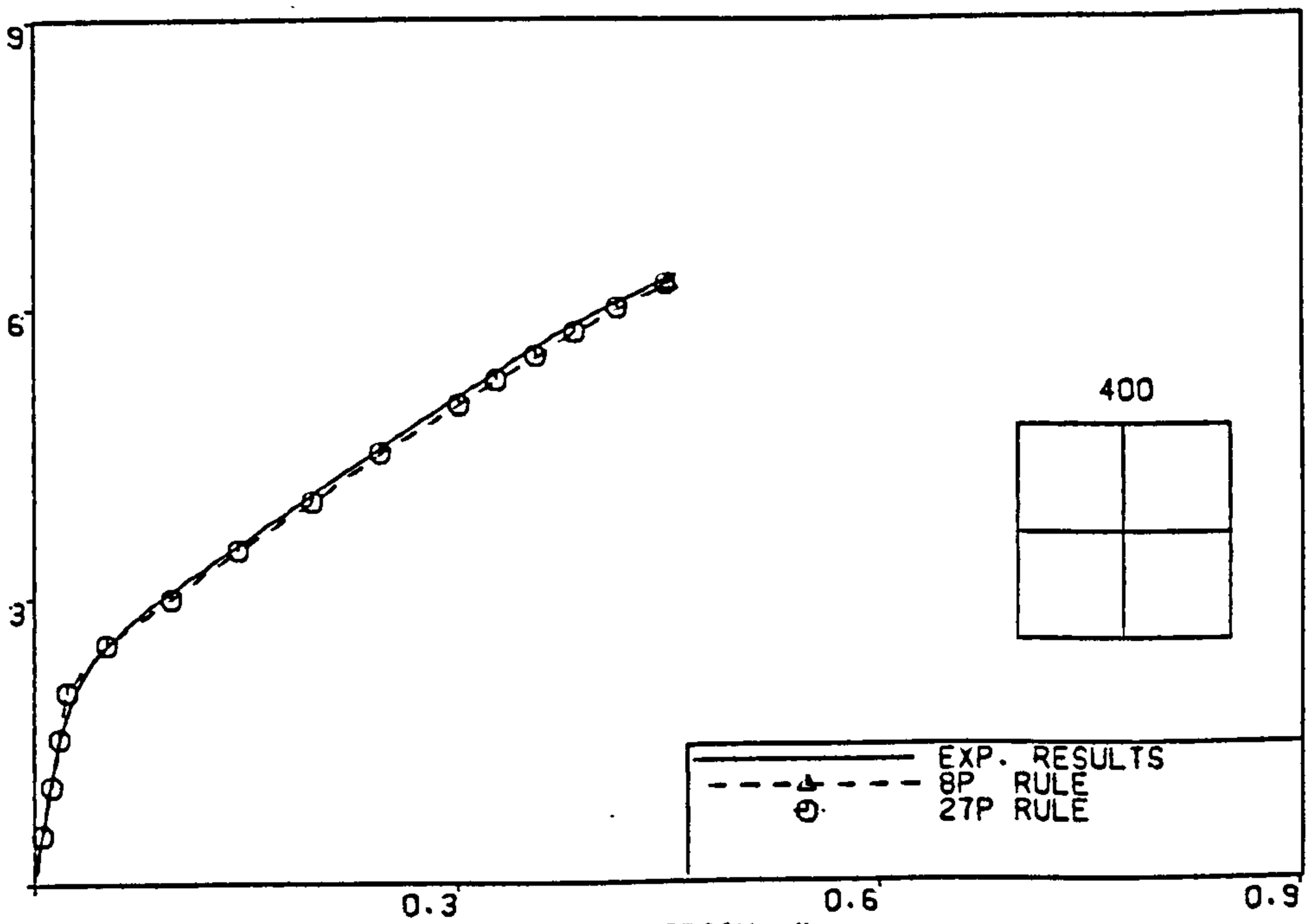

Fig. 6.13 Panel PV27 - Effect of the integration rules.

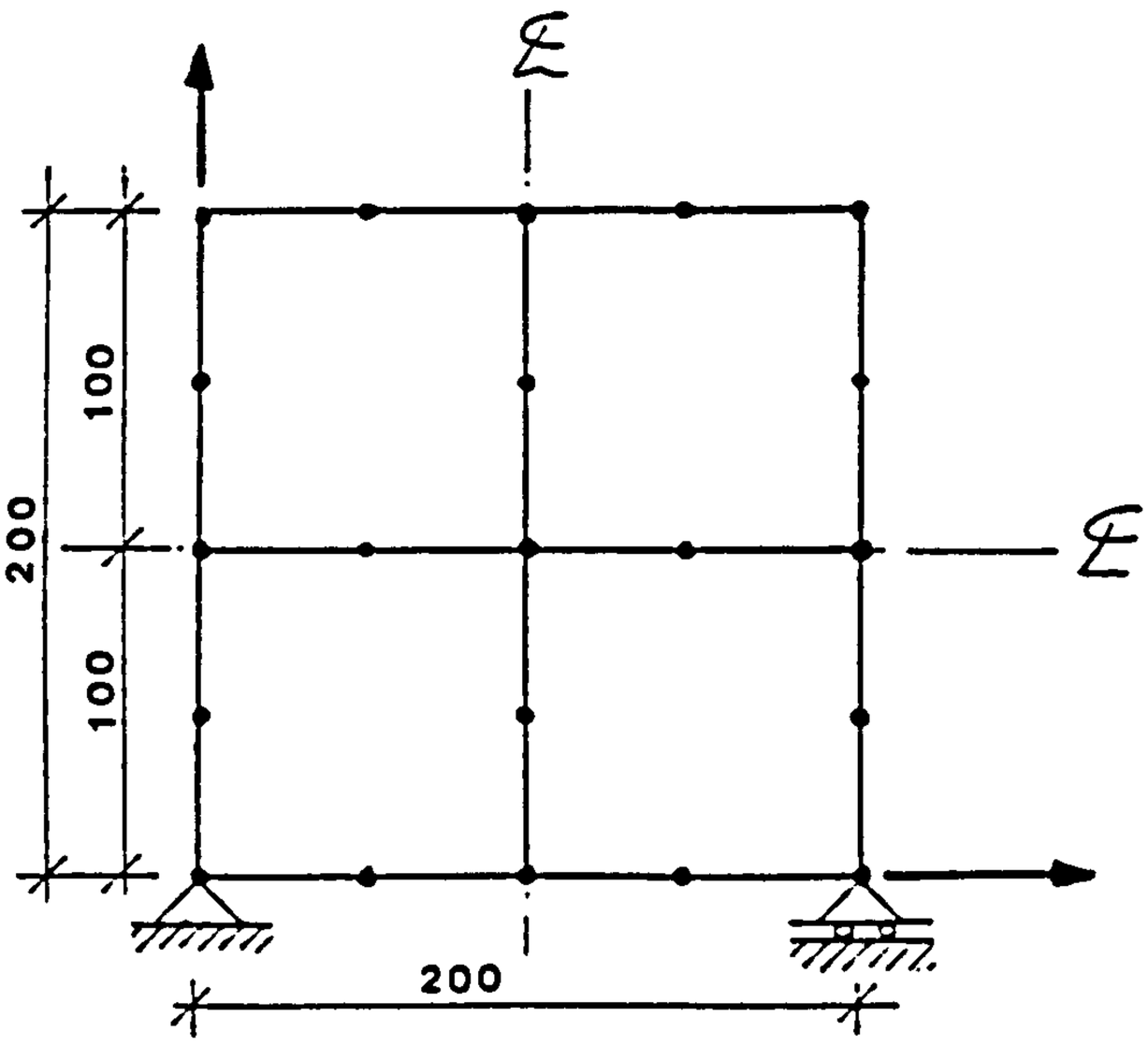

Fig. 6.14 Finite element mesh and boundary conditions for panel PV27.

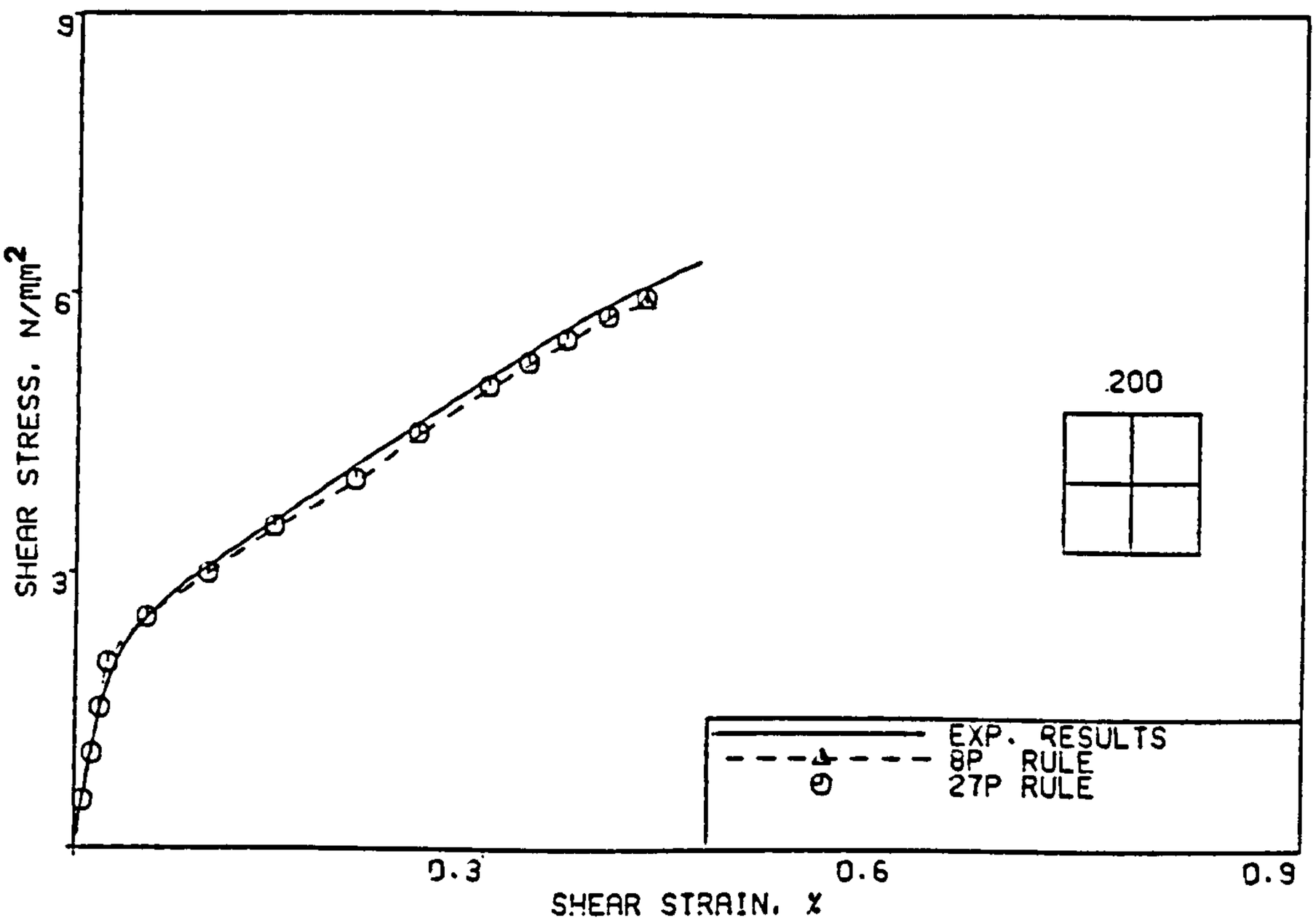

Fig. 6.15 Panel PV27 - Effect of the element size.

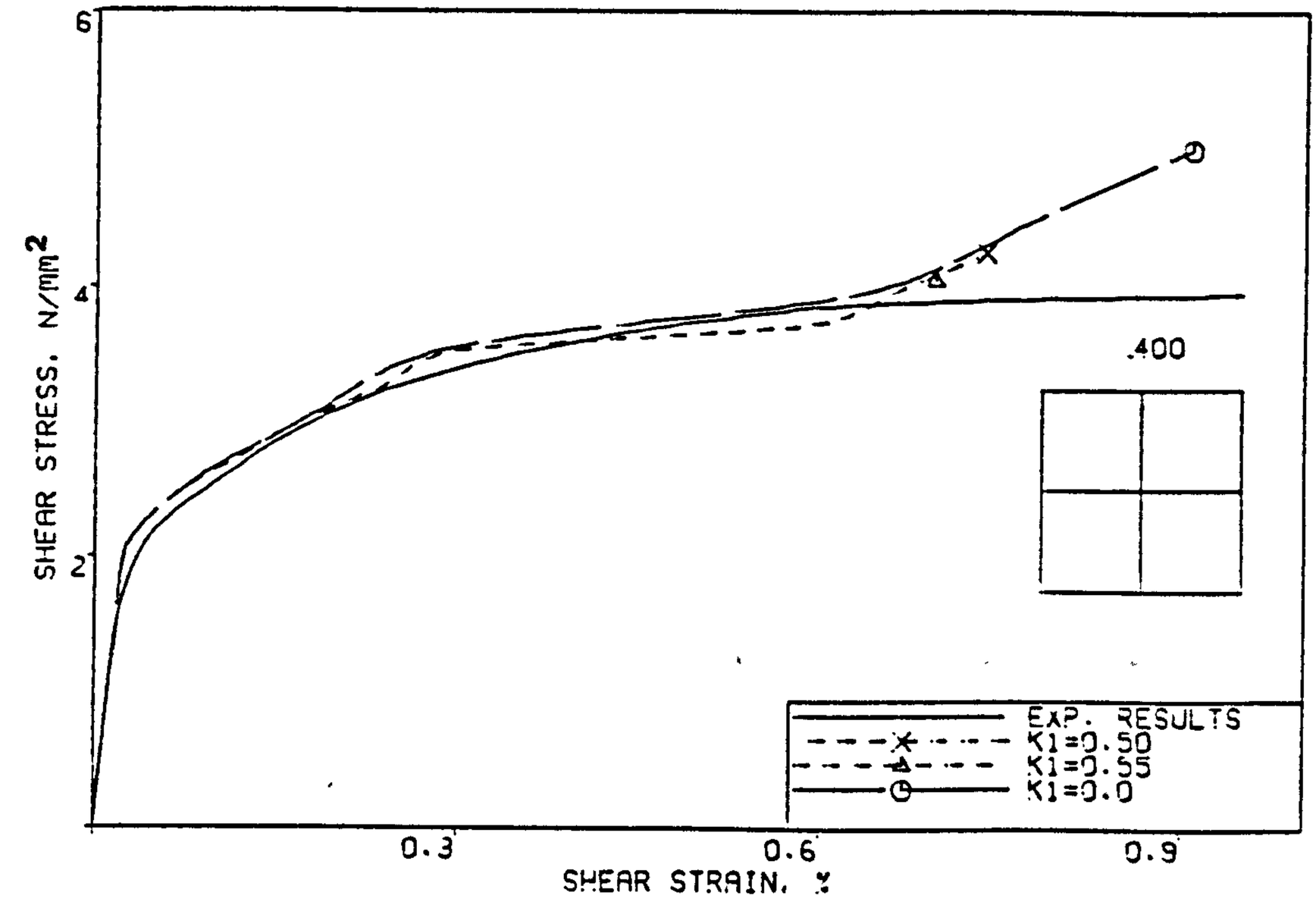

Fig. 6.16 Panel PV19 - Effect of the compression reduction parameter, k_1.

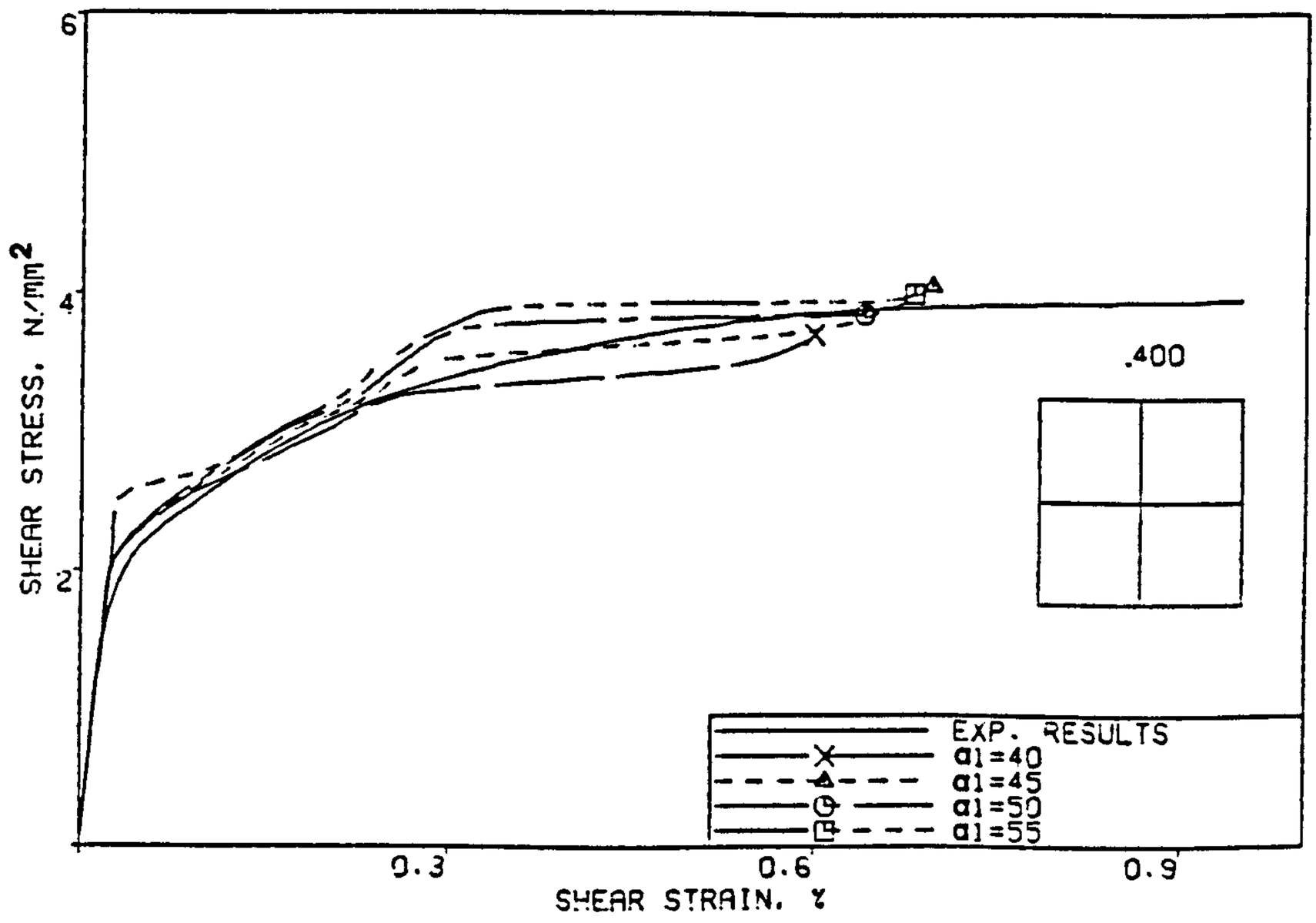

Fig. 6.17 Panel PV19 - Effect of the tension-stiffening parameter, α_1.

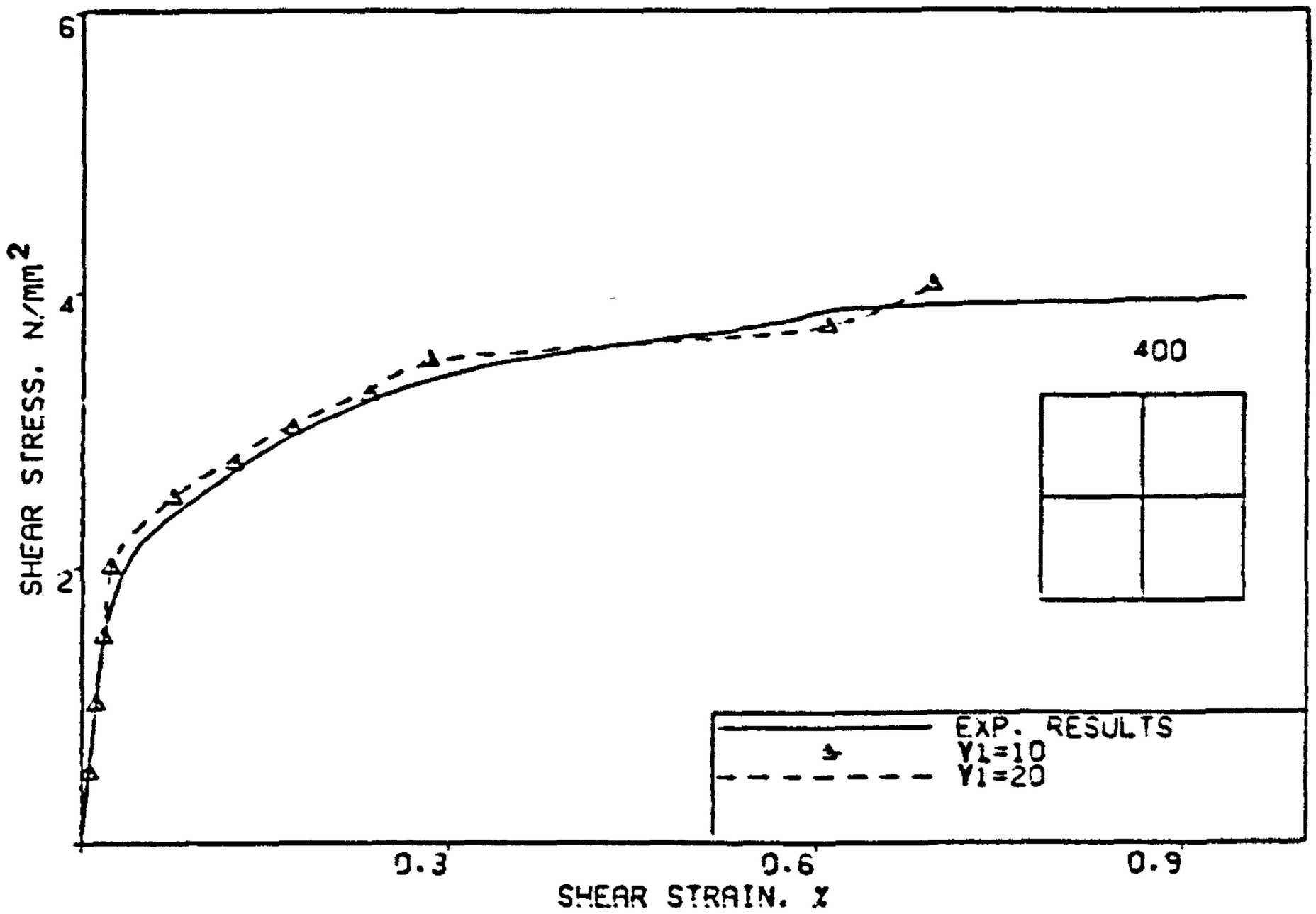

Fig. 6.18 Panel PV19 - Effect of the shear retention parameter, γ_1.

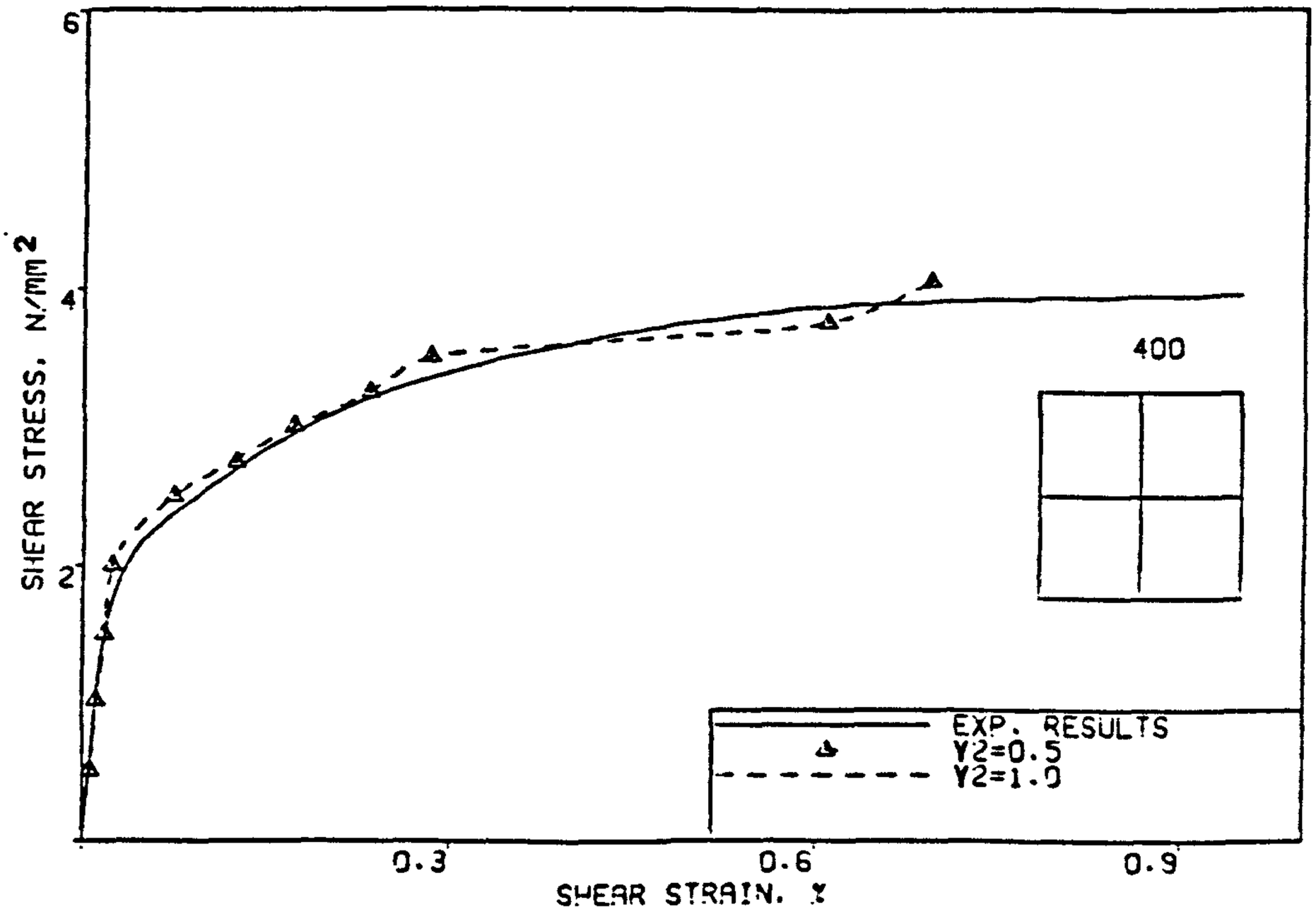

Fig. 6.19 Panel PV19 - Effect of the shear retention parameter, γ_2.

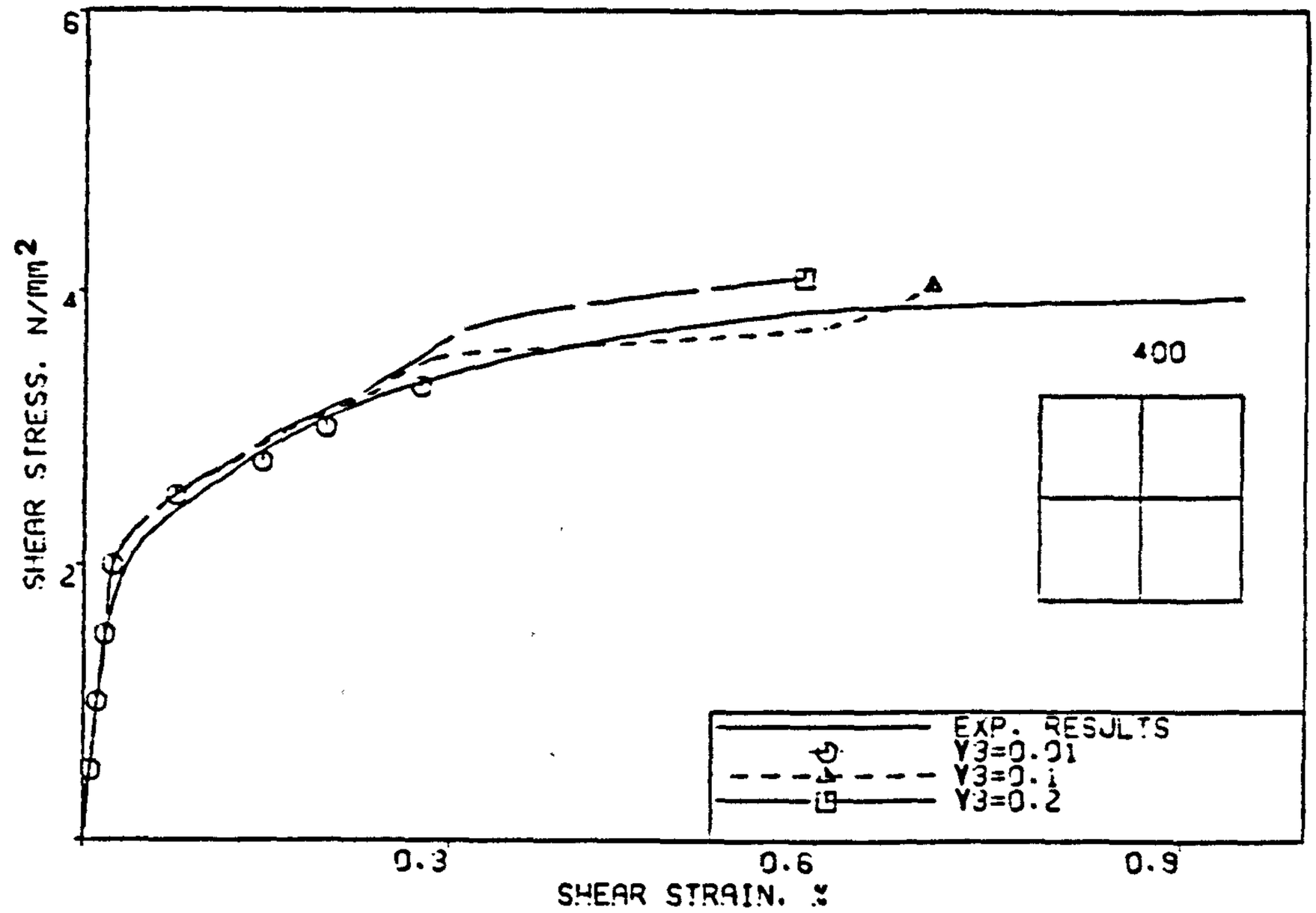

Fig. 6.20 Panel PV19 - Effect of the shear retention parameter, γ_3.

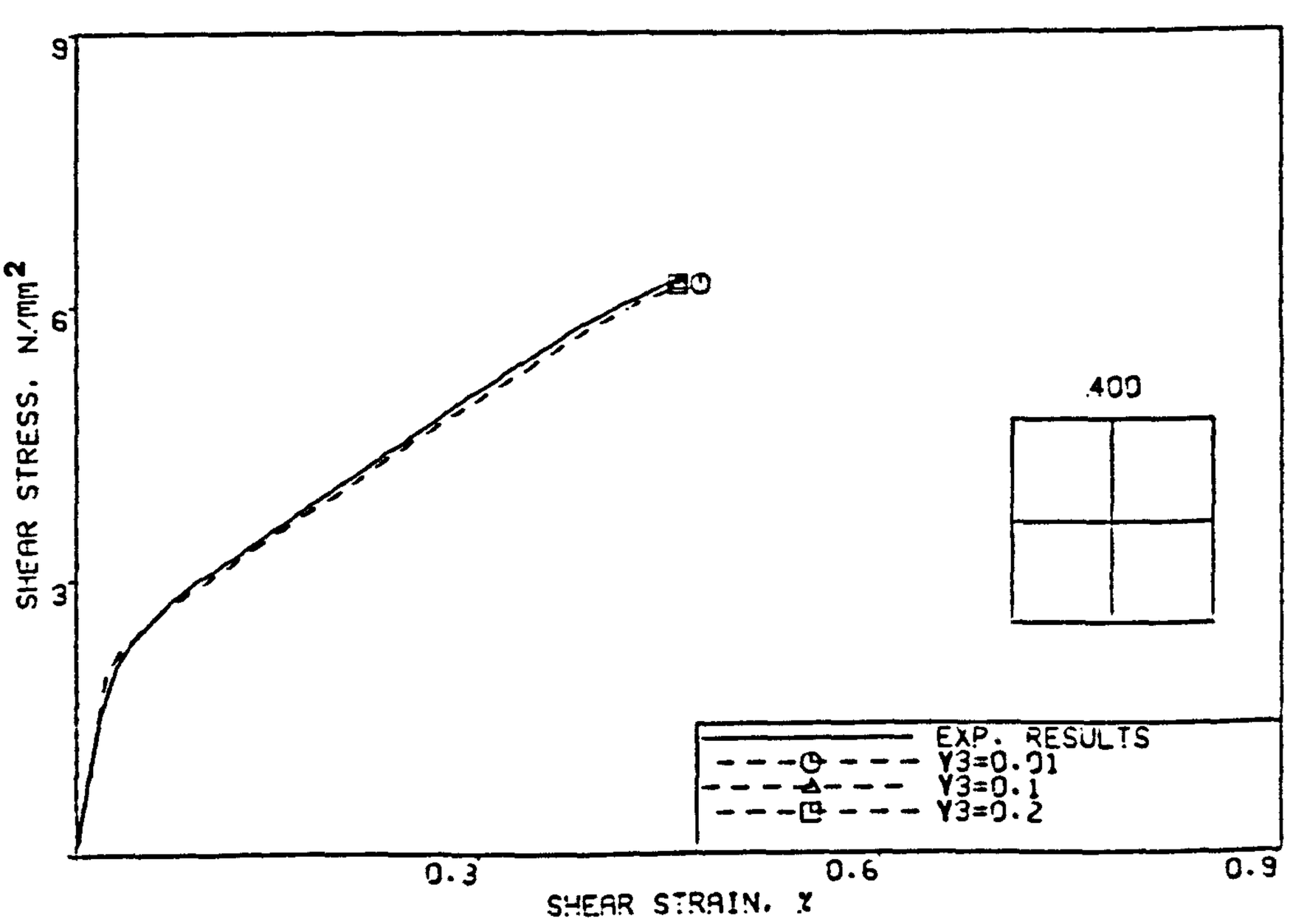

Fig. 6.21 Panel PV27 - Effect of the shear retention parameter, γ_3.

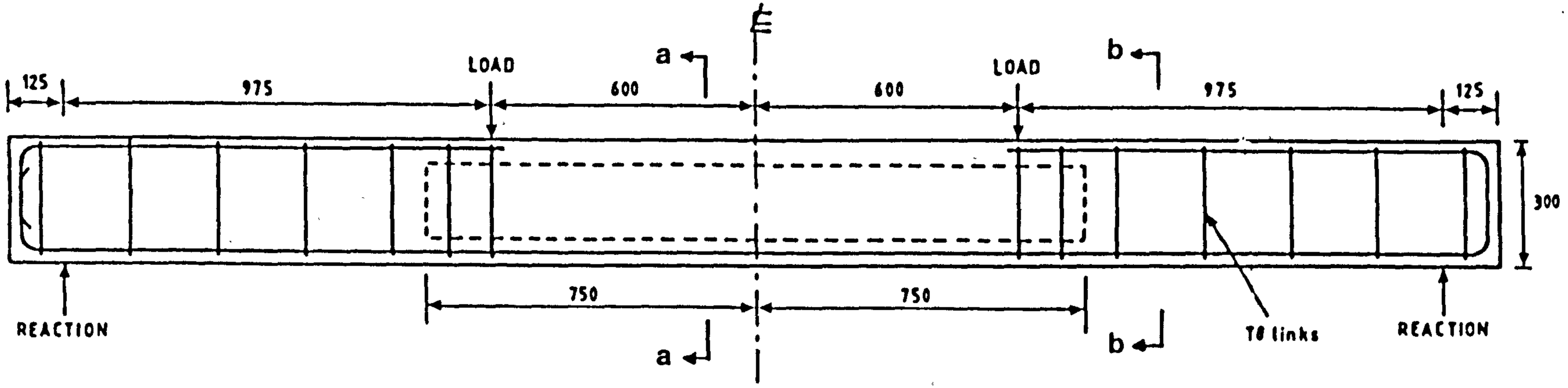

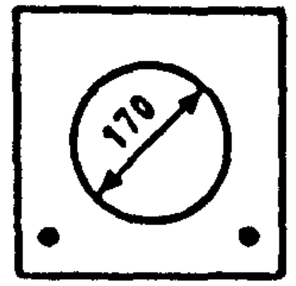

sec.a-a

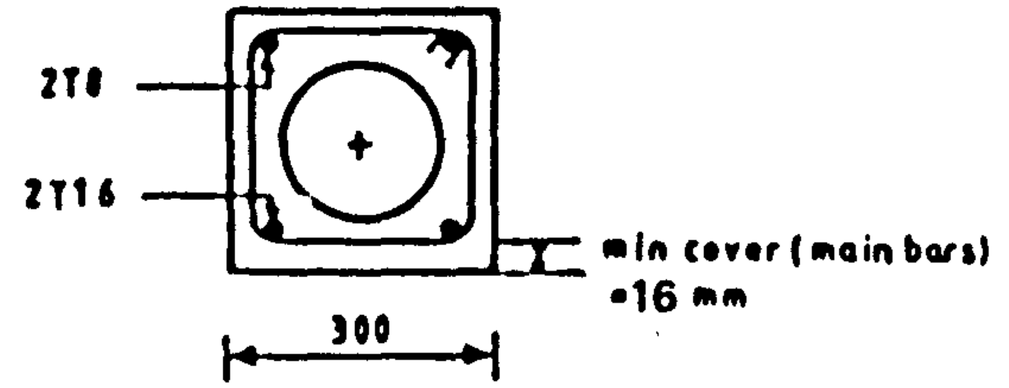

sec.b-b

Fig. 6.22 Dimensions and reinforcement details of a typical voided slab strip, L9, (Ref. 8).

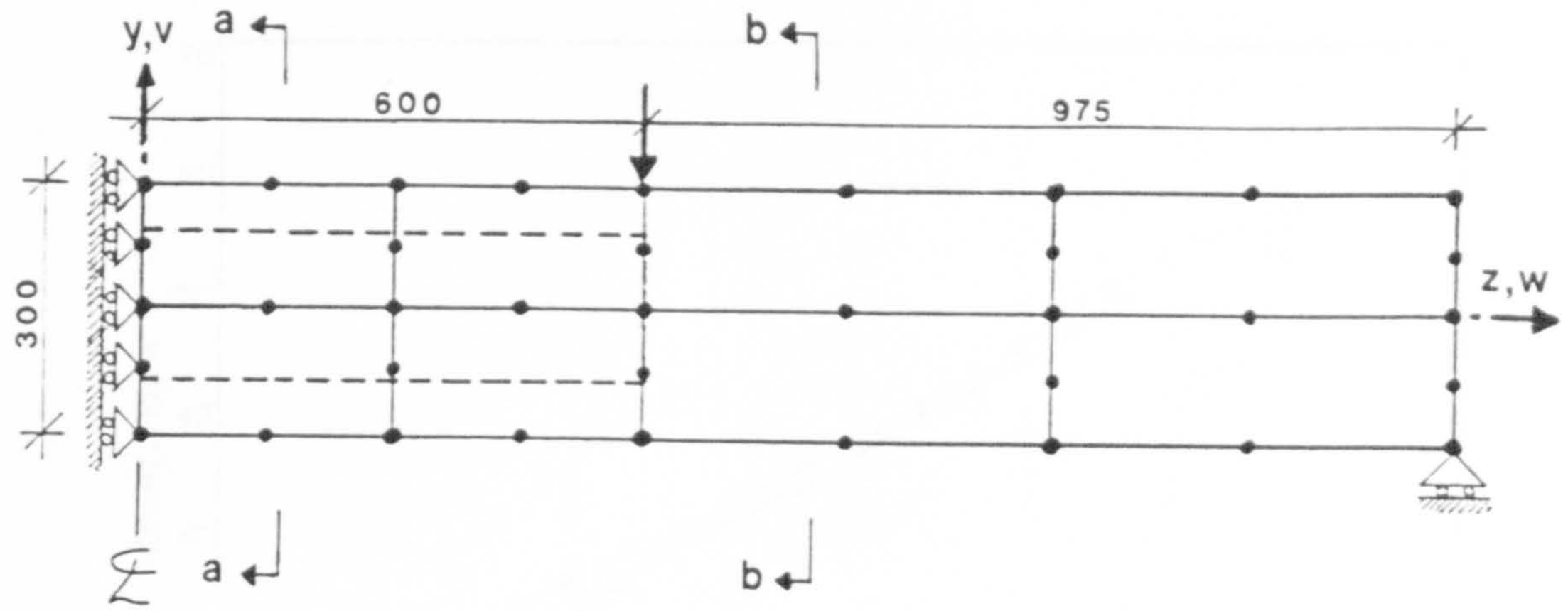

Fig. 6.23 Finite element mesh and boundary and symmetry conditions used for Oduyemi and Clark voided slab strips.

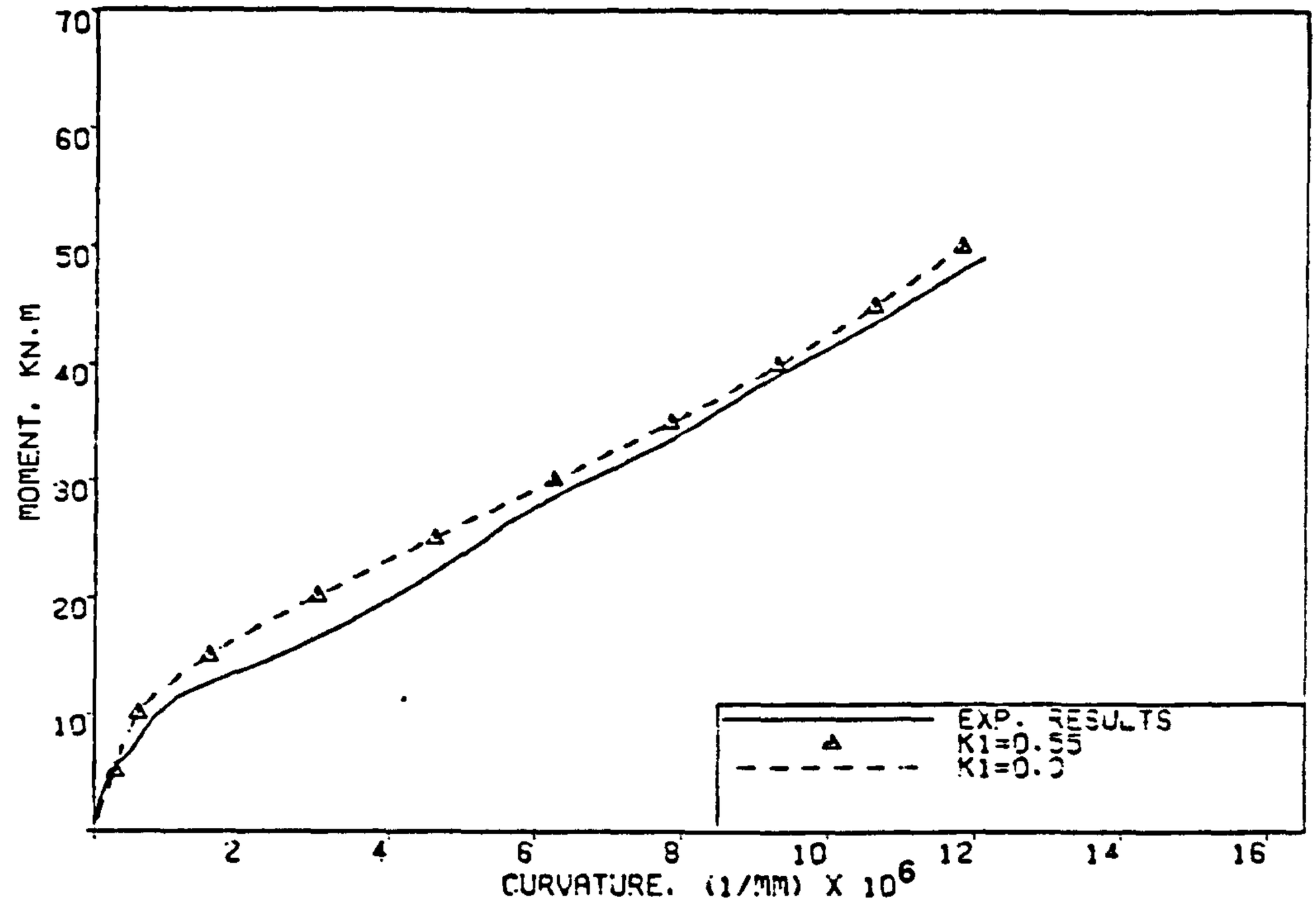

Fig. 6.24 Moment–curvature relationships for strip L9.

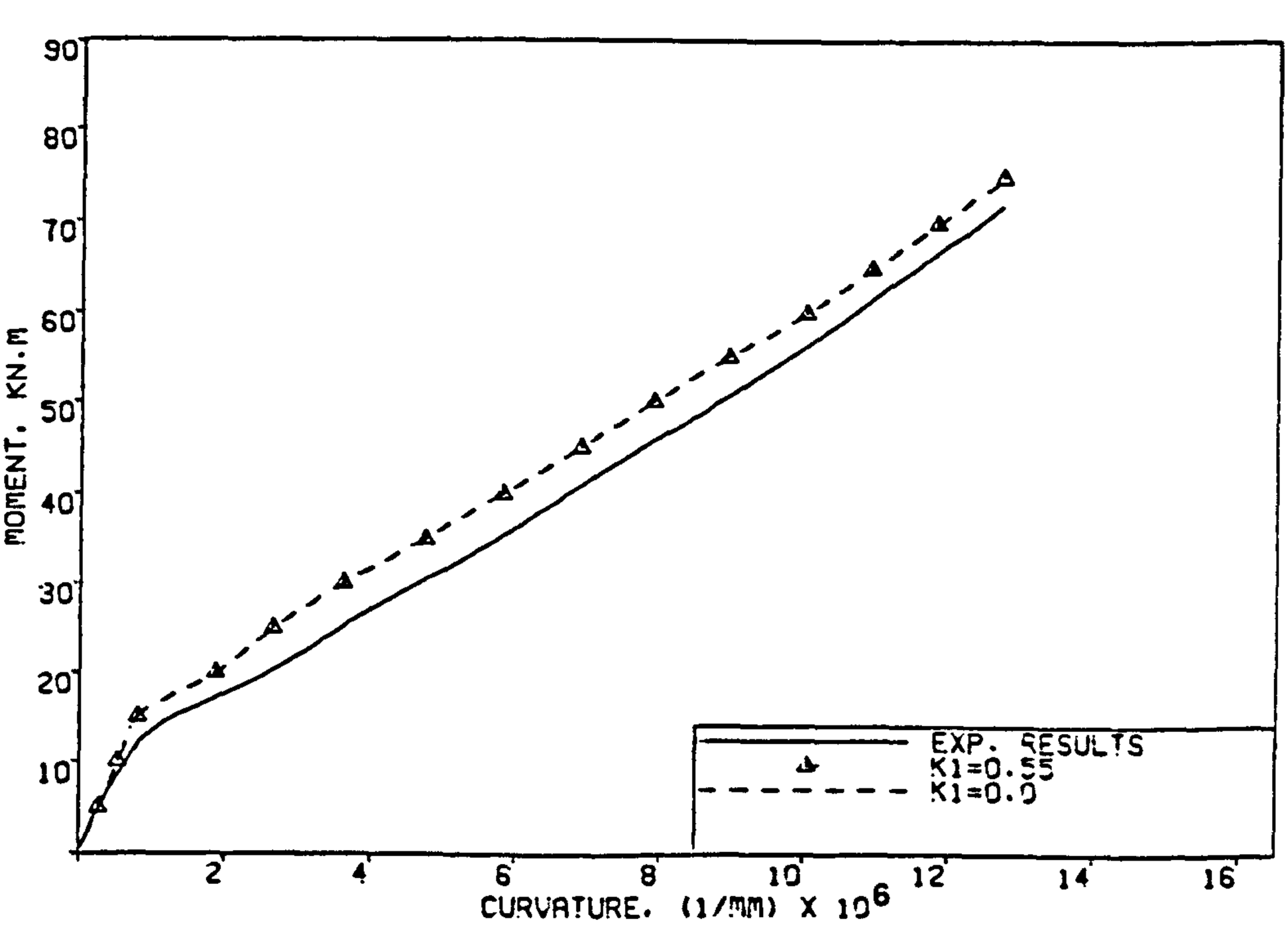

Fig. 6.25 Moment–curvature relationships for strip L10.

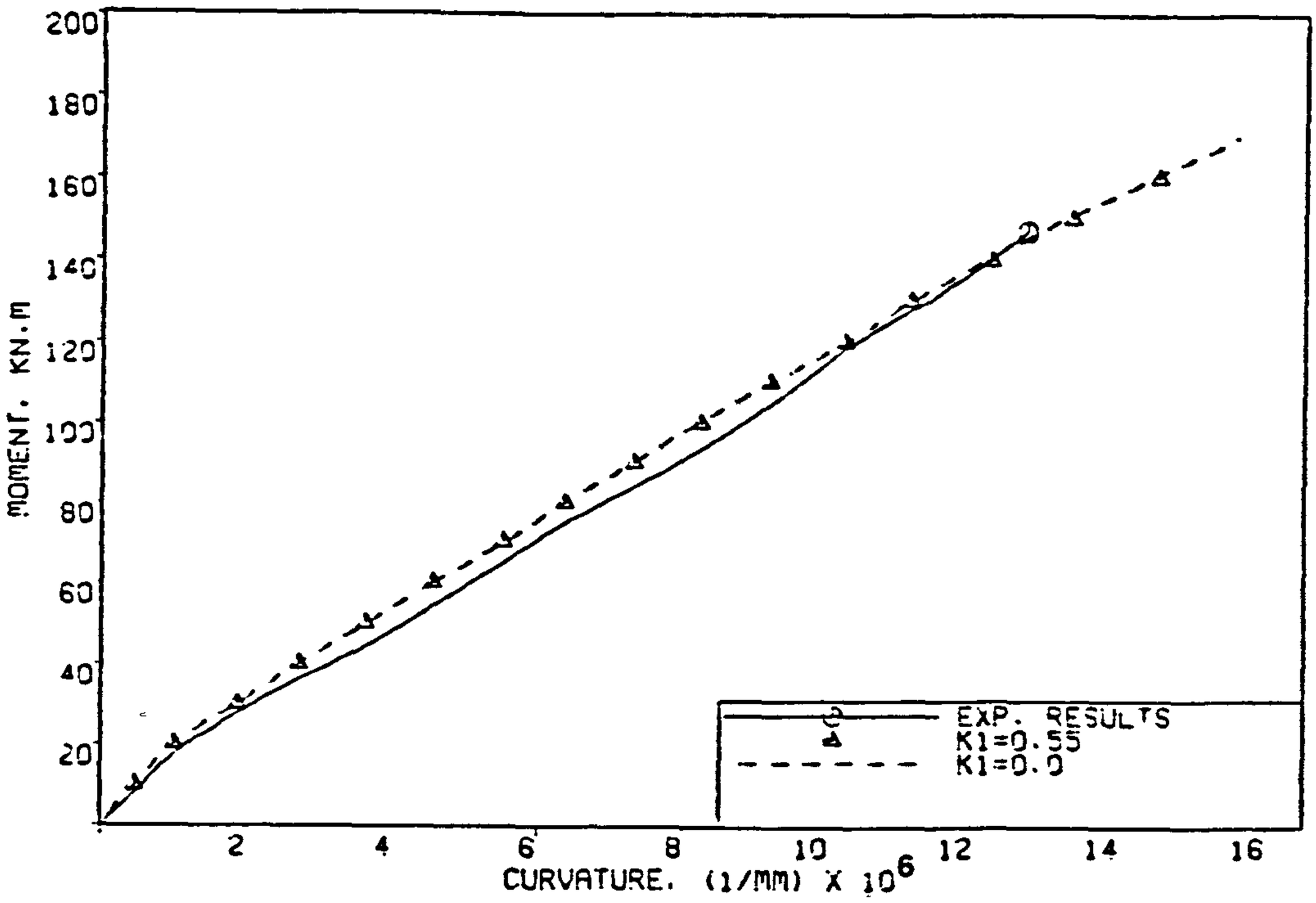

Fig. 6.26 Moment–curvature relationships for strip L11.

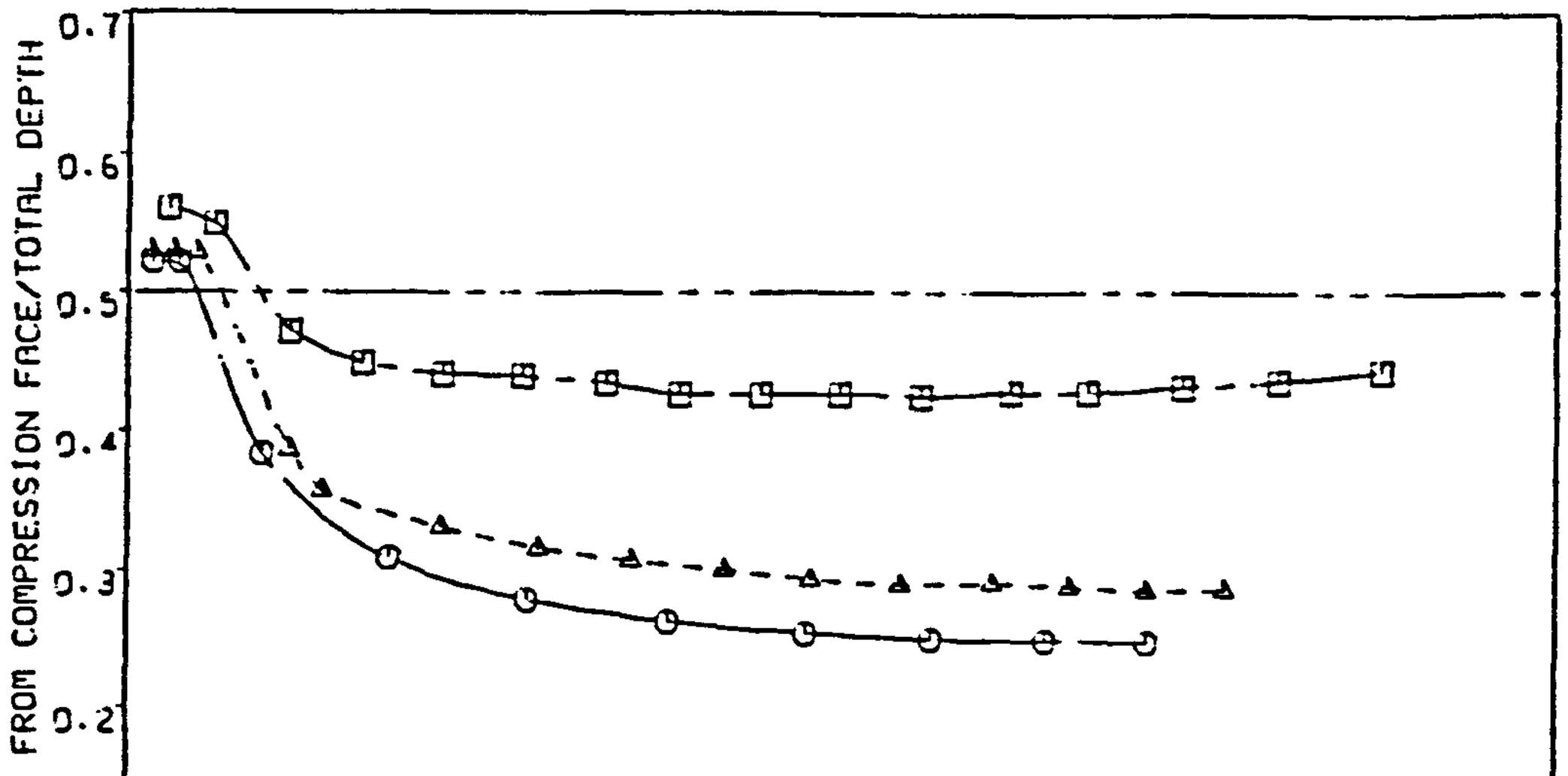

Fig. 6.27 Variation of the compression zone depth for Oduyemi and Clark voided slab strips.

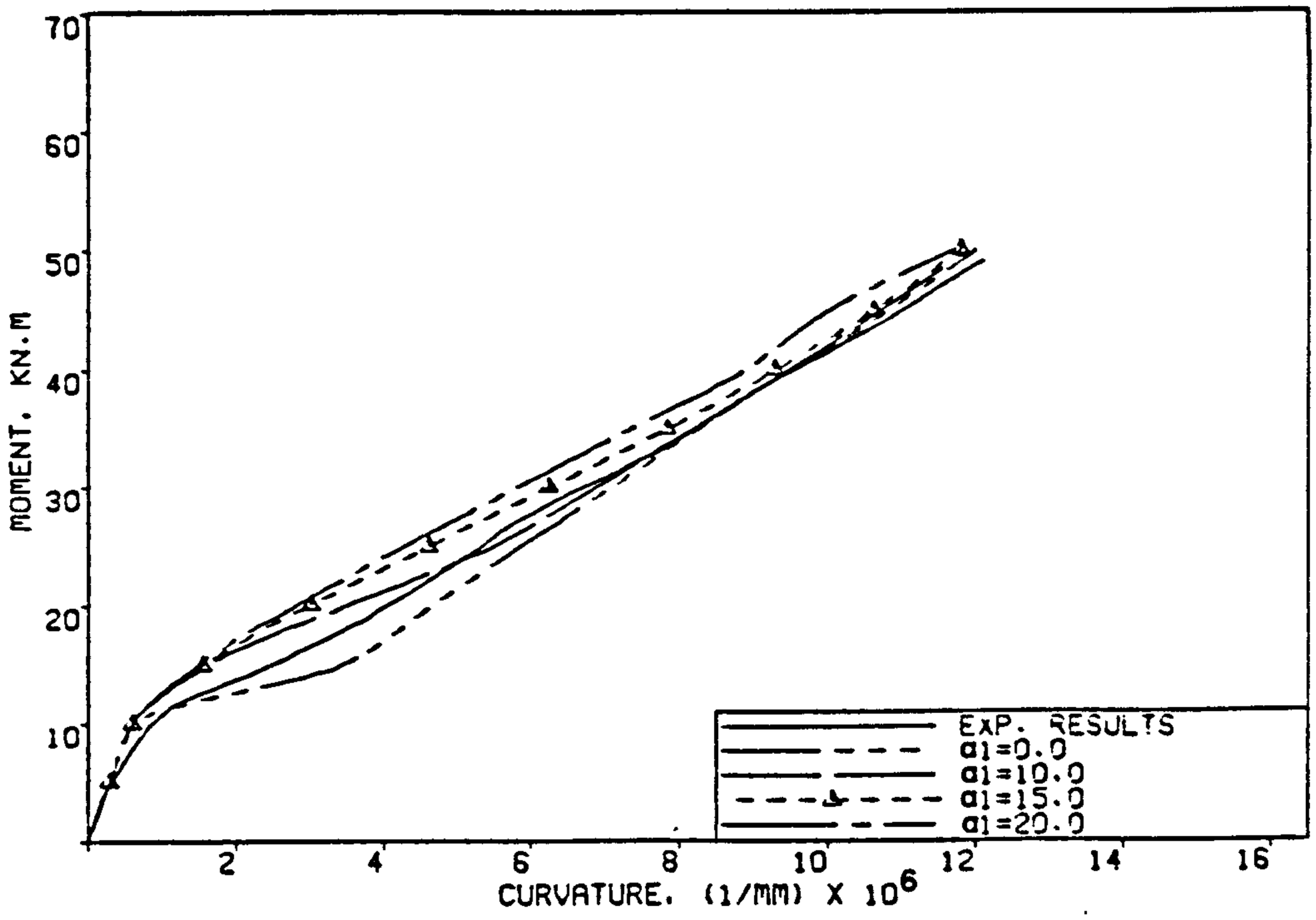

Fig. 6.28 Effect of Tension-stiffening parameter α_1 on the moment-curvature relationship of strip L9.

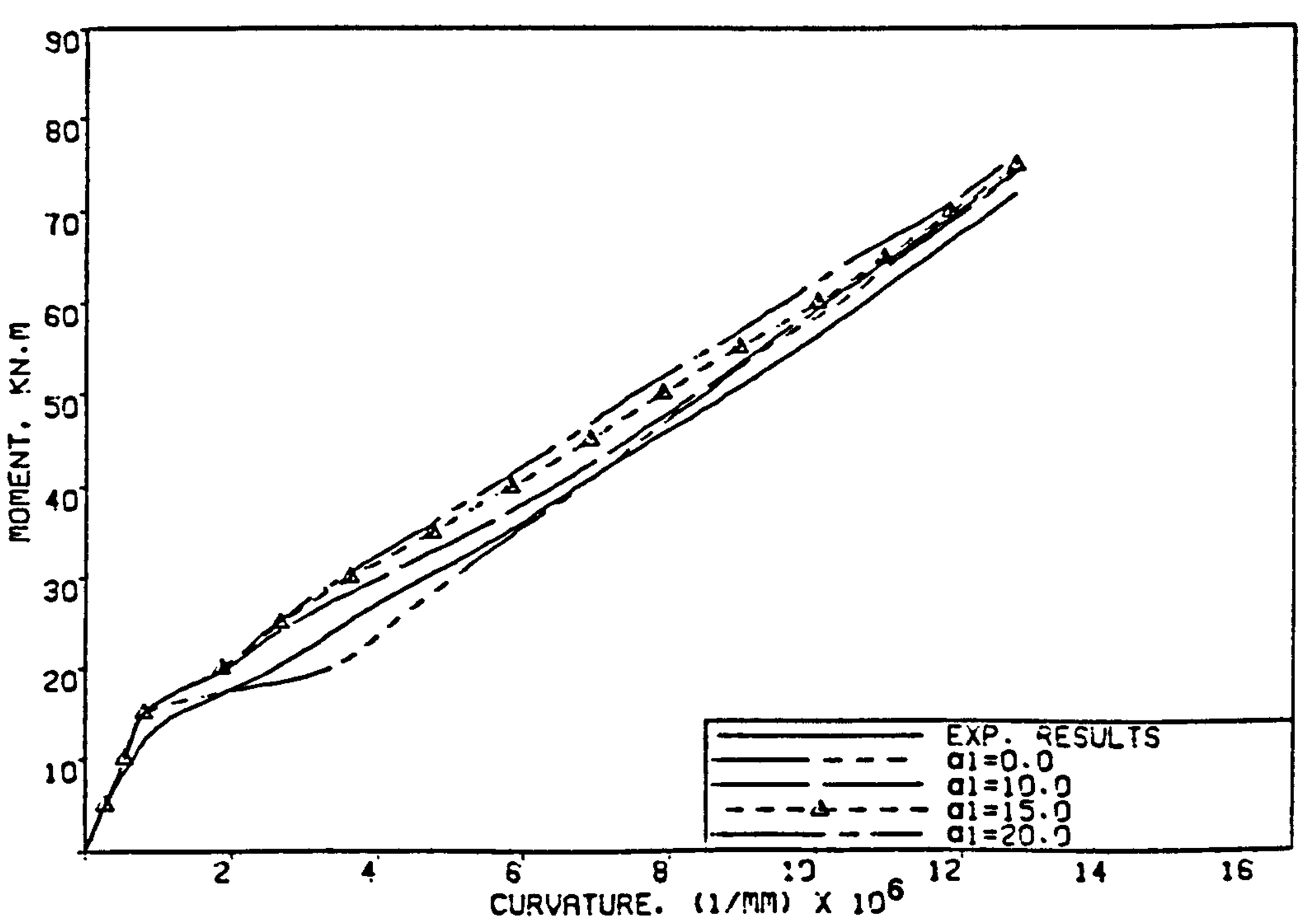

Fig. 6.29 Effect of Tension-stiffening parameter α_1 on the moment-curvature relationship of strip L10.

REFERENCES

1. Vecchio, F. and Collins, M.P., "The Response of Reinforced Concrete to In-plane Shear and Normal Stresses", Publication No. 82-03, University of Toronto, Canada, 1982.

2. Milford, R.V. and Schnobrich, W.C., "Numerical Model for Cracked Reinforced Concrete", Proc. Int. Conf. on Computer Aided Analysis and Design of Conc. Struct., Eds. Damjanic et al., Vol. I, Split, Yogoslavia, September 1984, pp. 71-84.

3. Cervenka, V., "A Constitutive Model for Reinforced Concrete", J. of the Amer. Conc. Inst., Vol. 82, November-December 1985, pp. 877-882.

4. Crisfield, M.A. and Wills, J., "Numerical Comparisons Involving Different 'Concrete-Models'", IABSE Colloquium on Numerical Modelling of Reinforced Concrete, Delft, 1987, pp. 177-187.

5. Vecchio, F.J. and Collins M.P., "The Modified Compression-Field Theory for Reinforced Concrete Elements Subjected to Shear", J. of the Amer. Conc. Inst., March-April 1986, pp. 219-230.

6. Oduyemi, T.O.S. and Clark, L.A., "Tension-stiffening in Longitudinal Sections of Circular Voided Concrete Slabs", Proc. Instn. Civ. Engrs, Part 2, Vol. 83, December 1987, pp. 861-874.

7. Oduyemi, T.O.S. and Clark, L.A., "Prediction of Crack Widths in Circular Voided Concrete Slabs Subjected to Longitudinal Bending", Proc. Instn. Civ. Engrs, Vol. 85, June 1988, pp. 259-270.

8. Oduyemi, T.O.S., "Stiffness and Cracking of Voided Slab Bridges", Ph. D. Thesis, University of Birmingham, 1986.

CHAPTER SEVEN

ANALYSIS OF REINFORCED CONCRETE BEAMS LOADED IN TORSION AND TORSION AND BENDING

7.1 Introduction

This Chapter deals with the problem of torsion of reinforced concrete beams. Two sets of example have been considered, the first set analysed are six rectangular beams subjected to pure torsion from the series of tests conducted by Hsu [1]. The second set includes two rectangular beams loaded with torsion and bending and tested by Collins et al [2]. The examples were chosen so that a wide range of parameters affecting different aspects of behaviour could be considered. The finite element solutions are compared with the results of the experimental tests.

It should be noted that for reinforced concrete beams loaded in pure torsion, the resulting state of stress on the wider and shorter faces is a pure shear. Therefore, similar to the panels subjected to pure shear presented in the previous Chapter, the inclusion of a model for reducing the concrete compressive strength can substantially improve the prediction of a finite element analysis of members which fail due to torsional loads. The models incorporated in the computer program to reduce the compressive strength of concrete due to presence of the tensile straining of transverse reinforcement have been compared. Parametric studies to investigate

the effect of some important material and solution parameters on the non-linear finite element analysis have also been carried out.

7.2 Reinforced Concrete Beams Under Pure Torsion

Hsu [1,3] conducted a series of tests on plain and reinforced concrete rectangular beams subjected to pure torsion. A total of 10 plain and 53 reinforced concrete beams were tested to cover the effects of a wide range of parameters including the amount of reinforcement, spacing of stirrups and longitudinal bars, the ratio of the volume of longitudinal bars to volume of stirrups, concrete strength, depth to width ratio of the cross-section and scale effects. Results of the tests were used to calibrate the first ACI torsion design criterion [4]. Six of these beams have been chosen for the present study because the detailed information of all the aspects of behaviour was available. The selected beams were designated as B2, B3, B4, B5, G3 and G4. Beams B2, B3, B4 and B5 had the same cross-section with a depth to width ratio of 1.5. These beams were identical except that the amount of reinforcement was different in each beam. Beams G3 and G4 were of a larger depth and had a depth to width ratio of 2.0. They each had different percentage of reinforcement. In all the beams considered, the provided steel was equally divided between the longitudinal bars and stirrups.

7.2.1 Description of the Test Specimens

A typical test beam, B3, is shown in Fig. 7.1. The total length of all beams considered was 3099 mm. (122 in.). At each end of the beam, a length of 635 mm. (25 in.) was reinforced with about 30% additional stirrups to avoid local failure, close to the clamping heads, due to the stress concentration. The effective length was therefore reduced to 1829 mm. (72 in.). The cross-section used for beams B2, B3, B4 and B5 was 254 mm.X381 mm. (10 in.X15 in.), Fig. 7.1. For beams G3 and G4, the cross-section was 254 mm.X508 mm. (10 in.X20 in.). The reinforcement was intermediate grade deformed bars with modulus of elasticity of about 196.5 kN/mm^2. The reinforcing cages consisted of four longitudinal corner bars and closed stirrups uniformly distributed over the effective length of the beam. Dimensions of the cross-sections, centre-to-centre distances between stirrup legs, steel ratios for the longitudinal bars and stirrups and the strength properties of the reinforcement are given in Table 7.1 for all the beams considered.

The specimens were tested in a specially designed torsion test rig [5]. The torsional moments were applied through clamping heads at both ends of the specimen. At each end, a length of 356 mm. (14 in.) of the beam was placed into the clamping head. The angle of twist was measured at the middle of the wider face of the beam over a length of 1346 mm. (53 in.).

Table 7.1 Dimensions of cross-sections and reinforcement details of Hsu's beams

Beam designation	Cross-section		Stirrups						Longitudinal bars		
	Width mm	Depth mm	Vert. legs c/c mm	Horiz. legs c/c mm	Spacing mm	Diameter mm	Steel ratio	Yield stress kN/mm²	Diameter mm	Steel ratio	Yield stress kN/mm²
B2	254	381	216	343	181	12.7	0.00823	320	15.88	0.00827	316
B3	254	381	216	343	127	12.7	0.0117	320	19.05	0.0117	328
B4	254	381	216	343	92	12.7	0.0161	323	22.22	0.0160	320
B5	254	381	216	343	70	12.7	0.0213	321	25.40	0.0211	330
G3	254	508	216	470	150	12.7	0.00882	328	19.05	0.0088	339
G4	254	508	216	470	114	12.7	0.0120	321	22.22	0.0120	326

7.2.2 Test Observations

During the testing of all specimens, two different types of behaviour were observed: these occurred before and after cracking of concrete. Before cracking the beams behaved essentially as plain concrete members. The stresses in the reinforcement were small and torque–twist curves were identical to those of plain concrete beams [1,3].

When cracking occurred, the angle of twist significantly increased under a constant torque and the stresses in the reinforcement increased suddenly. The behaviour indicates that the equilibrium condition that existed in the beam was upset by the cracking so that the beam sought a new equilibrium configuration by transferring the load to the reinforcement. At the end of this stage of behaviour, the torque–twist curve began to rise again with a torsional stiffness, measured as the slope of the torque–twist curve, of only a fraction of that before cracking. As the applied torque increased, the slope of the curve decreased at an increasing rate until the peak torque was reached. The ultimate torque of the beams depends, to a large extent, on the amount of reinforcement. At the ultimate stage, the stresses in the longitudinal bars and the longer legs of the stirrups can both reach yield when small amount of reinforcement were used, for example beams B2 and G3. Furthermore, principal compressive strains exceeding 0.004 were measured in the concrete at the centre of the wider faces [1].

Cracks, inclined approximately 45 degrees to the axis of the beam, occurred on the wider and shorter faces almost simultaneously.

With increasing torque, additional cracks occurred and some of the cracks on the wider faces turned into the shorter faces with a direction almost perpendicular to the longitudinal axis. These cracks combined with existing 45-degree cracks at the shorter faces so that some cracks on the shorter faces looked like S-shaped curves. This pattern of cracks did not change until failure. Fig. 7.2 shows the crack pattern after failure for beam B3. An important phenomenon that was observed after cracking of the concrete where the length of the beam increased with increasing torque [1].

7.2.3 Finite Element Idealisation and Material Properties

Because the beams were tested under pure torsion, a segment of 914.4 mm. in length, half the effective length of the beam, has been considered in the finite element analyses. Except where otherwise stated, the segments were generally modelled using twelve quadratic brick elements, Fig. 7.3a. The longitudinal bars and the stirrups were embedded into the brick elements and were placed in their correct positions. At both ends of the segment, a set of equivalent nodal forces was applied to produce the required torque. The proportions of these forces were obtained using the technique described in section 5.4. The equivalent nodal forces and the boundary conditions imposed at both ends of the segment are shown in Figs 7.4 for beams B2 to B5. These boundary conditions maintain the stability of the beam and allow the post-cracking extension of the beam in the z direction to occur. In addition, the imposed boundary conditions allow any possible post-cracking extensions in the x and y directions that may occur at the restrained cross-sections.

The external torque was initially applied in equal increments of about 10% of failure torque. These increments were reduced at stages close to the ultimate torque. The numerical tests have been generally carried out using the 15b point integration rule. Unless otherwise stated , a convergence tolerance of 5% and the modified Newton–Raphson method, KT2a,in which the stiffness matrix is updated at the 2nd, 12th, 22nd.. etc iteration of each loading increment have been used. Line searches have been implemented in all the numerical tests to accelerate convergence. The material properties and the additional material parameters adopted for the beams analysed are outlined in Tabels 7.2, 7.3, and 7.4.

7.2.4 Results of the Analyses, Beam B4

The experimental and numerical torque–twist curves obtained for beam B4 are shown in Fig.7.5. The finite element solutions are in good agreement with the experimental results throughout the entire range. The post–cracking torsional stiffness and ultimate torque were predicted reasonably well using the reduced concrete compressive strength according to model A. The predicted collapse torques were 51.9, 49.9 and 46.1 kN.m for values of the compressive reduction parameter k_1 of 0.50, 0.55 and 0.60 respectively. These values were close to the experimental ultimate torque, 47.4 kN.m. However, when k_1 was set to zero, i.e $\lambda = 1.0$, a very stiff post–cracking response was obtained and the predicted ultimate torque was 65.5 kN.m, about 40% higher than the experimental value.

Table 7.2 Material properties and additional material parameters of Hsu's beams B2 and B3

Concrete	Beam B2	Beam B3
Young's modulus, E (N/mm^2)	25500	25500
Comp. strength, f'_c (N/mm^2)	28.6	28.1
Tensile strength, f_t (N/mm^2)	2.43	2.30
Poisson's ratio, ν	0.2	0.2
Uniaxial crushing strain	0.005	0.005
Steel		
Young's modulus, E_s (N/mm^2)	196500	196500
Longitudinal bars		
Steel ratio, ρ_l	0.00827	0.0117
Yield stress, f_{ly} (N/mm^2)	316.0	328.0
Stirrups		
Steel ratio, ρ_s	0.01785	0.00713
Yield stress, f_{sy} (N/mm^2)	320.0	320.0
Hardening parameter, H'	2.10	2.10
Tension-stiffening parameters		
α_1	10.0	15.0
α_2	0.6	0.6
Shear retention parameters		
γ_1	10.0	10.0
γ_2	0.50	0.50
γ_3	0.10	0.10
Comp. strength reduction, Model A		
Comp. reduction parameter, K_1	0.60	0.55

Note: Where different material parameters have been used these are given in the text.

Table 7.3 Material properties and additional material parameters of Hsu's beams B4 and B5

Concrete	Beam B4	Beam B5
Young's modulus, E (N/mm^2)	25500	25500
Comp. strength, f'_c (N/mm^2)	30.6	29.1
Tensile strength, f_t (N/mm^2)	2.62	2.54
Poisson's ratio, ν	0.2	0.2
Uniaxial crushing strain	0.005	0.005
Steel		
Young's modulus, E_s (N/mm^2)	196500	196500
Longitudinal bars		
Steel ratio, ρ_l	0.0160	0.0211
Yield stress, f_{ly} (N/mm^2)	320.0	332.0
Stirrups		
Steel ratio, ρ_s	0.0161	0.0213
Yield stress, f_{sy} (N/mm^2)	323.0	321.0
Hardening parameter, H'	2.10	2.10
Tension-stiffening parameters		
α_1	15.0	15.0
α_2	0.6	0.6
Shear retention parameters		
γ_1	10.0	10.0
γ_2	0.50	0.50
γ_3	0.10	0.10
Comp. strength reduction, Model A		
Comp. reduction parameter, K_1	0.55	0.50

Note: Where different material parameters have been used these are given in the text.

Table 7.4 Material properties and additional material parameters of Hsu's beams G3 and G4

Concrete	Beam G3	Beam G4
Young's modulus, E (N/mm^2)	24800	24800
Comp. strength, f'_c (N/mm^2)	26.8	28.3
Tensile strength, f_t (N/mm^2)	2.58	2.54
Poisson's ratio, ν	0.2	0.2
Uniaxial crushing strain	0.005	0.005
Steel		
Young's modulus, E_s (N/mm^2)	196500	196500
Longitudinal bars		
Steel ratio, ρ_l	0.0088	0.0120
Yield stress, f_{ly} (N/mm^2)	339.0	326.0
Stirrups		
Steel ratio, ρ_s	0.00882	0.0120
Yield stress, f_{sy} (N/mm^2)	328.0	321.0
Hardening parameter, H'	2.10	2.10
Tension-stiffening parameters		
α_1	20.0	20.0
α_2	0.60	0.60
Shear retention parameters		
γ_1	10.0	10.0
γ_2	0.50	0.50
γ_3	0.10	0.10
Comp. strength reduction, Model A		
Comp. reduction parameter, K_1	0.50	0.45

Note: Where different material parameters have been used these are given in the text.

The experimental and all the numerical post-cracking torsional stiffnesses are similar, Fig. 7.5, for applied torque values below 35 kN.m. Therefore, the effects of reducing the concrete compressive strength are insignificant at this stage. Above this torque level, the slope of the torque-twist curve decreases as the applied torque increases. At this stage of the behaviour, different torsional stiffnesses were obtained from the numerical tests for each of the values of k_1.

All the numerical tests have been carried out with the tension-stiffening parameters α_1 and α_2 set to 15 and 0.6 respectively. Mohamed [6] analysed this beam with various values for α_1 and α_2. The torque-twist curves obtained were appreciably stiffer than the experimental results. The best fitting was obtained by setting the values of α_1 and α_2 to zero. It was suggested that for pure torsion analysis the tension-stiffening affects should be neglected altogether. The Author believes that part of the cause of the stiff response in the study was probably because the reduction in concrete compressive strength due to transverse tensile strain was not considered.

7.2.4.1 Variation of the displacements

The distributions of the displacements in the x, y and z directions at various cross-sections of beam B4 have been investigated using the finite element mesh of Fig. 7.3a and the boundary conditions shown in Fig. 7.6, by which the middle cross-section of the beam was restrained against twisting. Fig. 7.7

compares the distribution of the displacements in the x and y directions along typical longer and shorter edges of the middle cross-section, section A-A, at loading stages just after cracking, T=20.5 kN.m, and close to failure, T=46.1 kN.m. The figure shows that the restrained cross-section can extend in both x and y directions as a result of concrete cracking, curves A.

At the free end, section B-B, the beam experienced both an extension due to the cracking and a rotation due to the applied torque. Fig. 7.8 shows the resulting distribution of the u and v displacements along the edges of the free end, curves B, at applied torque level of 46.1 kN.m. The displacements occurred due to twisting of the beam, curves B-A, may be obtained by subtracting the extension occurred at the middle section, curves A, from the total displacements, curves B. Finally, variations of the total u and v displacements over both cross-sections considered are shown in Figs. 7.9 and 7.10 for applied torque of 46.1 kN.m.

A similar analysis has been carried out for the displacement in the z direction. Fig 7.11 shows the distribution of the w displacement along a typical longer edge of the middle section at applied torques of 20.5 and 46.1 kN.m. It can be seen that the edge of the restrained section was only warped. This warping increases as the applied torque increases.

Because of cracking, the length of the beam increases with increasing torque. The longitudinal extension is proportional the distance from the restrained cross-section. Fig 7.12 shows the

distribution of the w displacement along a typical longer edge of the free end at applied torque of 46.1 kN.m, curve B. The curve represents the resultant of the longitudinal extension of the beam and warping of the edge. The extension due to cracking is represented in the figure by the curve B-A. This curve reveals that the extension in the z direction was partially arrested at the corners by the longitudinal bars.

The variation of the total w displacement over the middle section, sec. A-A, and the free end, sec. B-B, is shown in Figs 7.13a and 7.13b for an applied torque of 46.1 kN.m. Fig 7.13c Represents the longitudinal extension occurring at the free end. The figure shows that, apart from the corners where the extension is arrested by the longitudinal steel, the extension that occurred along the edges of the section is larger than that which occurred at the centre of the section.

7.2.4.2 Parametric study

To investigate the effects of some of the material and solution parameters on the non-linear finite element analysis of reinforced concrete beams in torsion, beam B4 has been chosen to carry out a parametric study. The parameters considered were the compressive strength reduction models, tension-stiffening parameters α_1 and α_2, integration rule, convergence tolerance, solution algorithm and element aspect ratio. In each numerical test, one parameter has been considered to vary, the other parameters being held constant in order to isolate the effects of the parameter considered. For the sake of

consistency, the CPU time recorded at the last converged increment of loading has been considered in the comparisons between the different numerical tests.

7.2.4.2.1 Effect of concrete compressive strength reduction models

Three different models to reduce the concrete compressive strength after cracking have been incorporated in the present work. These models are examined in this section for the case of pure torsion. Fig. 7.14 shows the finite element solutions obtained using Cervenka's proposal [7], model A with k_1 = 0.55, Vecchio and Collins's model B [8] and the modified Vecchio and Collins's model C [9]. The predicted collapse torques were 49.9, 53.1 and 50.6 kN.m respectively. Failure torques of models A and C were slightly higher than the experimental value, 47.4 kN.m, by about 5% and 7% respectively. For model B, the collapse torque was overestimated by about 12%. The overall behaviour obtained by the different models is in good agreement with the experimental curve. However, the torque-twist curve of model A is closer to the experimental results compared with the relatively stiffer curves of models B and C.

7.2.4.2.2 Effect of the tension-stiffening parameters

The variation of the tension-stiffening parameters α_1 and α_2 can strongly affect the post-cracking behaviour of reinforced concrete members. It was mentioned in section 3.4.2.3.1 that values in the range of 5 - 25 and 0.2 - 1.0 have been used for α_1 and α_2

respectively in the finite element analysis of flexural members and deep beams. However for beams under torsion, Phillips and Mohamed [10] suggested neglecting the tension-stiffening parameters in order to predict reasonable post-cracking response. In the present study, the variation of these parameters has been considered in presence of a concrete compressive strength reduction model.

Numerical tests with values of α_1 equal to 10, 15, 20, 25 and zero, i.e no tension-stiffening, have been carried out. In these tests, α_2 was set to 0.6. Fig.7.15 shows that the variation of the parameter α_1 has a negligible effect on the collapse torque and only affects the post-cracking torsional stiffness at applied torque levels below 40 kN.m. Beyond this level, the variation in the torsional stiffness for different values of α_1 is very small. The overall behaviour obtained from these tests ranges from the very soft response when α_1 was set to zero to the relatively stiff response for α_1 = 25. The best fit to the experimental results was obtained for α_1 = 15.

To study the effects of the parameter α_2, which represents the sudden loss in the tensile stress at instant of cracking, numerical tests have been carried out with α_2 equal to 0.0, 0.5, 0.6, 1.0. In these tests α_1 was set to 15. Results of the analyses also revealed that the variation of α_2 has insignificant effects on the behaviour at loading stages beyond 40 kN.m, Fig.7.16. Good agreement with the experimental torque-twist curve has been achieved for α_2 equal to 0.5 and 0.6. When α_2 was set to zero, the cracking torque was underestimated and the post-cracking response was very soft. For α_2 = 1.0, the cracking torque was overestimated and the post-cracking

response was relatively stiff compared with the experimental results. the best fitting was obtained when α_2 was set to 0.6.

During the numerical tests, it has been observed that most of the sampling points had cracked in two orthogonal directions. At the concrete core, some of the sampling points had three orthogonal cracks. At a sampling point, orthogonal cracks may have different tension-stiffening relationships according to the size and number of reinforcing bars crossing the crack and their orientation with respect to the cracked plane under consideration. Moreover, positions of the cracked sampling points with respect to reinforcing cage may affect the rate of stress release as the cracks widen. Therefore, the selected values for the tension-stiffening parameters, α_1 = 15.0 and α_2 = 0.6, represent the average stress-strain relationship for all cracks.

Results obtained from this study and those of sections 7.2.4 and 7.2.4.2.1 revealed that the predicted post-cracking torque-twist curve can be divided into two regions according to the parameters dominating the behaviour. At early stages after cracking, the response is significantly affected by the tension-stiffening parameters, while the reduction in concrete compressive strength has a negligible effect. However, at stages close to the ultimate torque the behaviour is strongly affected by reducing the compressive strength, while the tension-stiffening parameters have insignificant effects.

7.2.4.2.3 Effect of the integration rule

In order to confirm the conclusions drawn from section 5.5.1.2 concerning the accuracy and efficiency of the 15 point rules, beam B4 has been analysed using the three different 15 points rules and the 27 point rule. The resulting finite element solutions for different rules are shown in Fig. 7.17. The predicted torque–twist curves are generally in good agreement with the experimental results. A slightly stiffer response has been obtained for the 27 and the 14 point rules. This may be attributed to the relative distribution of the sampling points within the cross–section of the beam. The computation time required to carry out the analysis using the 27 point rule was substantially greater than those required for the 15 point rules. The relative CPU times recorded at the last increments of loading were 1.94, 1.18, 1.20 and 1.0 for the 27, 15a, 15b and 14 point rules respectively. Therefore, it may be concluded that for the finite element applications to reinforced concrete beams in torsion the 15 sampling point integration rules are accurate and computationally efficient when compared with the 27 point integration rule.

7.2.4.2.4 Effect of the convergence tolerance

A force convergence criterion has been adopted throughout the present work. This type of criterion, which is favoured by engineers, monitors equilibrium by setting the out–of–balance forces to be within an acceptable limit. Bergan and Holand [11] argued that the unbalanced forces often form equilibrium groups which does not

have much influence on the overall structural behaviour. To investigate this and in order to select a suitable convergence tolerance for the analyses of reinforced concrete beams under torsion, beam B4 has been tested for tolerances of 1%, 2%, 5% and 10%. These values ranging from a relatively tight tolerance to a slack one. All the tests have been conducted using the modified Newton-Raphson stiffness method Kt2a.

Results of the study are compared against the experimental curve in Fig. 7.18. The analytical solutions obtained for the tolerances considered are almost similar. However, a large difference in the computation time was observed for the different tests carried out. The relative CPU times recorded at the last converged increments of loading were 2.31, 1.86, 1.35 and 1.0 for convergence tolerances of 1%, 2%, 5% and 10% respectively. It may be concluded therefore that acceptable solutions of a relatively cheap cost can be obtained using a moderate convergence tolerance. A 5% tolerance has been selected for the present work.

7.2.4.2.5 Effect of the solution algorithm

To study the efficiency and accuracy of different non-linear solution algorithms, beam B4 has been analysed using the algorithms incorporated in the present finite element model. In these analyses, a constant convergence tolerance of 5% has been used. Results of the analyses revealed that there is no significant difference between the finite element solutions obtained, Fig. 7.19. However, a large difference between the recorded computation times has been observed.

The relative CPU times were 1.62, 1.80, 1.58, 1.51, and 1.0 for the initial, tangential, KT1, KT2 and KT2a stiffness methods respectively.

The KT2a stiffness method, which has been adopted in this work, updates the stiffness matrix more than once during increments of loading which require a large number of iterations to achieve convergence. These increments represent stages of loading at which large deformation occurs due to either cracking, yielding or substantial non-linear behaviour of concrete in compression.

7.2.4.2.6 Effect of the element aspect ratio

To investigate the effect of the element aspect ratio in application to reinforced concrete beams under pure torsion, three different finite element meshes has been considered in this study, Fig. 7.3. The analytical solution obtained for beam B4 using the finite element mesh shown in Fig. 7.3a, 12 elements, is compared with those obtained for the 18 elements meshes shown in Figs. 7.3b and 7.3c. The ratios of the element dimensions were 1:1:3.6, 1:1:2.4 and 1:1.5:3.6 for mesh A, mesh B, and mesh C, respectively. Fig. 7.20 shows that the numerical torque-twist curves of all meshes considered are almost similar. These results confirm the conclusion drawn from section 5.5.1.4 where the element aspect ratio does not seem to significantly affect the predicted finite solutions of beams under pure torsion. Therefore, the numerical tests can be carried out using the 12 element mesh of Fig. 7.3a.

7.2.4.3 Steel stresses

The variations of tensile stresses in the reinforcing steel of beam B4 have been investigated using the finite element mesh of Fig. 7.3b. Figs. 7.21a, 7.22a and 7.23a compare the theoretical torque-steel stress relations obtained for the longer and shorter legs of a typical stirrup and for a typical longitudinal bar with the corresponding experimental curves obtained from averaging the stresses from a number of bars. The tensile stresses were measured at central regions of the bars considered. The figures show that neither the stirrup nor the longitudinal bar carry any significant stresses prior to cracking. On cracking, the tensile stresses in the stirrups and the longitudinal bar increased suddenly. The predicted response for the longer stirrup leg and the longitudinal bar is in good agreement with the experimental results throughout the entire range. Figs 7.21a and 7.23a show that both the theoretical and the experimental stresses increase almost linearly with increasing torque.

For the shorter leg of stirrup, the experimental results show an irregular variation of tensile stresses as the applied torque increases, Fig 7.22a. Hsu [1] argued that this phenomenon cannot be explained by present theories. However, the finite element results revealed that, similar to the longer leg, the stresses at the shorter leg increased steadily with increasing torque.

The predicted distribution of tensile stresses at different stages of loading along the longer and shorter stirrup legs and along the longitudinal bar are shown in Figs. 7.21b, 7.22b and 7.23b

respectively. Finally, it can be seen from the figures that for the beam under consideration neither the stirrup nor the longitudinal bar yielded at failure.

7.2.5 Results of the Analyses, Beam B2

This beam was similar to beam B4 except that the amount of reinforcement provided was much smaller than that used in beam B4. The steel ratios for the longitudinal bars and stirrups were 0.00827 and 0.00823 respectively. The analytical torque-twist curves obtained for beam B2 are compared with the experimental curve in Fig. 7.24. The figure show that the cracking torque and the horizontal plateau caused by the sudden increase in the angle of twist during cracking have been reasonably predicted. Also, good agreement with the experimental results for the post-cracking behaviour and the predicted collapse torque has been achieved when the reduction of the concrete compressive strength due to transverse tensile strain is included. The experimental ultimate torque was 30.0 kN.m, while the analytical failure torques were 33.6 and 32.6 kN.m for values of k_1 equal to 0.55 and 0.6 respectively. When k_1 was set to zero, a relatively stiffer post-cracking response was obtained and the predicted collapse torque was 38.4 kN.m, about 28% higher than the experimental value. The numerical tests show that both the longitudinal steel and the longer legs of stirrups have been yielded prior to failure.

Referring to Fig. 7.24, the parameter k_1 has a negligible effect on the behaviour for applied torque levels below 25 kN.m. Above this

value, the torsional stiffness starts to decrease as the applied torque increases. These results are similar to those obtained for beam B4, see section 7.2.4.

The influence of the tension-stiffening parameter α_1 has been investigated by comparing the numerical results obtained for α_1 equal to 10 and 15. Fig 7.25 shows that for underreinforced beams such as beam B2 the variation of the parameter α_1 can slightly affect the torque-twist curve at stages close to the ultimate torque.

7.2.6 Results of the Analyses, Beam B3

Apart from the difference in the percentage of steel used, see Table 7.1, this beam was identical to beam B4. Fig 7.26 compares the experimental and analytical torque-twist curves. The figure show that the predicted response is similar to that of beam B4. The variation of the parameter k_1 has a negligible effect on the torque-twist curve just after cracking. The computed failure torques were 40.8 and 38.9 kN.m for k_1 equal to 0.55 and 0.6 respectively. These values are in reasonable agreement with the experimental ultimate torque, 37.6 kN.m. For k_1 equal to zero the computed collapse torque was 51.5 kN.m which is higher the experimental value by about 36%. The numerical tests show that both the longitudinal bars and the longer legs of stirrups yielded before failure of the beam.

To investigate the analytical crack pattern, beam B3 has been analysed using the finite element mesh of Fig. 7.3b. The cracks

first appear at sampling points close to the middle of the wider and shorter faces of the beams at applied torque level of 17.9 kN.m. These cracks were inclined approximately at 45 degrees to the longitudinal axis of the beam, Fig. 7.27a. When the applied torque was increased to 22.4 kN.m, additional cracks occurred, on the wider and shorter faces, close to the top and bottom edges of the beam. As in the experimental pattern, these cracks were inclined at angles substantially greater than 45 degrees to the longitudinal axis, Fig. 7.27b. The predicted pattern of cracks was almost similar to the experimental crack pattern shown in Fig. 7.2.

7.2.7 Results of the Analyses, Beam B5

This beam was reinforced with a relatively large amount of steel compared to beam B4. The provided ratios for the longitudinal bars and stirrups were 0.0211 and 0.0213 respectively. The numerical solutions for different values of k_1 are compared in Fig. 7.28 with the experimental results. The solutions obtained were in good agreement with the experimental curve. The computed collapse torques were 55.8 and 53.1 kN.m for k_1 equal to 0.5 and 0.55 respectively. These values are close to the experimental collapse torque, 56.2 kN.m. When k_1 was set to zero, a very stiff post-cracking response was obtained and the collapse torque was overestimated by about 45%, the computed torque was 81.6 kN.m. As in the experimental test, the predicted mode of failure was crushing of concrete prior to yielding of steel.

7.2.8 Results of the Analyses, Beam G3

Compared with the previous beams, beam G3 had a larger depth of 508 mm., the depth of the previous beams was 381 mm., see Table 7.1. The percentage of reinforcement provided was similar to beam B2, the steel ratios were 0.0088 and 0.00882 for the longitudinal bars and stirrups. Fig. 7.29 compares the experimental torque–twist curve and the finite element solutions obtained for k_1 equal to 0.45, 0.5 and zero. The computed ultimate torques were 49.7, 48.6 and 56.6 kN.m respectively. For k_1 equal to zero, the collapse torque was overestimated by about 15%, the experimental failure torque was 49.2 kN.m, and the predicted post–cracking behaviour was stiffer than the experimental torque–twist curve. In the numerical tests, both the longitudinal bars and the stirrup longer legs yielded before failure.

The effect of the tension–stiffening parameter α_1 has been studied for this underreinforced beam by setting α_1 equal to 15 and 20. Fig. 7.30 confirms the results obtained for beam B2, where for underreinforced concrete beams in torsion the variation of the parameter α_1 can slightly influence the post–cracking response close to failure.

7.2.9 Results of the Analyses, Beam G4

This beam was identical to beam G3 apart from a larger amount of steel being provided, the steel ratio was 0.012 for both the longitudinal bars and stirrups. Fig. 7.31 shows that the numerical results obtained were in good agreement with the experimental

torque–twist curve. The predicted collapse torques were 66.4 and 65.6 kN.m for k_1 equal to 0.4 and 0.45 respectively. When k_1 was set to zero, a relatively stiff post–cracking response was obtained and the computed failure torque was 78.4 kN.m which is about 21% higher than the experimental value. The finite element solutions show that the longer legs of the stirrups yielded before failure while the longitudinal bars were about to yield when the concrete crushed.

7.3 Reinforced Concrete Beams under Combined Torsion and Bending

Collins et al [2] tested two series of rectangular reinforced concrete beams under combined bending and torsional loads. All the test specimens contained both longitudinal and transverse reinforcement. The beams in the first series had equal amount of tension and compression longitudinal steel, while in the beams of the second series the area of tension steel was greater than that of the compression steel. Two beams, designated RE2 and RE4, from the first series were chosen for the present study mainly because their experimental torque–twist curves were available. Both of the selected beams had the same dimensions and amount of reinforcement. They only differed in the ratio of the applied torque to the bending moment, which was 0.88 for beam RE4 and 2.61 for beam RE2.

7.3.1 Description of the Beams and Test Observations

The beams had a 165X254 mm. (6.5X10 in.) cross–section, Fig. 7.32, and were tested over a 2438 mm. (8 ft.) span. Each beam was

tested with one end being clamped against torsion and the other end being free to twist. The bending load was applied at the one-third points by means of a hydraulic jack and a spreader beam. The torsion was applied by a jack at the end of an outrigger arm [2]. The jacks were hydraulically interconnected so that during the test the ratio of torsion to bending moment remained constant. The load was applied in about 10 increments up to failure.

The behaviour of the specimens with lower ratios of torsion to bending, such as beam RE4, were influenced primarily by flexure. Cracks appeared first at the bottom face of the beam and then extended to the side surfaces. For the beams with high ratios of torsion to bending, e.g beam RE2, cracks were first visible on the side surfaces. They formed at about 45 degrees to the longitudinal axis of the beam and gradually extended, at almost constant inclination, to the top and bottom of the member. Both beam RE4 and RE2 failed by yielding of the bottom steel and the formation of the compression hinge on the top surface.

7.3.2 Finite Element Idealisation and Material Properties

By taking advantage of symmetry, a segment representing one half of the beam was used for the numerical tests. The finite element meshes used in the analyses are shown in Fig. 7.33. At each end of the segment, the external torque was modelled by a set of equivalent nodal forces using the technique described in section 5.4. For flexural loading, the concentrated force applied at the one-third point was modelled as a line load uniformly distributed across the

width of the top face. The equivalent nodal forces and the boundary conditions imposed at both ends of the segment are shown in Fig. 7.34.

The reinforcement cages were prefabricated from plain round bars and then they spot welded. The cages consisted of four longitudinal corner bars and closed stirrups uniformly distributed over the beam at 76 mm. (3 in.) spacing. The properties of reinforcing bars and concrete and the additional material parameters used in the analyses are given in Table 7.5.

7.3.3 Results of the Analyses

Graphs of the experimental and theoretical torques versus the total twist of the test length, 2438 mm., are shown in Figs. 7.35 and 7.36 for beams RE4 and RE2 respectively. The figures show that both the initial and post-cracking torsional stiffnesses and the cracking torque were reasonably predicted. As expected for beam RE4, in which the influence of bending was relatively large (T/M = 0.88), the onset of cracking and hence the departure from the initial, uncracked, behaviour took place at a lower torque compared to beam RE2, T/M = 2.61. As in the tests, cracks formed first at sampling points close to the bottom face of beam RE4 almost perpendicular to the longitudinal axis of the beam and they gradually extended to the side surfaces. In beam RE2, the cracks appeared first on the side surfaces at about 45 degrees to the axis of the beam and they gradually propagated towards the top and bottom of the beam.

Table 7.5 Material properties and additional material parameters of Collins et al beams

Concrete	
Young's modulus, E (N/mm^2)	26700
Comp. strength, f'_c (N/mm^2)	31.7
Tensile strength, f_t (N/mm^2)	3.15
Poisson's ratio, ν	0.2
Unixaial crushing strain	0.003
Steel	
Young's modulus, E_s (N/mm^2)	200000
Longitudinal bars	
Bar diameter, mm	12
No. of bars	4
Yield stress, f_{ly} (N/mm^2)	307
Steel ratio, ρ_l	0.0123
Stirrups	
Bar diameter, mm	10
Spacing, mm	76
Yield stress, f_{sy} (N/mm^2)	338
Steel ratio, ρ_s	0.0151
Hardening parameter, H'	0.00
Tension-stiffening parameters	
α_1	15.0
α_2	0.6
Shear retention parameters	
γ_1	10.0
γ_2	0.50
γ_3	0.10
Comp. strength reduction, Model A	
Comp. reduction parameter, k_1	0.55

Note: Where different material parameters have been used these are given in the text.

The numerical tests have been carried out using a reduced concrete compressive strength according to model A. For beam RE4, T/M = 0.88, the predicted collapse torque was 9.0 kN.m for values of the compression reduction parameter k_1 of 0.5 and 0.55, Fig 7.35. This value is close to the experimental ultimate torque, 8.5 kN.m. The numerical solutions show that the bottom longitudinal bars yielded prior to failure and that ultimately the beam failed by crushing of the concrete. When k_1 was set to zero, the computed failure torque was 10.5 kN.m, about 24% higher than the experimental value.

For beam RE2, T/M = 2.61, the computed collapse torque was 11.0 kN.m for k_1 equal to 0.55 which is slightly higher than the experimental value, 9.5 kN.m. The tensile longitudinal bars yielded at failure and the beam failed by crushing of the concrete. When k_1 was set to zero, the predicted ultimate torque was 15 kN.m which is higher than the experimental value by about 53%. Finally, it can be seen from Fig 7.36 that that predicted response close to the ultimate stage was stiffer than the experimental behaviour. This is probably because a fixed crack model has been used in this study.

It is worth noting that the post-cracking response and the prediction of the ultimate torque of beams with large torque to bending ratio can be significantly affected by reducing the concrete compression strength compared to beams with small torque to bending ratio, Figs 7.35 and 7.36.

To study the effect of element size and number of elements within the cross-section of the beam, the numerical solution obtained for

beam RE2 using the finite element mesh shown in Fig 7.33a, which has 4 elements in the cross-section, is compared with that obtained for the finite element mesh shown in Fig. 7.33b, which has 6 elements in the cross-section. Fig. 7.37 shows that the analytical torque-twist curves obtained for both meshes are almost identical. Therefore, the numerical examples can be carried out using 4 elements in the cross-section.

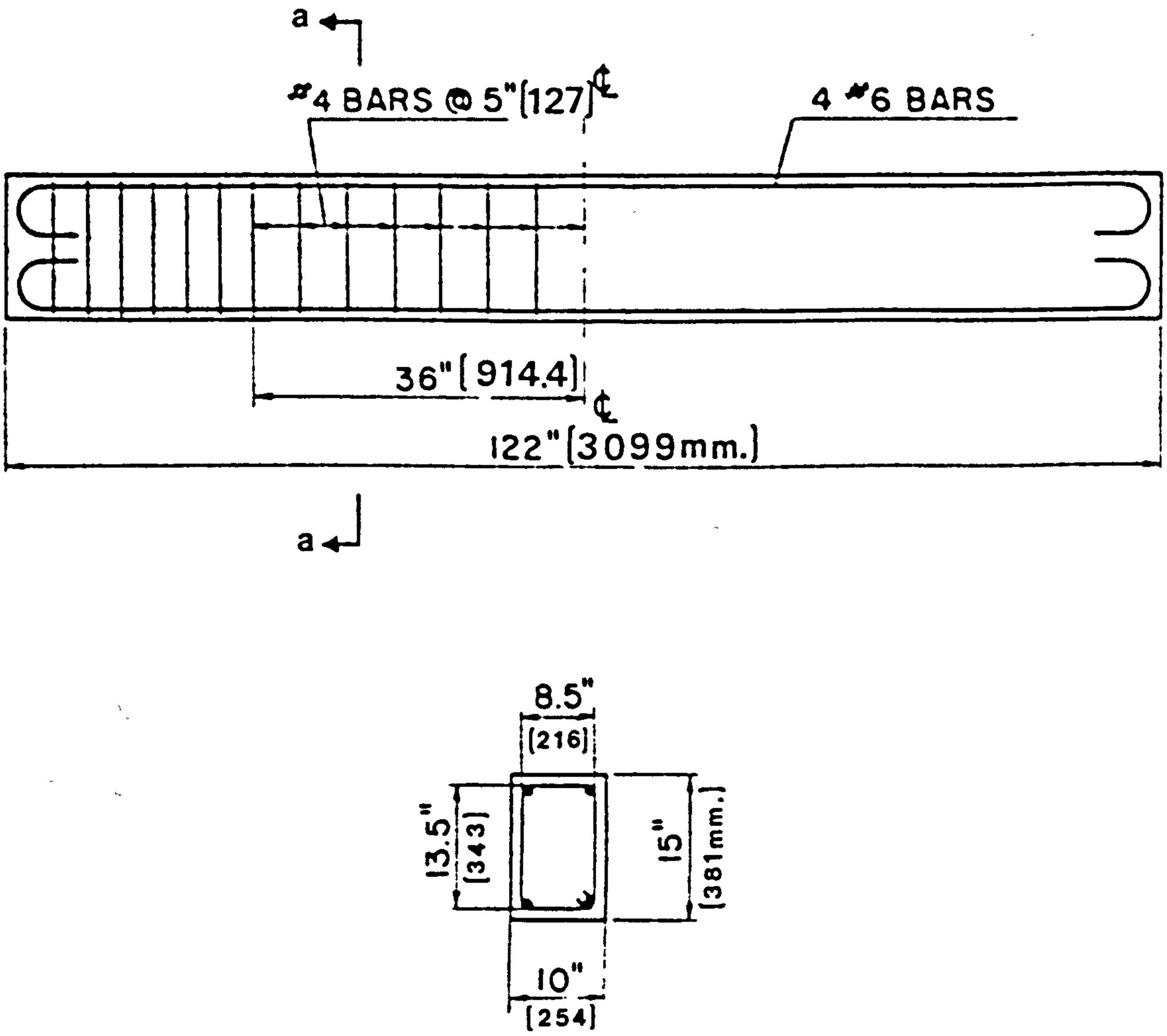

sec. a-a

Fig. 7.1 Dimensions and reinforcement details for a typical test beam, B3, (Ref. 2).

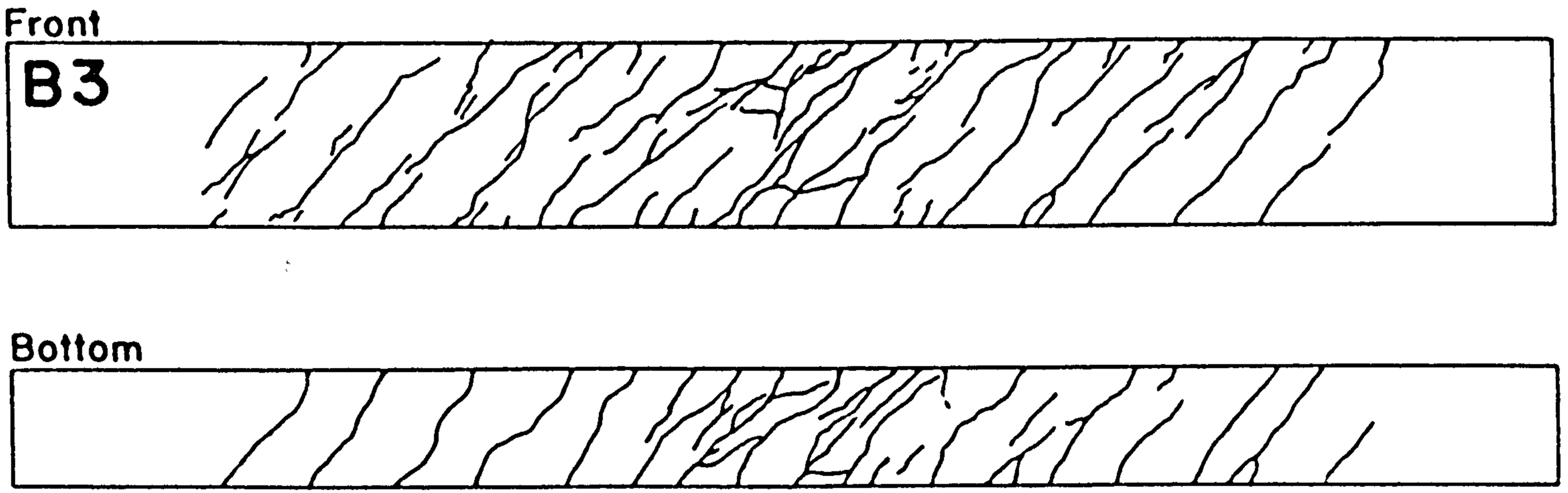

Fig. 7.2 Experimental crack pattern of beam B3, (Ref. 2).

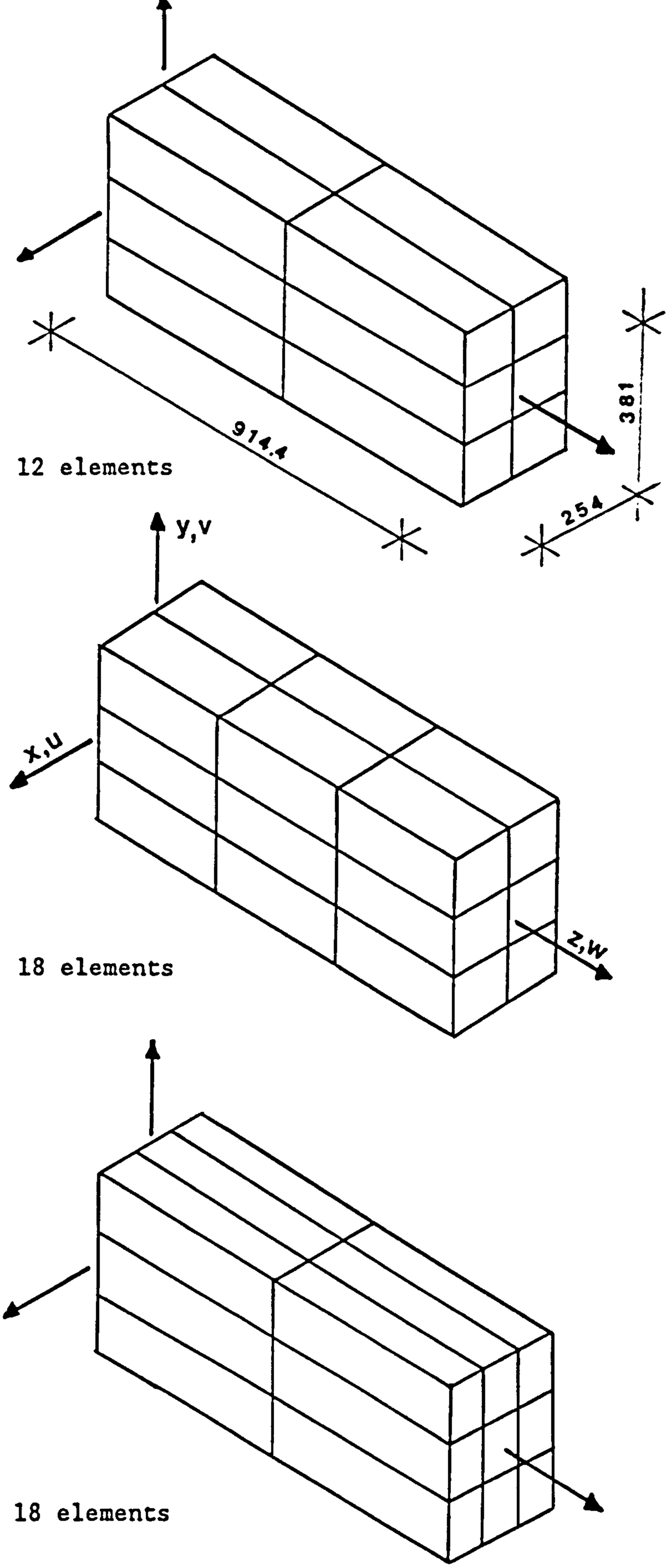

a) Mesh A, 12 elements

b) Mesh B, 18 elements

c) Mesh C, 18 elements

Fig. 7.3 Finite element meshes used for Hus's beams.

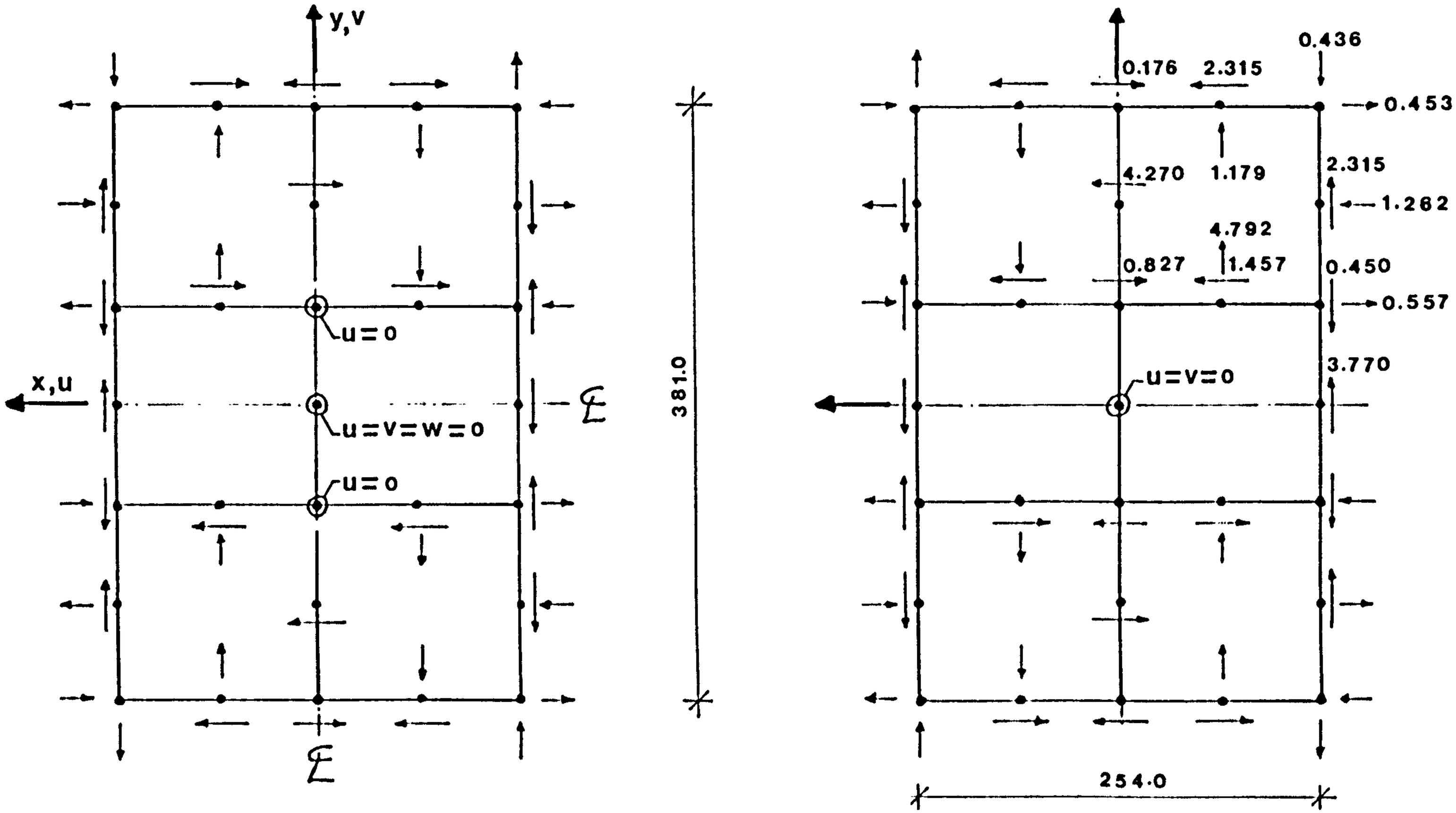

a) Left end, z = 0.0 T = 6.4 kN.m b) Right end, z = 914.4

Fig. 7.4 Equivalent nodal forces and boundary conditions used for beams B2 to B5.

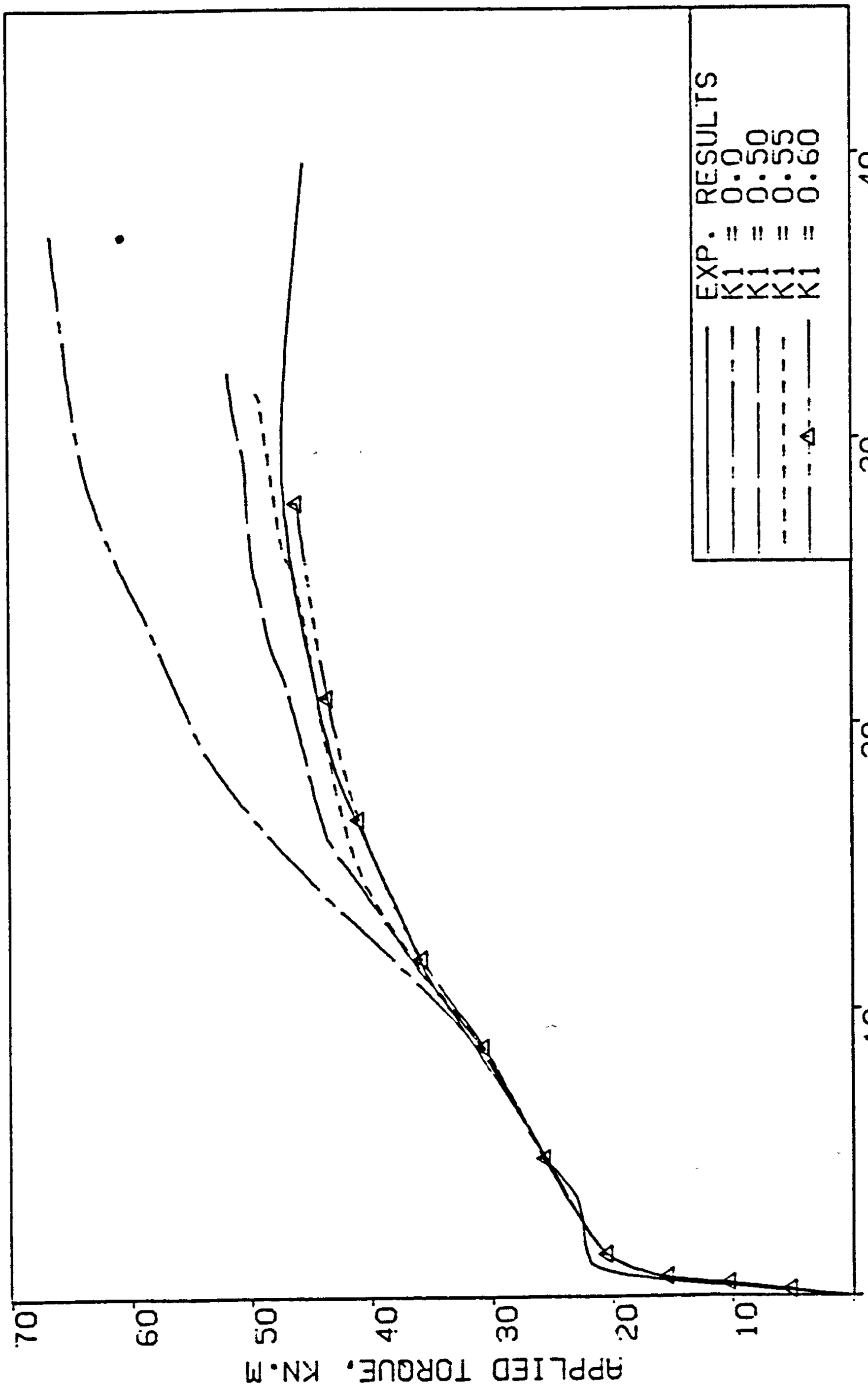

Fig. 7.5 Beam B4 - Effect of the compression reduction parameter k_1 on the torque–twist behaviour.

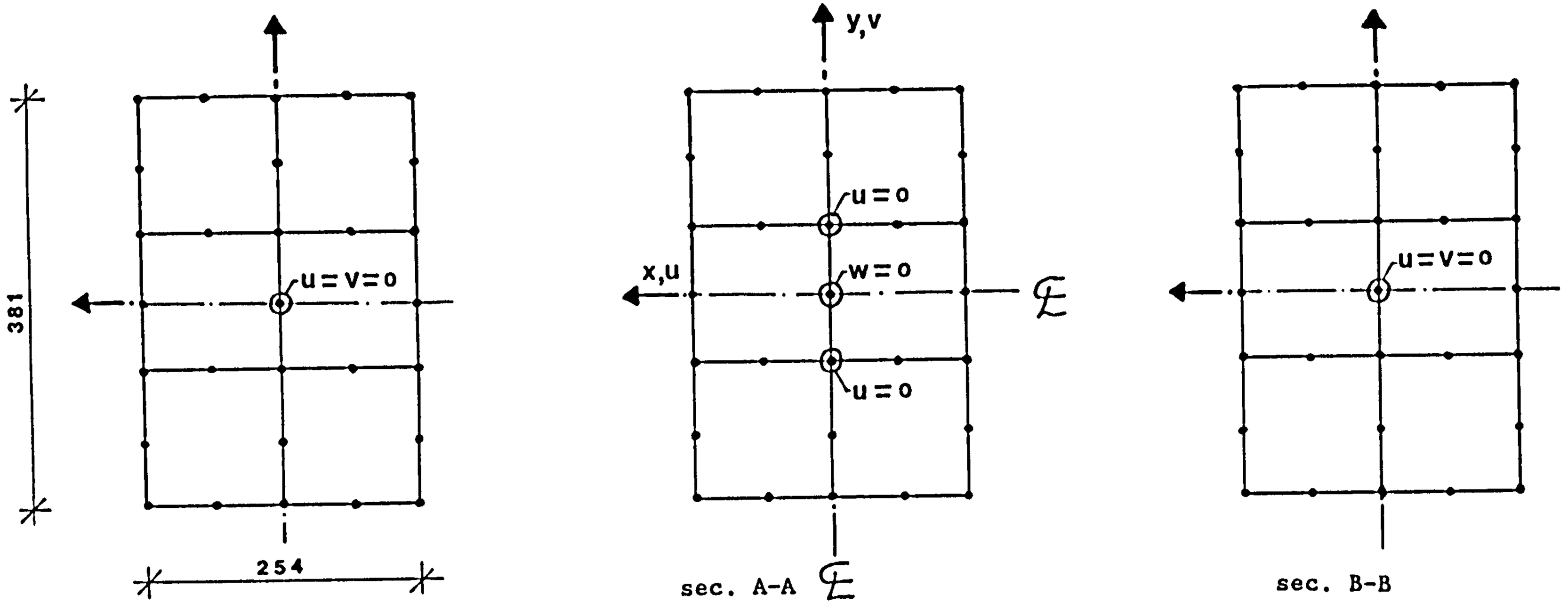

a) Left end, z = 0.0

b) Middle section, z = 457.2

c) Right end, z = 914.4

Fig. 7.6 Beam B4 – Boundary conditions used to study variation of the displacements.

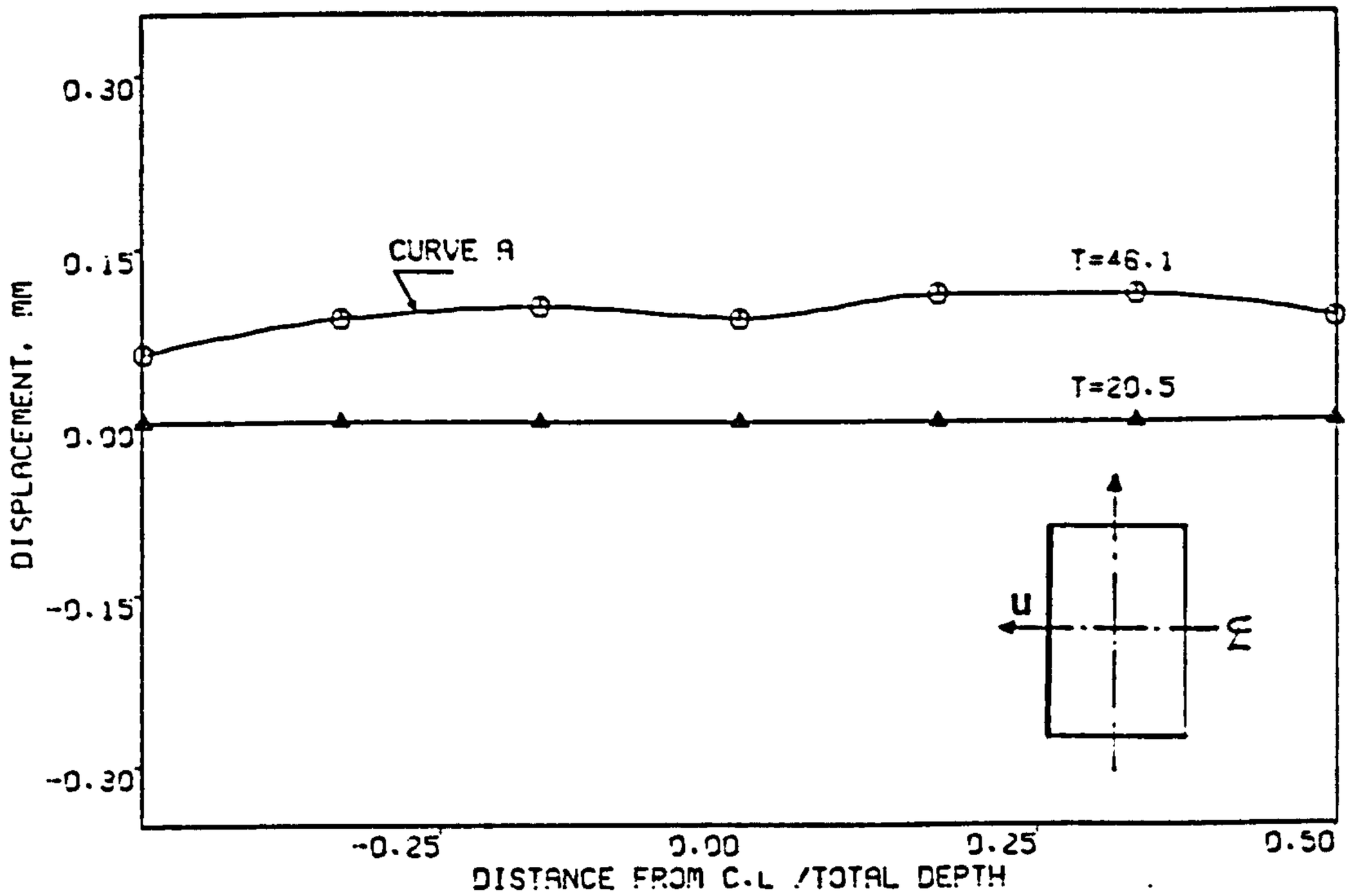

a) Displacement in the x direction, u displacement.

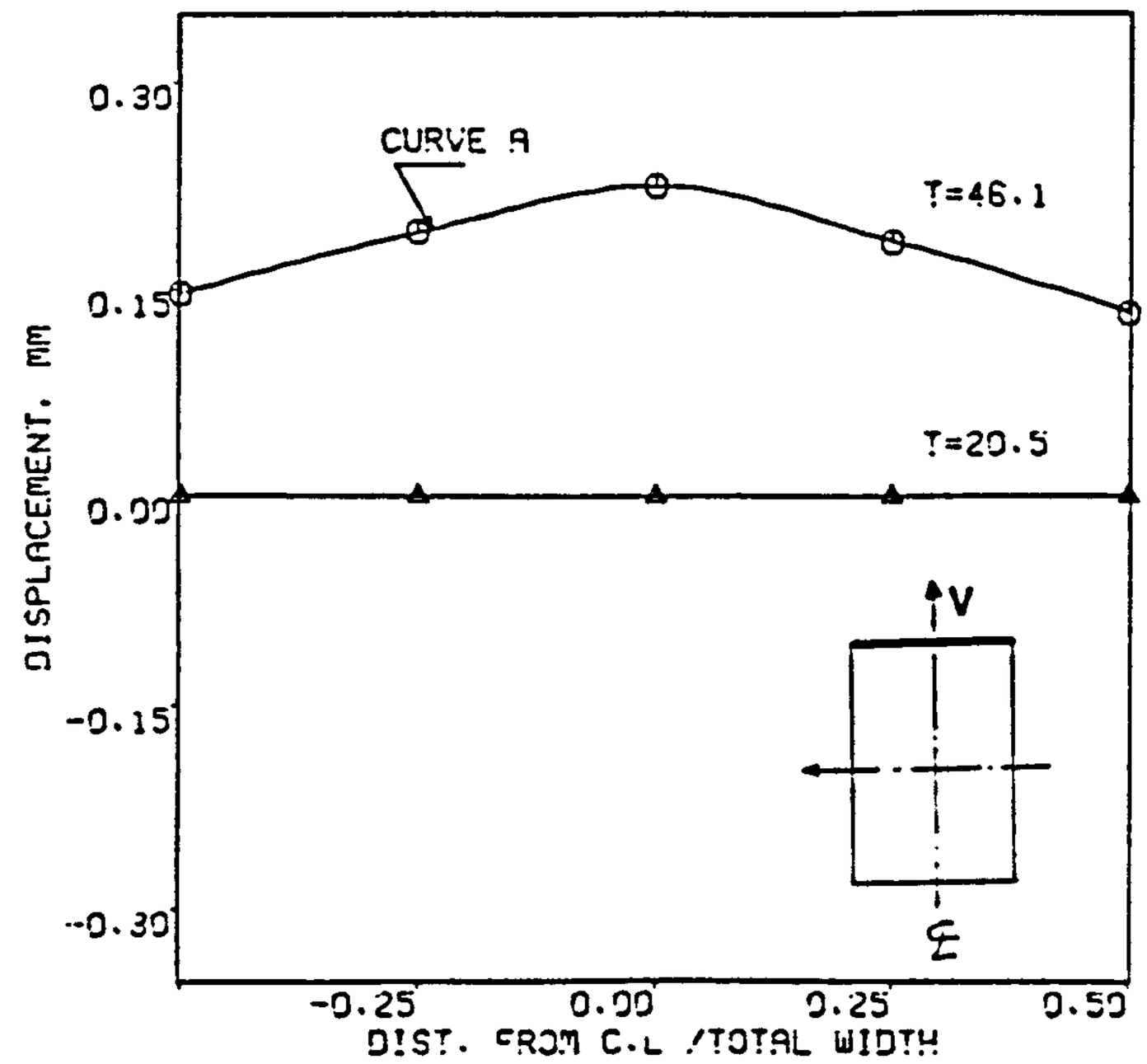

b) Displacement in the y direction, v displacement.

Fig. 7.7 Beam B4 – Distribution of the displacements in the x and y directions along typical edges of the middle cross-section, sec. A-A.

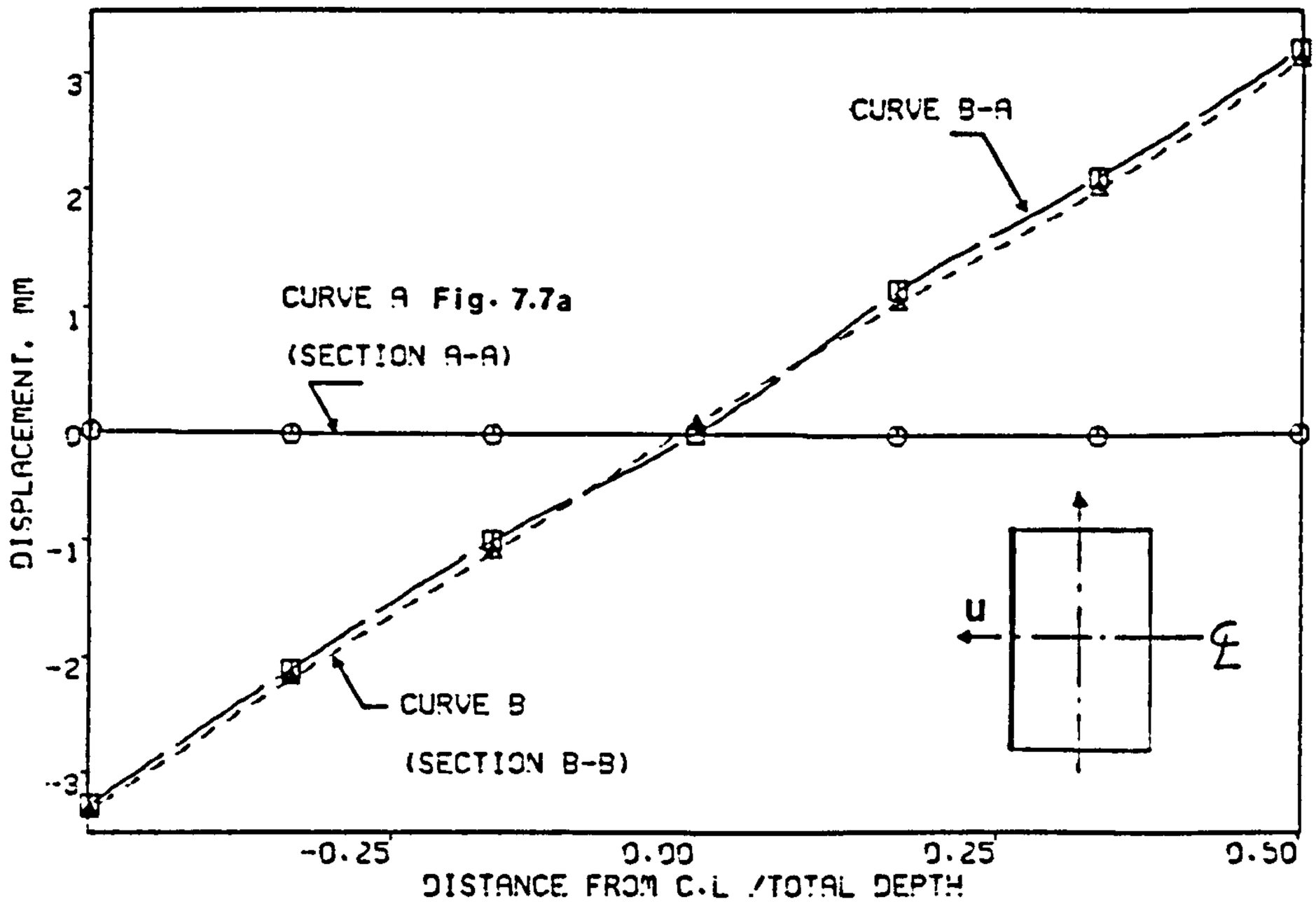

a) Displacement in the x direction, u displacement.

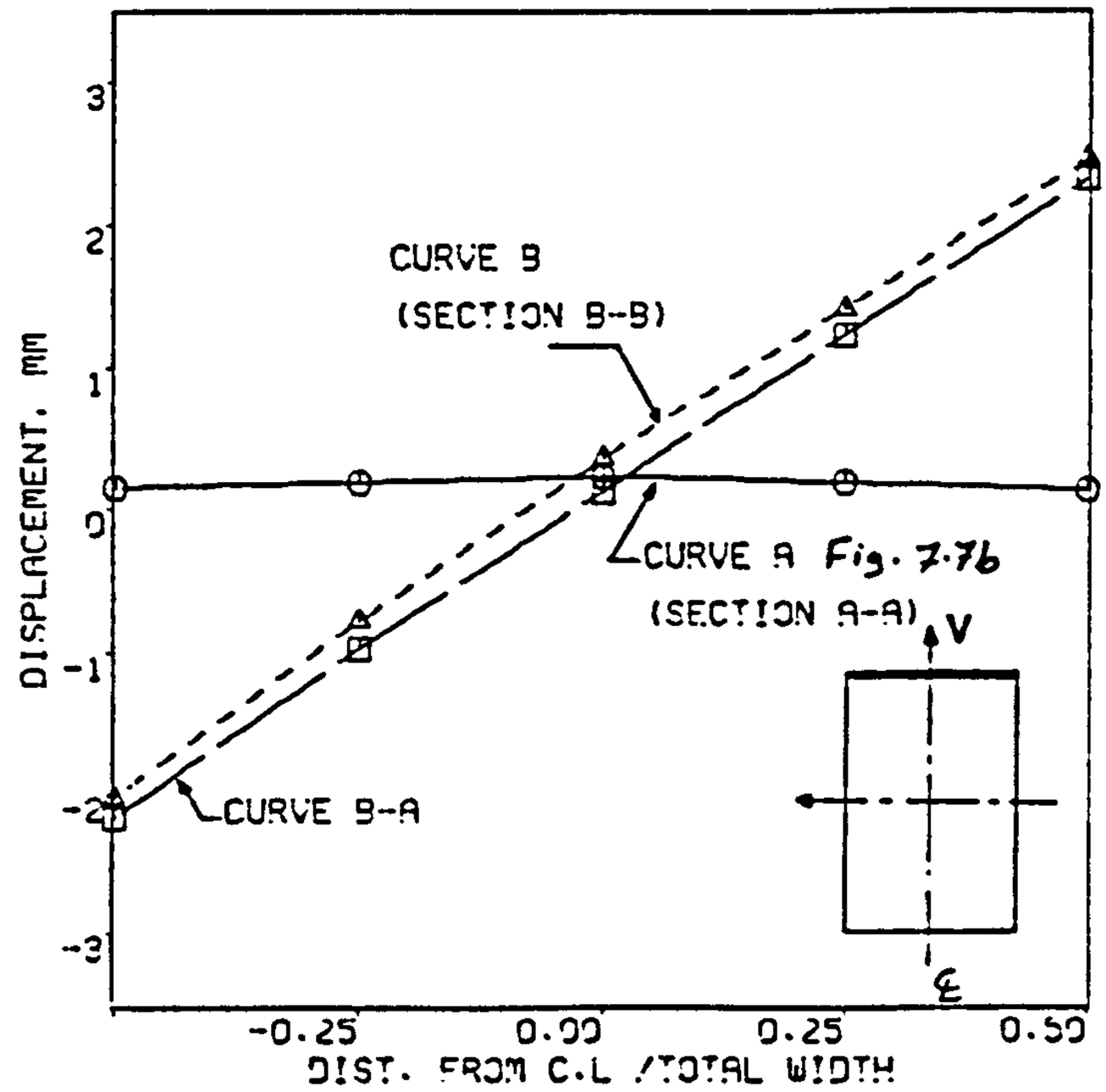

b) Displacement in the y direction, v displacement.

Fig. 7.8 Beam B4 – Distribution of the displacements in the x and y directions along typical edges of the free end, sec. B-B, for applied torque of 46.1 kN.m.

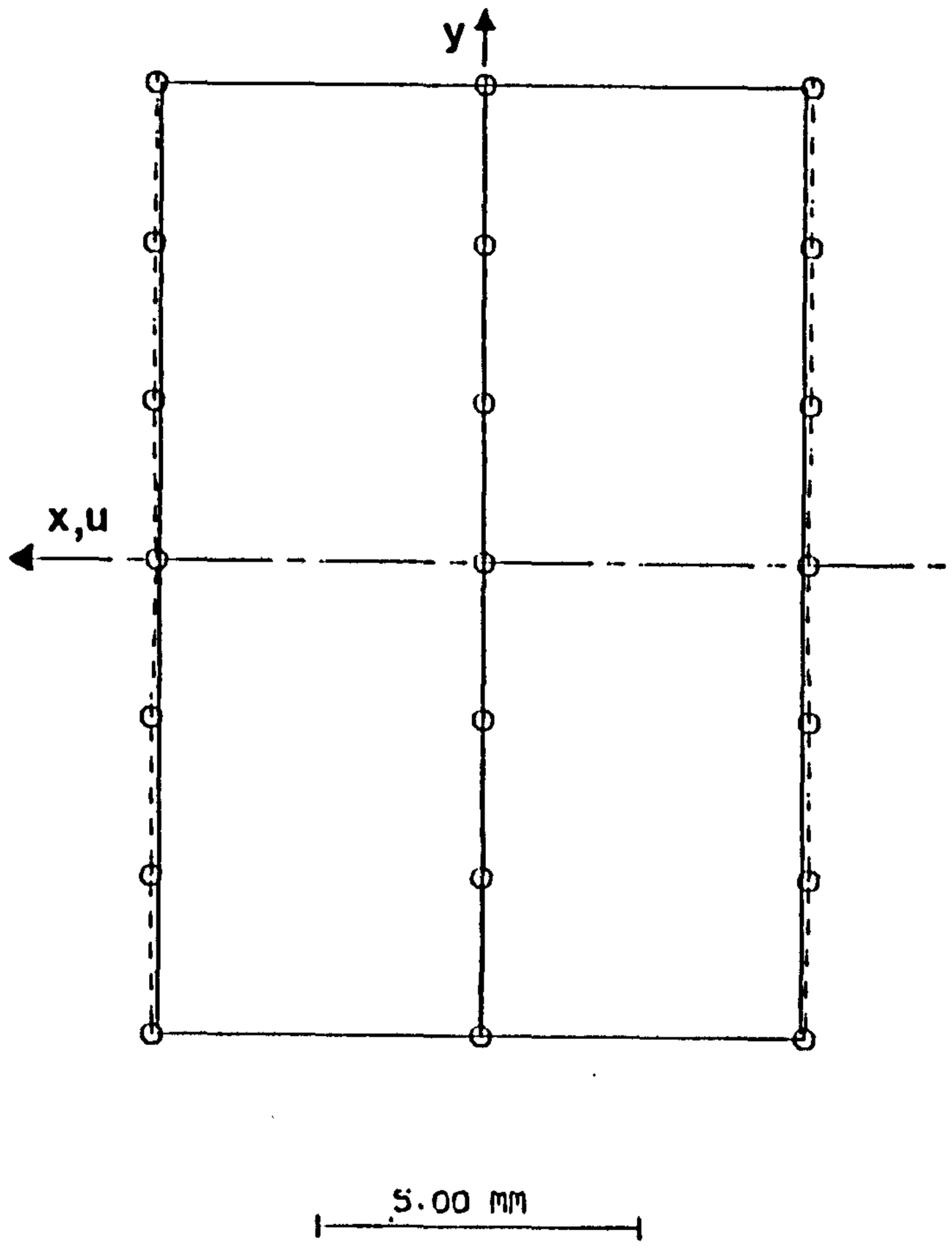

a) Middle section, sec. A-A.

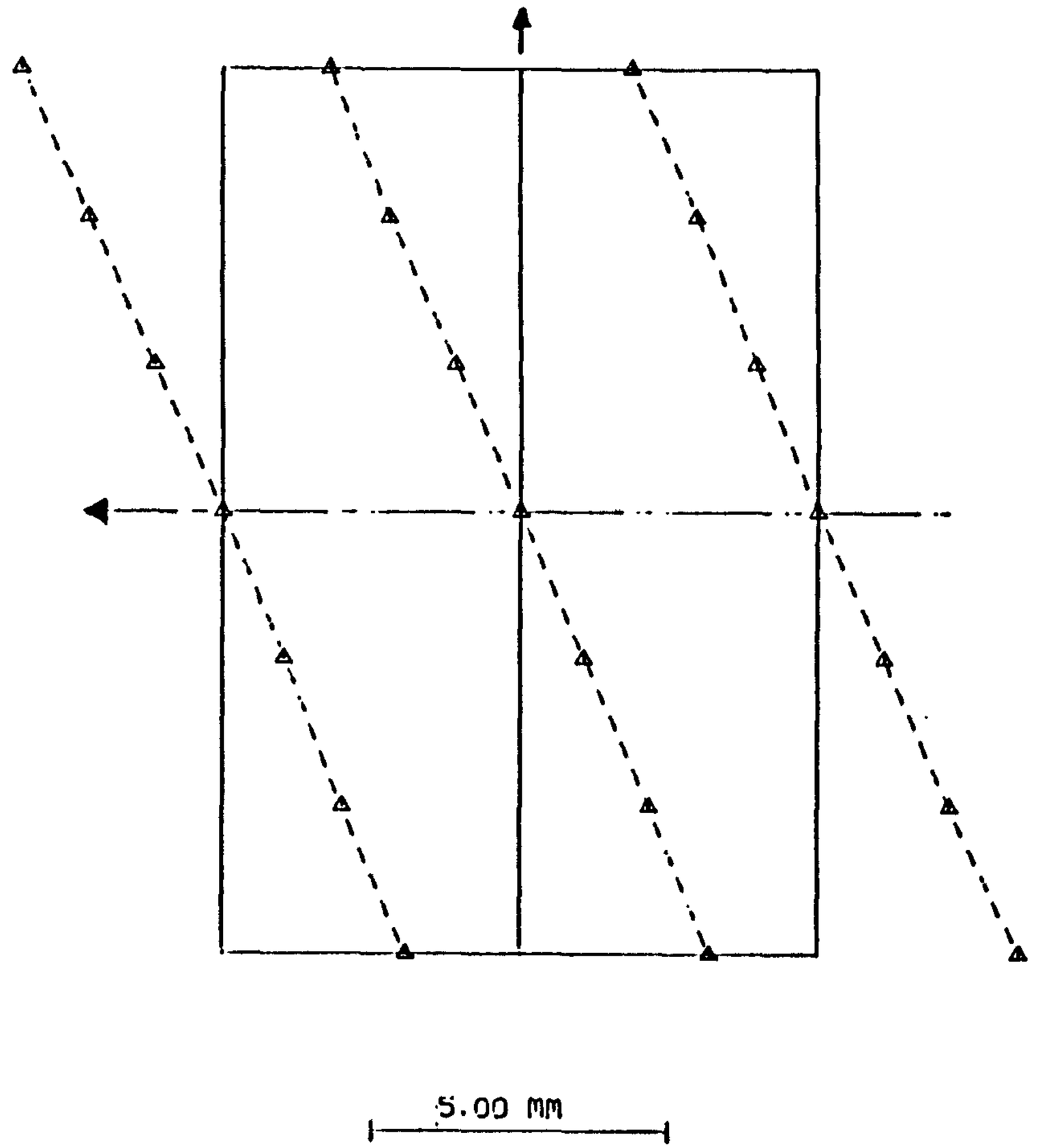

b) Free end, sec. B-B.

Fig. 7.9 Beam B4 – Variation of the displacement in the x direction over the middle and free end cross-sections for applied torque of 46.1 kN.m.

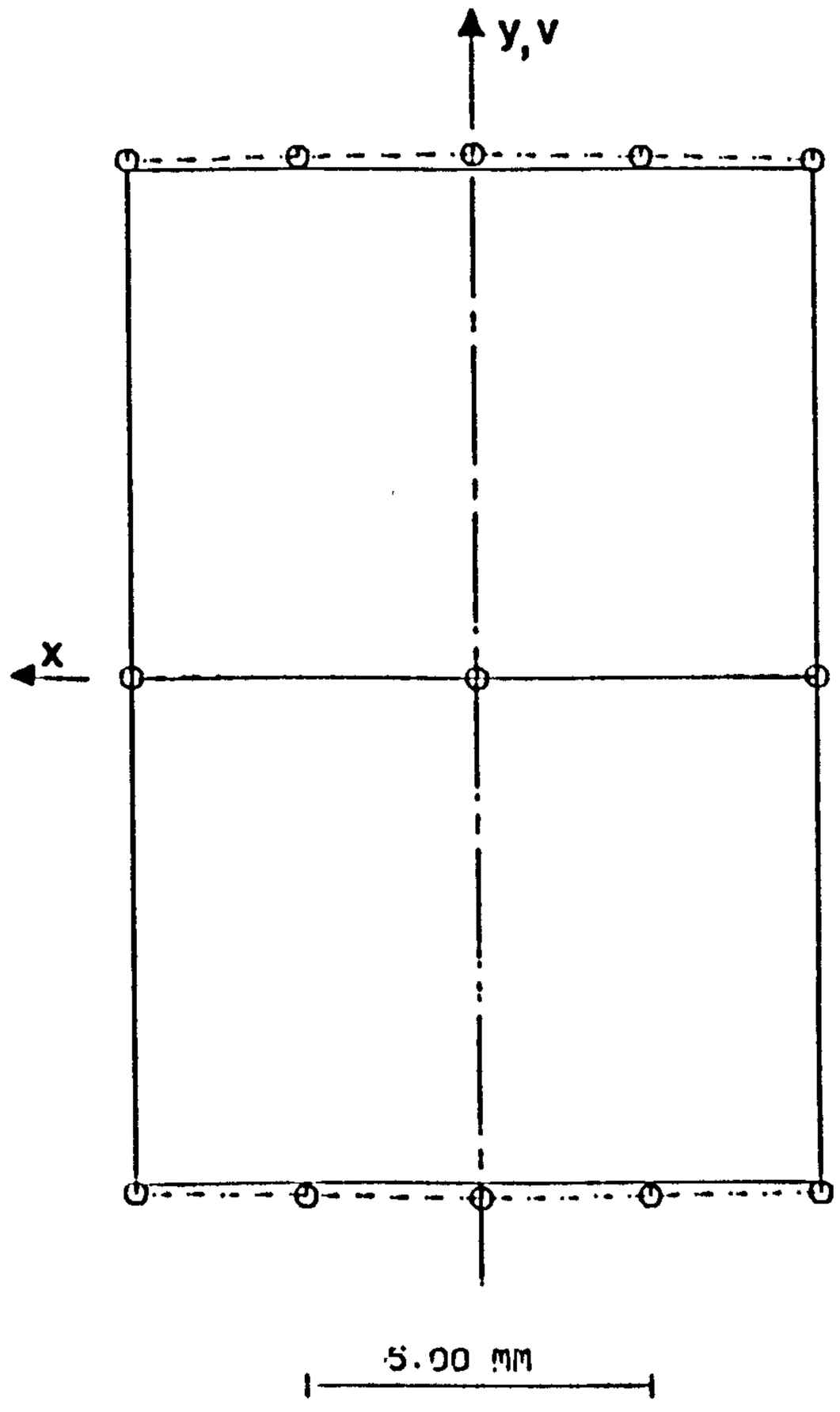

a) Middle section, sec. A-A.

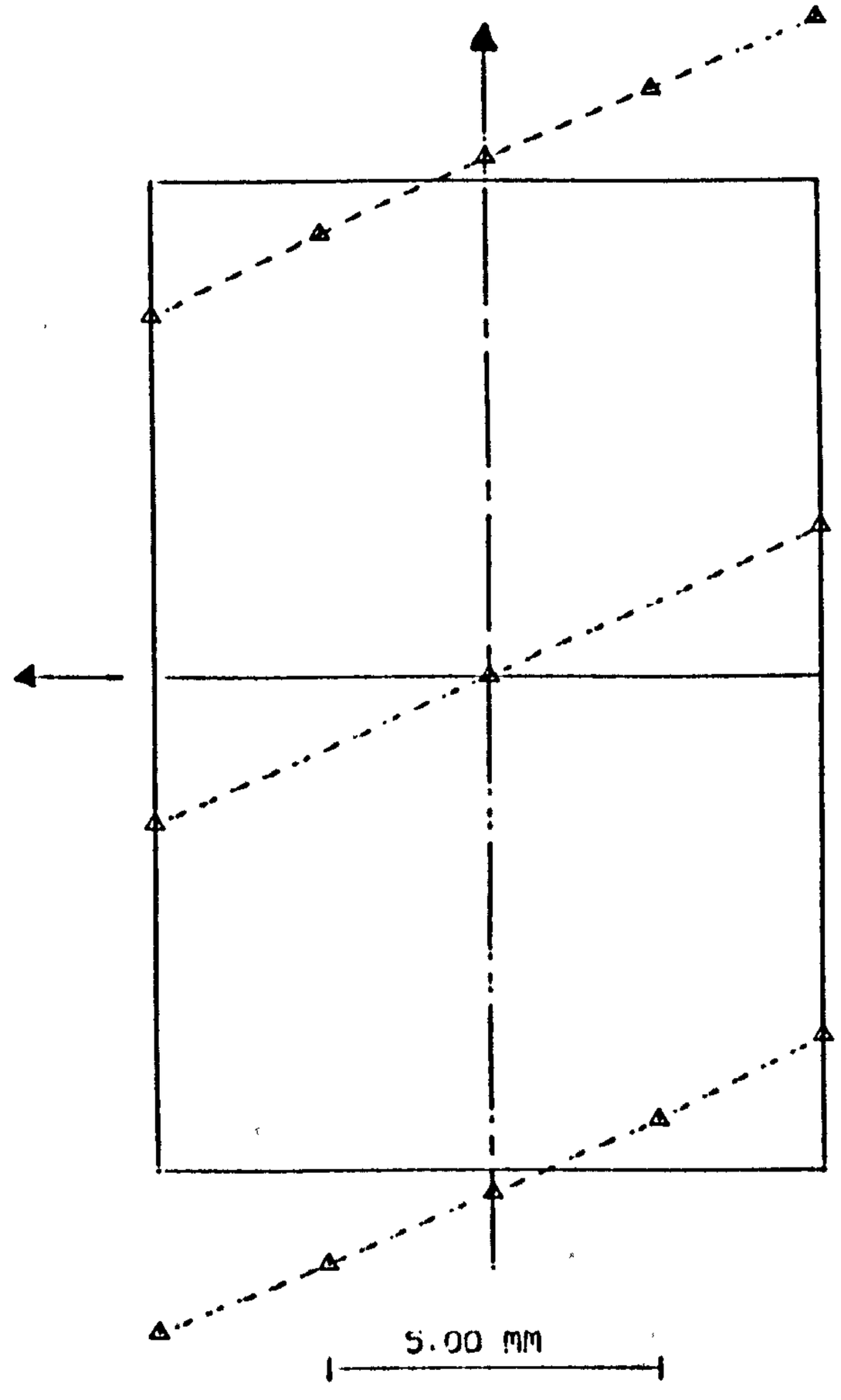

b) Free end, sec. B-B.

Fig. 7.10 Beam B4 – Variation of the displacement in the y direction over the middle and free end cross-sections for applied torque of 46.1 kN.m.

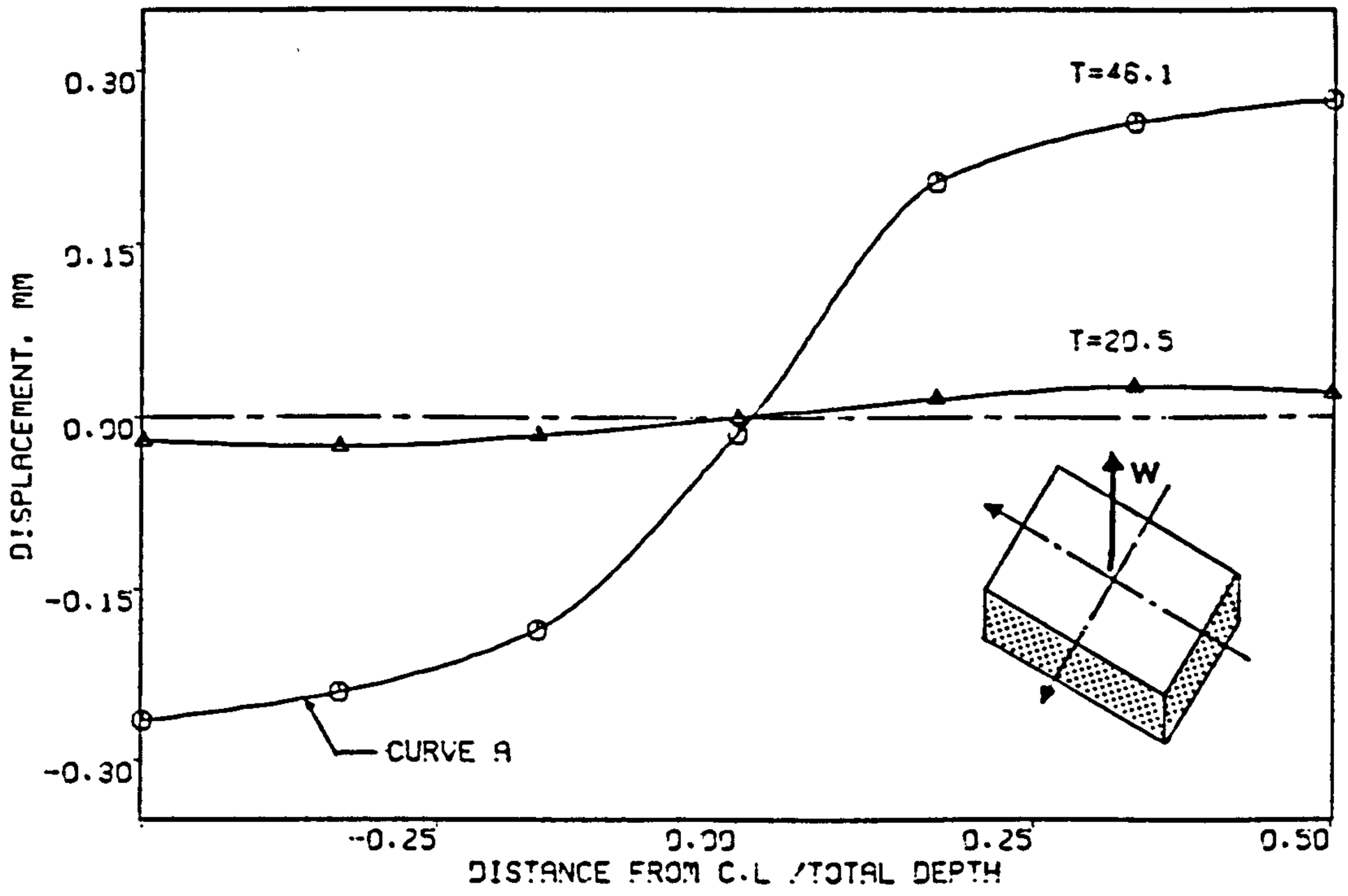

Fig. 7 11 Beam B4 – Distribution of the displacement in the z direction along a typical longer edge of the middle cross–section, sec. A–A.

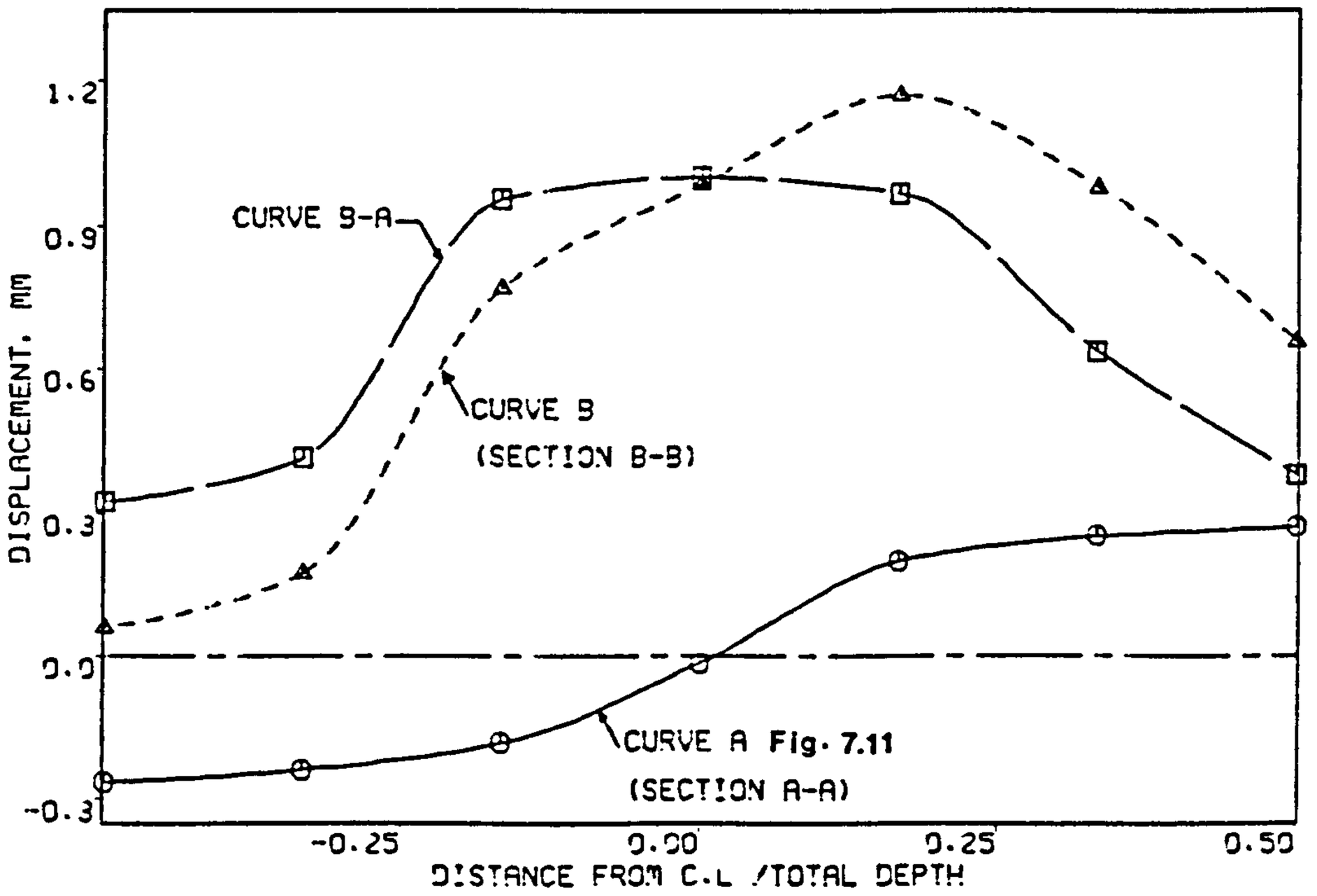

Fig. 7.12 Beam B4 – Distribution of the displacement in the z direction along typical edges of the free end, sec. B–B, for applied torque of 46.1 kN.m.

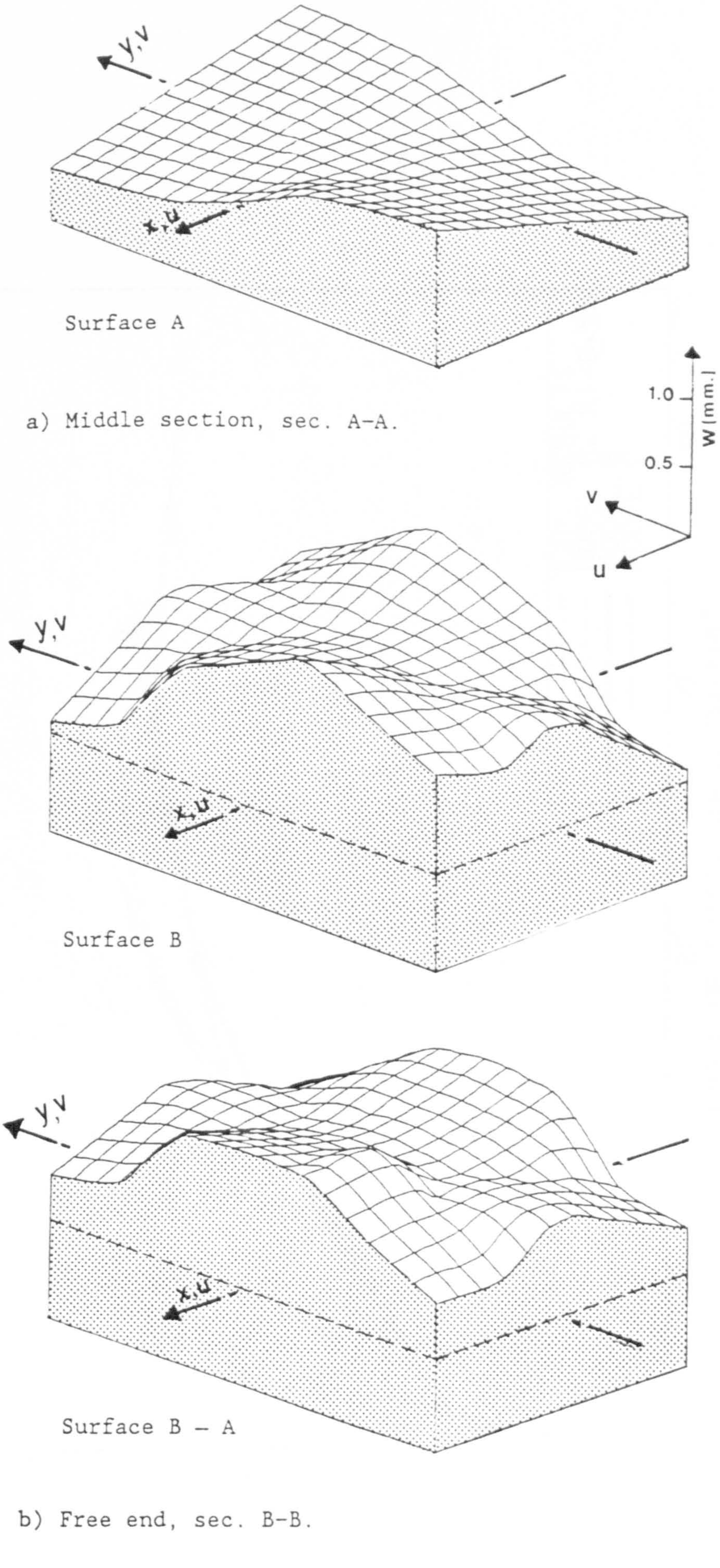

a) Middle section, sec. A-A.

b) Free end, sec. B-B.

Fig. 7.13 Beam B4 – Variation of the displacement in the z direction over the middle and free end cross-sections for applied torque of 46.1 kN.m.

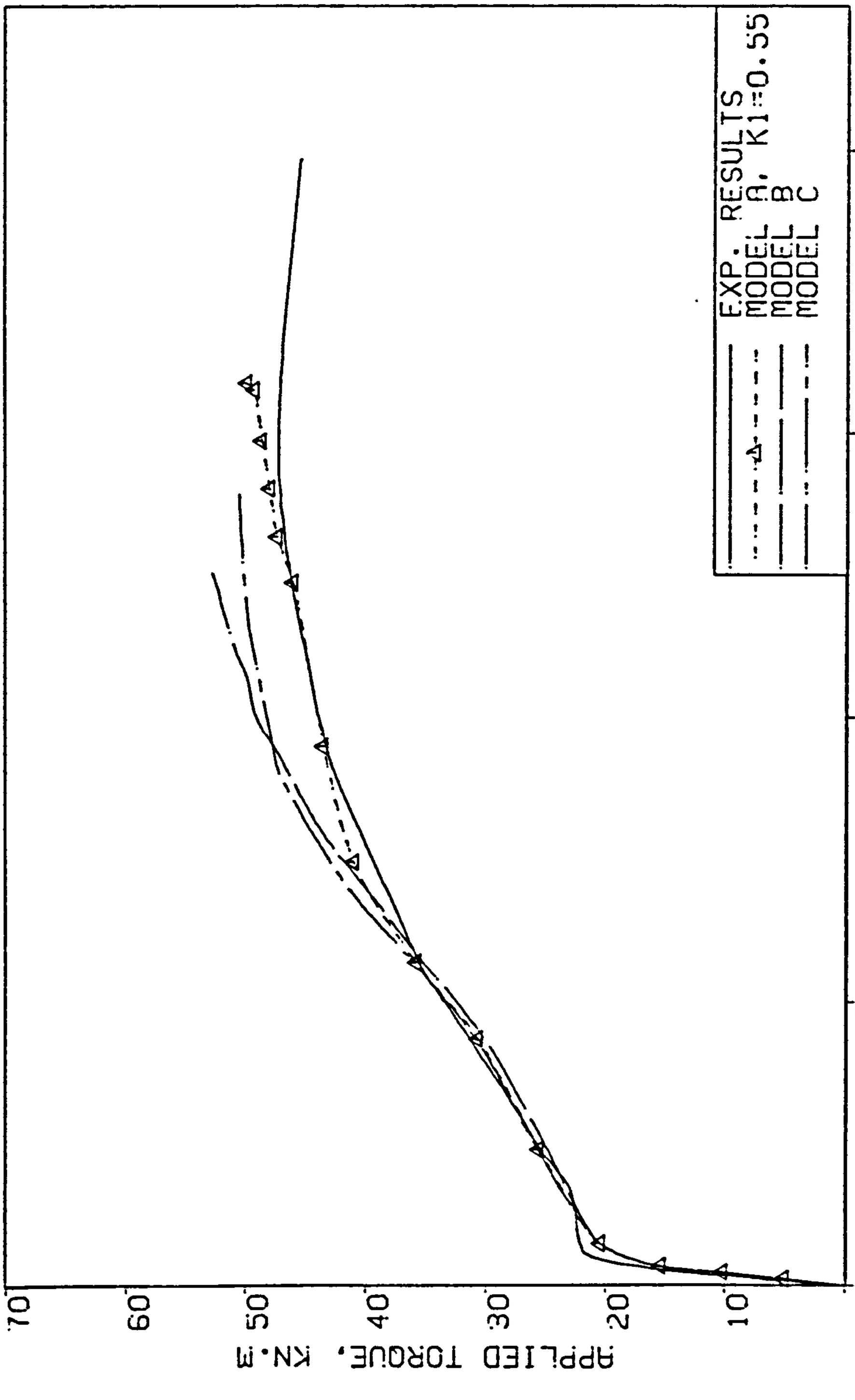

Fig. 7.14 Beam B4 - Effect of concrete compression strength reduction models on the torque–twist behaviour.

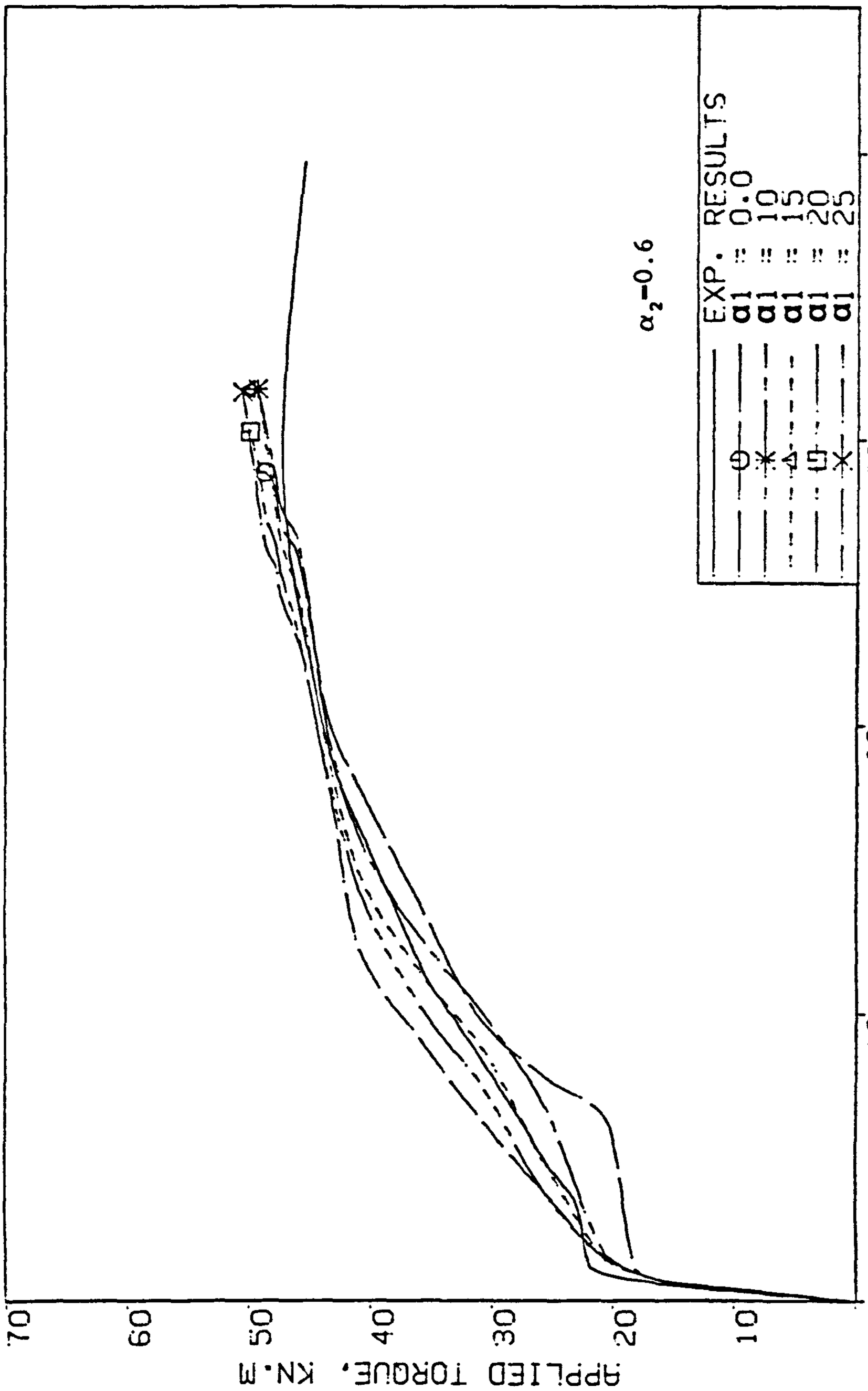

Fig. 7.15 Beam B4 – Effect of the tension–stiffening parameter α_1 on the torque–twist behaviour.

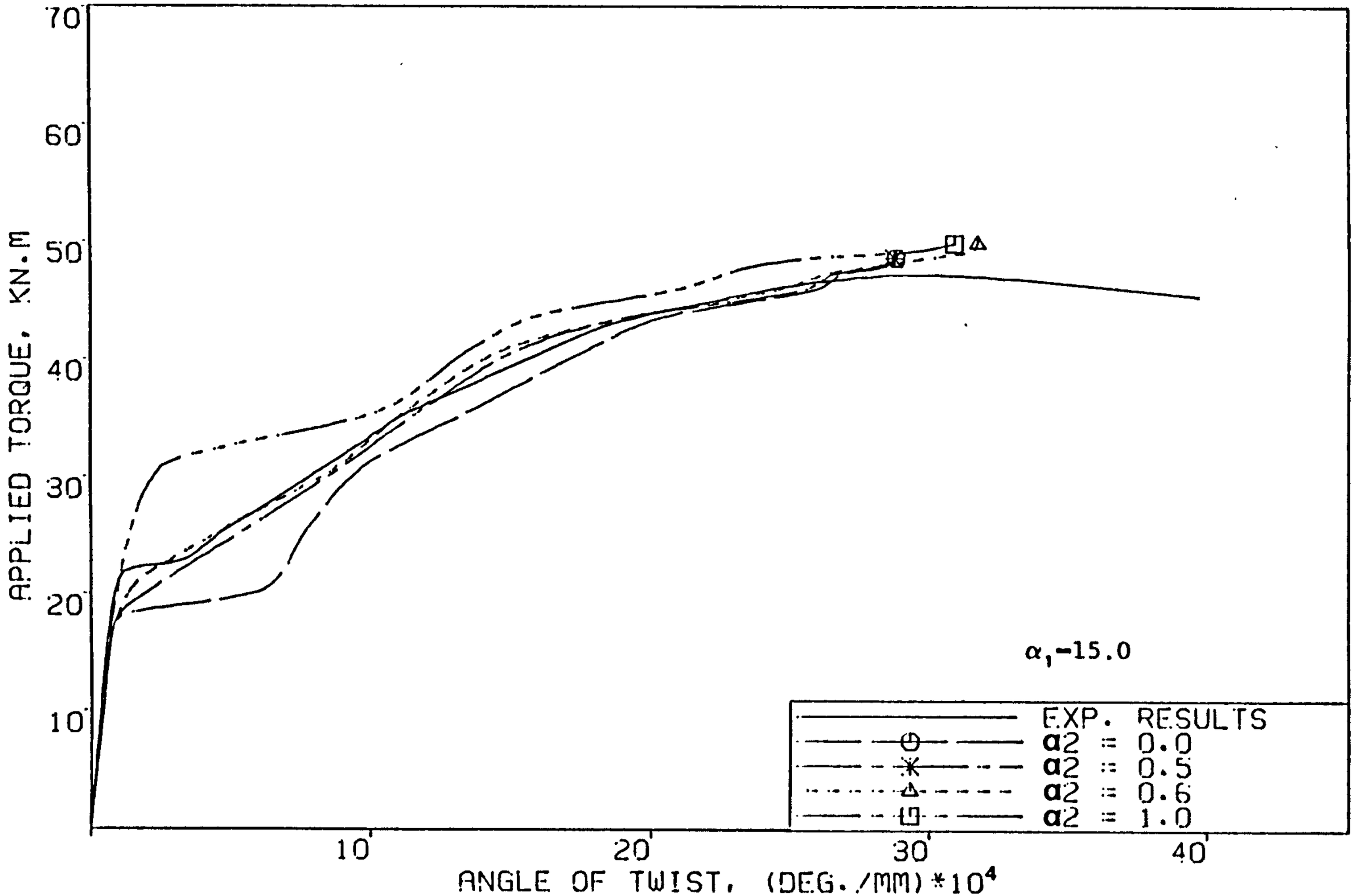

Fig. 7.16 Beam B4 - Effect of the tension-stiffening parameter α_2 on the torque-twist behaviour.

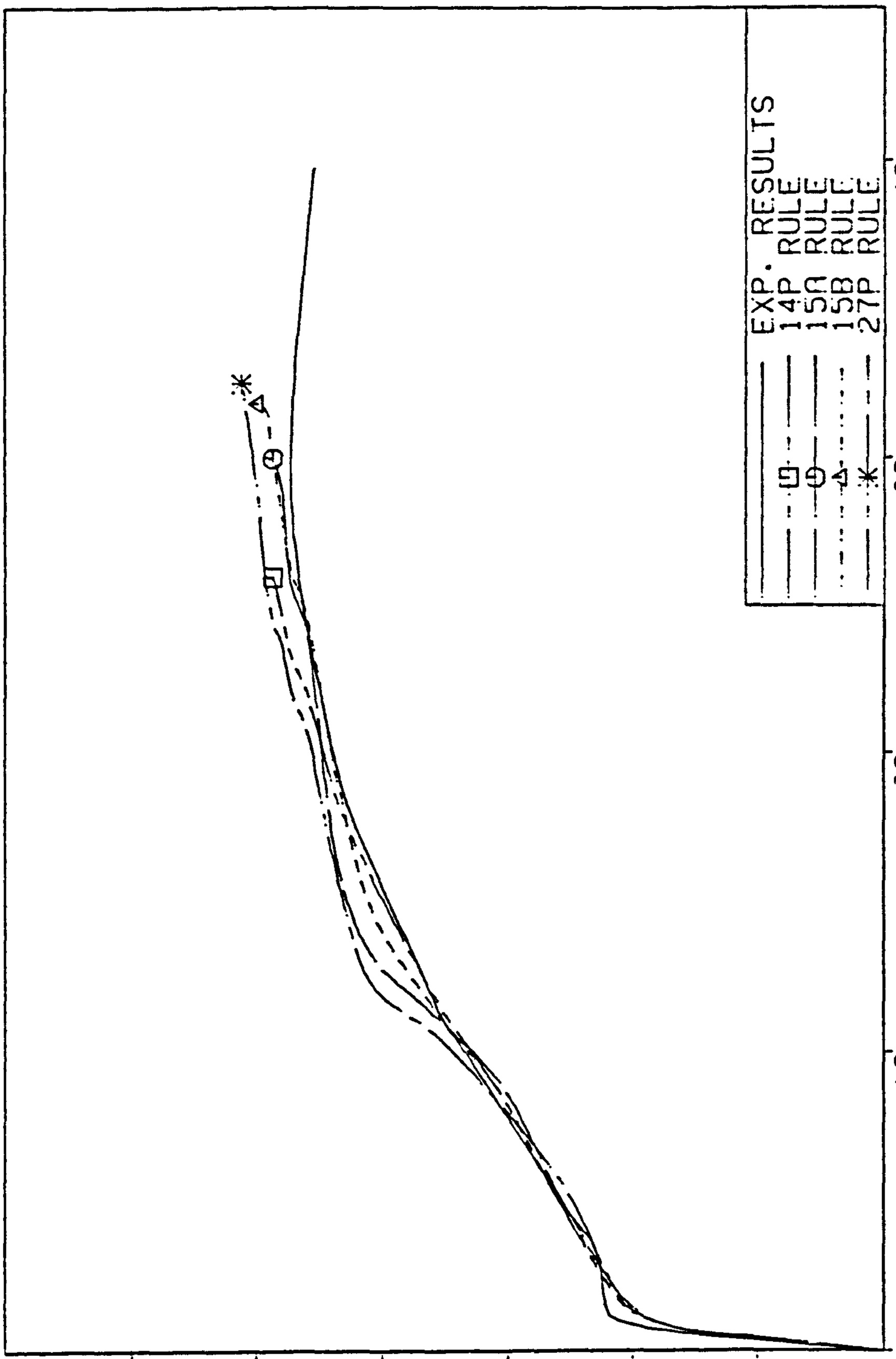

Fig. 7.17 Beam B4 - Effect of the integration rules on the torque-twist behaviour.

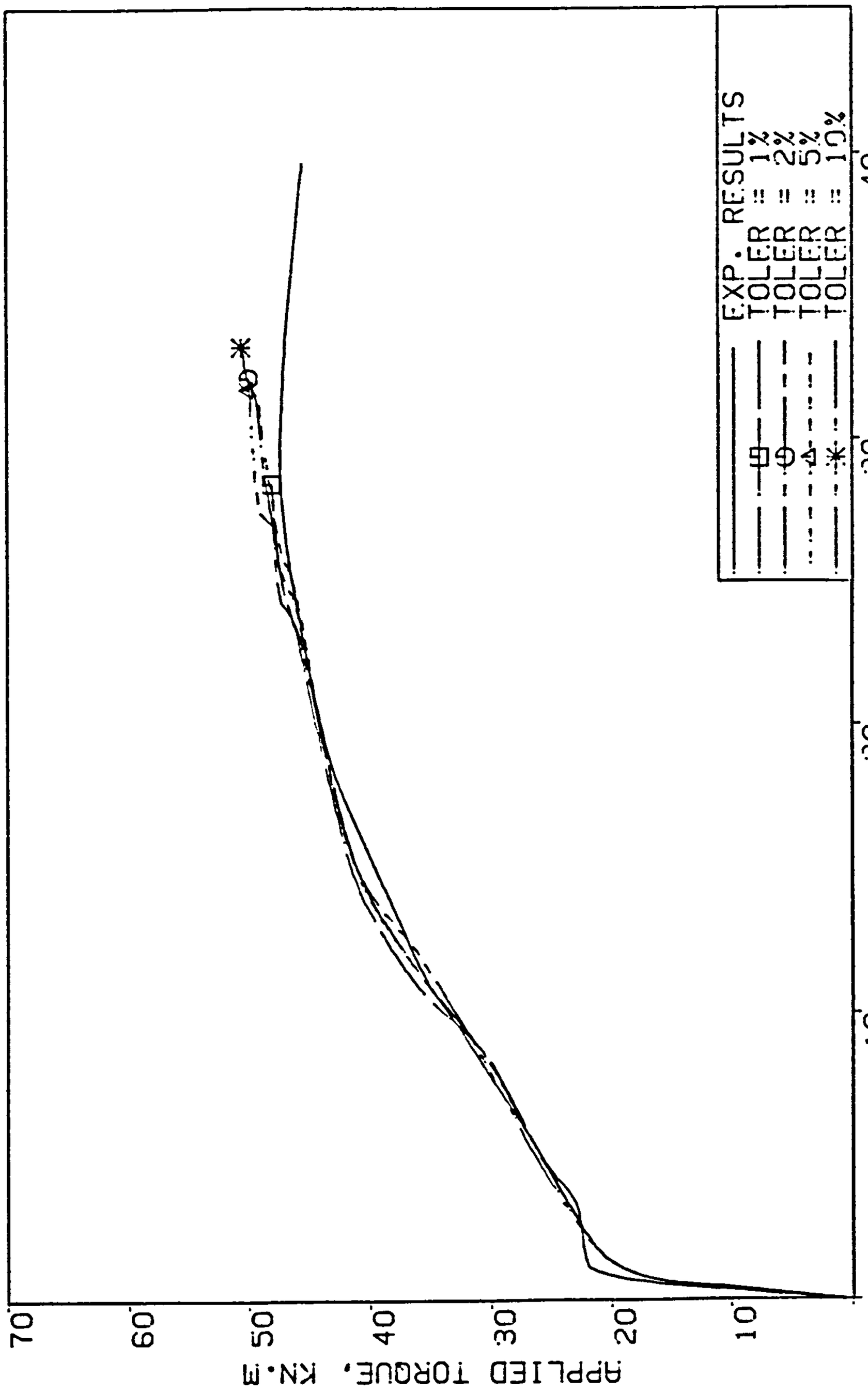

Fig. 7.18 Beam B4 - Effect of the convergence tolerance on the torque-twist behaviour.

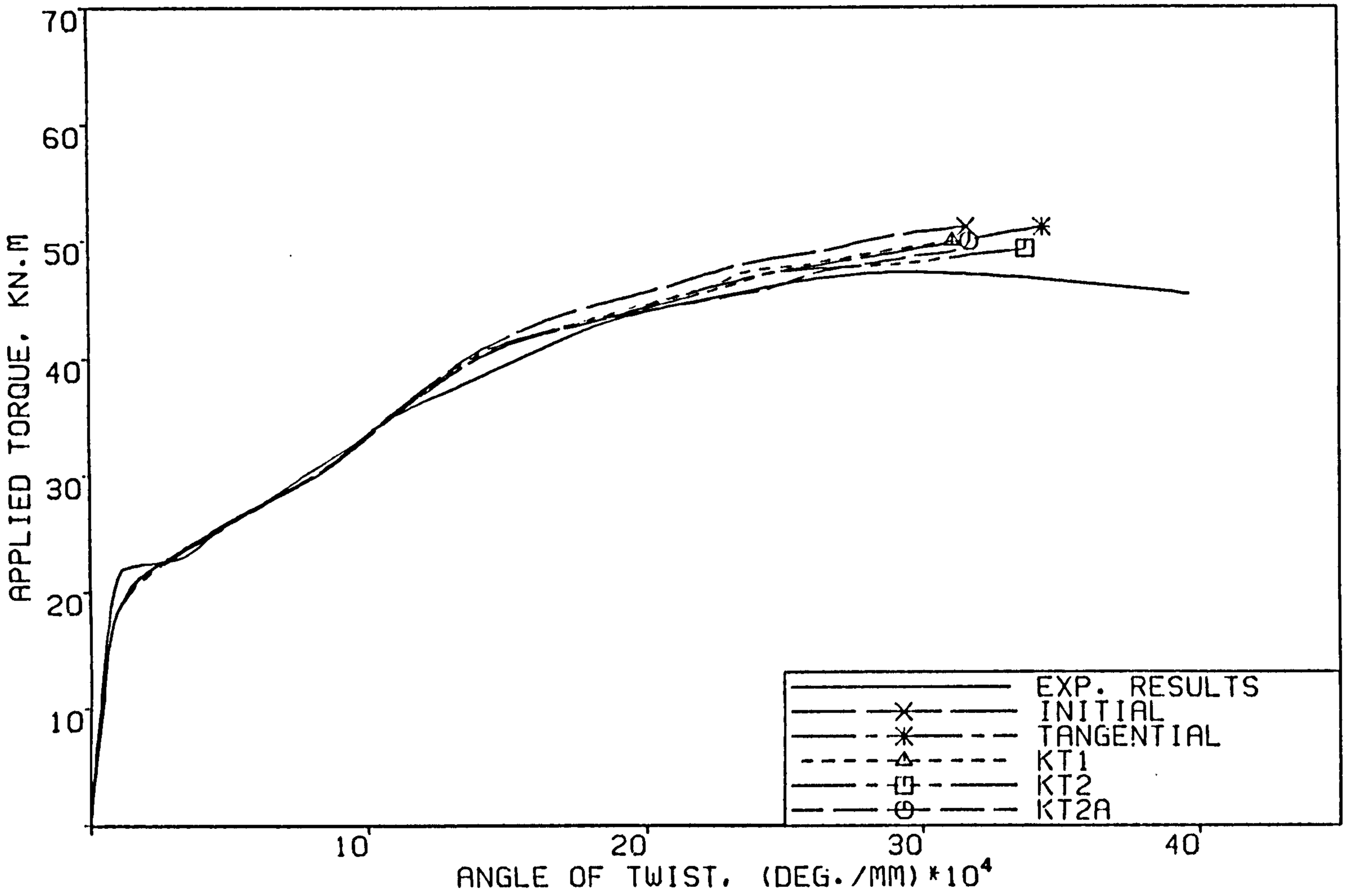

Fig. 7.19 Beam B4 - Effect of the solution algorithm on the torque-twist behaviour.

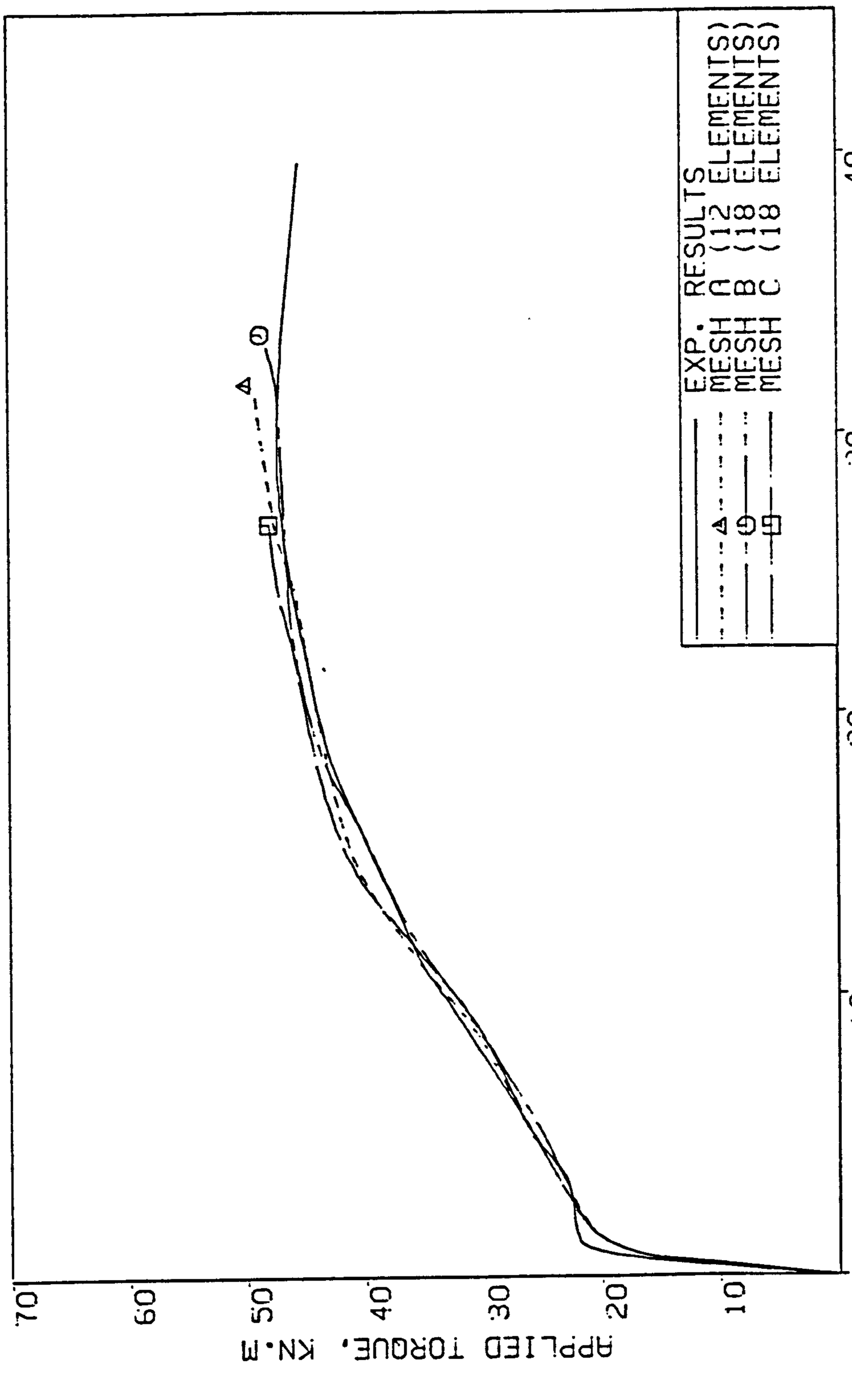

Fig. 7.20 Beam B4 - Effect of the element aspect ratio on the torque-twist behaviour.

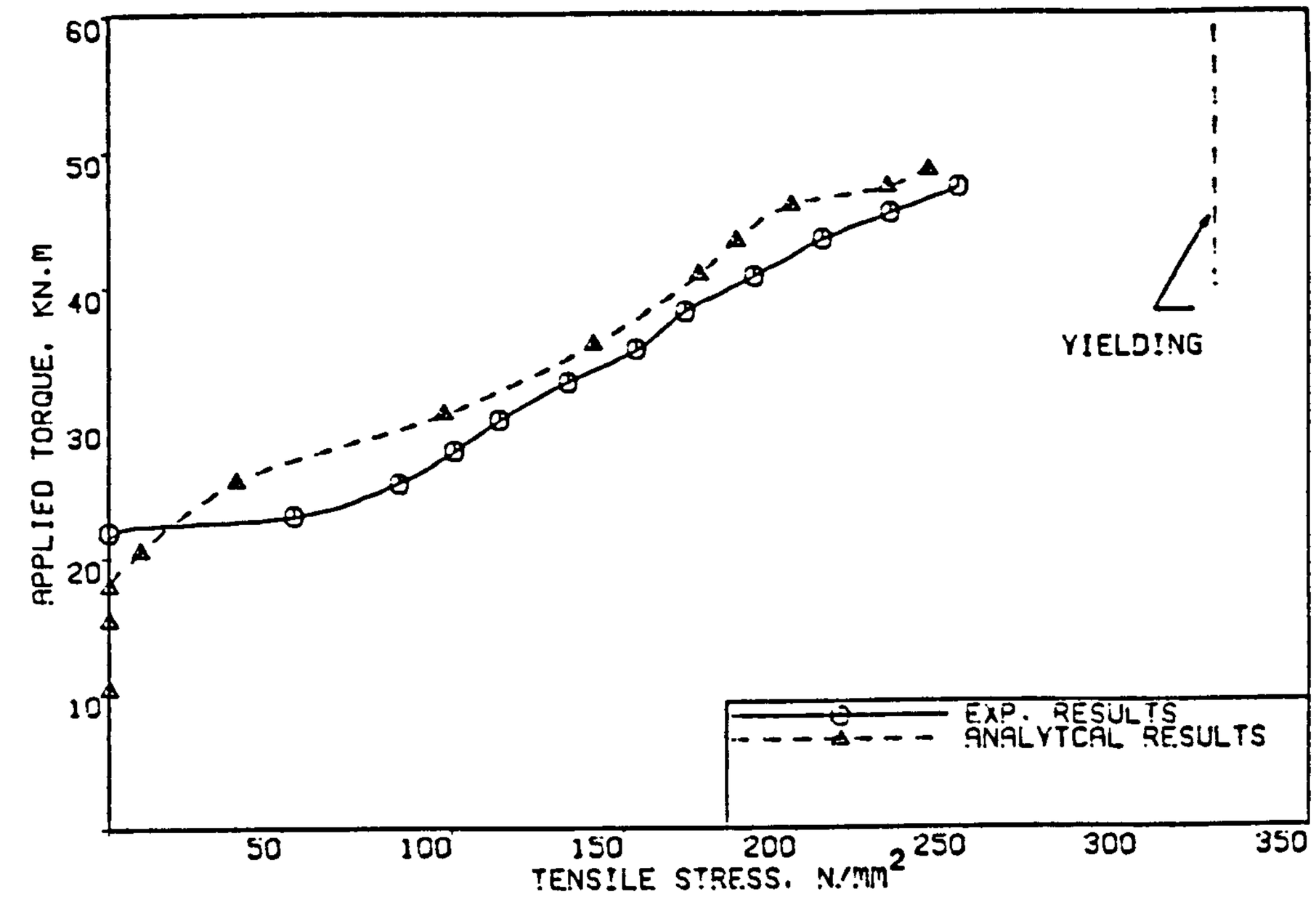

a) Torque–tensile stress relations.

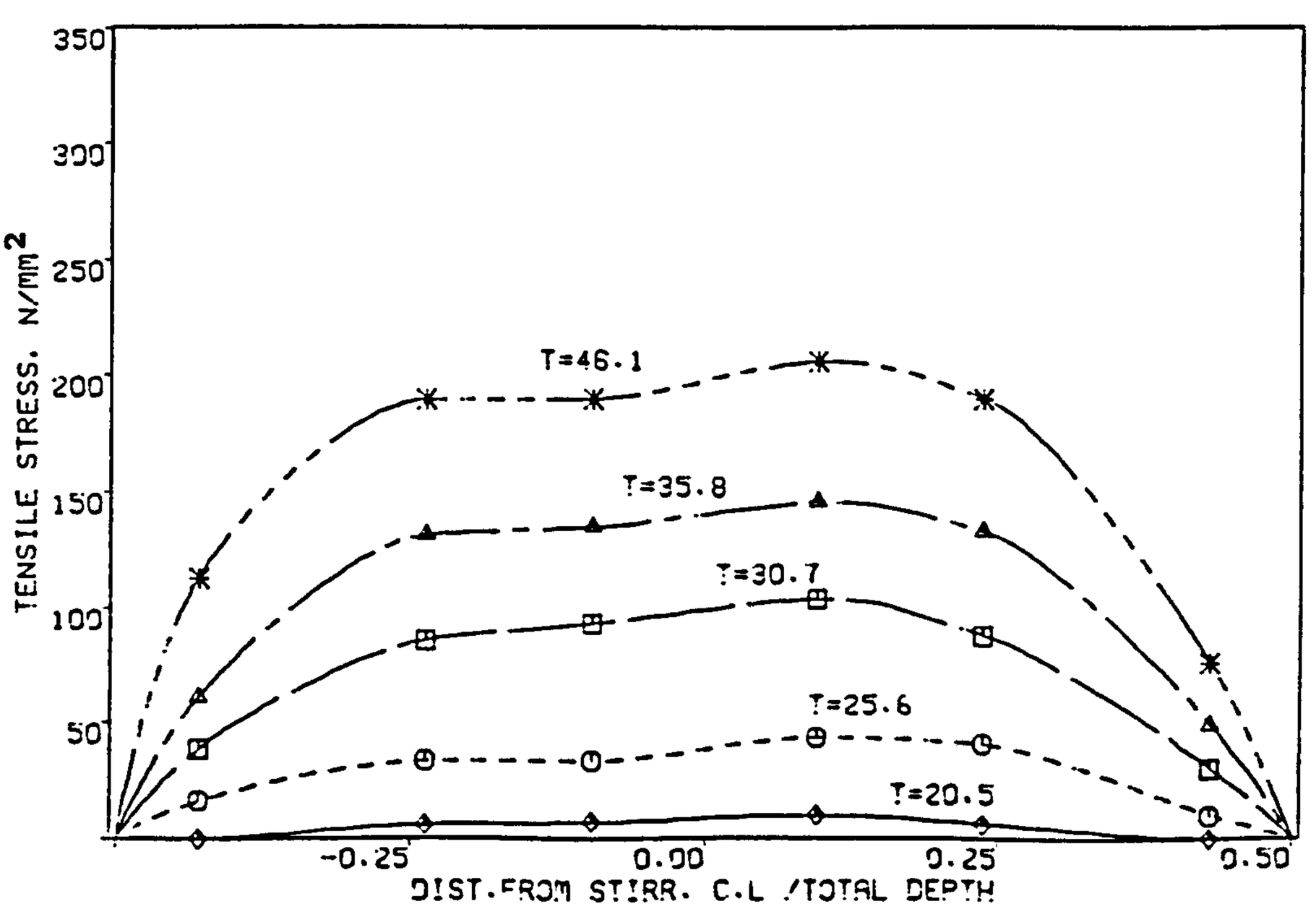

b) Distribution of tensile stresses at different stages of loading.

Fig. 7.21 Beam B4 – Variation of steel stresses for a typical longer leg of stirrup.

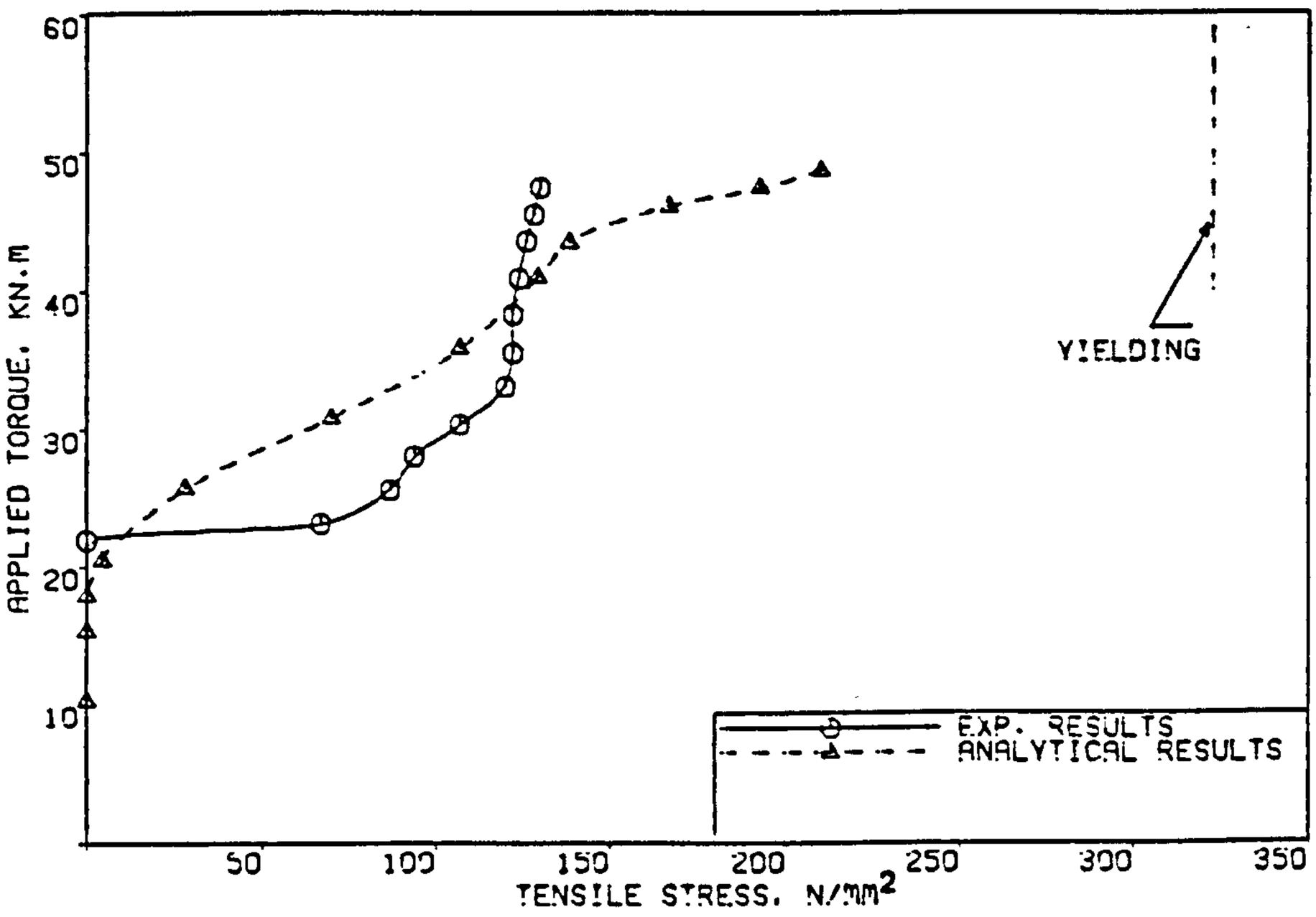

a) Torque–tensile stress relations.

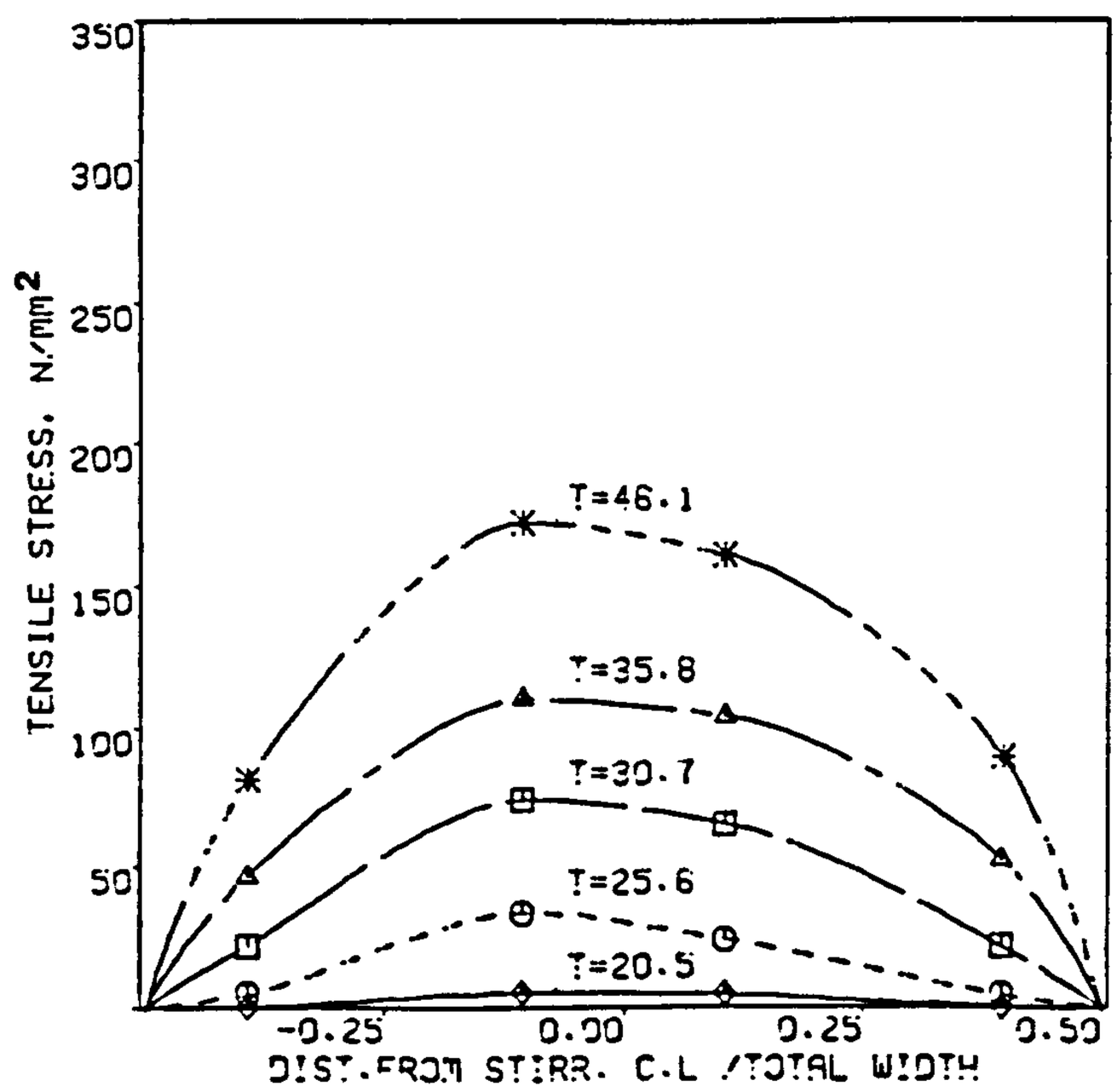

b) Distribution of tensile stresses at different stages of loading.

Fig. 7.22 Beam B4 – Variation of steel stresses for a typical shorter leg of stirrup.

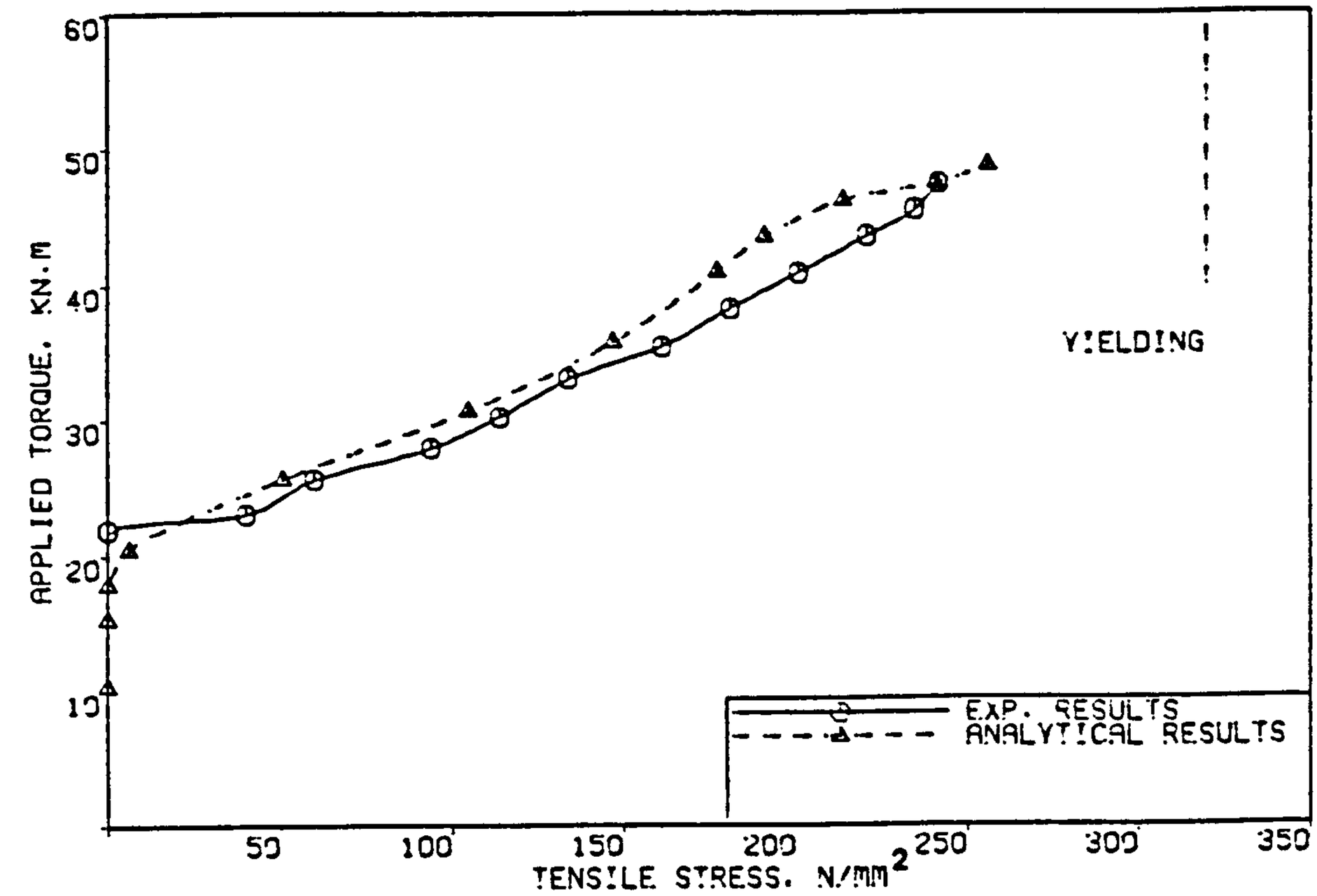

a) Torque–tensile stress relations.

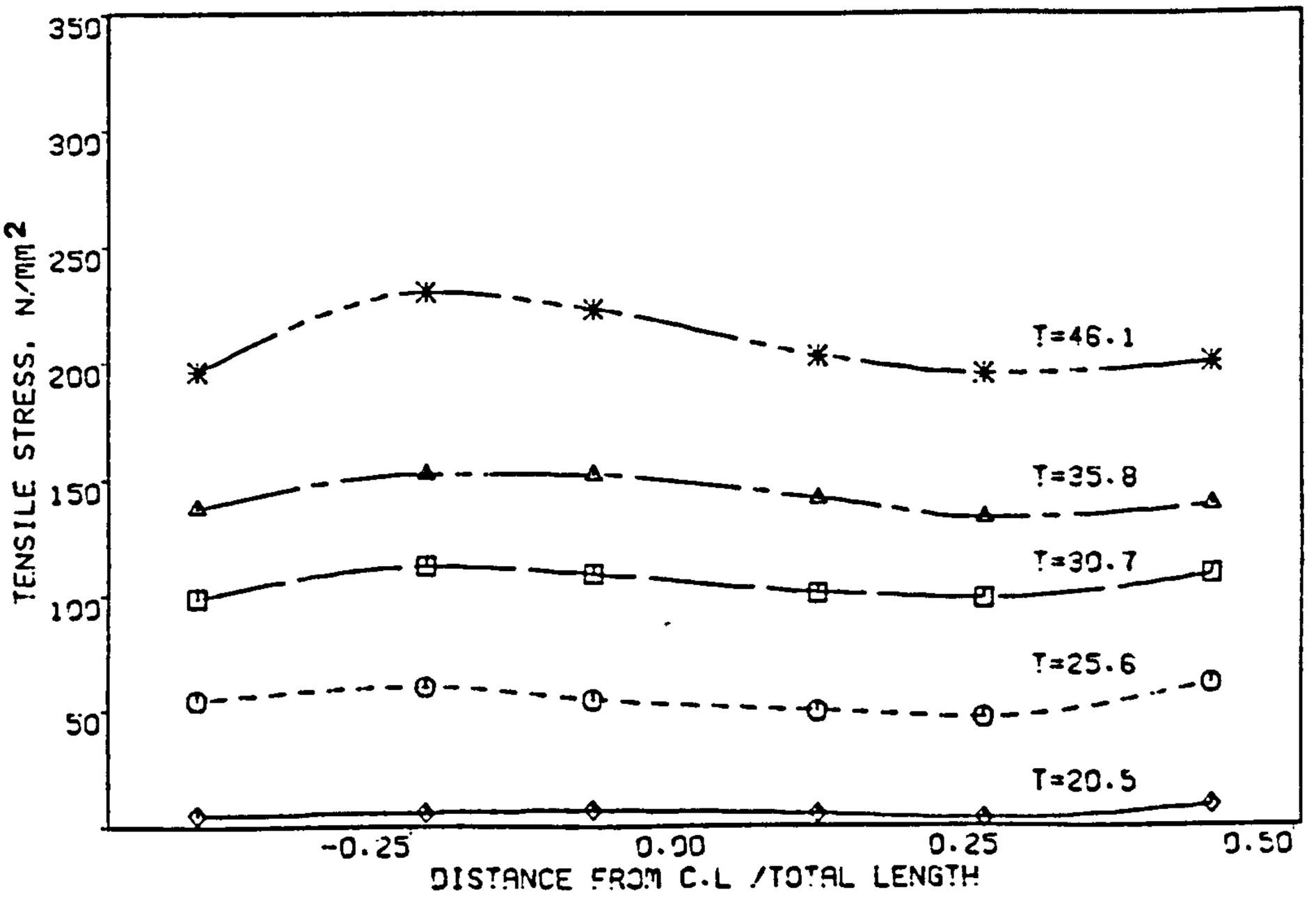

b) Distribution of tensile stresses at different stages of loading.

Fig. 7.23 Beam B4 – Variation of steel stresses for a typical longitudinal bar.

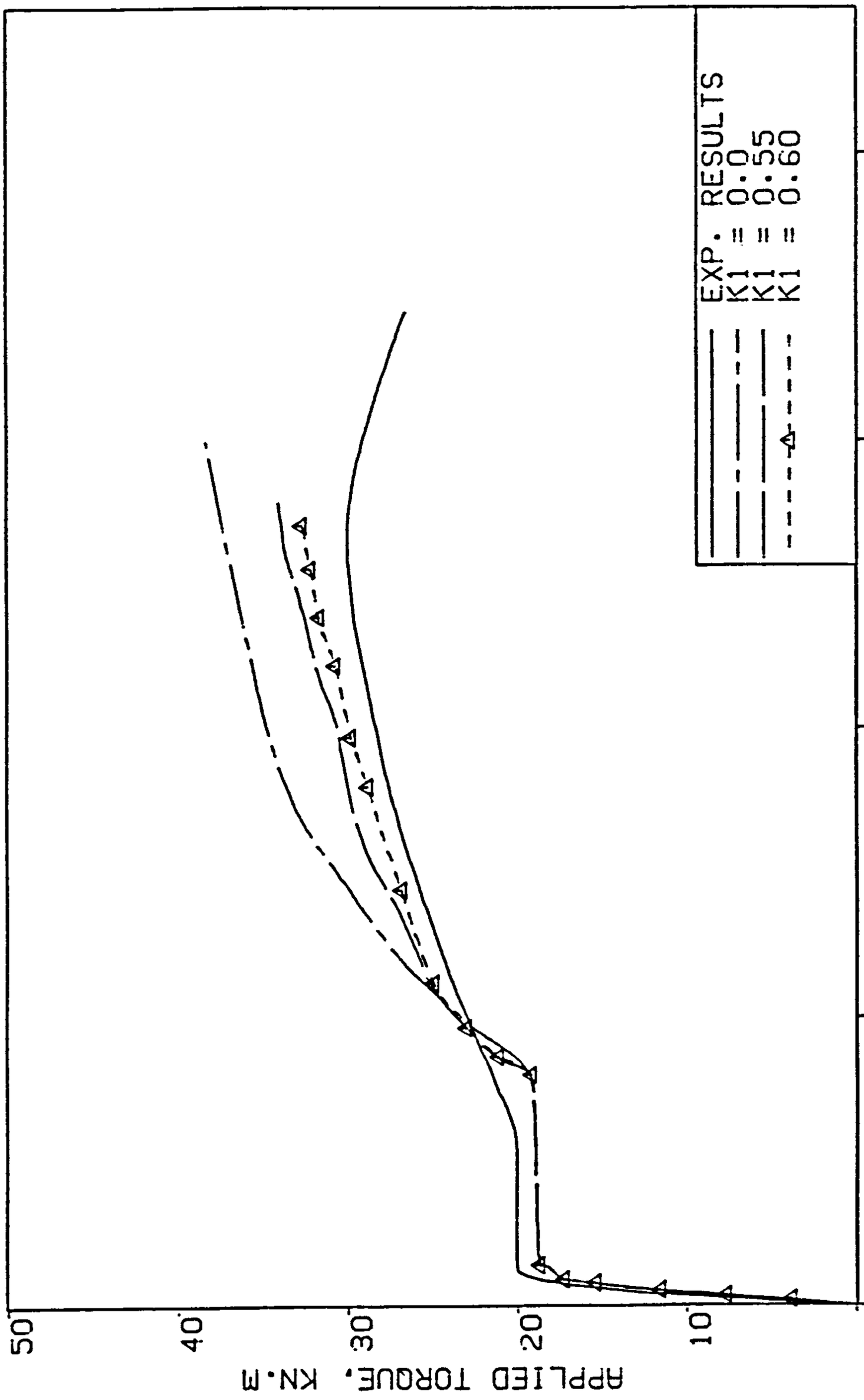

Fig. 7.24 Beam B2 - Effect of the compression reduction parameter k_1 on the torque–twist behaviour.

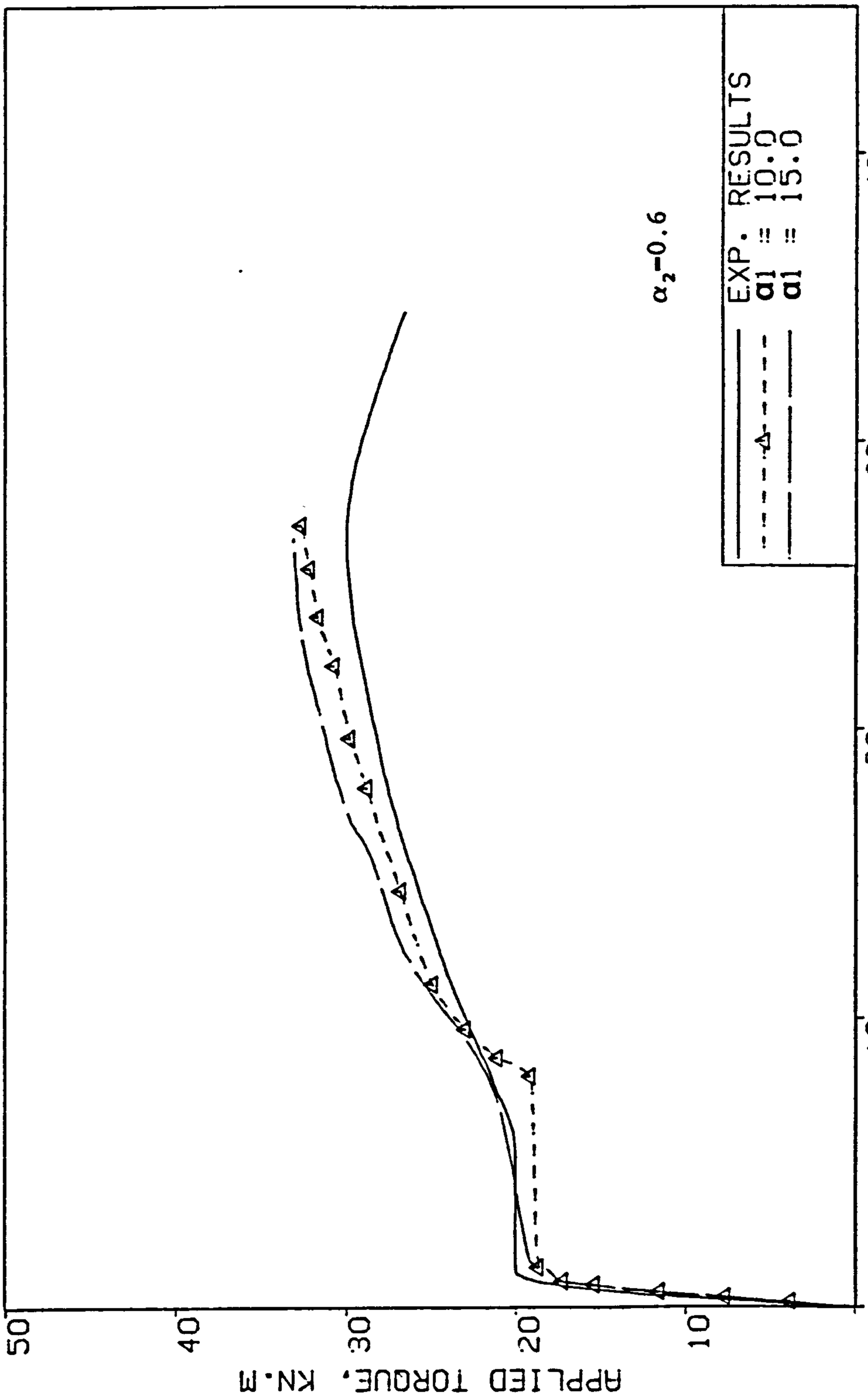

Fig. 7.25 Beam B2 - Effect of the tension-stiffening parameter α_1 on the torque-twist behaviour.

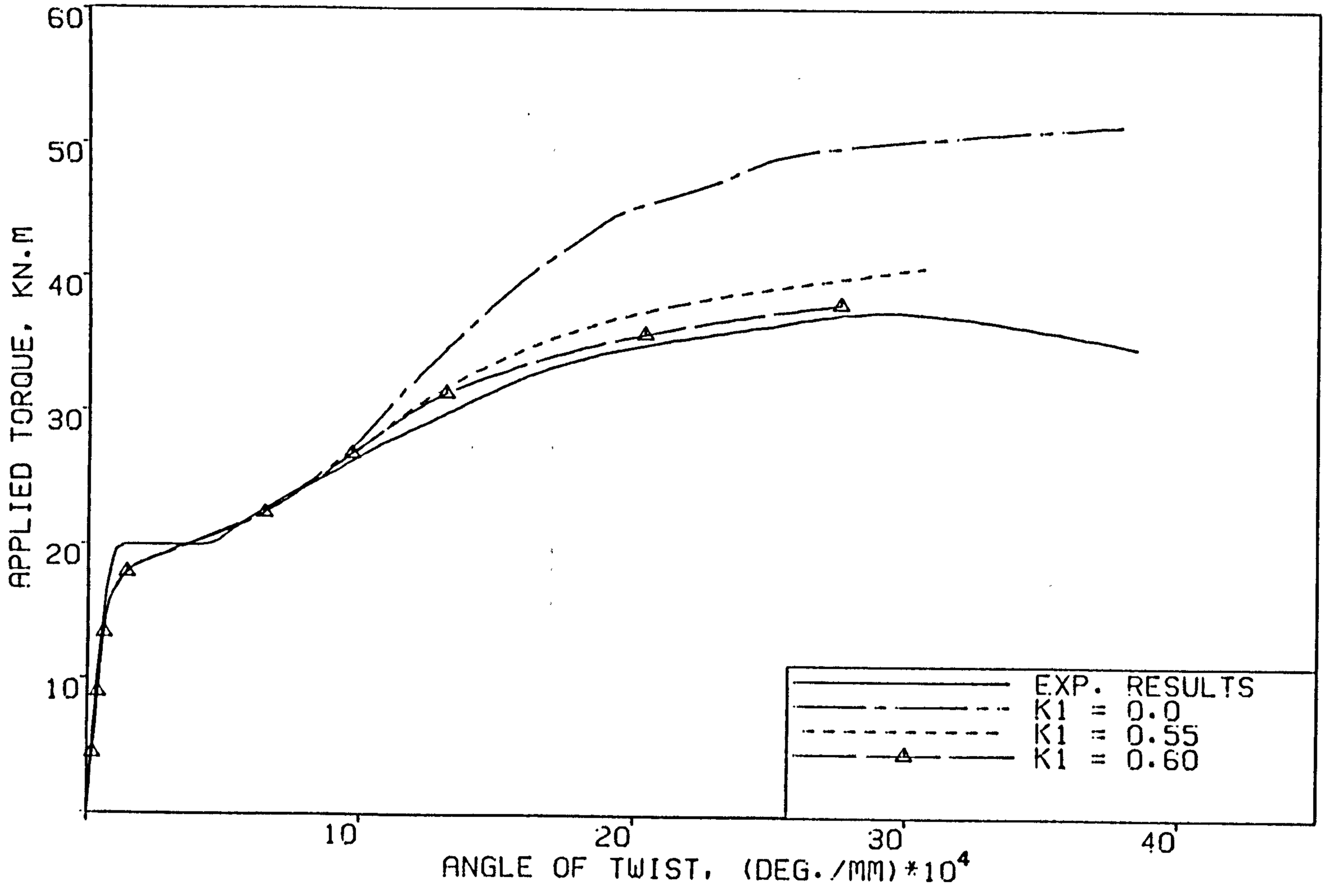

Fig. 7.26 Beam B3 - Effect of the compression reduction parameter k_1 on the torque-twist behaviour.

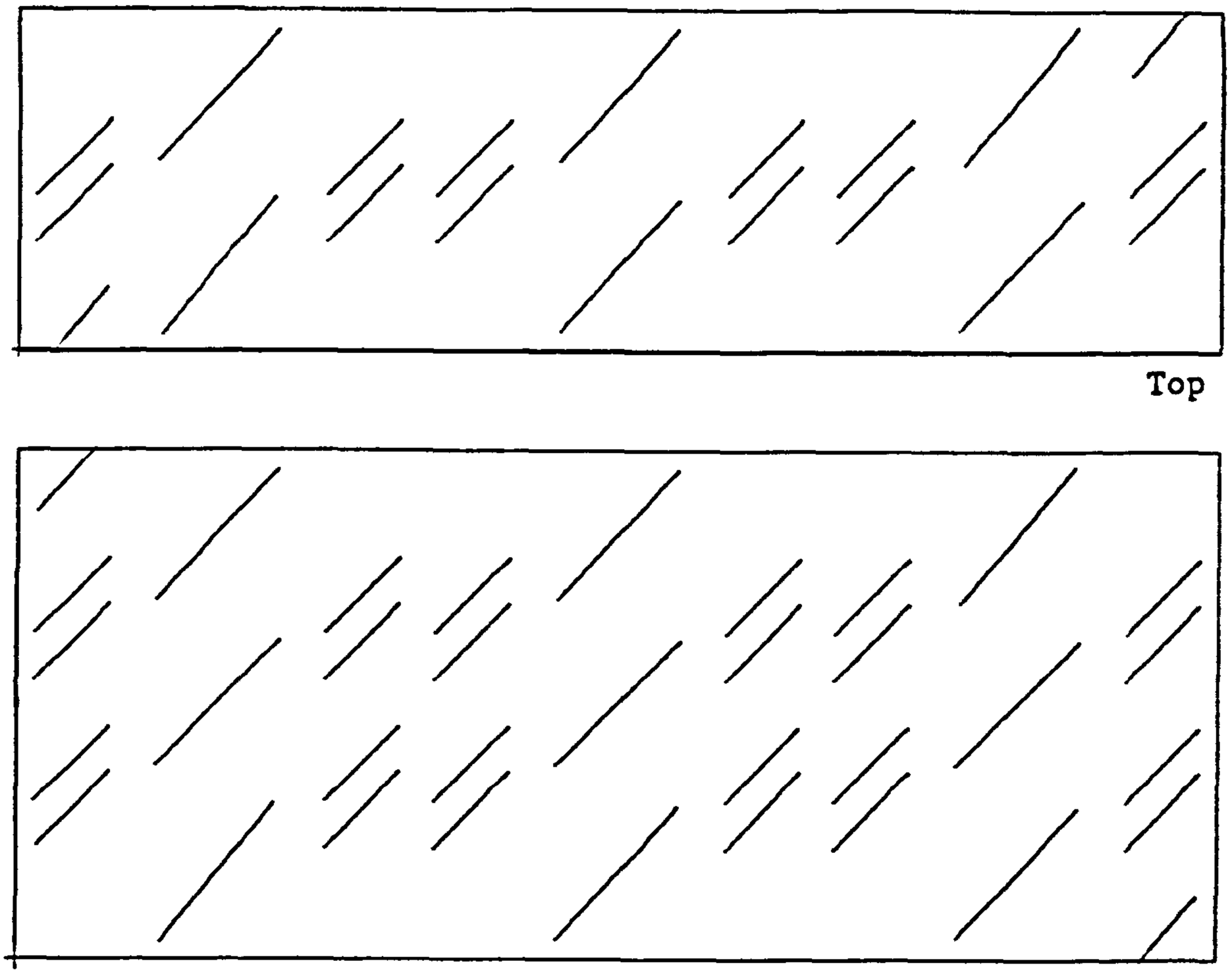

a) T = 17.9 kN.m

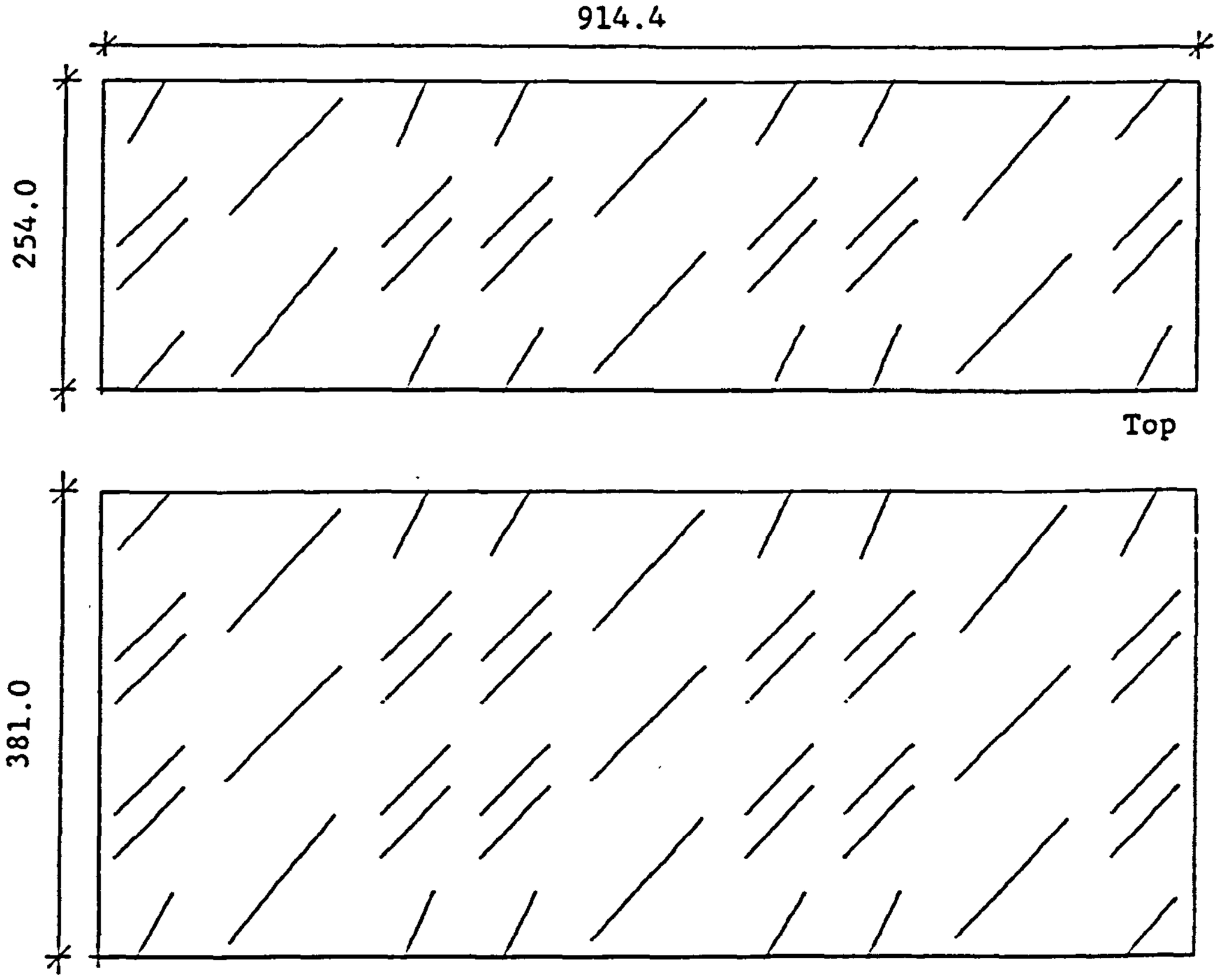

b) T = 22.4 kN.m

Fig. 7.27 Beam B3 – Analytical crack pattern.

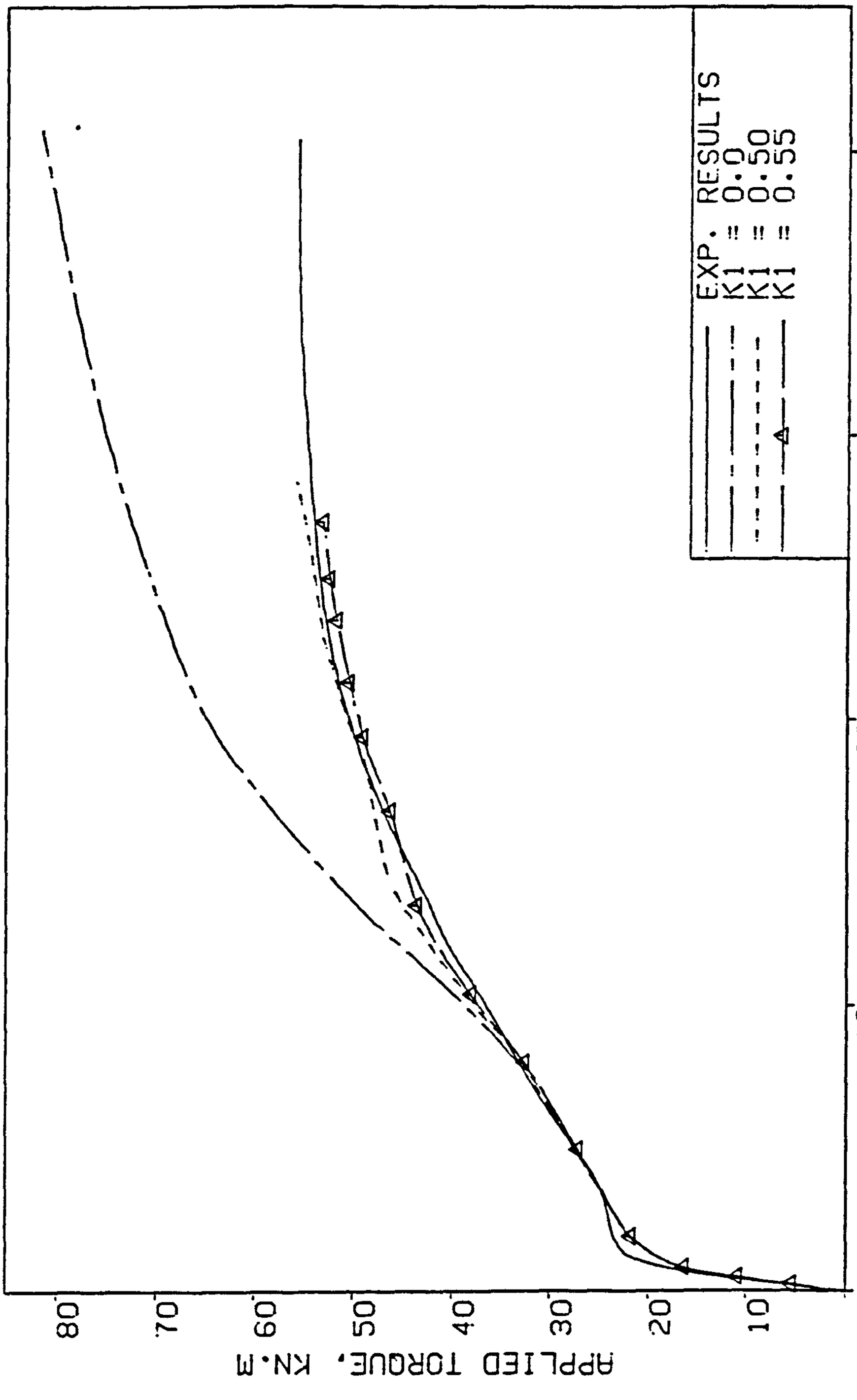

Fig. 7.28 Beam B5 – Effect of the compression reduction parameter k_1 on the torque–twist behaviour.

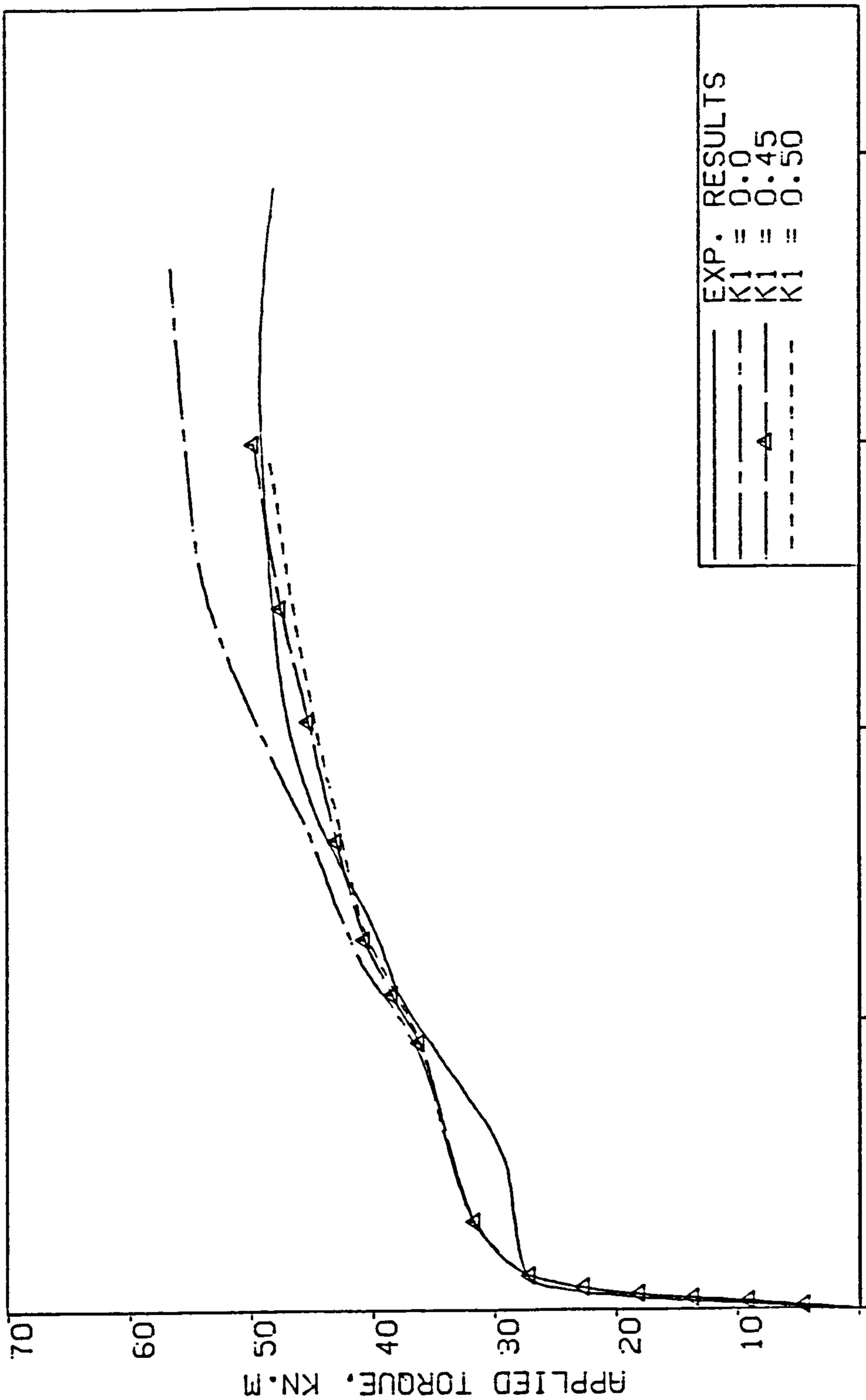

Fig. 7.29 Beam G3 – Effect of the compression reduction parameter k_1 on the torque–twist behaviour.

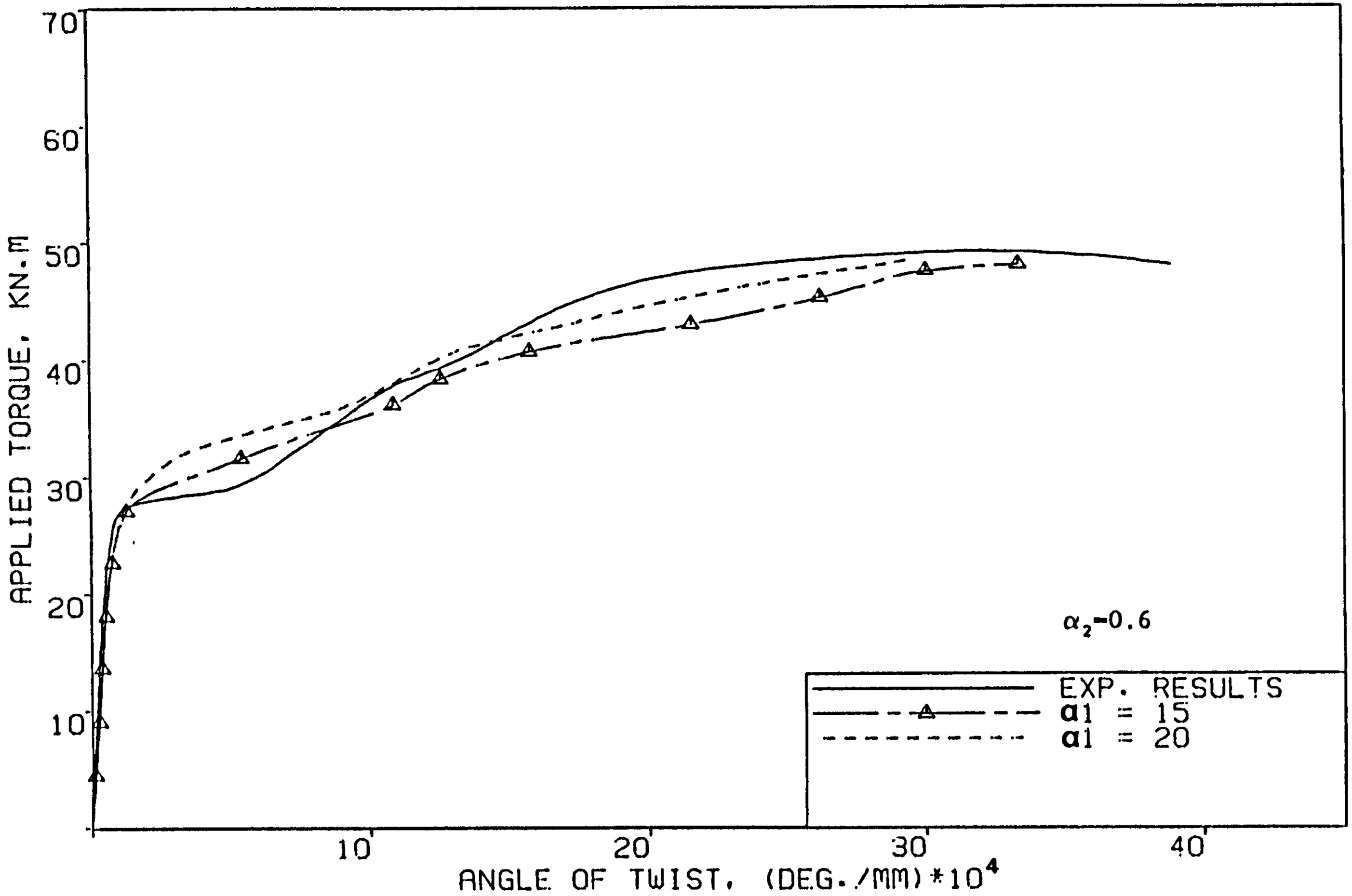

Fig. 7.30 Beam G3 - Effect of the tension-stiffening parameter α_1 on the torque-twist behaviour.

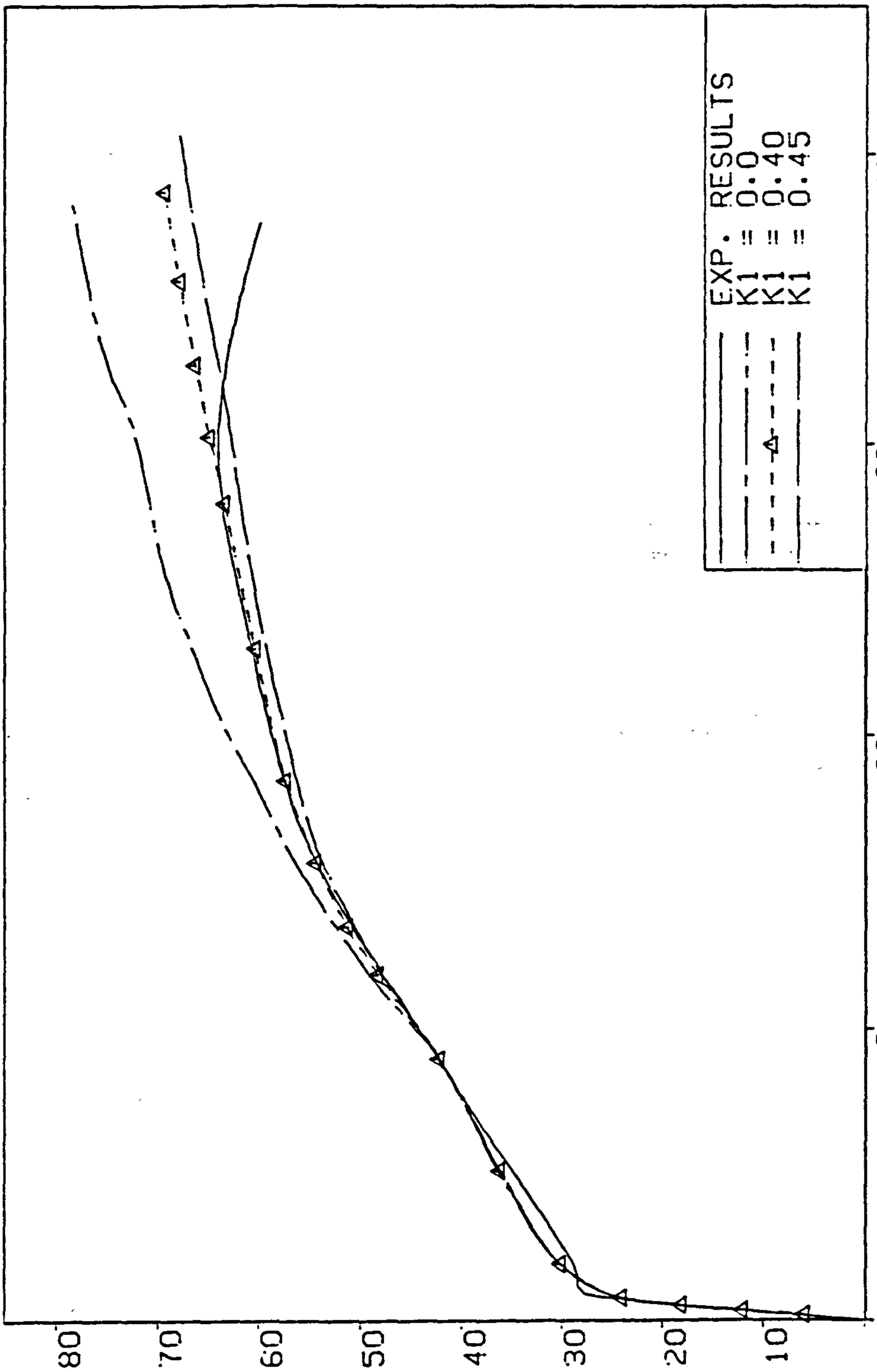

Fig. 7.31 Beam G4 – Effect of the compression reduction parameter k_1 on the torque–twist behaviour.

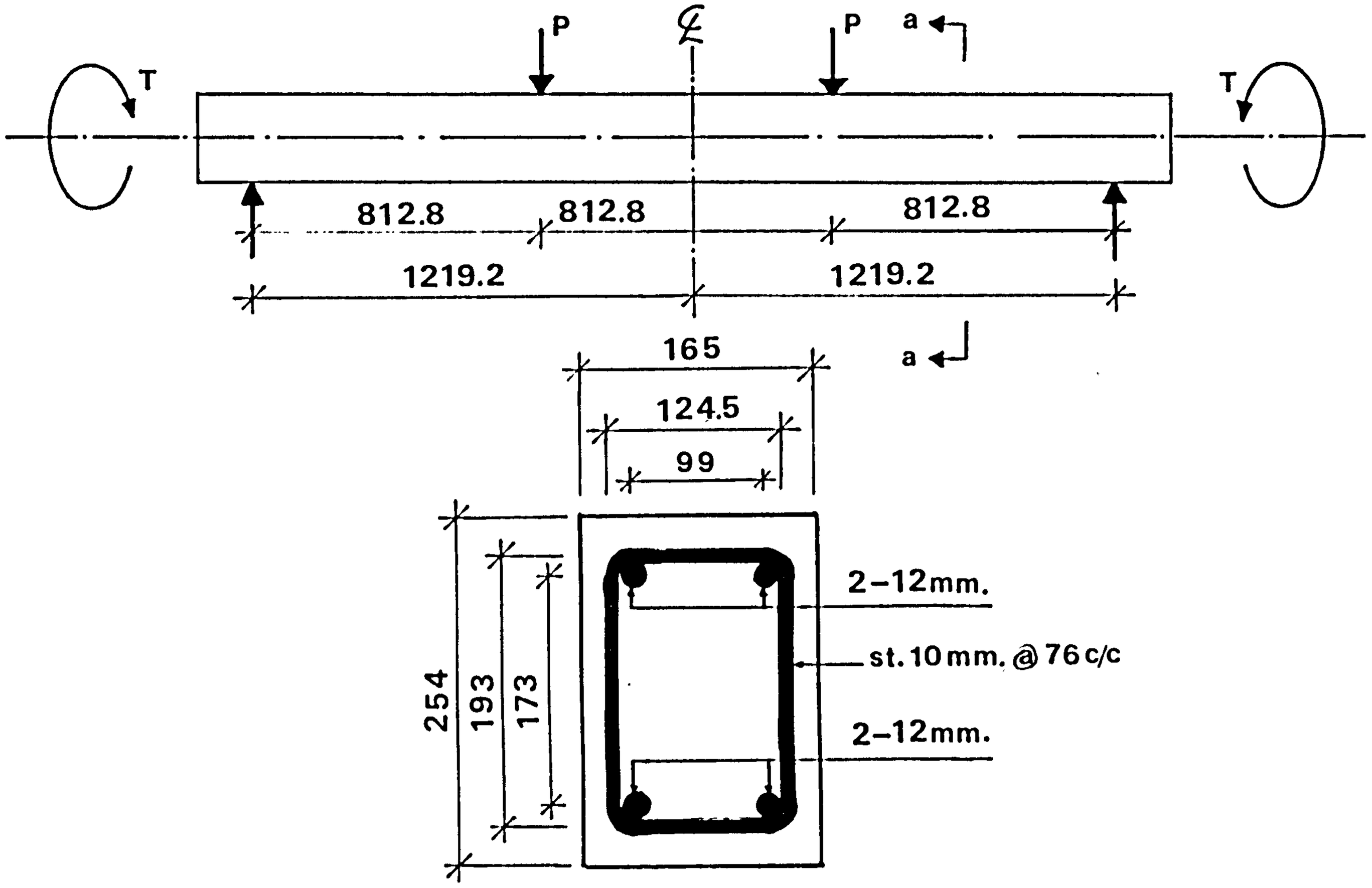

Fig. 7.32 Dimensions and reinforcement details of Collins et al beams.

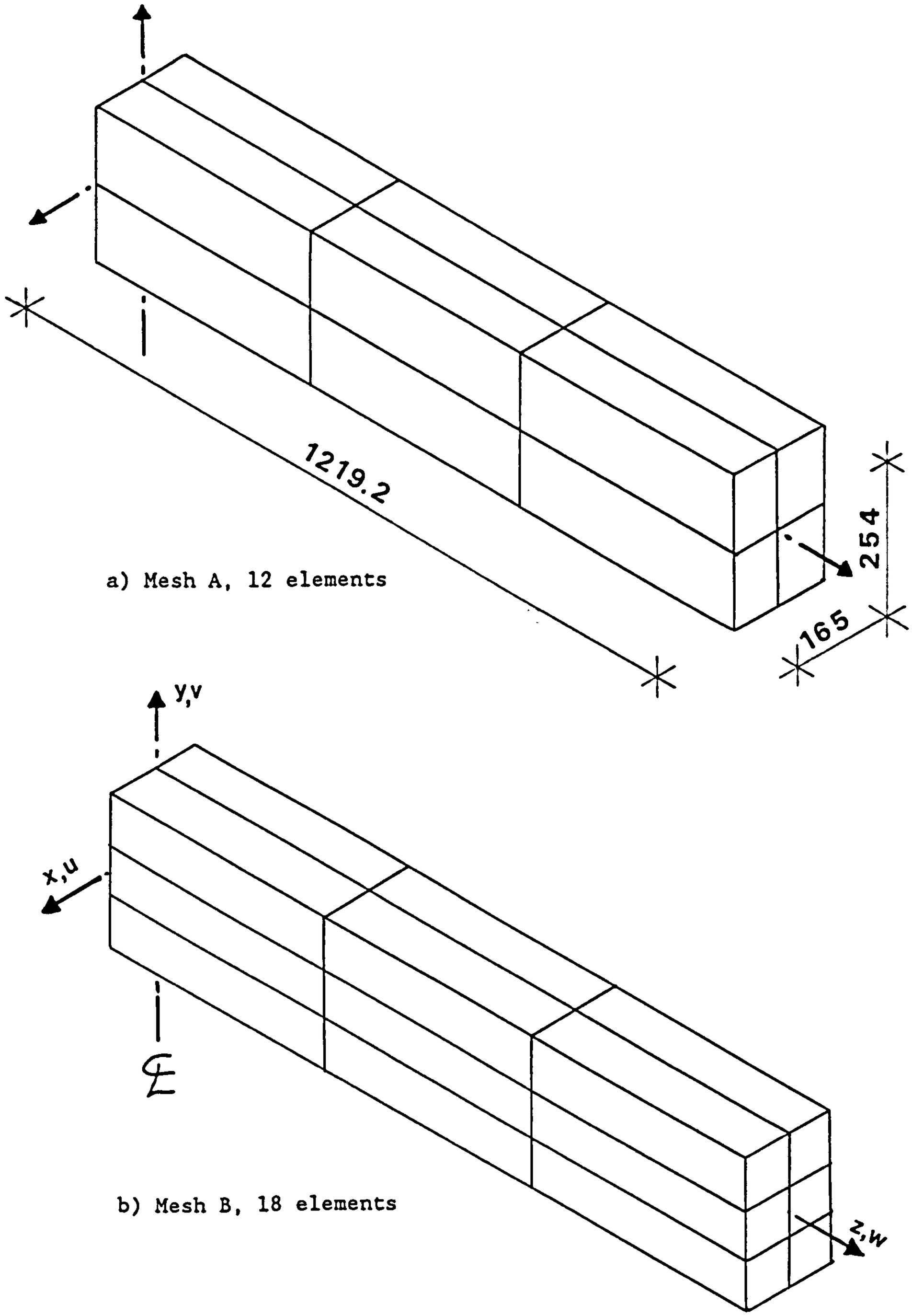

a) Mesh A, 12 elements

b) Mesh B, 18 elements

Fig. 7.33 Finite element meshes used for Collins et al beams.

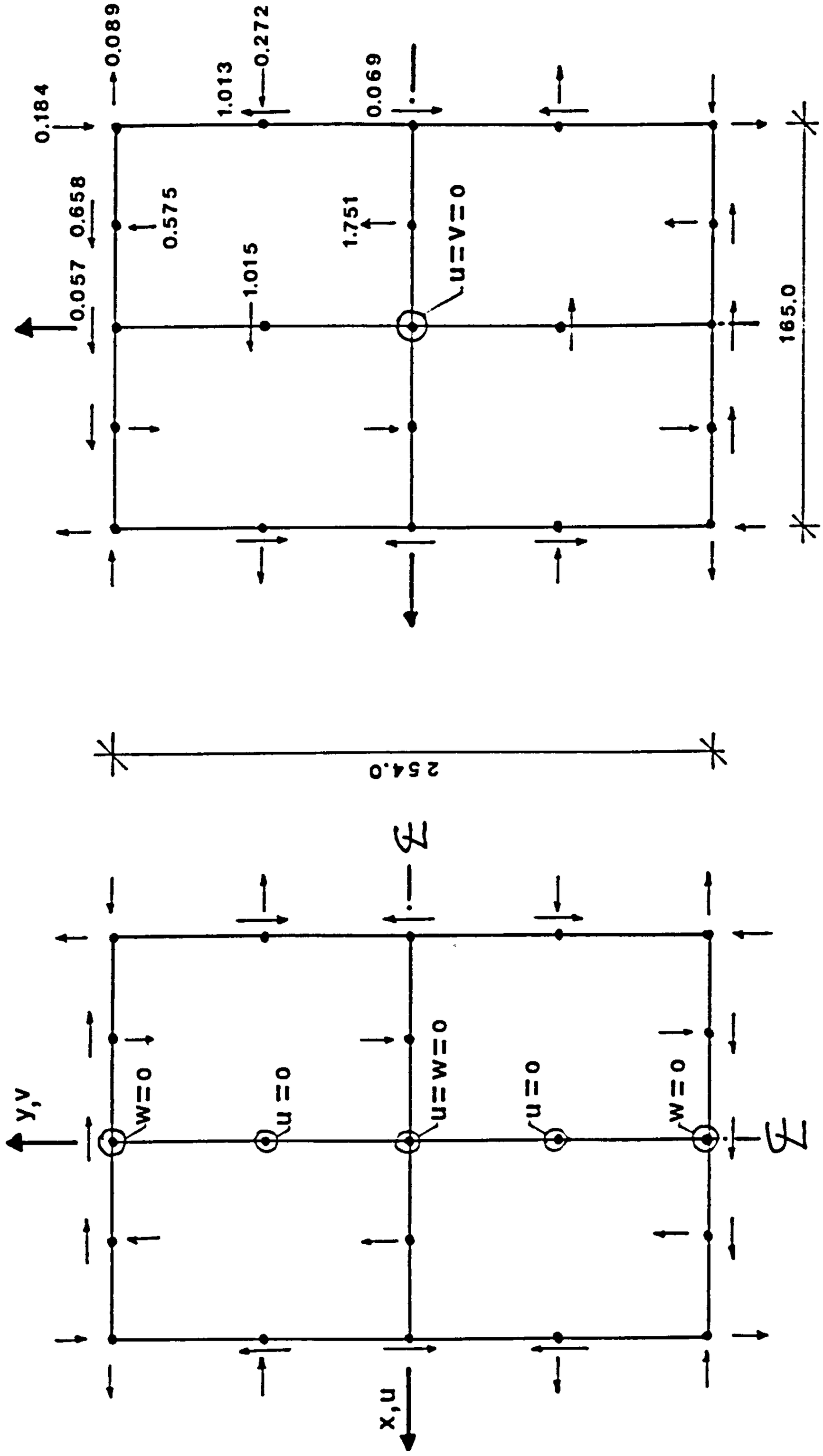

a) Left end, z = 0.0 T = 1219.2 b) Right end, z = 1219.2

Fig. 7.34 Equivalent nodal forces and boundary conditions used for Collins et al beams, mesh A.

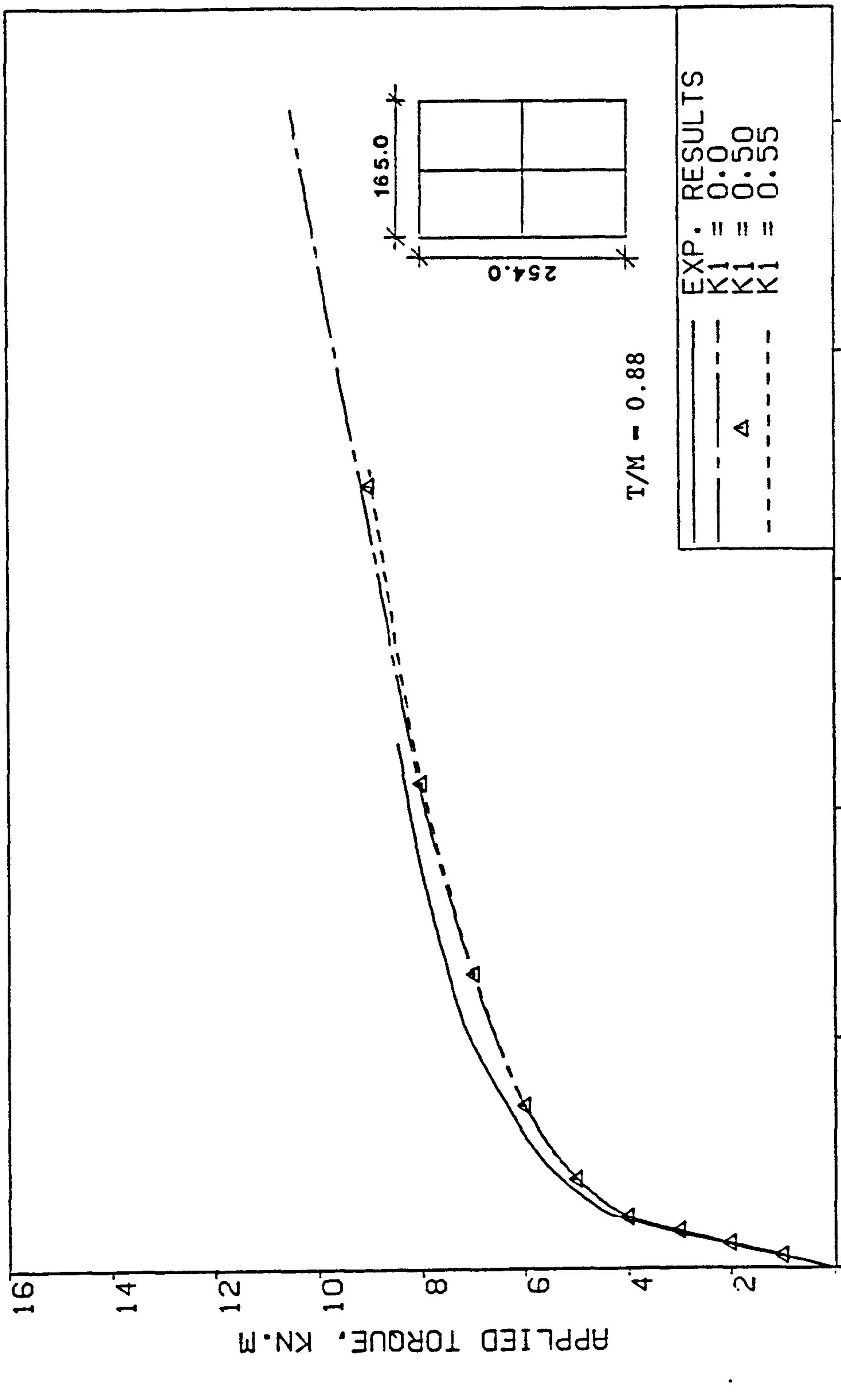

Fig. 7.35 Beam RE4 – Effect of the compression reduction parameter k_1 on the torque–twist behaviour.

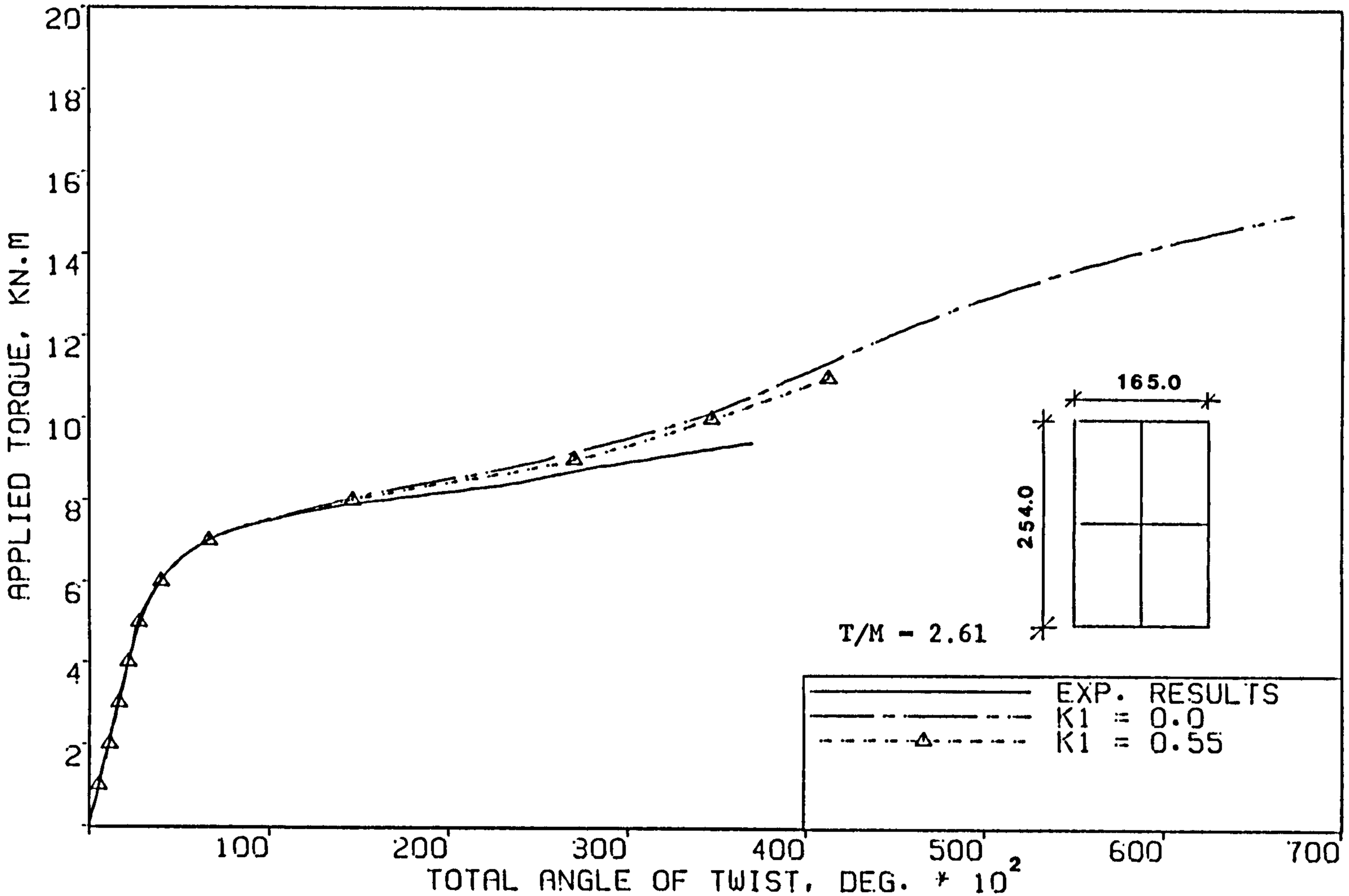

Fig. 7.36 Beam RE2 - Effect of the compression reduction parameter k_1 on the torque-twist behaviour.

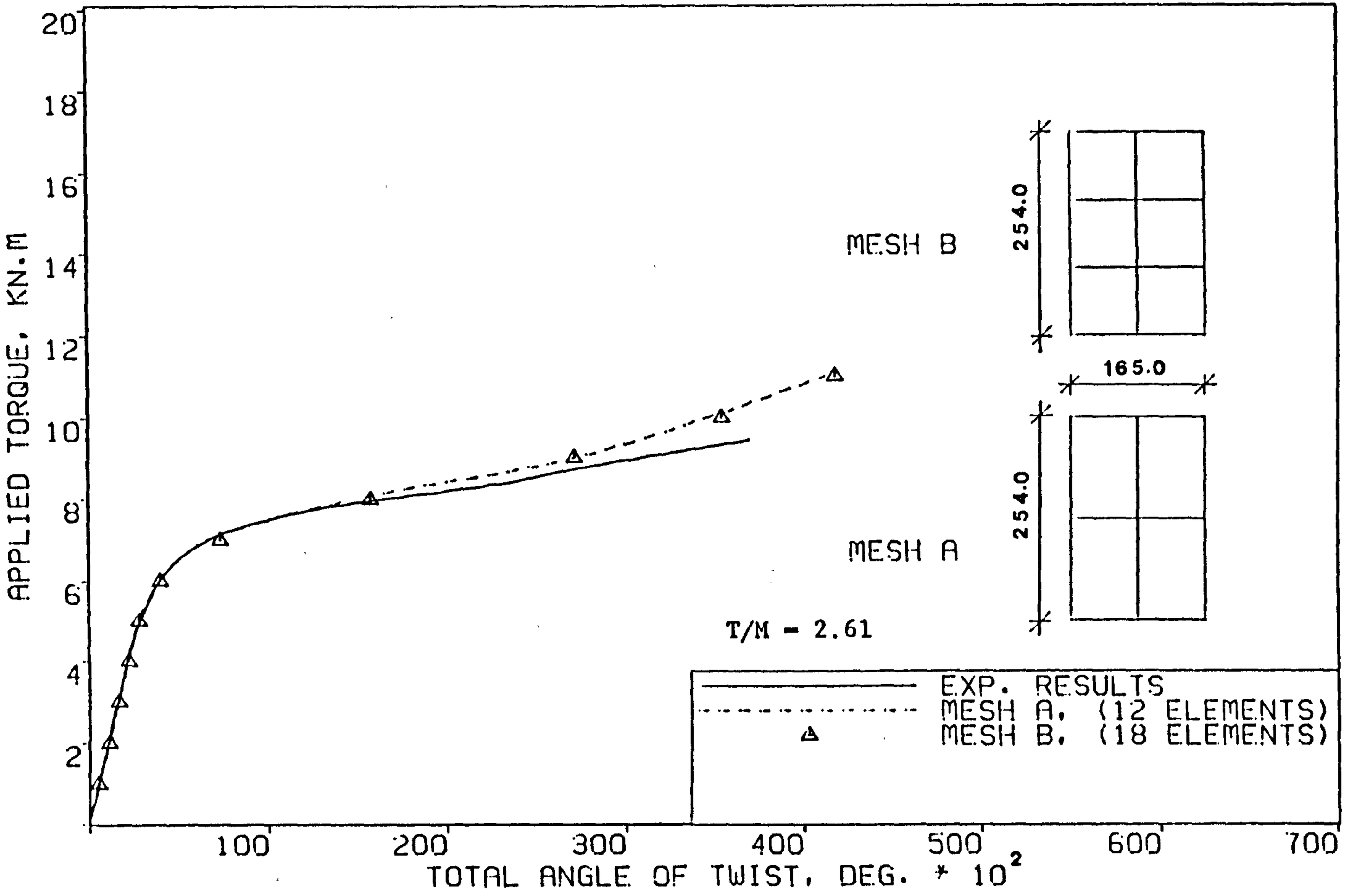

Fig. 7.37 Beam RE2 - Effect of mesh size on the torque-twist behaviour.

REFERENCES

1. Hsu, T.T.C, "Torsion of Structural Concrete–Behaviour of Reinforced Concrete Rectangular Members", Torsion of Structural Concrete, SP-18, Amer. Conc. Inst., Detroit, 1968, pp. 261–306.

2. Collins, M.P., Walsh, P.F., Archer, F.E. and Hall, A.S., "Ultimate Strength of Reinforced Concrete Beams Subjected to Combined Torsion and Bending", Torsion of Structural Concrete, SP-18, Amer. Conc. Inst., Detroit, 1968, pp. 379–402.

3. Hsu, T.T.C, "Torsion of Structural Concrete–Plain Concrete Rectangular Sections", Torsion of Structural Concrete, SP-18, Amer. Conc. Inst., Detroit, 1968, pp. 203–283.

4. ACI Committee 318, "Building Code Requirements for Concrete (ACI 318-71)", Amer. Conc. Inst., Detroit, 1971.

5. Hsu, T.T.C. and Mattock, A.H., "A Torsion Test Rig", J. of PCA Research and Dcevelopment Laboratories, Vol. 7, No. 1, January 1965, pp 2-9.

6. Mohamed, M.S., "A Finite Element and Experimental Study of Reinforced Concrete Beams in Torsion", Ph.D. Thesis, University of Glasgow, 1986.

7. Cervenka, V., "A Constitutive Model for Reinforced Concrete", J. of the Amer. Conc. Inst., Vol. 82, November–December 1985, pp. 877–882.

8. Vecchio, F. and Collins, M.P., "The Response of Reinforced Concrete to In–plane Shear and Normal Stresses", Publication No. 82-03, University of Toronto, Canada, 1982.

9. Vecchio, F.J. and Collins M.P., "The Modified Compression–Field Theory for Reinforced Concrete Elements Subjected to Shear", J. of the Amer. Conc. Inst., March-April 1986, pp. 219-230.

10. Phillips, D.V. and Mohamed, M.S., "Analysis of Reinforced Concrete Beams in Torsion", Proc. 2nd Int. Conf. Civ. and Struct. appl. of Comput., London, December 1985, pp 305-311.

11. Bergan, P.G. and Holand, I., "Non–Linear Finite Element Analyses of Concrete Structures", Comput. Meth. in Appl. Mech. and Eng., Vol. 17/18, 1979, pp. 443-467.

CHAPTER EIGHT

SUMMARY AND CONCLUSIONS

8.1 Summary

A computer program suitable for the non-linear finite element analysis of three-dimensional reinforced concrete, or steel, structures under monotonically increasing load has been developed. The 20 noded isoparametric brick element has been used to model the concrete and reinforcement bars are simulated as axial members embedded within the concrete elements. The numerical integration has been generally carried out using the 15 point Gaussian type integration rules. Efficiency and accuracy of these rules have been compared with the 27(3X3X3) point Gaussian rule.

In view of the scatter of experimental results for concrete and the variation of material properties throughout a reinforced concrete member, the numerical material models are kept as simple as possible so they can be simply implemented in finite element programs. However, such models should be able to simulate the main aspects of the behaviour. In the present study, a plasticity model for concrete in compression and a smeared crack model for concrete in tension have been used.

In compression, the behaviour of concrete is simulated by an elasto-plastic work hardening model followed by a perfectly plastic plateau which is terminated at the onset of crushing. The growth of

subsequent loading surfaces is described by an isotropic hardening rule. A parabolic equivalent uniaxial stress–strain curve has been used to represent the work hardening stage of behaviour and plastic straining is controlled by an associated flow rule.

In tension, linear elastic behaviour prior to cracking is assumed. Cracking is governed by the attainment of a maximum principal stress. A smeared crack model with fixed orthogonal cracks has been used. A maximum of three sets of orthogonal cracks are assumed to form at a sampling point. Closing and re–opening of these cracks are allowed to occur. The post–cracking tensile stress–strain relation and the reduction in shear modulus of cracked concrete with increasing tensile strain are modelled using bilinear curves.

Because the present work is devoted towards the analysis of reinforced concrete members which fail in shear or torsional modes, special emphasis has been given to model the degradation in the compressive strength of concrete due to the presence of tensile straining of transverse reinforcement. Three different models have been have been incorporated in the developed computer program based on the proposals of Cervenka [1] and Vecchio and Collins [2,3].

Reinforcing bars are assumed to be capable of transmitting axial forces only. The behaviour of reinforcement is simulated by an elastic linear work hardening model. Perfect bond is assumed between steel end concrete.

The non–linear equations of equilibrium have been solved using an incremental–iterative technique operating under load control. The

non-linear solution algorithms used in this work are the standard and the modified Newton-Raphson methods. Line searches have been implemented to speed up convergence.

The inclusion of material models for both steel and concrete allowed the computer program to be used for investigating the problem of elasto-plastic torsion of homogeneous solid members. Numerical tests are described which have been carried out for beams of different cross-sections subjected to pure and warping torsion. Results of the finite element analyses have been compared with the available exact or approximate analytical solutions. Parametric studies to investigate the effects of warping restraint, different types of elements, different integration rules and mesh refinement have been carried out. An iterative scheme has been proposed to determine the correct distribution of the external applied nodal loads equivalent to the elastic pure torque.

The program has been tested by analysing reinforced concrete panels loaded in pure shear and voided slab strips under pure bending. The numerical results obtained for these two sets of problems have been compraed with the experimental tests. The ability of the material model to simulate the behaviour of reinforced concrete subjected to longitudinal compression coupled with transverse tension is demonstrated by analysing the panels tested by Vecchio and Collins [2]. The models proposed to reduce the concrete compressive strength due to orthogonal cracking have been used and compared. The effects of tension-stiffening, shear retention and other important parameters have been also investigated.

The three-dimensional finite element model has also been used to study the behaviour of reinforced concrete beams loaded in pure torsion and torsion in combination with bending. The numerical solutions have been compared with the experimental torque-twist curves. The effect of reducing the concrete compressive strength in presence of orthogonal cracks on the post-cracking stiffness and ultimate strength of torsional members has been investigated. Parametric studies to investigate the effect of some of important material and solution parameters have been carried out.

8.2 Conclusions

Based on the numerical tests described in the previous Chapters the following conclusions can be drawn with regard to the results obtained for elasto-plastic members loaded in torsion and reinforced concrete members under various loading states.

8.2.1 Elasto-Plastic Members under Torsion

1. The three-dimensional finite element model adopted in this work has been successfully used to predict the elasto-plastic behaviour of beams subjected to torsion. Results of the numerical tests using the 20 noded isoparametric brick element demonstrate the validity of the present approach for both pure and warping torsion problems. The assumed quadratic displacement function is effective and accurate enough to represent the warping displacements of the cross-sections when compared with

the cubic displacement function.

2. The 15 sampling point integration rules that have been used in the present work are predict accurately the torque-rotation relationship in both the elastic and the elasto-plastic stages of behaviour, and are computationally efficient compared to the 27 point integration rule.

3. The iterative scheme which has been proposed in order to simulate the external torque as an equivalent set of nodal loads has proved to be effective in determining the correct distribution of the applied loads on the nodes of the loaded cross-section. In the elasto-plastic range the elastic distribution of loads has been used. The results obtained from the finite element analysis are still close to the theoretical results.

4. For I-beams with warping restraint, the finite element solution shows that the predicted collapse torque converges to the value predicted by Dinno and Merchant [4]. These results lend support to the finding of Baba and Kajita [5] that Merchant's upper bound is a reasonably accurate method for estimating the plastic collapse torque of I-sections beams subjected to warping torsion.

8.2.2 Reinforced Concrete Members

1. The three-dimensional finite element model adopted is able to simulate the behaviour of reinforced concrete members in which

shear or torsion dominates. In particular, the behaviour associated with the presence of longitudinal compressive stresses coupled with tensile straining of transverse reinforcement has been investigated. Results of numerical tests carried out for members loaded in pure torsion and torsion plus bending indicate that the post-cracking stiffness and the ultimate capacity of torsional members can be predicted reasonably well by the inclusion of the degradation in the compressive strength of cracked concrete. A similar conclusion can also be drawn from the analyses carried out for reinforced concrete panels loaded in pure shear.

2. The unconservative nature of Rausch's equation [6] can be attributed to not accounting for the deterioration in the compressive strength of concrete struts caused by the tensile straining of longitudinal bars and stirrups. The reduced compressive stress requires that the depth of the compression zone to equilibrate the tensile forces in the reinforcement to be significantly increased. Hence, the actual lever arms of internal couples are considerably less than those assumed by Rausch's equation, (1.5), the centre-to-centre distances between stirrup legs. This conclusion is further supported because the predicted torque-twist relations obtained for a number of beams analysed without considering the degradation in the compressive strength of concrete were appreciably stiffer than the experimental curves and the collapse torques were considerably overestimated. However, the correlation of the finite element solutions obtained for these beams with the experimental results has been significantly improved by the inclusion of the reduction

in the compressive strength of cracked concrete.

3. The models incorporated in the present study to reduce the concrete compressive strength have been compared by analysing a panel loaded in pure shear and a beam under pure torsion. The finite element solutions show that the overall behaviour obtained using the three different models is in good agreement with the experimental results. However, the best fit to the experimental curves was obtained using the model based on Cervenka's proposal [1].

4. For beams under pure torsion, the numerical tests revealed that the behaviour at early stages after cracking does not seem to be significantly affected by reducing the compression strength of cracked concrete. However at loading stages close to the ultimate torque, the post-cracking torsional stiffness is strongly affected by reducing the concrete compressive strength.

5. The degradation in concrete compressive strength has a negligible effect on the stiffness of reinforced concrete panels loaded in pure shear but can significantly reduce the collapse loads. A similar conclusion was also arrived at by Cervenka [1].

6. For beams loaded in combined torsion and bending, the effect of reducing the compressive strength of cracked concrete on predicting the ultimate torque increases as the ratio of the torque to the bending moment increases.

7. The inclusion of the reduction of the concrete compressive

strength does not have a significant influence on reinforced concrete flexural members. Results of numerical tests carried out for voided slab strips under pure bending show that neither the post-cracking response nor the ultimate moment have been affected by reducing the compressive strength. However, it may be useful to include a compression strength reduction model in all finite element applications for reinforced concrete since the mode of failure is usually not known before the analysis is conducted.

8. It was found that for members in which the principal directions may rotate after cracking, the predicted response close to the ultimate stage was stiffer than the experimental behaviour. This is probably because a fixed crack model has been used in the present study.

9. The inclusion of tension-stiffening models for the cracked concrete can significantly improve the correlation of the predicted torsional stiffness with the experimental results at early stages after cracking. A response softer than the experimental torque-twist curves was obtained when the tension-stiffening effects were neglected. However as the angle of twist increases, the tension-stiffening effect becomes progressively less significant and can be generally neglected at very high twist. A similar conclusion can be drawn from analysing the voided slab strips under bending.

10. The results obtained for beams under torsion confirmed that in the presence of a compressive strength reduction model, the

tension-stiffening parameters should be similar to those used for members in which bending dominates.

11. The post-cracking longitudinal extension that occurs in reinforced concrete beams under torsion has been predicted. The numerical tests show that the extension that occurred along the edges of the cross-section is larger than that which occurred at the centre of the section, and the extension is locally arrested at the corners by the presence of longitudinal bars. In addition, it was found that the member can also extend transversly as a result of concrete cracking.

12. In finite element analysis of reinforced concrete members loaded in torsion, the 15 sampling point rules are accurate and computationally efficient compared with the 27(3X3X3) point rule. These conclusions were similar to those drawn from the analyses of elasto-plastic members under torsion.

13. Acceptable results with a relatively cheap cost have been obtained from the analyses of reinforced beams in torsion and panels in pure shear using force convergence tolerances ranging from 2% to 5%.

8.3 Suggestions for Further Research

1. The program could be used to carry out full range tests of reinforced concrete members under torsion and torsion in combination with bending and shear to obtain information that

would help in the development of more accurate and refined design procedures.

2. The three-dimensional finite element model could be used to investigate the behaviour of reinforced concrete slab systems and biaxially loaded short columns.

3. More experimental data is needed to gain a better understanding of the behaviour of reinforced concrete subjected to longitudinal compression coupled with transverse tension. Such data would help in the development of more refined compression strength reduction models.

4. The accuracy and versatility of the developed computer program could be improved with the inclusion of the following refinements.

a) To implement a displacement control incrementation scheme in order to trace the structural response beyond the ultimate load.

b) To include the effects of geometrical non-linearities in order to extend the versatility of the program to investigate the torsional behaviour of elasto-plastic flanged members in presence of large displacements, the effects of membrane forces on the behaviour of plates and slabs and to study the behaviour of slender columns under biaxial loading.

c) To improve the performance of the cracking model by using a multi-directional crack model [7,8].

d) To use a plastic-fracturing model [9] in order to account for softening of concrete in compression.

REFERENCES

1. Cervenka, V., "A Constitutive Model for Reinforced Concrete", J. of the Amer. Conc. Inst., Vol. 82, November–December 1985, pp. 877-882.

2. Vecchio, F. and Collins, M.P., "The Response of Reinforced Concrete to In-Plane Shear and Normal Stresses", Publication No. 82-03, University of Toronto, Canada, 1982.

3. Vecchio, F.J. and Collins M.P., "The Modified Compression-Field Theory for Reinforced Concrete Elements Subjected to Shear", J. of the Amer. Conc. Inst., March-April 1986, pp. 219-230.

4. Dinno, K.S. and Merchant, W., "A Procedure for Calculating the Plastic Collapse of I-Sections under Bending and Torsion", Struct. Engr. Vol. 43, 1965, pp. 219-221.

5. Baba, S. and Kajita, T., "Plastic Analysis of Torsion of a Prismatic Beam", Int. J. for Num. Meth. in Eng., Vol. 18, 1982, pp. 927-944.

6. Rausch, E., "Design of Reinforced Concrete in Torsion" (Berechnung des Eisenbetons gegen Vendrehung), Ph.D. Thesis, Technische Hochsechule, Berlin, 1929 (in German).

7. De Borst, R., "Computational Aspects of Smeared Crack Analysis", In the Computational Modelling of Reinforced Concrete Structures, Eds. Hinton, E. and Owen, R., Pineridge Press, Swansea, U.K., 1986, pp. 44-83.

8. Rots, J.G, "Computational Modelling of Concrete Fracture", Ph.D. Thesis, University of Technology, Delft, 1988.

9. Bazant, Z.P. and Kim, S.S., "Plastic-Fracturing Theory for Concrete", J. of the Eng. Mech. Div., ASCE, Vol. 105, June 1979, pp. 407-428 with Errata in Vol. 106.